UNIVERSITÉ DE LIMOGES

ÉCOLE DOCTORALE N°521: SCIENCES ET INGÉNIERIE POUR L'INFORMATION

FACULTÉ DES SCIENCES ET TECHNIQUES

Laboratoire XLIM, Département C^2S^2: Composants Circuits Signaux et Systèmes Hautes Fréquences et

Orange Labs, Unité ASHA: Advanced Studies on Home and Access Networks

Anée: 2012 Thèse N°58-2012

Thèse

pour obtenir le grade de

DOCTEUR DE L'UNIVERSITÉ DE LIMOGES

Spécialité: Électronique des Hautes Fréquences et Optoélectronique

presentée et soutenue par

Luiz ANET NETO

le 14 Décembre 2012

ÉTUDE DES POTENTIALITÉS DES TECHNIQUES DE MODULATION MULTIPORTEUSE POUR LES FUTURS RÉSEAUX D'ACCÈS OPTIQUE WDM ET TDM PON

Thèse dirigée par **Christelle AUPETIT-BERTHELEMOT** et **Naveena GENAY**

Jury:

Didier Erasme	Professeur, InstitutMines-Telecom/Telecom ParisTech	**Président**
Michel Joindot	Professeur Associé, Laboratoire FOTON, ENSSAT	**Rapporteur**
Jianming Tang	Professeur, Bangor University	**Rapporteur**
Christelle Aupetit-Berthelemot	Professeur, Université de Limoges/ENSIL	**Examinateur**
Naveena Genay	Ingénieur R&D, Orange Labs Lannion	**Examinateur**
Iyad Dayoub	Maître de Conférences HDR, Université de Valenciennes	**Examinateur**
Jean-Michel Dumas	Professeur, Université de Limoges/ENSIL	**Examinateur**

To my parents, Dora and Luiz,

to my grandfathers, Luis and Carlos,

to my dearest friend, Teresa

y para ti.

Acknowledgments

I would like to thank Thierry Stephant, Bernard Le Floch and Bernard Landousies for supporting this thesis at first place and for their interest on the research topic I was lucky to work with. I would also like to thank Raymond Quéré for supporting the partnership between Orange Labs and the University of Limoges under which this thesis was realized. I express my gratitude to the members of the jury for accepting the invitation to evaluate this work: Michel Joindot, Jianming Tang, Didier Erasme, Iyad Dayoub and Jean-Michel Dumas. I particularly thank Didier for all the fruitful discussions and for his help on some publications we could do together and Jianming for very kindly receiving me in Bangor in my first year of thesis.

This work would not have been possible without the guidance and the help of many individuals that contributed and extended their valuable assistance in the completion of this study. I would like to thank my supervisors Naveena Genay, for her support, kindness and serenity, principally during the stressful moments and Christelle Aupetit-Berthelemot, for her sympathy, availability and, above all, enthusiasm. I am also especially grateful to Benoît Charbonnier, for patiently sharing his knowledge whenever I needed and for helping me make some sense out of my confusion and Philippe Chanclou, for unceasingly and energetically instigating me to get the most out of this work and for always figuring it out whenever I got stuck in my experiments. I would also like to thank Philippe and Stéphane Gosselin for their experienced and intelligent opinions on *real-life* optical networking. I could not forget to thank Nicolas Brochier and Jean-Luc Barbey for unhesitatingly supporting and helping me in my submarine network discovery. I also thank Suzanne Salaun, for giving me a first chance in Orange. Let me also thank the colleagues from 3S Photonics Victor Rodrigues and Emmanuel Grard for the their collaboration and for developing such performing lasers.

I would also like to express my deep sense of gratitude to all colleagues in the unit ASHA in Orange Labs with whom I was lucky to share such a convivial, friendly and pleasant atmosphere during these three years. The least I can do is thank them one by one: Ahmed Gharba, Anna Pizzinat, Aurélien Lebreton, Bernard Landousies, Bertrand Le Guyader, Fabia Raharimanitra, Fabrice Bougart, Francis Richard, Floriant Frank, Jacky Etrillard, Joffray Guillory, Laurent Guillo, Maxime Leroux, Moufida Feknous, Thanh-Nga Duong, Philippe Guignard, Qian Deniel, Rongping Zhang, Sebastien Deniel, Sylvain Meyer and Quang Trung Le. I specially thank Alexandre Brongniart and Joffray Guillory for the many discussions about OFDM which helped me improve my work. I must also thank Joffray, for all the philosophical inquires about EVM and BER conventions and the colleagues from other units: Karinne Sevilla, Philippe Niger and Pierre Jaffré, for the animated discussions during lunch. I am grateful to Fabienne Saliou and Thomas Anfray, who managed to demonstrate that it was possible to dance the cha-cha-cha with any existing music in the world. I cherish with fondness the memory of that night of much laughing in Turin. I could not forget to thank Oscar Olvera, not only for his company during much time and for his untiringly funny "corte de urubu" jokes but also for the many gastronomical invitations to his place and also Abdesselem Kortebi for patiently listening to my repetitive and pessimistic forecasts about Brazilian soccer. Let me also thank the colleagues from XLIM: Thierno Barry and Fréjus Sanya (why are you staring at me?), for warmly welcoming me in my visits to Limoges and for introducing me to the African culinary art and Marie-Claude Lerouge, for doing the impossible to help me with all administrative processes in the University.

I cannot forget to thank Ricardo Ribeiro and Pablo Barbero for awakening my interest in optical research when I was still an undergraduate student back in Brazil.

I would like to express my gratitude to my lovely and beautiful Patricia Ruiz, who has endured this long process with me, always offering support and love in spite off my too often bad temper and for helping me solving my logical and programming-related issues during these years. I would also like to thank Patri as well as my *breizhilian* friends Vinicius, Luiz Felipe and Kedar for their efforts on keeping me from assassinating my social life and for inadvertently helping me rendering this work less arduous.

Last but certainly not the least, I thank my parents for their love, support, guidance and for giving me the means for pursuing my dreams. They are and will always be my most inspiring examples. The only thing keeping this experience from being perfect was the distance separating us. Let me finish by showing my most sincere gratitude to a special friend who never lets me forget He is always by my side.

Summary

Preface

Information revolution is knocking at the door. From mobile devices enabling connectivity anytime-and-anywhere to cloud storage systems, 3D and high definition video broadcasting and many other bandwidth-hungry services, telecommunication networks are being increasingly solicited whether in the long-haul or access spheres.

While in the long-haul the price of a specific solution is disseminated through a thicker "data pipe" allowing thus more complex and expensive approaches, cost-effectiveness is a critical aspect in access networks. Indeed, the choice of a specific technology will have a great influence on the price of the services that are provided to the final user. Since the access bottleneck cannot be eliminated by using exclusively currently-installed copper-based solutions, the future of access networks passes necessarily through an optical transmission approach which must allow exploiting the optical fiber's increased bandwidth and reduced attenuation in a way that is economically viable to the subscribers.

Passive Optical Networks (PON) appear as the most appropriate solution for doing so since they allow the mutualization of great part of the network's infrastructure between several subscribers in a point-to-multipoint (P2MP) fashion. Currently deployed Gigabit PON have permitted a huge dissemination of Fiber-To-The-Premises (FTTP) systems all over the world principally in Asia but are close to exhaustion in some countries. That is why many efforts have started to be made to conceive what is known as Next-Generation Passive Optical Networks (NG-PON). The first step (NG-PON1) of this evolution has already been standardized and should soon begin to be deployed and some prototypes are already being evaluated today. It is based on 10Gb/s/wavelength capable systems that focus principally on keeping most of the legacy infrastructure unchanged. The second step (NG-PON2) targets sustainable 1Gb/s/user and must be capable of accommodating different uses, from the standard Fiber-To-The-Home (FTTH) to mobile backhauling or hybrid fiber+copper/coaxial solutions or even greenfield scenarios. Actually, it will most likely imply a paradigm shift in terms of transmission approach with significant changes in the network infrastructure.

This is because the transmission of bits through "naive" ON/OFF keying of the light emitted by a source is not a good solution for circumventing the limitations imposed by the fiber's chromatic dispersion when increased bit-rates and/or transmission distances are required. Several candidates exist to address this issue. One of them is Orthogonal Frequency Division Multiplexing (OFDM). OFDM has been adopted with huge success in many standards and benefits from increased robustness to dispersion and very high spectral efficiencies. As far as its usage on a PON is concerned, it would not only allow transferring the system complexity from the optical plan to the electronic domain, the latter supported by Moore's conjecture, but would also provide the dynamics that lack on today's "rigid" optical systems through the sharing of the subcarriers amongst the subscribers.

This thesis focuses on the study of the pros and cons of intensity-modulated and directly detected (IMDD) OFDM for next generation passive optical networks. It will be oriented on three main axes: the physical phenomena ruling the transmission through an optical fiber, the digital signal processing techniques necessary for better understanding the modulation and demodulation of an OFDM signal and finally the difficulties and possibilities of implementation in several different PON architectures. To do so, we divide this work into four parts.

Chapter 1 is dedicated to a brief review of PON standards and the perspectives of its evolution towards NG-PON2, including the main requirements and possible technological candidates. Part I brings a theoretical overview on the mechanisms of propagation through an optical fiber and the transceiver's characterization with a special focus on the typical frequency response of a dispersive IMDD channel. It also addresses the main mechanisms of the modulation and demodulation procedure of an OFDM signal, including time and frequency synchronization techniques, different optical OFDM transmission approaches, adaptive bit and power loading algorithms and multi-user techniques for sharing the OFDM subcarriers amongst different users of a PON. Even though the objective of this part is to give a theoretical basis necessary for the comprehension of the present work, we always try to illustrate it with real-life examples, either by showing some typical problems that had to be dealt with throughout this work or by means of simulations using real measured parameters. Part II is dedicated to a purely experimental investigation on the performances of OFDM either in the upstream or downstream directions of a PON. Not only do we try to assess the concurrent use of OFDM with other multiplexing approaches such as time and wavelength but we also manage to highlight the advantages and drawbacks of each solution vis-a-vis of its implementation in a real network. Part III also brings some other interesting results that could not be classified into upstream/downstream, namely an algorithm proposal to address the energy consumption of the transceivers. Finally, in Part IV we summarize and conclude this work.

This thesis has been carried out in the department ASHA (Advanced Studies on Home and Access networks) of Orange Labs/France Telecom in collaboration with the institute XLIM, department C^2S^2 (Composants, Circuits, Signaux et Systèmes Haute Fréquence) of the Université de Limoges. It has been realized within the framework of projects EPOD (Enhanced PON using OFDM Modulation Format), ALPHA (Architectures for Flexible Photonic Home and Access Networks), MODULE (Modulation Duale d'un Composant Intégré), TRILOB (modules de Transmission et Réception pour Liaison Optique à fort Budget), BONE (Building the Future Optical Network in Europe) and FAON (Frequency Based Access Optical Network).

Chapter 1

Context and Motivations

1.1 Introduction

We start this chapter by showing the importance of optical network solutions in view of nowadays' accelerating trend towards higher bandwidths. Then, we highlight the advantages of the point-to-multipoint optical architecture and we introduce different approaches used in the deployment of the optical fiber to the final user. We also recall the existing PON standards and we finish with the perspectives and key factors on the evolution towards future passive optical networks.

1.2 The Importance of Optical Access Networks

The current massive fiber deployment which is increasingly closer to end users has its origin on the relentless use of multimedia services through internet and highlights a growing need for higher bandwidths in access networks. Bandwidth-hungry services such as high definition telepresence, telemedicine and remote surgery, online gaming, 3D and HD video broadcasting, personal cloud storage systems and the increasing number of mobile devices allowing ubiquitous connectivity (anytime, anywhere) are just some examples that point out to the importance of enabling alternatives capable of providing higher throughputs. Indeed, non-fiber based solutions such as Digital Subscriber Line are not capable of solving the access bottleneck issue and should soon reach exhaustion. Figure 1.1 (from [1]) shows the minimum bandwidth requirements of some services.

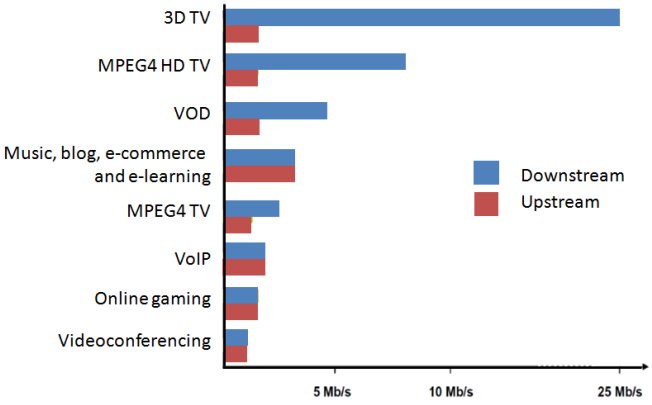

Figure 1.1: Bandwidth requirements per service (March 2012).

Cisco's Visual Networking Index [2] announced a monthly IP traffic of 20.2 exabytes (10^{18} bytes) in 2010 and forecasts that this number should quadruple by 2015. Other amazing pre-

dictions include the increase of video traffic:

> "It would take over 6 million years to watch the amount of video that will cross global IP networks each month in 2016."

and mobile traffic, which is expected to witness a 18-fold increase between 2011 and 2016. Figures 1.2 (a) and (b) show respectively Cisco's projection of global consumer internet traffic to 2016 by subsegment and geography which highlight a dramatic increase in bandwidth demand. We should basically notice here the predominance of video traffic over other services and the stringent throughput requirements in Asia.

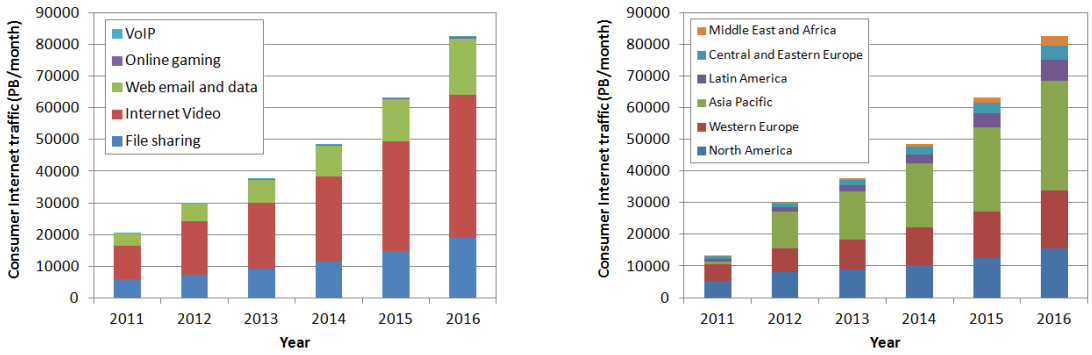

(a) (b)

Figure 1.2: Cisco's projection of global consumer traffic in petabytes per month to 2016 by (a) subsegment and (b) geography.

Fiber optical systems are the only solution capable of coping with such radical and urgent demands due to a considerably higher bandwidth and lower attenuation.

1.3 Point-to-point vs Point-to-multipoint

The most simplistic approach to connect the subscribers or Optical Network Termination (ONT)[1] of an optical network to the central office or Optical Line Termination (OLT) is by associating one fiber to each user in a point-to-point (P2P) fashion, such as depicted in Figure 1.3(a). Despite the fact that this approach allows guaranteeing the whole of the network physical resources to each user individually, we do not need to go far to see that it becomes extremely unpractical for increasing number of subscribers due to the needed investments in fiber deployment and management.

The biggest advantage of point-to-multipoint (P2MP) approaches on the other hand is that they enable the mutualization of the network feeder fiber, thus allowing considerable cost savings. Sharing of fiber resources can be enabled by a simple optical coupler, which allows the outside plant (feeder fiber + distribution network) to remain passive, i.e., needless of electrical powering. Such networks are known as Passive Optical Networks (PON) and are depicted in Figure 1.3(b). The network resources can be distributed to the final users through wavelength, time and/or frequency multiplexing techniques, whose pros and cons will be discussed throughout this thesis[2].

[1] An ONT is a ONU (Optical Network Unit) in which one single subscriber terminates one of the endpoints of the Optical Distribution Network. In this work, we adopt the more general term ONU, which may imply a multi-user hybrid approach.

[2] From know on, we adopt the term "multiplexing" for downstream PON transmissions (from OLT to ONU) and "multiple access" for the upstream (from ONU to OLT).

The reader should notice that the optical power budget of a PON, i.e., the difference between the transmitted and received powers, will determine the maximum number of splitter stages or, equivalently, subscribers in the network.

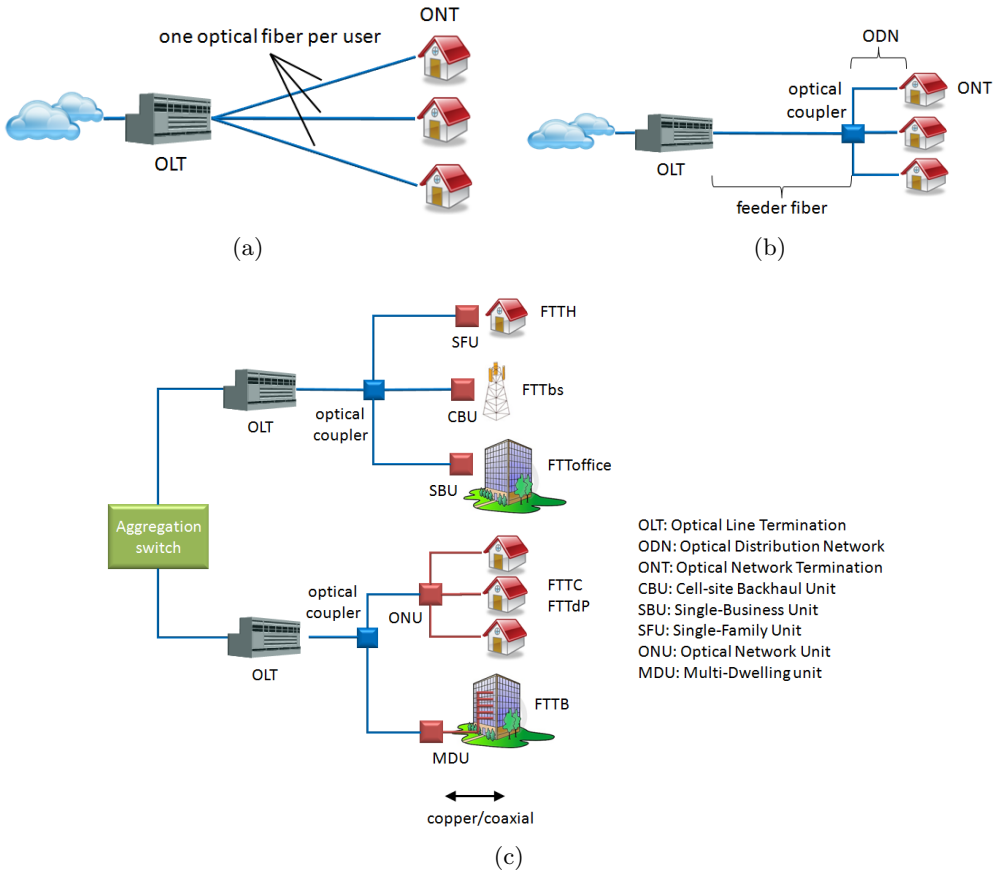

Figure 1.3: (a) Optical point-to-point network. (b) Passive optical network. (c) Hybrid passive optical network.

1.4 FTTx: What does "x" Mean to Who?

Even though the number of Fiber-To-The-Home (FTTH) deployments have considerably increased in the last years, the fiber does not necessarily need to arrive at the subscriber's residence. Indeed, the optical access network can be complemented by other types of distribution approaches such as copper or coaxial-based links, as we can see in Figure. 1.3(c). In this case, the network is said to have a hybrid architecture

Different fiber deployment strategies adopted around the world have caused the creation of a wave of acronyms to designate the optical access network. We can mention, for instance, Fiber-To-The-distribution-point (FTTdp), Fiber-To-The-Curb (FTTC), Fiber-To-The-Premises (FTTP), Fiber-To-The-Building (FTTB), Fiber-To-The-base-station (FTTbs) and etc. These reflect a specific choice in terms of architecture that is made considering the services that need to be provided to the final users. Actually it also depends on several particularities of each specific environment on each country, such as the urbanization level and predominance of collective housing, the efficiency of existing telecom infrastructure, the financial implication of public actors and the national regulations [1].

For example, British Telecom has started large scale fiber deployments in 2010 targeting mostly FTTC with Very-High-Bit-Rate Subscriber Line 2 (VDSL2) over existing copper connections from street cabinets and a smaller percentage of FTTP all the way down to the customer

premises. They have also engaged a commercial plan in which they consider selling fiber access to other service providers.

In Japan, where the number of fiber subscribers has already exceeded the number of Asymmetric Digital Subscriber Line (ADSL) clients, most of NTT's services are provided using FTTH for single family houses. The remainder is assured using a combination of an Ethernet-based P2P systems and VDSL for multiple dwelling houses. China Telecom and China Unicom, on the other hand, have heavily invested on the deployment of FTTB solutions.

In France, Fiber-To-The-Last-Amplifier (FTTLA) solutions have been boosted by Numéricâble who kept the coaxial distribution inside the buildings to serve each apartment while Orange and SFR[3] maintained the classical passive P2MP approach and Free still struggles with a P2P business plan. The current census of French's regulation authority (ARCEP) accounts for 1.5 million home-passed (eligible) properties with pure FTTH, (45% with at least 2 operators via passive access) and 4.4 million with Hybrid fiber+coaxial access (29% of which are outside very dense zones). The number of FTTH subscribers by the first term of 2012 is estimated to 220000, representing an increase of 60% over a year whereas the statistics are considerably larger for FTTLA (495000 subscribers) despite a lesser increase of about 30% over a year. Orange will continue its investment program and plan to bring optical connectivity to 60% of French households by 2020.

The reader is referred to [1] for a very interesting analysis on different funding models concerning the deployment of high bit-rate infrastructures.

1.5 PON Overview

Passive Optical Networks have been standardized by two different bodies: the Institute of Electrical and Electronics Engineers (IEEE) for systems mostly deployed in Asia and the International Telecommunication Union (ITU) in Europe and America.

Within IEEE, the Ethernet PON (EPON or GEPON) IEEE 802.3 standard has been completed in 2004 targeting $1Gb/s$ symmetrical bit-rates and being mostly adopted in China and Japan. The main objective of this standard was to preserve compatibility with Ethernet framing. The following generation, known as 10G-EPON and standardized as IEEE 802.3av in 2009, stipulates either symmetrical (designation PR) $10Gb/s$ or asymmetrical (designation PRX) $10Gb/s$ downstream and $1.25Gb/s$ upstream bit-rates. Optical power budgets are divided into three classes: PR(X)10 from 5 to $20dB$, PR(X)20 from 10 to $24dB$ and PR(X)30 from 15 to $29dB$. The minimum split-ratio is 16 for PR(X)10 and 20 and 32 for PR(X)30. The minimum transmission distances are $10km$ for PR(X)10 and $20km$ for PR(X)20 and 30. Chosen upstream wavelengths are in the 1310 and $1270nm$ windows for reduced impact of chromatic dispersion and the downstream wavelength is $1577nm$. Table 1.1 summarizes the 10G-EPON specifications.

Within the ITU, the earliest PON generation was based on Asynchronous Transfer Mode (ATM) operation and was known as APON. It was later improved to provide $622Mb/s$ downstream and $155Mb/s$ upstream under the Broadband PON (BPON) standard ITU-T G.983. At the present time, ITU-T G.984 Gigabit PON (GPON), ratified in 2008, is widely deployed in Europe and North America. It supports either symmetrical $2.5Gb/s$ or asymmetrical $2.5Gb/s$ downstream with $1.25Gb/s$ upstream transmissions. These systems use simple Non-Return-to-Zero (NRZ) modulation, broadcast-and-select for the downstream and Time Division Multiple Access (TDMA) in the upstream to allow sharing capability. Downstream and upstream transmissions are made respectively at 1310 and $1490nm$. Optical budget is stipulated between 13 and $28dB$ (class B+) allowing 1:32, 1:64 through up to $20km$. Extended budgets allowing $17-32dB$ (class C+) operation by means of an active components in the outside plant have also been standardized under ITU-T G984.6.

[3] Actually, SFR network is composed by a mix between point-to-pont and point-to-multipoint, with a priority, however, for point-to-multipoint solutions.

Name	Downstr. bit-rate (Gb/s)	Upstr. bit-rate (Gb/s)	Downstr. wavelength (nm)	Upstr. wavelength (nm)	Optical budget (dB)	Minimum Split Ratio	Range (km)
PRX10	10.31	1.25	1577	1310(±50)	5-20	16	10
PRX20					10-24	16	20
PRX30					15-29	32	20
PR10		10.31		1270(±10)	5-20	16	10
PR20					10-24	16	20
PR30					15-29	32	20

Table 1.1: IEEE 802.3av 10G-EPON specifications.

Name	Downstr. bit-rate (Gb/s)	Upstr. bit-rate (Gb/s)	Downstr. wavelength (nm)	Upstr. wavelength (nm)	Optical budget (dB)	Split Ratio	Range (km)
Nominal 1	9.95	2.49	1577	1270(±10)	14-29	Up to 1023	20-60
Nominal 2					16-31		
Extended 1					18-33		
Extended 2					20-35		

Table 1.2: ITU-T XG-PON1 specifications.

The following next generation passive optical network (NG-PON1) was standardized as ITU-T G.987 and is known as XG-PON1. It keeps the broadcast and select and TDMA approaches and uses a wavelength overlay ($1575 - 1580nm$ downstream and $1260 - 1280nm$ upstream) to guarantee compatibility with currently deployed Gigabit-PON. XG-PON1 should allow compatibility with class B+ optical budgets plus $1.5dB$ due to the insertion losses of the filtering device that must be added in the network. The supported throughputs are $10Gb/s$ in the downstream and $2.5Gb/s$ in the upstream. Table 1.2 summarizes the specifications for ITU-T's XG-PON1.

XG-PON1 may be considered as a mid-term upgrade towards a following generation, known as NG-PON2. As such, its main objectives are to allow the coexistence with currently deployed GPON and reuse of the outside plant [3]. XG-PON1 specifies 14 to $29dB$ (Nominal 1) optical budget for applications that are not co-existent and 16 to $31dB$ (Nominal 2) for applications that are coexistent; and at least 1:64 split ratio and $20km$ reach. It is also compliant with the RF video channel at $1550nm$. The reader is referred to [4] for a synthesis of XG-PON1 physical layer specifications.

1.6 Perspectives and Key factors on the Evolution Towards NG-PON2

At the present time, the standardizations on $10Gb/s$ Next Generation PON are mostly finished. The first field trials on XG-PON (ITU-T G.987) and 10GE-PON (IEEE 802.3av) have been carried out in the United States [5] and Asia [6] and some compliant XFP modules are already available in the market [7–9].

However, despite the fact that NG-PON is only in the first flush of its youth as the successor of currently deployed GPON (ITU-T G.984) and GEPON (IEEE 802.3), discussions about a following generation capable of offering beyond $10Gb/s$ capacity and known as NG-PON2 have already started at the Full Service Access Network (FSAN), the pre-standardization consortium (Figure 1.4) that will guide ITU's decisions. To allow for such evolution, a new technological approach might have to be envisaged, the current existing techniques being unable to provide

for the desired performances. The minimum bit-rate requirement for an individual NG-PON2 feeder is $40Gb/s$ downstream and $10Gb/s$ upstream. These values were driven by a per-customer target throughput of $1Gb/s$.

(a) (b)

Figure 1.4: FSAN members: (a) Telcos. (b) Vendors.

As it always happens with new telecommunication technologies, NG-PON2 guidelines will be determined on the one hand by vendors willing to have the necessary volume of sales that justifies their investments on a new solution and, on the other hand, by operators who will prioritize the less risky, disruptive and expensive alternative vis-a-vis their currently installed infrastructure. Indeed, from the point of view of an operator, the following generation of passive optical networks should offer the needed scalability and flexibility that will allow addressing current and future services through a seamless, perennial and, of course, cost-effective approach.

FSAN's timetable forecasts the first NG-PON2 systems to be deployed in 2015 meaning that the first equipment must be ready for evaluation and testing by 2014. A first standard is not expected, however, before mid-2013 at the earliest and the first pre-recommendation document should be delivered to ITU by the end of 2012 with a clear technological choice [10]. Bearing in mind these deadlines, it may be possible that some operators may not even get to deploy NG-PON1, the upgrading being done directly from GPON to NG-PON2. Once FSAN has concluded its studies, the ITU will start working on the physical layer, the media access controller and the customer premise equipment requirements.

In this section, we highlight some of NG-PON2 drivers and desirable requirements and review the trade-offs of potential technological candidates identified by the FSAN. Optical OFDM is one of such candidates. Figure 1.5 (adapted from [11]) shows the potential NG-PON2 solutions and migration paths.

1.6.1 Drivers and Requirements

Basically, NG-PON2 should focus on the four principal axes:

- Offering higher bit-rates than current technologies

We are witnessing today an ever-increasing demand for higher bit-rates and this should significantly impact all spheres of networking, including the access domain. Services like High-Definition telepresence allowing virtual meetings with life-sized, high-definition video and spatially distributed audio; telemedicine and remote surgery; video instant messaging with always-on connectivity; real-time data backup with personal cloud storage solutions; on-line gaming platforms; fixed access and mobile backhauling and 3D/HD/Super-HD/Ultra-HD video distribution (linear or VOD) are just some examples of applications demanding high bandwidths.

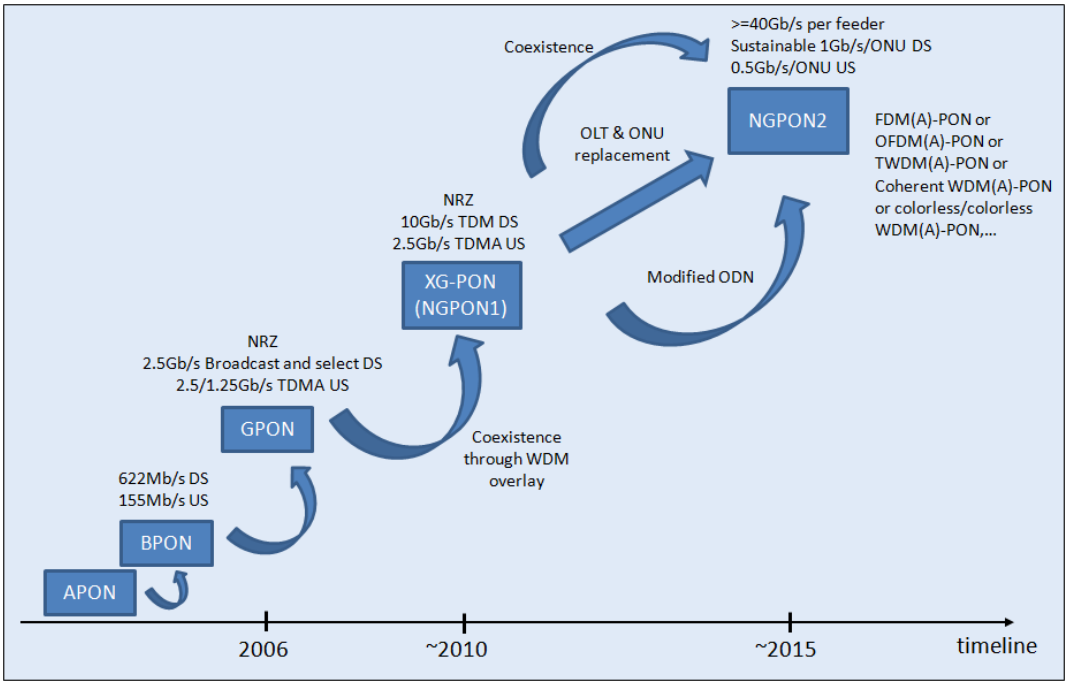

Figure 1.5: Potential NG-PON2 candidates and migration paths.

In general, video services are expected to represent the most part of the traffic by 2014 and some reports suggest that residential bandwidth requirements could surpass $250Mb/s$ by 2015 [11, 12]. The questions to be answered are whether a service or application capable of exhausting the capacity of current networks will really appear by 2020 and, if so, what will it be like.

This new "killer application" can be simply one (or a set) of the mentioned applications but may also be a whole new kind of massive content-rich service [12]. Indeed, this analysis should go way beyond a simple deterministic forecast of the bandwidth consumption. It should also consider the increasing democratization of technology and the resulting sociological phenomenon behind the "hyper-connectivity" tendency thus taking into account the needs of the users to have fast and reliable access to the network anytime and anywhere.

For example, data transmission has been responsible for most of the mobile traffic during the Olympic Games this year [13], showing an increase from 20% in 2008 (Beijing) to 80%. YouTube has registered a traffic augmentation of 40% in the first day of competition while the mobile application WhatsApp has witnessed an increase of 430% during the opening ceremony. Other surprising statistics include raises of 217% of the video streaming and 182% of the SMS. Data traffic is expected to rise up to 95% against only 5% of voice traffic in the Olympic Games in Rio in 2016. These are absolute proofs of the high popularization of mobile devices and their influence on the bandwidth requirements of the network.

- Allowing network consolidation through a reduction in the number of central offices and an increase in the number of subscribers in the network

The concentration of a higher number of clients per node will not only enable the simplification of the network structure and facilitate its management but may also allow significant cost savings due to a reduced number of access sites.

Such task is constrained to the enhancement of the optical budget and to the extension of the transmission distances. Indeed, the power of the emitter and the sensitivity of the receiver will have a direct influence on the split-ratio and extent of the network and that's why the use of optical amplification and even optical-electrical-optical regeneration has been considered in reach-extended solutions. The choice of an active or passive outside plant should also be taken into account.

Strictly speaking, the maximum range of a PON will be notably limited by the fiber's chromatic dispersion if an ordinary intensity modulation and direct detection approach is used, such as it is the case in current GPON. NG-PON2 should be capable of reaching at least $60km$ and serving at least 64 users. If we consider a loss of $3.5dB$ per $1:2$ splitter and $0.22dB/km$ in the $1550nm$ window, we may then conclude that NG-PON2's optical budget will require at least $34.2dB$, without considering the insertion losses of the filtering devices if ever they are introduced in the network either for guaranteeing operation with former generations or as a part of NG-PON2 solution.

We should also remark that extending the optical budgets of future networks could potentially allow for the integration of metropolitan and access networks.

- Preserving interoperability with formerly deployed generations and services while maintaining cost-effective solutions at the user side

Telecommunication networks never evolve abruptly. It is always necessary to guarantee the operation of legacy solutions through a smooth migration until the following generation is capable of maintaining the continuity of all services. This process is ideally transparent to the final user, avoids the disruption of the existing network and the wholesale upgrade of customers and should not inflect a huge increase in the price of the provided services. Co-existence of different generations may happen either exclusively on the feeder fiber or also on the distribution network [11] and it would be greatly preferable if the new generation is capable of reusing legacy infrastructure or at least avoiding dramatic changes on the deployed equipment.

NG-PON2 would have to reuse the deployed optical splitters and operate in the wavelengths that are not occupied by current generations. Indeed this raises an interesting point that should be of concern of Wavelength Division Multiplexing (WDM)-based candidates: the wavelength spectrum availability. Figure 1.6 (from [11]) shows the wavelength plans of currently deployed and future 10GE/XG-PON optical access networks. We can easily see that there is not much available spectrum for NG-PON2. The situation becomes even more critical if we remember that transmitter lasers designed to be low-cost are not wavelength-locked and may drift with ambient temperature variation, consuming thus the spectrum similarly to coarse WDM wavelength bands [10].

To aggravate the situation, the filtering specifications of an analogue video overlay provided by some operators such as Verizon and NTT could require a huge part of band C, precisely where the fiber losses are the least and where we could benefit from the use of erbium-doped fiber amplifiers. One solution to this issue is migrating this video channel to some sort of in-band IP-based service.

It should be noted, however, that although the minimum changes in the network infrastructure are highly desirable, NG-PON2 might contemplate major architecture changing through new technical approaches such as new ONU and OLT and even modified ODN (see Figure 1.5). That's one strong point differentiating NG-PON2 from NG-PON1.

- Providing long-term flexibility for current and future applications

Choosing a future-proof solution is the only way through which service providers will obtain the return on the investments they have made. The new generation should be able to cope with different types of legacy systems either for matters of a smooth migration but also for enabling, for instance, the coexistence of several NG-PON2 systems from different operators in the same infrastructure for regulatory impositions. It should also be capable of adapting to the evolution on the customers' demands on different scenarios so that a new capital expenditure (CAPEX) is avoided. By the way, the NG-PON2 system should ideally have the ability of being upgraded in a modular fashion, without the need of changing the whole set of equipments each time the users' demands grow.

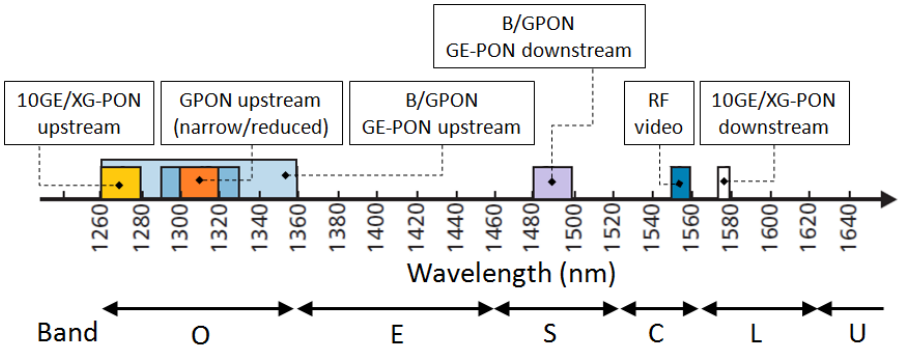

Figure 1.6: Wavelength plan of PON systems.

Flexibility would also be important for enabling network operation with different kinds of services whether they are used to serve mobile backhauling, business customers, FTTH clients or legacy low-bit-rate systems.

1.6.2 Possible Candidates. How Would OFDM Fit-in?

There are four main candidates for future NG-PON2. These are pure WDM, coherent ultra-dense WDM (UDWDM), hybrid time and wavelength division multiplexing (TWDM) and, of course, OFDM.

- Pure WDM

In WDM PON, one wavelength is attributed to each user of the network. Since the subscriber has the whole capacity of the optical channel to himself, it allows creating a virtual (or logical) P2P network based on a passive P2MP architecture. Other advantage of the solution is that it enables low latencies and modular capacity upgrades through simple stacking of wavelengths.

There are several variants of the WDM-PON approach which can be separated into two groups depending on whether the transceivers are “colored” or “colorless”. Colored WDM is based on the use of tunable transmitters and receivers at the OLT and ONU. In the colorless approach, a reflective device can be used at the ONU to modulate the light seeded by a source. Examples of colorless transmitters include reflective semiconductor optical amplifiers (RSOA) and reflective electroabsorption modulators with semiconductor optical amplifiers (R-EAM-SOA). As far as the source of seeded light in colorless WDM-PON is concerned, we can mention different approaches including wavelength reuse [14] and self-injection [15].

One first disadvantage of WDM-PON is that it needs a filtering device such as an arrayed waveguide grating (AWGg[4]) to perform wavelength assignment to the users, which would demand a change on the outside plant of the network. In addition, as previously discussed, the wavelength spectrum availability is a serious issue that should impose considerable limitations to ordinary WDM solutions. Furthermore, an optimal approach would include either strictly controlled wavelengths or temperature-insensitive AWGg to allow good alignment between the transceivers and the ports of the multiplexers/demultiplexers.

Finally, since wavelength is the only sharing resource of the network, the needed flexibility required by NG-PON2 should be guaranteed through a wavelength-agile approach. However, a wavelength-agility with potentially hundreds of subscribers has never been witnessed before in the optical network world. At the same time, the question on whether tunable devices will be capable of maturing in time to allow a cost-effective approach to NG-PON2 still raises heated discussions in the community and colorless solutions are still not able to provide the needed requirements even though they manage to allow wavelength-agnostic operation. In addition,

[4]Here, we add a “g” to the acronym only to differentiate it from the one used for Arbitrary Waveform Generator

they must be able to circumvent Rayleigh backscattering and crosstalk from residual downstream signal [16].

- UDWDM

Nokia Siemens Networks is the main force behind UDWDM [17, 18]. The solution uses coherent transmission technology from the transport network to provide reaches up to $100km$ and more than 1000 channels separated by $3GHz$ (with $1GHz$ separation between upstream and downstream wavelengths) in the C-band on a so called Next Generation Optical Access (NGOA). Based on the one-wavelength-per-user principle, the solution is capable of providing minimum bit-rates of $1Gb/s$/subscriber and up to $43dB$ optical budget obtained thanks to the coherent detection. UDWDM provides a more interesting solution than ordinary WDM as far as the wavelength spectrum availability issue is concerned.

Other advantages include the effort to merge access and aggregation networks, the possibility of rearranging users for matters of power saving or resiliency without geographic redundancy in case of network interruption and modular evolution allowing a "pay-as-you-grow" system. We can also mention the possibility of separating the traffic belonging to different operators through different spectrum assignments. This would allow a new business model in which the network infrastructure is controlled by an utility company or municipality that leases the available wavelengths to service providers.

The main disadvantage of the solution resides on the coherent transmission itself. Indeed, such approach is significantly more complex than currently adopted intensity modulation and direct detection and might consequently impose prohibitive costs for the transponders. The technological challenges on implementing advanced systems that will likely require photonic integration might also be a concern.

- TWDM

The hybrid time and wavelength division multiplexing has been backed up by Alcatel-Lucent and Huawei. Basically, it consists of stacking at least four 10GE/XG-PON wavelengths to provide $40Gb/s$ downstream capacity. Since it builds up on existing schemes, TWDM is regarded as the less risky and disruptive alternative and, above all, the most readily implementable.

However, it somewhat inherits the disadvantages of both TDM and WDM. If in the short-term time multiplexing can undoubtedly be used to relax the flexibility requirements for the wavelength domain, the approach should still face the same problems as pure WDM in the mid-term, namely an extra insertion loss arriving from the wavelength combiner device over typically already tight optical budgets and the need to cost-effectively implement wavelength-agile operation and circumventing the wavelength spectrum shortage problem. In addition, it will also be subjected to TDM's scheduling mechanisms and burst mode operation which will affect the latency of the system and harness the maximum achievable bit-rate to the number of active users in the network.

Furthermore, by keeping naive NRZ modulation, TWDM will be subjected to the same chromatic dispersion reach limitations of previous generations unless some sort of dispersion compensation mechanism, preferably electronic, is adopted. The reader is referred to [19] for a recent demonstration of $40Gb/s$ transmission using a TWDM prototype system.

- OFDM

Orthogonal Frequency Division Multiplexing is probably the technique that has been the most widespread among current communication standards. It is adopted for instance in Very High Bit-rate Digital Subscriber Line, Wireless Local Area Network and even 3GPP Long Term Evolution.

As far as the optical domain is concerned, OFDM offers four main advantages. These are increased robustness to chromatic dispersion, high spectral efficiency, simple implementation by

means of digital signal processing and capacity of providing an extra dimension for sharing the network resources amongst users.

OFDM is based on a divide-to-conquer approach. Instead of transmitting a high bit-rate flow on a single electrical carrier, it divides the information into a set of parallel lower bit-rate sub-channels, allowing thus increased robustness to chromatic dispersion. Indeed, it transforms a frequency selective channel into a collection of quasi-flat additive white Gaussian noise sub-channels and enables the transmission over longer fiber spans than NRZ-based systems.

In addition, OFDM offers high spectral efficiencies per optical channel not only because it allows the subcarriers to overlap without interfering with each other but also because the mapping and power of each subcarrier can be adaptively changed to provide a higher throughput. Also, it can be easily implemented by means of well-known and highly performing digital signal processing algorithms such as the Fast-Fourier-Transform (FFT). Indeed, OFDM allows transferring all the "hard work" from the optical plane to the electronic sphere, which is a considerable advantage if we remember that the evolution of electronics has always outperformed that of the optical components.

Last but not least, OFDM can provide the very useful ability of allowing the resources of the networks to be shared by means of a subcarrier allocation. This could potentially relax the constraints in terms of wavelength-agility or time-slot attribution of the network if ever a WDM or TDM solution is adopted in parallel with OFDM.

The biggest disadvantages of OFDM are its high sensitivity to time and frequency synchronization issues and the higher peak-to-average power ratios if compared to conventional single-carrier systems. Furthermore, since optical OFDM would potentially address much higher bandwidths that those provided by current standardized solutions, the sampling ratios of the digital-to-analogue and analogue-to-digital converters might also impose some limitations in terms of cost-effectiveness and power consumption, principally at the subscriber premises.

In this thesis, we will assess different experimental approaches that will evidence the many advantages of OFDM compared to naive NRZ. We will focus on the intensity modulated and directly detected OFDM solution which has some considerable advantages compared to other coherently-detected approaches. Our main goal here is not to try to convince the readers that OFDM should be privileged to the detriment of other candidates but rather to show that it could be quite easily adopted in many cases with other multiplexing solutions to provide simplification of the network and relaxation of the system constraints.

References

[1] Yves Gassot, Valérie Chaillou, and Roland Montagne. *L'accès au très haut débit*. Tech. rep. IDATE, 2012 (cit. on pp. 3, 5, 6).

[2] Cisco. *Visual Networking Index: Forecast and Methodology, 2011 to 2016*. May 2012. URL: http://www.cisco.com/en/US/solutions/collateral/ns341/ns525/ns537/ns705/ns827/white_paper_c11-481360.pdf (cit. on p. 3).

[3] Huawei. *Next-generation PON evolution*. 2010. URL: http://www.google.com/url?sa=t&rct=j&q=&esrc=s&source=web&cd=1&cad=rja&ved=0CCMQFjAA&url=http%3A%2F%2Fwww.huawei.com%2Filink%2Fen%2Fdownload%2FHW_077443&ei=ew1LUIihBISm0AWt84DADQ&usg=AFQjCNF0vluI0lZqfgQB1jppFW7dba5vnw (cit. on p. 7).

[4] Fabrice Bougart. *Optical Access Transmission: XG-PON system aspects*. ITU-T. Feb. 2010. URL: http://www.itu.int/en/ITU-T/studygroups/com15/Documents/tutorials/Optical_access_transmission.pdf (cit. on p. 7).

[5] S. Jain et al. "World's first XG-PON field trial". In: *Optical Fiber Communication (OFC), collocated National Fiber Optic Engineers Conference, 2010 Conference on (OFC/NFOEC)*. Mar. 2010, pp. 1 –3 (cit. on p. 7).

[6] M. Fujiwara et al. “Field trial of 79.5-dB loss budget, 100-km reach 10G-EPON system using ALC burst-mode SOAs and EDC”. In: *Optical Fiber Communication Conference and Exposition (OFC/NFOEC), 2012 and the National Fiber Optic Engineers Conference*. Mar. 2012, pp. 1 –3 (cit. on p. 7).

[7] OESolutions. *10GE/XG-PON Transceivers*. URL: www.oesolution.com (cit. on p. 7).

[8] Ligent Photonics. *10GE/XG-PON Tansceivers*. URL: http://www.ligentphotonics.com/ (cit. on p. 7).

[9] Ltd Shenzhen C-Light Network Communication Co. *10GE-PON Transceivers*. URL: http://www.c-light.com/ (cit. on p. 7).

[10] Gazettabyte. *FSAN adds WDM for next-generation PON standard*. July 2012. URL: http://www.gazettabyte.com/home/2012/7/30/fsan-adds-wdm-for-next-generation-pon-standard.html (cit. on pp. 8, 10).

[11] P. Chanclou et al. “Network operator requirements for the next generation of optical access networks”. In: *Network, IEEE* 26.2 (Mar. 2012), pp. 8 –14. ISSN: 0890-8044. DOI: 10.1109/MNET.2012.6172269 (cit. on pp. 8–10).

[12] Moufida Feknous. “Analyse et optimisation de l’agrégation dans les réseaux d’accès optiques de demain.” Rapport d’avancement de thèse (cit. on p. 9).

[13] G1.globo.com. *Internet representou 80% do tráfego móvel nas Olimpíadas de Londres*. Aug. 2012. URL: www.g1.globo.com/tecnologia/noticia/2012/08/internet-representou-80-do-trafego-movel-nas-olimpiadas-de-londres.html (cit. on p. 9).

[14] T. Duong et al. “Low cost Multi Band-OFDM for remote modulation of colourless ONU in hybrid WDM/TDM-PON architecture”. In: *Optical Communication (ECOC), 2007 33rd European Conference and Ehxibition of* 1 (Sept. 2007), pp. 1 –2 (cit. on p. 11).

[15] Qian Déniel et al. “Transmission Jusqu’à 10Gbit/s basée sur un Laser à Cavité Externe Utilisant un RSOA et un Réseau de Bragg Photo-inscrit sur Fibre pour WDM PON”. In: *Journées Nationales d’Optique Guidée (JNOG)*. 2012 (cit. on p. 11).

[16] J.L. Wei et al. “SOA intensity modulator-enabled colourless transmission of adaptively modulated optical OFDM signals for WDM-PONs”. In: *OptoElectronics and Communications Conference, 2009. OECC 2009. 14th*. July 2009, pp. 1 –2. DOI: 10.1109/OECC.2009.5214084 (cit. on p. 12).

[17] Nokia Siemens Networks. *Ultra Dense Wave Division Multiplexing connectivity*. Nokia Siemens Networks. 2012. URL: www.google.fr/url?sa=t&rct=j&q=udwdm&source=web&cd=3&cad=rja&ved=0CC0QFjAC&url=http%3A%2F%2Fwww.nokiasiemensnetworks.com%2Fsites%2Fdefault%2Ffiles%2Fdocument%2Fudwdm_exec_wp_100412_rm.pdf&ei=oINGUNujBuPE0QWUx4H4DA&usg=AFQjCNHTHiOoJwls36kKr_L9Dant-fEoZw (cit. on p. 12).

[18] Jun Shan Wey. *UDWDM PON, the Clear Technology Winner for NGPON2*. Nokia Siemens Networks. Mar. 2012. URL: http://www.ofcnfoec.org/osa.ofc/media/Default/2012/Presentations/5_ShanWey_NFOEC-Workshop-on-NGPON2_UDWDM.pdf (cit. on p. 12).

[19] Yiran Ma et al. “Demonstration of a 40Gb/s time and Wavelength Division Multiplexed passive optical network prototype system”. In: *Optical Fiber Communication Conference and Exposition (OFC/NFOEC), 2012 and the National Fiber Optic Engineers Conference*. Mar. 2012, pp. 1 –3 (cit. on p. 12).

Part I

Theoretical Overview, Simulations and Inputs for Experimental Work

Chapter 2

Transceiver Characterization and Fundamentals of Propagation in Optical Fibers

2.1 Introduction

In order to understand the performances of a passive optical network, we first need to understand the limitations imposed by the propagation through an optical fiber and the impacts of the optical transceivers in the transmission. We start this chapter by presenting in section 2.2 the main characteristics of the modulation approach used in this work: the intensity modulation and direct detection of a signal. In section 2.3, we address the most important characteristics of the optical components used in the transmission chain so that a preliminary insight on how they will influence the performances of the system can be provided. Such investigation is later upheld by the experimental results shown in Part II, in which the characteristics of the components are detailed according to each experimental contribution.

In section 2.4, we briefly review the linear and non-linear phenomena ruling the propagation of a signal through an optical fiber namely the chromatic dispersion, attenuation and non-linear effects. In section 2.5, we focus on a frequency-domain analysis of the propagation to highlight the influence of fiber dispersion and laser chirp on the frequency response of an IMDD channel. A whole section has been dedicated to this subject since it is a recurrent topic in this work.

2.2 Optical System Description

In the IMDD approach, the information is transmitted through variations of the intensity of the light emitted by the source. After propagation through an optical fiber, the signal is directly detected by the receiver, which converts the received optical field into an electrical current through a square-law detection process.

The main advantage of the IMDD approach is its simplicity and low-cost if compared to coherent transmissions, i.e., the only parameter needed to be detected is the light intensity. This is the reason why this technique has been used in all PON standards until now. This is also the main advantage of the approach if compared to other solutions for future generations. Indeed, while in very-long reach optical systems the massive data-flow justifies a more expensive and complex modulation technique, cost and simplicity should be the key factors determining the evolution of optical access networks, specially from an user-end equipment point of view.

Nevertheless, the IMDD solution also has its disadvantages. The first main drawbacks is the limitation imposed by fiber dispersion. Indeed, since the IMDD consists of an intensity modulation in nature, it generates a double-side-band modulated optical field (ODSB). The

phase differences between those bands which are imposed by fiber dispersion after propagation will degrade the transmission since the detected current will be found from the mixing of such bands and the optical carrier at the receiver side.

In the case of a direct modulation, which is the focus of this work, another important limitation concerns the laser chirp which consists of a parasite variation of the source's center frequency with the polarization current during the modulation. Indeed, the modulation of the polarization current will induce some changes in the carriers concentration inside the semiconductor which will affect its refractive index. More details on the dispersion and chirp effects are given in sections 2.4 and 2.5.

The main objective of this thesis is precisely to demonstrate that it is possible to circumvent such obstacles by using a modulation technique more adequate than standard NRZ and thus maintain the simple and cost-effective intensity modulation and direct detection approach. Indeed, not only we demonstrate that OFDM is particularly suitable for point-to-multipoint networks due to the frequency domain sharing capabilities that it offers but also that such scheme can be used to provide higher bit-rates and extended transmission ranges without requiring the use of complex electronic or optical dispersion compensation techniques.

Figure 2.1 shows a simple block-diagram representing a typical IMDD experimental setup. We use a single-longitudinal-mode laser, which can be, for instance, a DFB, a VCSEL, an EAM or even an RSOA-FBG. A bias-tee is necessary for fixing the appropriate polarization point of the emitter, as we will see in subsection 2.3.1.1. The signal then propagates through a SSMF span and a Variable Optical Attenuator (VOA) is responsible for simulating the desired split ratio of the PON[1]. For instance, we should count at least $17dB$ for a realistic split ratio of 1:32, meaning that besides the $15dB$ needed to serve the 32 subscribers, we should also count $2dB$ of insertion loss in the coupler. Other more conservative calculations consider $3.5dB$ per $1:2$ splitter stage which gives $17.5dB$ for a 1:32 split ratio (5 stages).

At the receiver side, a PIN photodiode or Avalanche Photodiode (APD) converts the received light into electrical current by means of a square-law process. This means that the electrical current will be proportional to the intensity of the received electrical field. The direct-detection scheme will play an important role on the characteristic frequency response of a dispersive IMDD channel, as we will see in section 2.5.

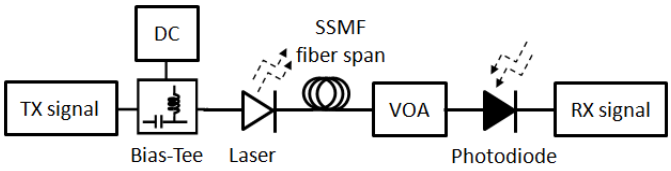

Figure 2.1: Basic optical bloc-diagram for the IMDD approach.

In the next section, we identify the most important characteristics of the transmitters and receivers in our experiments and give a first perception on how they will affect the transmission.

2.3 Transmitters and Receivers Characterization

2.3.1 Linear Operation Regime

One fundamental point that must be investigated when setting the components that are used in the transmission chain (whether they are optical or electrical) is their linear operation specifications. In the following of this subsection, we discuss some measurements that can be realized to infer that information.

[1]In our case, it would be injudicious to use the VOA to infer about the maximum allowed fiber length of the network since the used OFDM signals, which are generally large-band, will be strongly influenced not only by the fiber attenuation but also by its frequency response.

2.3.1.1 Emitter's $P \times i$ Curve

A priori, the operation point of a light source under intensity modulation may be relatively easily found by inspecting its power variation with the bias current, as shown in Figure 2.2(a). The source's bias point and RF power (peak-to-peak tension/current) must be chosen such that the modulating signal becomes completely positive and the regions under the threshold and over the saturation of the emitter are avoided:

$$\begin{cases} max\left(s\left(t\right)\right) < V_{sat} \\ min\left(s\left(t\right)\right) > V_{th} \end{cases} \tag{2.1}$$

with V_{sat} and V_{th} being respectively the emitter's saturation and threshold voltages (currents). In Figure 2.2(a) we see an example of biasing when the light source is modulated by an OFDM signal (please refer to chapter 3 for the details on the signal creation). Other interesting approaches for modulating the light source exist such as the asymmetrically-clipped OFDM (please, refer to subsection 3.3.10). Figure 2.2(b) shows the experimental setup used for the $P \times i$ characterization.

In Figure 2.3 we compare the $P \times i$ curves of a Vertical Cavity Surface Emitting Laser (VCSEL) from Raycan and a Distributed Fedback Laser (DFB) from 3SP, which was conceived in the framework of EPOD project. The first remarkable difference between both emitters concerns their linear regions. In fact, the highly linear DFB laser has been expressly conceived to better accommodate the transmission of multilevel signals[2]. The VCSEL, on the other hand, has been originally designed to operate under NRZ modulation.

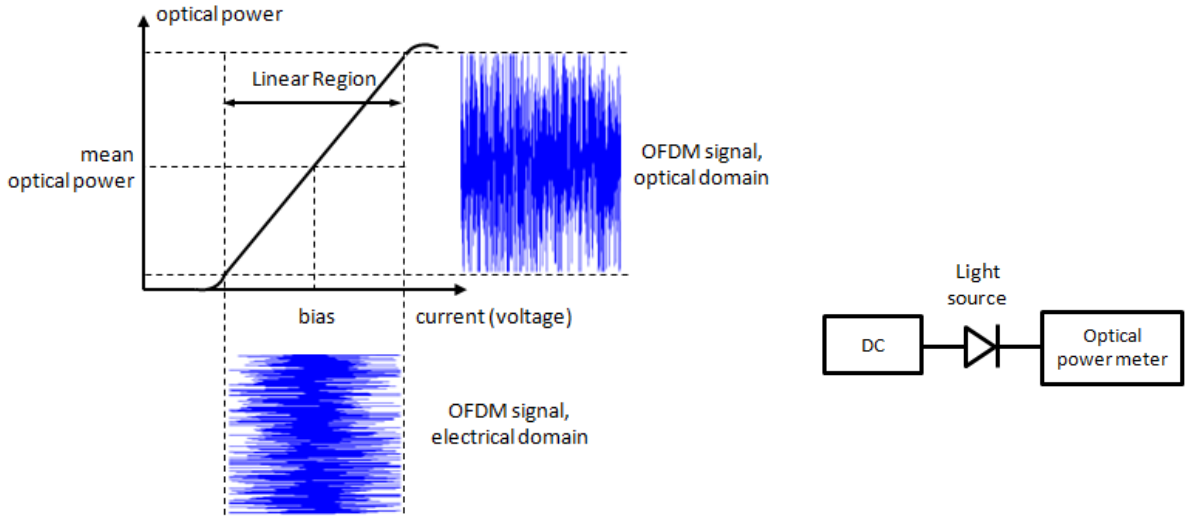

Figure 2.2: (a) Typical $P \times i$ curve of a laser. (b) Experimental setup.

Another interesting point is that the VCSEL will provide a lower power consumption because it needs a much weaker bias current than the DFB to operate. However, we can also notice by analyzing the slope of the curves that it also has a lower electro-optical conversion efficiency. This should be penalizing to the optical budget of the network since the emitter will deliver a lower mean optical power.

In short, despite the higher power consumption, we should expect better transmission performance with the DFB not only because of a better electro-optical conversion parameter but also because of an extremely large linear region that will allow a considerable gain in terms of modulating signal power.

[2]Such signal is also referred to as an analog signal to distinguish it from current sequences of zeros and ones of an OOK modulation.

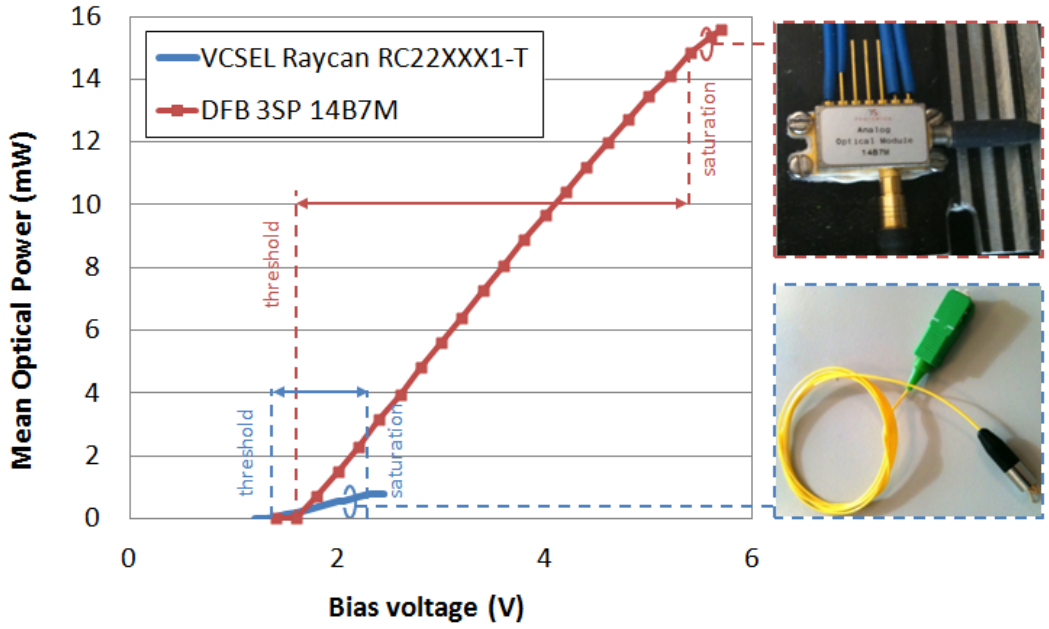

Figure 2.3: $P \times i$ curves of the VCSEL Raycan RC22XXX1-T and a DFB 3SP 14B7M.

2.3.1.2 Transmission Chain IM3

Even though the $P \times i$ curve is quite an easy and practical way of choosing a good polarization point for the emitter, it should not be considered as the single information for optimizing the transmission parameters. Indeed, the reader should be reminded that the $P \times i$ curve represents a static measurement done simply by varying the direct current (DC) output of a tension or current source and measuring the emitter's mean output optical power.

It does not take into account the dynamic characteristics of the emitter, i.e., the case in which the source is actually modulated by a signal. We will see later in this memoir (chapter 4) that the linearity of the electro-optical conversion also depends on the nature of the modulating signal and on the physical phenomena related to the modulation of the emitter and the propagation through the optical fiber. We should also remember that the $P \times i$ curve does not provide any clues on the linearity of the receiver or other components in the transmission chain such as an electrical amplifier.

A more judicious measurement consists of evaluating the system's third order intermodulation (IM3) characteristics [1–3]. Indeed, if multiple tones are injected into a non-linear device, they will mix together and generate harmonics and intermodulation products. The most dangerous intermodulation products are those falling closest to the fundamental tones, as depicted in Figure 2.4(a).

In the case of two fundamental tones f_1 and f_2, these are $2f_1 - f_2$ and $2f_2 - f_1$, which are called third order intermodulation distortion (IM3) since their power levels increase by a factor of three if compared to the fundamental tones's power variation on a logarithmic scale. The IM3 is used as the figure of merit to characterize the linearity of any device.

The point $[IIP3, OIP3]$ in the curve shown in Figure 2.4(b) is the point at which the prolongation of the fundamental and IM3 curves intercept in the $P_{input}(dBm)$ versus $P_{output}(dBm)$ plane. Once the IM3 of the chain has been calculated, it is possible to define a certain power back-off thanks to which we will be able to assure that the transmission won't suffer any kind of degradation arriving from the components' nonlinearities in the dynamic operation.

Other interesting characteristics given by this analysis are the Spurious-Free Dynamic Range (SFDR), an operation region in which the third order intermodulation products are below the

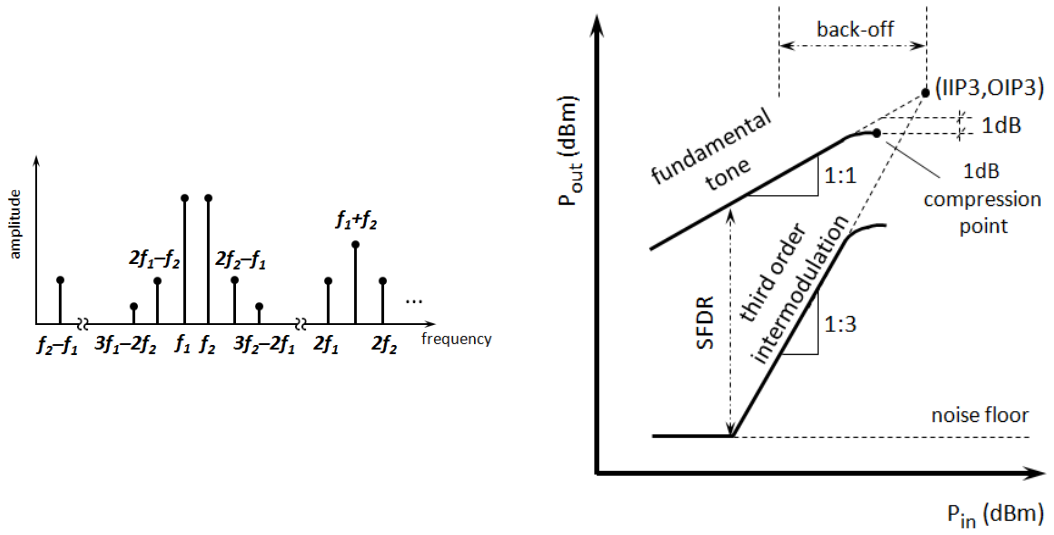

(a) (b)

Figure 2.4: (a) Harmonics and intermodulation products generated by the nonlinear operation of a device which is submitted to two signals at frequencies f_1 and f_2. (b) Evolution of output signal and third order intermodulation product with input power on a nonlinear device.

system's noise floor, and the $1dB$ compression point. The $1dB$ compression point indicates that the output signal is $1dB$ below the value that it would have if the device was still under linear operation. In other words, it points out the power level from which the output signal will be distorted due to the nonlinear operation of the device.

Figure 2.5 shows the experimental setup used to measure the transmission chain intermodulation characteristics. Two local oscillators LO_1 and LO_2 are responsible for creating the fundamental tones f_1 and f_2 which are added together with a power coupler. This signal is used then to directly modulate the light source after proper biasing. A VOA sets the desired mean input power at the photodetector. Finally, an electrical spectrum analyzer (ESA) is used to find the power levels of the signals and intermodulation products for different input powers at the local oscillators.

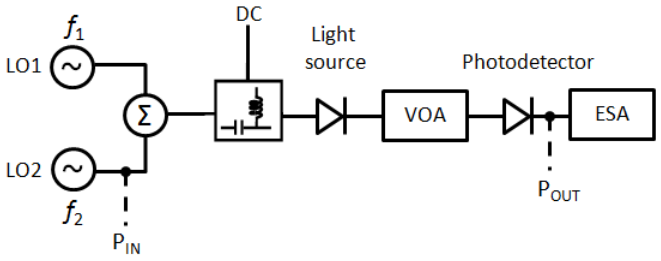

Figure 2.5: Experimental setup for the third order intermodulation characterization of an IMDD transmission chain.

Before proceeding to the IM3 characterization of the emitter and receiver, it is interesting to firstly evaluate the nonlinear characteristics of the components used in the experiments themselves, namely the power coupler and the ESA. In appendix A, we estimate the conditions under which the nonlinearities of the measurement equipment will not affect the characterization of the transmission chain.

2.3.1.3 Optimizing the Transmission using Performance Indicators

We have seen that even if the $P \times i$ measurement provides an easy and fast initial estimate of the emitter's linear operation region, it should not be considered as the only information in the optimization of the transmission parameters. The IM3 characterization is very interesting not only because it provides a "dynamic" evaluation parameter but also because it may be used to characterize the nonlinearities of the whole transmission chain, including the photodetector and even other electrical components such as an electrical amplifier.

Though the IM3 consists of a more complete characterization method, it has two main inconveniences. Firstly, it demands a specific experimental setup and even if the measurement procedure is automated, such as was the case for the results shown in annex A, it is relatively time-consuming, specially for large frequency spans. Secondly, the simple two-frequencies scenario that is set for the IM3 measurement is somewhat distant from the actual nature of an OFDM signal. As we will see in chapter 3, an OFDM signal is composed of a set of several close-together tones which in a nonlinear regime may interact one with another to create intermodulation products and harmonics in a much more complex way than the simple two-frequencies arrangement.

A much more practical and faster evaluation consists of analyzing the OFDM transmission performance indicators. The values of Error Vector Magnitude (EVM), Signal-to-noise Ratio (SNR) and Bit Error Rate (BER) can give a sufficient number of clues to allow finding the best operation conditions of the transmission chain. These performance parameters are detailed in section 3.6. The optimization can also be reached by investigating the throughput of the transmission. Indeed, in section 3.7, we will see that the OFDM subcarriers can be adapted to the channel's SNR in order to optimize the transmission bit-rate. Several examples of optimization using such parameters are recalled throughout the experimental work shown in part II.

2.3.2 Bandwidth

Whether we think about an electrical or optical component, the analog bandwidth is an extremely important parameter characterizing the devices that compose the transmission chain. Indeed, it is straightforward to affirm that the modulation bandwidth of such devices will limit the transmission throughput. In this subsection, we focus on the modulating characteristics of the optical transceivers.

The modulation bandwidth of a semiconductor laser can be found from a modified version of the rate equations governing the electron-hole combination dynamics in the laser cavity. It includes the non-linearity of the cavity gain and the phase modulation phenomenon arriving from the change in the concentration of carriers due to the intensity modulation (see subsection 2.3.3) [4, 5]. Consequently, the characteristic frequency response and modulation bandwidth of a laser will be strongly related to its relaxation oscillation frequency and damping rate. Figure 2.6(a) shows the frequency response of the DFB prototype 14B7M from 3SP with different bias currents. As reported in [4, 6], we can notice an increase in its 3dB bandwidth with the bias current.

The modulation bandwidth of a photodiode on the other hand is mainly determined by the time the carriers take to travel to the electrical contacts after the absorption process [7]. Figure 2.6(b) shows the opto-electrical frequency responses of an APD from Picometrix model AT10SFA-AC conceived for $10Gb/s$ NRZ operation for different mean input optical powers.

2.3.3 Laser Chirp

The chirp of the light source is a phenomenon arriving from the changing of its polarization current during the intensity modulation process. The intensity modulation will cause a variation on the density of the carriers inside the cavity of the emitter thus directly affecting its refractive index. As a consequence, the modulating signal will be accompanied by a parasite modulation

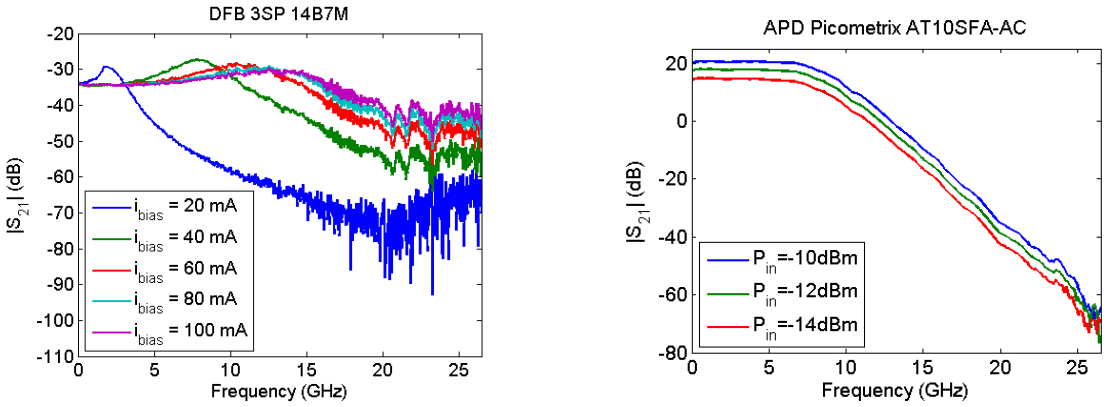

(a) (b)

Figure 2.6: Bandwidth of (a) DFB laser 3SP 14B7M with different bias currents and (b) APD Picometrix with different input mean optical powers.

term. This parasite term may be represented by two different contributions characterizing a phase or frequency modulation component which are respectively referred to by some authors as the transient and adiabatic contributions of the chirp. Their strength will depend on the characteristics of optical source.

We are mostly used to a time-domain evaluation of the chirp effects on the transmission [4] and this is because of the modulation that is currently adopted in the optical access networks standards. However, for signals that do not have a time-domain representation as simple as ordinary NRZ, the frequency-domain evaluation of the chirp becomes much more interesting and elucidating. The chirp will also have a strong influence on the laser's spectral linewidth which, together with the phase noise arriving from the spontaneous emissions in the cavity, may present some severe broadening.

In section 2.5 we describe in detail the effects of the interplay between chirp and chromatic dispersion in the IMDD channel frequency response. In section 4.2, we propose a practical, easy and fast method for measuring the chirp parameters of single-longitudinal-mode sources that can be used with different components regardless their adiabatic and transient chirp characteristics. In section 6.3, we show some limiting aspects arriving from the spectral linewidth augmentation due to laser chirp in a WDMA-FDMA-OFDM upstream transmission.

2.3.4 Photodetectors Sensitivity

The photodetector's sensitivity is the minimum required mean optical power that allows attaining a certain BER with a specific modulation scheme, generally NRZ and under a specific bit-rate. It is a very important parameter since it has a direct influence on the network performance in terms of optical budget.

APD photodiodes generally present better sensitivities than PIN photodiodes thanks to a built-in first gain stage through avalanche multiplication [8]. They allow for higher optical budgets but are generally constrained to smaller modulation bandwidths.

2.3.5 Emitter and Receiver Noise Sources

Spontaneous emissions are the stronger phenomenon behind the generation of noise in a semiconductor laser. They will add a small component to the coherent stimulated field that randomly perturbs both amplitude and phase of the emitted light [4]. The Relative Intensity Noise (RIN) is a frequency-dependent contribution that characterizes the variations in the power emitted by the source. It is considerably stronger near the relaxation oscillation frequency of the laser

but decreases rapidly for higher modulation frequencies. It can be found from the spectrum of the photodetected signal using an ESA and is usually measured as a relative variation in the square of the optical power in dB/Hz over the RIN bandwidth [9]. Typical values of RIN are between -110 and $-130dB/Hz$ but high-quality sources can achieve less than $-170dB/Hz$ [10]. An experimental method for measuring the RIN of DFB lasers is proposed in the application note shown in [11].

With respect to the receiver, the two fundamental noise mechanisms are the shot and thermal noises. Shot noise arrives from the fact that the current in the photodetection is in fact a flow of electrons that are generated at random times [4]. Thermal noise, on the other hand, is a function of the Shunt resistance of the detector and also the thermal motion of electrons in the electrical contacts of the component [12].

A quantified and individual evaluation of the effects of each of these noise sources is not provided in this thesis. Instead, we focus on a qualitative analysis of the "global noise" influence on the transmission chain, which is measurable through the SNR of the OFDM subcarriers. Some clues on the subject are however given in [13] but a thorough evaluation in the OFDM modulation context remains a prospect for future work. For a detailed mathematical description of the transmitter and receiver noise characteristics, please refer to [4, 6, 14].

2.4 Propagation through an Optical Fiber

It is possible to infer about the principles that rule the propagation of an electromagnetic field through the optical fiber by solving Maxwell's equations in a cylindrical medium with the appropriated boundary conditions. The solution shows that the fiber will support a certain number of guided modes, each one related to a specific propagation constant, as well as some unguided radiated modes, which are not relevant in this work. The reader is referred to [4, 6] for the detailed mathematical analysis of the problem.

All the experiments throughout this memoir are subjected to the single mode propagation condition under which only the fundamental mode HE_{11} of the fiber exists. It consists of a hybrid mode with non-zero electric and magnetic components in the direction of propagation. The single mode condition can be easily satisfied with the appropriated fiber parameters (core radius and core-cladding refractive index difference) of any single-mode optical fiber operating in the O-L bands[3] nowadays.

Having only one propagating mode means that the transmission system will not suffer from modal dispersion, i.e., the time-domain signal spreading arriving from the different speeds of the guided modes. It is important, however, to remember that even the single-mode fiber is not truly single mode. The fundamental mode can be decomposed into two degenerated modes with orthogonal polarizations. The electromagnetic wave will be most strongly polarized in one of the polarization axes depending on the strongest component of its electric field. Due to fiber birefringence, each polarization will propagate with a specific velocity, leading to a differential group delay (DGD) between the perpendicular components. To make matters worse, birefringence changes randomly along the propagation axis of "real-world" deployed fibers. Indeed, temperature variations or small departures from the cylindrical symmetry of the fiber caused by random variations in the core shape and stress-induced anisotropy may result in a mixing of the two polarization states, leading to a power exchange between the two components. The DGD is one of the parameters that characterize the polarization mode dispersion (PMD), and can considerably degrade the performance of the transmission. Since we restrain this memoir mainly to the access networks context (except for the experiment on section 7.2), we do not evaluate the effects of PMD in our transmissions. Indeed, it is admitted that they will be far less restrictive than those of chromatic dispersion.

[3] Refer to subsection 2.4.2

In the following sections, we should then exclude the effects of Modal Dispersion and PMD from the analysis of the propagation through an optical fiber.

2.4.1 Non-Linear Schrödinger Equation

At this point, it is interesting to introduce the equation that rules the propagation of the information envelope that is transmitted along the fiber. This is done by means of the slowly varying envelope approximation (SVEA), which separates the rapidly varying part of the electromagnetic field from the modulation contribution. The wavelength-dependent propagation constant about the optical carrier frequency w_0 can be evaluated by expanding it in Taylor series:

$$\begin{gathered}\beta(w) = \beta_0 + (w - w_0)\beta_1 + \tfrac{1}{2}(w - w_0)^2\beta_2 + \tfrac{1}{6}(w - w_0)^3\beta_3 + ..., \\ \beta_n = \tfrac{\partial^n \beta(w)}{\partial w^n}|_{w=w_0}\end{gathered} \tag{2.2}$$

where β_0 is related to the phase velocity of the field, β_1 to its group velocity, i.e., the velocity of the information envelope, β_2 to the chromatic dispersion, β_3 to the Third-Order Dispersion (TOD) and all other terms to higher order dispersion elements.

Generally, we may say that the TOD contribution becomes important in three situations:

1. when the wavelength is near the zero-dispersion wavelength of the fiber and $\beta_2 \to 0$;
2. when the wavelength is modulated by ultrashort pulses and the truncation of $\beta(w)$ in the third term becomes more severe or
3. when we want several channels of a WDM system to undergo similar dispersion values (actually, the TOD represents the slope of the chromatic dispersion curve).

Let us suppose that the most important contribution to the expansion of $\beta(w)$ is the chromatic dispersion, so that equation 2.2 can be truncated in the third term.

Furthermore, since we are considering only the information envelope and not the rapidly varying optical field, it is possible to ignore the term β_0. Also, if we change from a static to a moving referential with velocity $v_g \equiv \frac{1}{\beta_1}$, the term β_1 can also be eliminated from the analysis. After all manipulations, the only dispersion term to be considered in equation 2.2 is β_2 and the propagation of the information envelope may be found from the general field equation:

$$\frac{\partial A(z,t)}{\partial z} = -j\frac{\beta_2}{2}\frac{\partial^2 A(z,t)}{\partial t^2} - \frac{\xi}{2}A(z,t) + j\gamma|A(z,t)|^2 A(z,t) \tag{2.3}$$

Equation 2.3 is known as the non-linear Schrödinger equation (NLSE) and characterizes the changes of the time-domain information envelope $A(z,t)$ as a function of the length z of the fiber. The first term on the right-hand side of the equation represents the chromatic dispersion. The second and third terms are respectively related to the attenuation and the nonlinear effects on the fiber. In the next sections, we give a brief description of those effects.

2.4.2 Attenuation

Even though the losses incurred by optical fibers to the propagating electromagnetic field are very low compared to other confined medium like copper or coaxial cables, they cannot be neglected. Since late seventies, the first generation of optical lightwave systems already allowed transmission ranges in the order of $10km$ in the $800nm$ window, which was considerably higher than the maximum distance permitted with coaxial cables at that time.

At early eighties, with the birth of the second-generation of optical communication systems, operation in the $1300nm$ window was already possible with an attenuation coefficient

of $0.5dB/km$. The development of sources in the neighborhoods of $1500nm$ allowed conceiving fibers with an even lower attenuation ($0.2dB/km$), giving rise to a third generation in the mid-eighties.

Finally, thanks to the progress on Erbium Doped Fiber Amplification (EDFA) technologies in early nineties, the limitations imposed by fiber losses seemed finally transcended, paving the way for the development of intercontinental fiber optic submarine communications in the fourth-generation. Actually, despite the fact that optical amplification can be used to compensate the losses imposed by fiber attenuation, the limitations imposed by the noise arriving from amplified spontaneous emissions in the amplifiers prevents a signal from being indefinitely amplified. Indeed, the noise figure of an amplifier is a very important parameter that sets the number of cascaded elements that can be used on a transmission link as a function of the desired optical signal to noise ratio.

The principle behind the attenuation in optical fibers is relatively simple. The reduction in the average power of an optical signal with the transmission distance z can be represented by the Beer-Lambert law:

$$P(z) = P_0 e^{-\xi z} \tag{2.4}$$

where P_0 is the mean launched optical power and ξ the fiber attenuation coefficient.

The two major contributions to fiber attenuation are the material absorption and the Rayleigh scattering.

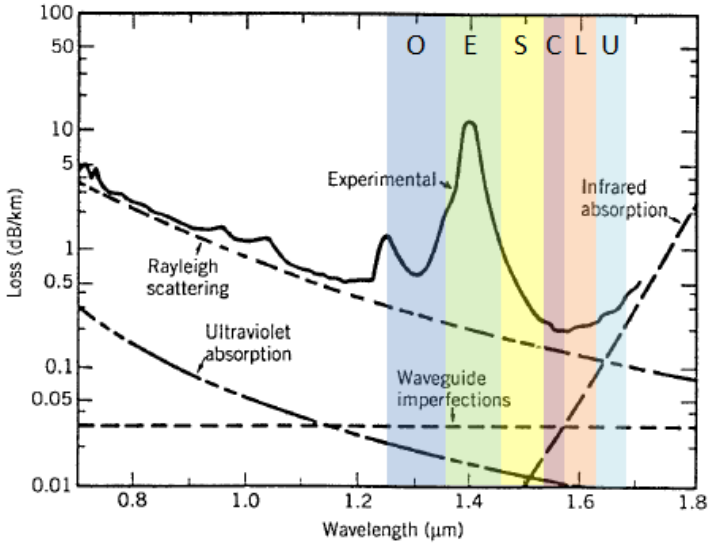

O band: "Original", 1260 – 1360nm
E band: "Extended", 1360 – 1460nm
S band: "Short", 1460 – 1530nm
C band: "Conventional", 1530 – 1565nm
L band: "Long", 1565 – 1625nm
U band: "Ultra-long", 1625 – 1675nm

Figure 2.7: Fiber attenuation contributions and operation bands.

On the one hand, material absorption is related to the energy loss caused by the electronic and vibrational resonances of the fiber molecules. It can be divided into an intrinsic contribution, arriving from the silica molecules of the fiber and an extrinsic contribution, due to impurities generated in the optical fiber fabrication process.

As far as the intrinsic losses are concerned, we can highlight the ultraviolet and infrared components (see Figure 2.7, adapted from [4]) whereas metal impurities and water vapors are the

principal responsible for the extrinsic losses. Indeed, the "water-peak" in the attenuation curve has for years limited the operation in the E band. However, the evolution in fiber fabrication processes made it possible to eliminate the hydroxyl radical to conceive the "zero water-peak fibers", also known as "dry fibers", under ITU-T's G.652.C and D recommendations.

On the other hand, Rayleigh scattering is inversely proportional to the operating wavelength and arrives from local microscopic fluctuations on the density of the silica molecules of the fiber, which lead to variations in its refractive index. Figure 2.7 shows an example of the loss spectrum of an optical fiber and the standardized operation bands.

Besides material absorption and Rayleigh scattering, other sources of attenuation exist such as the ones arriving from core/cladding imperfections and microbendings in the fiber or permanent/non-permanent optical connections. In Figure 2.8, we summarize the different types of attenuation in optical fibers.

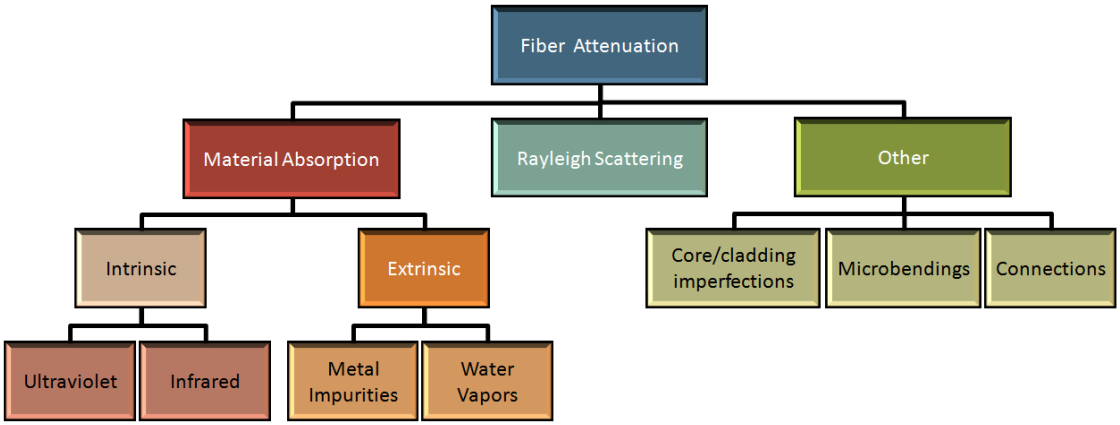

Figure 2.8: Different types of attenuation in optical fibers.

2.4.3 Chromatic Dispersion

The term β_2 in the NLSE is know as the group-velocity dispersion (GVD) parameter and can be either positive or negative depending on whether the operation wavelength is below or above the zero-dispersion wavelength of the fiber. When β_2 is negative, the system is said to be in the anomalous-dispersion regime and can accept the propagation of optical solitons through a balance with the fiber nonlinear effects (see [15]). In this regime, the high-frequency (blue-shifted) components of the pulse spectrum will travel faster than the low-frequency (red-shifted) components. When β_2 is positive, the transmission is said to be in the normal dispersion regime and the red-shifted components of the pulse spectrum will travel faster than the blue-shifted components.

The GVD parameter is related to the dispersion coefficient D of the fiber by:

$$D = \frac{-2\pi c\beta_2}{\lambda^2} \tag{2.5}$$

From the Sellmeier equation[4], it is possible to find the typical chromatic dispersion contribution at a certain wavelength, as shown in Figure 2.9(a). Physically speaking, the chromatic dispersion is related to the characteristic resonance frequencies at which the silica absorbs the electromagnetic radiation through oscillations of bound electrons [4]. From Figure 2.9(a) we can see that such interaction depends on the sum of two contributions:

1. material dispersion (D_m), which states the refractive-index dependency on the wavelength of the source (which is never perfectly monochromatic) and

[4]The Sellmeier equation empirically describes the variation of the refractive index with the wavelength of the source in silica fibers.

2. waveguide dispersion (D_w) which depends on the fiber parameters.

By changing the characteristics of the waveguide, it is possible, for instance, to design fibers such that the zero-dispersion wavelength is shifted (dispersion-shifted fibers - DSF) and even to tailor the waveguide contribution such that the total dispersion is relatively small over a wide wavelength range (dispersion-flattened fibers). In other example, GVD is made normal with a relatively large magnitude to conceive dispersion compensating fibers (DCF, refer to chapter 7.2 for a practical example). Holey Fibers [16–24] can also present some very interesting dispersion characteristics but have not yet attained industrial maturity.

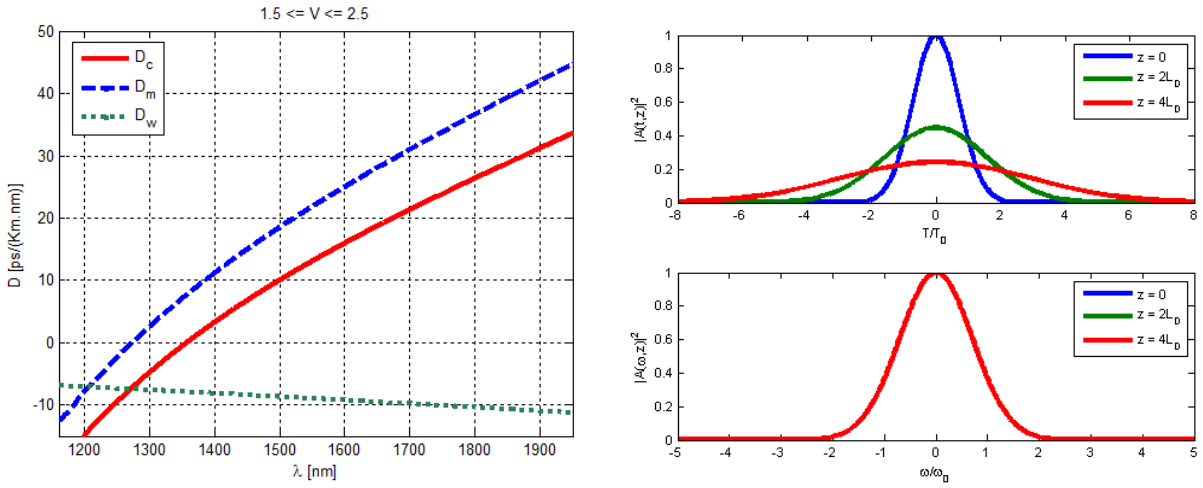

(a) (b)

Figure 2.9: (a) Material, waveguide and chromatic dispersions on silica fibers. (b) Time and frequency domain variation of the pulse with the propagation distance.

For matters of comprehension, let us analyze the effects of the chromatic dispersion separately from the other effects of propagation. We admit that the nonlinear effects will not affect the information envelope in the NLSE, which is true if the mean optical power and effective area of the fiber are such that the incident power density of light in the fiber is not too high. Secondly, without lost of generality, we can also ignore the effects of fiber attenuation, which will only affect the information envelope's amplitude.

Figure 2.9(b) shows the time and frequency domain variation of a propagating Gaussian envelope submitted only to the chromatic dispersion effects of the fiber. The advantage of the Gaussian waveform is that the frequency domain signal can be easily found by means of a Fourier transform of the time-domain signal[5]. The parameter T_0 is the original pulse width before propagation. $L_D = T_0^2/|\beta_2|$ is called the dispersion length and represents the fiber length over which the dispersion in the pulse becomes important for a standard On-Off-Keying (OOK) signal.

It can be seen that dispersion will induce some broadening in the time-domain signal which will be as strong as the fiber length is high. It should be noticed, however, that the the module of the signal spectrum remains unchanged. Indeed, the dispersion will cause a linear variation of the instantaneous frequency of the wave arriving from a variation in the spectrum's phase. Figure 2.10 outlines this effect in both time and frequency domains for a propagation in the anomalous regime. Dispersion is expected to spread the time-domain signal in both anomalous and normal dispersion regimes, the only difference being if either high or low frequency components will travel faster in the fiber.

[5]The Fourier transform of a Gaussian function is also Gaussian.

Figure 2.10: Pulse spreading due to chromatic dispersion .

The effects of chromatic dispersion are quite easily evaluated for a NRZ-modulated signal by means of a time-domain analysis with an eye-diagram verification, with which it is possible to infer the pulse broadening caused by it. However, such analysis is not as simple and direct for signals with advanced modulation schemes. In section 2.5, we switch to a frequency-domain analysis of the chromatic dispersion that will help to characterize the optical fiber as a frequency-selective channel and to investigate the effects of such channel over an OFDM transmission.

2.4.4 Nonlinear Effects

The response of any dielectric material becomes nonlinear for intense electromagnetic fields[6]. The nonlinear coefficient γ of the NLSE is more specifically related to the phase modulation induced by the Kerr Effect and is given by:

$$\gamma = \frac{2\pi \overline{n}_2}{\lambda A_{eff}} \tag{2.6}$$

where A_{eff} is the effective area of the fiber core and $\overline{n}_2$ is the nonlinear coefficient[7]. Actually, the Kerr effect states that the refractive index of the material varies with the intensity of the incident electromagnetic wave. By separately analyzing the nonlinear effects in the NLSE, we obtain:

$$\frac{\partial A\left(z,t\right)}{\partial z} = j\gamma |A\left(z,t\right)|^2 A\left(z,t\right) \tag{2.7}$$

which has a trivial solution:

$$\begin{aligned} A\left(z,t\right) &= A\left(z=0,t\right) e^{j\Phi_{NL}(z,t)} \\ \Phi_{NL}\left(z,t\right) &= P_0 \gamma z \left|A\left(z=0,t\right)\right|^2 \end{aligned} \tag{2.8}$$

Equation 2.8 states that the nonlinear effects will generate an intensity-dependent self-induced nonlinear phase modulation (SPM) which will lead to spectral broadening of the optical pulses as a consequence of the time-dependency of Φ_{NL}.

In addition, if more than one optical channel is transmitted through the fiber, the nonlinear phase shift of one channel will depend not only on its power but also on the power of the other channels. This is known as cross-phase modulation (XPM). If three or more co-propagating channels are influenced by the fiber nonlinear effects, then the intermodulation products of the three wavelengths can cause energy transfers between them and even interchannel cross-talk. This phenomenon, known as Four-Wave Mixing (FWM) is very troublesome if the wavelengths are matched in phase (which is more likely to occur near the zero-dispersion wavelength).

Besides the nonlinear phase modulation term represented in equation 2.8, we may also mention other contributions to the nonlinear effects in the fiber, namely the stimulated scattering. The stimulated scattering can be divided into two different contributions: Raman Scattering (SRS) and Brillouin Scattering (SBS).

Contrary to Rayleigh scattering, both SRS and SBS represent an inelastic process which causes changes in the frequency of the scattered light. They originate from the scattering of one

[6]Consider the ratio between the mean optical fiber and the fiber effective area.

[7]$\overline{n}_2$ should not be confused with the refractive index of the cladding. It is generally given in cm^2/W.

photon to a lower energy photon which may excite a phonon[8] and cause loss of power of the transmitted wavelength.

On the one side, SBS is related to the acoustic phonons due to a tendency of materials to become compressed in the presence of an electric field (electrostriction). The incident optical pulsing wave generates an acoustic wave propagating in the opposite direction, which result in the change of the optical pulse frequency. The beating between the scattered wave and the pump increases the acoustic wave amplitude, generating a positive feedback. Ultimately, all power of the original wave can be transferred to the scattered wave. Generally, the scattered light is shifted by about $11GHz$.

On the other side, SRS is related to the optical phonons. The optical channel is scattered by the silica molecules when some photons give up their energy to lower-energy photons and the remaining energy is absorbed by the silica molecules generating some molecular vibration. SBS may cause a wavelength shift of some dozens of THz but, contrary to SBS, scattering occurs in all directions of propagation. There is also a positive feedback when the beating between the pump and the scattered wave in both directions continues to stimulate molecular oscillations.

Figure 2.11 sums up the different types of nonlinear effects on fibers.

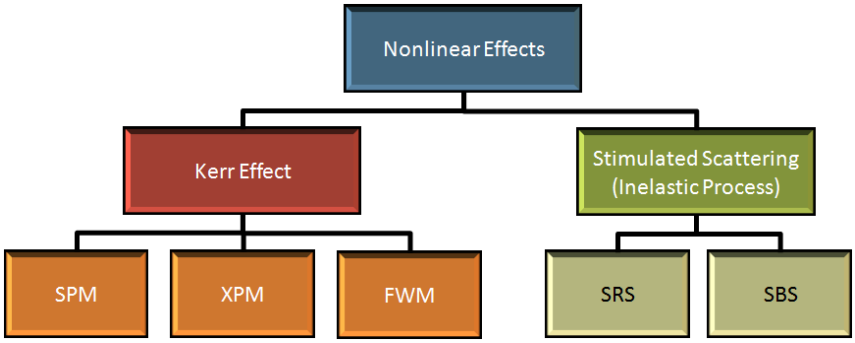

Figure 2.11: Different types of attenuation in optical fibers.

2.5 Frequency Response of Dispersive IMDD Channels

The interest of measuring the frequency response of a channel is manifold. Firstly, it is especially helpful to evaluate the impacts of the dispersion on signals that do not have a time-domain representation as simple as that of a NRZ signal. In addition, it allows estimating the channel and some of the components' parameters by comparing the measurements with existing mathematical models. Furthermore, after an experimental validation of the model, it is possible to verify how some of its parameters may influence the system's performance and the required conditions to attain optima transmission conditions.

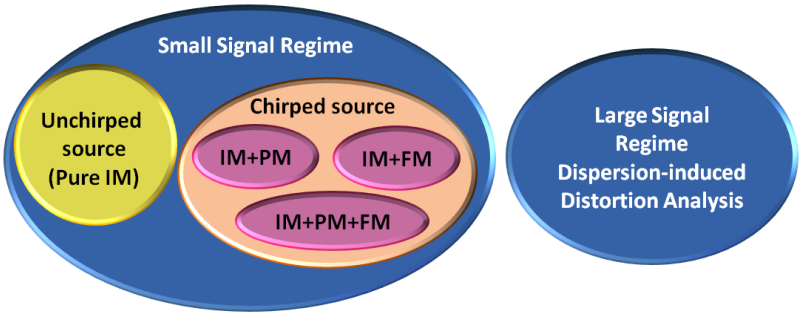

Figure 2.12: Different spheres of IMDD channel modeling.

[8]Collective excitation of atoms or molecules.

Many mathematical models that address the dispersive IMDD channel response have been proposed in the literature. The majority of them limits the analysis to what is known as the Small-Signal Regime (SSR) in which the modulating signal's power is very low compared to the mean optical power of the signal. This assumption greatly facilitates the evaluation of the propagation of the information envelope through an optical fiber but constrains the validity of this model to a somewhat specific case.

In the SSR sphere we can still separate the reports into two groups. In the first of them, the effects of the chirp of the light source is not considered and the modulating signal is composed of a pure intensity modulation term [25, 26]. In the second type, the chirp effect in the light source is considered and the modulating signal will be composed by both intensity and phase modulation terms. Both terms are coupled one to another and will characterize the parasite frequency modulation of the optical carrier that is created by the variations of the polarization current in the intensity modulation process, as described in subsection 2.3.3.

In the chirped IMDD channel models, we can still consider either the effects of a pure phase modulation [27] or frequency modulation separately or both of them at the same time [28–31]. In chapter 4.2, we use the Nelder-Mead simplex fitting algorithm to deduce the chirp parameters of different types of single-longitudinal mode light sources, including a DFB, an EML and an Reflective Semiconductor Optical Amplifier (RSOA) with Fiber Bragg Grating (FBG) from the measurements of the channel frequency response done with a network analyzer.

If the reports on the SSR are relatively numerous, complete works addressing the Large-Signal Regime (LSR) are still very scarce. Actually, in the LSR, the direct-detection of the ODSB signal after propagation may induce distortions in the signal. Such distortions increase with the signal power and the accumulated dispersion in the link and render channel modeling way more complicated than it is in the SSR, principally if the modulating has multiple subcarriers, which is the case of an OFDM signal.

Figure 2.12 shows the mentioned spheres of the IMDD models found in the literature. In the following of this section, we review the general SSR IMDD channel transfer function and evoke some results found in other reports on the subject. In section 4.3 we deal with the LSR and detail some interesting results on the procedure of optimization of the OFDM signal power for different lengths of optical fiber.

2.5.1 Small-Signal Regime, Single-tone Modulation

As we have seen in section 2.4, thanks to chromatic dispersion, the modulation sidebands of the signal and the optical carrier will propagate with different velocities in the fiber. This will translate into some phase variations in the received signal spectrum. At the receiver side, the signal is down-converted from the optical to the electrical domain and the original modulation signal can be retrieved thanks to the mixing between the optical carrier and the modulation sidebands.

However, due to the squared-law nature of the opto-electrical conversion, at certain frequencies the chromatic dispersion $\times$ fiber length product will cause the two modulation sidebands to be in counterphase, thereby producing a dip in the amplitude of the channel's frequency response. This response also depends on the chirp parameter of the laser and the power of the modulating signal. The following of this section presents a brief mathematical review of the phenomenon based on the work reported in [31].

Let us consider an optical source centered at $\omega_0 = 2\pi\nu_0$ which is modulated by both intensity and phase modulation components. The complex optical field at the output of the light source is given by:

$$E_{in}(t) = \sqrt{I_{in}(t)}e^{j\Phi_{in}(t)}e^{j\omega_0 t} \tag{2.9}$$

where $I_{in}(t)$ is the single-tone intensity modulation (IM) signal:

$$I_{in}(t) \equiv P_{in}(t) = P_0 \left(1 + m_{IM} \cos\left(\omega t + \varphi_{IM}\right)\right), \tag{2.10}$$

P_0 is the average output power, m_{IM} the intensity modulation index, ω the angular modulation frequency and φ_{IM} an initial phase associated to the intensity modulation term. The DC term stands for the necessary bias, as seen in subsection 2.3.1.1. As expected, the amplitude modulation term is proportional to $\sqrt{P_{in}(t)}$.

$\Phi_{in}(t)$ represents the single-tone phase modulation (PM) component:

$$\Phi_{in}(t) = m_{PM} \cos\left(2\pi f t + \varphi_{PM}\right) \tag{2.11}$$

with m_{PM} being the phase modulation index and φ_{PM} an initial phase associated to the phase modulation. To simplify the subsequent analysis, let us write $E_{in}(t)$ as a function of the phase difference $\Delta\varphi = \varphi_{PM} - \varphi_{IM}$ so that:

$$\begin{aligned} I_{in}(t) &= P_0 \left(1 + m_{IM} \cos\left(\omega t\right)\right) \\ \Phi_{in}(t) &= m_{PM} \cos\left(2\pi f t + \Delta\varphi\right) \end{aligned} \tag{2.12}$$

The term $\Phi_{in}(t)$ in 2.9 is used to take into account the modulation of the optical frequency of the light source caused by $I_{in}(t)$ [32]. Indeed, the chirp of the light source arises due to the changing of its polarization current during the intensity modulation process: $P_{in}(t)$ will cause a variation in the carriers' density and this will directly affect the source's refractive index. Consequently, the PM contribution is coupled to the IM term, meaning that Φ_{in} is a function of P_{in}. The reader is referred to [33–35], for more details on the subject.

As seen in subsection 2.4.3, after propagation through a length L of Standard Single-Mode Fiber (SSMF), the resultant frequency-domain signal can be conveniently expressed by:

$$E_{out}(\omega) = E_{in}(\omega) e^{-j\beta(\omega)L} \tag{2.13}$$

with $E_{in}(\omega)$ being the frequency-domain equivalent of $E_{in}(t)$, both signals related one to the other by the Fourier Transform. As far as the propagation constant is concerned, only the term associated to the chromatic dispersion is considered. We should remember that in a squared-law detection, the received electrical signal is proportional not to the optical field itself but to its intensity. This is why we chose to represent $E_{in}(t)$ as a function of an intensity component in 2.9.

Once the field expressions in the time and frequency domains after propagation have been defined, it is possible to infer the electrical current detected by the photodiode. That's exactly where and how the small-signal assumption comes in handy. Indeed, in the SSR, the relation between amplitude and intensity modulations is approximately linear:

$$\sqrt{P_{in}(t)} \cong \sqrt{P_0} \left(1 + \frac{m_{IM}}{2} \cos\left(\omega t\right)\right) = A_0 \left(1 + m_{AM} \cos\left(\omega t\right)\right) \tag{2.14}$$

with m_{AM} being the amplitude modulation index and A_0 the mean amplitude of the signal. In addition, the expansion of the phase component $\Phi_{in}(t)$ in Bessel functions [36–38] is also simplified and we can verify relatively easily the characteristic channel frequency response of the fiber. In [31], the authors demonstrate that the modulus of the transfer function of a dispersive IMDD channel will be given by:

$$H_{IMDD}(\omega) = \left| \cos(\theta) - \sin(\theta) H_{IM \leftrightarrow PM}(\omega) \right| \tag{2.15}$$

where:

$$\theta = \frac{L D \lambda_0^2 \omega^2}{4\pi c} \tag{2.16}$$

is the phase term related to the fiber chromatic dispersion. $H_{IM\leftrightarrow PM}(\omega)$ is the complex small-signal transfer function between phase and intensity modulation of the light source characterizing its chirp. Equation 2.15 shows that the source's chirp and the fiber dispersion are perfectly described in the amplitude of the channel's transfer function for any propagating distance different from zero.

Many particular cases may be found from 2.15. For instance, if we consider the simplest case of an unchirped light source, then $H_{IM\leftrightarrow PM}(\omega) = 0$ and the optical field $E_{in}(t)$ at the input of the fiber is composed of a pure intensity modulation term. In this case, the modulus of the channel transfer function is [25, 31]:

$$H_{IM\leftrightarrow PM}(\omega) = |\cos(\theta)| \tag{2.17}$$

Equation 2.17 characterizes a frequency-selective channel with sharp dips located at:

$$\omega_k = \frac{2\pi}{\lambda_0}\sqrt{\frac{c\left(n+\frac{1}{2}\right)}{LD}},\ n = 0, 1, 2, ... \tag{2.18}$$

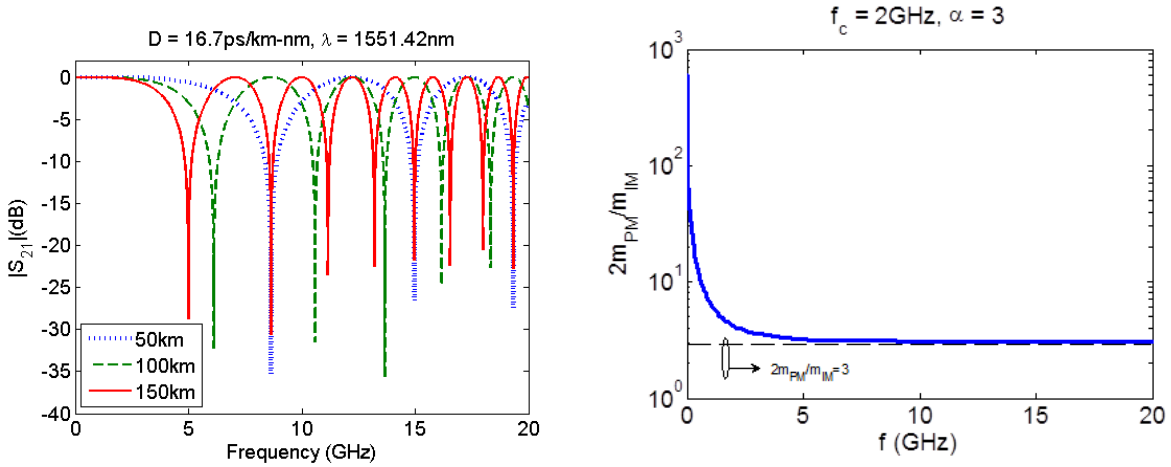

(a) (b)

Figure 2.13: (a) Examples of channel frequency response with pure IM and different fiber lengths. (b) Variation of the ratio between phase and amplitude modulation indices with the modulation frequency for the case of a laser with both PM and FM components.

Using (2.18), the fiber dispersion coefficient can be easily inferred with a network analyzer from the resonance frequencies of $H_{IMDD}(\omega)$ if the parameters λ_0 and L are known beforehand. Also, the number of lobes per frequency span in the channel increases with the length and dispersion coefficient of the fiber, as seen in Figure 2.13(a).

Indeed, as far as a frequency domain analysis is concerned, the dispersion-induced frequency selectivity of the channel constitutes the main limitation when increasing the range of high bit-rate IMDD NRZ transmissions since the fiber losses can be easily surpassed by means of an optical amplification in the link (see section 2.4.2).

For the generalized case, $H_{IM\leftrightarrow PM}(\omega)$ can be defined by:

$$H_{IM\leftrightarrow PM}(\omega) = \frac{2m_{PM}}{m_{IM}}e^{j\Delta\varphi} = a + jb(\omega) \tag{2.19}$$

The parameter a represents a pure PM component that will change both the dips' positioning and the lobes' height whereas $b(\omega)$ may be thought of as frequency modulation (FM) term which will have a direct effect on the depth of the dips of the channel. Note that the PM and FM terms

represent one same sort of "angle modulation", the frequency modulation term being found from the time-derivative of the phase modulation component. The only difference between them is a phase-shift of $\pi/2$ and the modulation frequency dependency in FM.

This proposal becomes clearer if we take the example of a single longitudinal mode laser. The interaction between phase and intensity modulation in a laser is described with the help of its rate equations, which show how the changes in the carriers' density will influence the optical field inside the laser cavity. In [34], it is demonstrated that the relation between the instantaneous frequency $\nu(t)$ (i.e., the time derivative of the phase modulation component) and the optical power $P(t)$ is given by:

$$\nu\left(t\right) = \nu_0 + \Delta\nu = \frac{\alpha}{4\pi}\left(\frac{1}{P\left(t\right)}\frac{dP\left(t\right)}{dt} + \kappa P\left(t\right)\right) \tag{2.20}$$

with:

$$\Delta\nu\left(t\right) = \frac{1}{2\pi}\frac{d\Phi\left(t\right)}{dt} \tag{2.21}$$

where α is the linewidth enhancement factor, also known as the Henry parameter and κ is a laser-specific parameter known as the adiabatic chirp constant. κ is related to the thermal effects in the laser and depends on several of its characteristics such as the gain saturation, the carriers' lifetime and the confinement factor. The left and right-hand side terms inside the parenthesis in 2.20 are also called by some authors the transient and adiabatic components of the chirp respectively. In our notation, these terms correspond respectively to the PM and FM contributions. From 2.20 and 2.21, if we admit that:

$$\frac{1}{P\left(t\right)} \cong \frac{1}{P_0} \tag{2.22}$$

$$\nu_0 = \frac{\alpha\kappa P_0}{4\pi} \tag{2.23}$$

it is possible to find the laser small-signal transfer function:

$$H_{IM\leftrightarrow PM}(\omega) = \alpha\left(1 - j\frac{\omega_c}{\omega}\right) \tag{2.24}$$

with:

$$\Delta\varphi = \tan^{-1}\left(-\frac{\omega_c}{\omega}\right) \tag{2.25}$$

$$\frac{2m_{PM}}{m_{IM}} = \alpha\sqrt{1 + \left(\frac{\omega_c}{\omega}\right)^2} \tag{2.26}$$

$$\omega_c = \kappa P_0 \tag{2.27}$$

which gives for the general channel transfer function [28–30]:

$$H_{IMDD}\left(\omega\right) = |\cos\left(\theta\right) - \sin\left(\theta\right)\alpha\left(1 - j\frac{\omega_c}{\omega}\right)| \tag{2.28}$$

The parameter ω_c is called corner frequency. It states a frequency value from which the transient chirp effects on the channel response start to be stronger than the adiabatic chirp effects. If the phase and intensity modulation terms $P_{in}(t)$ and $\Phi_{in}(t)$ are in phase, i.e., $\Delta\varphi = 0$, the familiar expression $\alpha = 2m_{PM}/m_{IM}$ results. In this case, the laser chirp is mostly influenced by the pure PM term (transient chirp) and the channel transfer function will be:

$$H_{IMDD}(\omega) = |\cos(\theta) - \alpha \sin(\theta)| = \sqrt{1+\alpha^2}\cos\left(\theta + \tan^{-1}(\alpha)\right) \tag{2.29}$$

The reader should notice that making $\alpha = 0$ in 2.29 would directly lead to 2.17. In addition, from 2.25, the phase-match between intensity and phase modulation components will happen either if the modulation frequency obeys $\omega \gg \omega_c$ or if $\omega_c \approx 0$. Indeed, equation 2.29 is used in [27] to characterize the small-signal IMDD transfer function of a channel that has an electroabsorption modulator ($\omega_c \approx 0$) as the transmitter.

In [28–30], equation 2.28 is used this time to describe a system with a directly modulated laser. In this case, it is possible to notice the importance of the FM component for modulation frequencies below the laser's characteristic parameter ω_c. The channel's transfer function should converge, however, to the one obtained with an electroabsorption modulator for all $\omega \gg \omega_c$.

The ratio $2m_{PM}/m_{IM}$ between the phase and intensity modulation indices can also be found through an evaluation of the signal modulation sidebands either in the optical domain with a high-resolution Optical Spectrum Analyzer (OSA) [39] or by means of a transposition of the optical spectrum to the electrical domain. The last method can be implemented for instance with the optical heterodyne approach, in which a second laser serves as a local oscillator or even with the Gated-Delayed Self-Homodyne (GDSH) technique, which is implemented with a Mach-Zehnder interferometer and a gated signal [40–43]. Other examples of optical discriminators include the Fabry-Perot and Michelson interferometers [44, 45].

Figure 2.13(b) shows the variation of $2m_{PM}/m_{IM}$ with the modulation frequency for an example in which $\alpha = 3$ and $f_c = \omega_c/2\pi = 2GHz$. As previewed by 2.26, for large modulation frequencies, the transfer function of 2.28 will converge to that of 2.29 and $2m_{PM}/m_{IM}$ to α.

Other interesting scenario arises if only the FM component exists in 2.28. In this case, the intensity and phase modulation components $P_{in}(t)$ and $\Phi_{in}(t)$ are in quadrature, i.e., $\Delta\varphi = \frac{\pi}{2}$ (the IM and FM components are in phase) and $H_{IM\leftrightarrow PM}(\omega)$ is a purely imaginary function that leads to:

$$H_{IMDD}(\omega) = |\cos(\theta) - j\sin(\theta)\frac{2m_{PM}}{m_{IM}}| \tag{2.30}$$

Particularly, the case where $2m_{PM}/m_{IM} = 1$ corresponds to an optical single-side band (OSSB) modulation, for which $H_{IMDD}(\omega) = 1$. This condition is reported in [46] for digital OOK transmissions with ameliorated robustness to fiber dispersion.

Table 2.1 recaps on the main small-signal IMDD channel transfer functions seen in this section and their applications when using lasers as transmitters.

Figure 2.14(a) shows an example that highlights the differences between the four small-signal transfer functions represented in Table 2.1. We take $\lambda_0 = 1551.42nm$, $D = 16.7ps/km \cdot nm$, $L = 100km$, $\alpha = 3$, $f_c = 2GHz$ and $2m_{PM}/m_{IM} = 0.75$ for the case in which $H_{IM\leftrightarrow PM}(\omega)$ is purely imaginary.

By comparing the IM and IM+PM curves of Figure 2.14(a), we can see that the α parameter will change, as expected, the position of the dips and the height of the lobes of the channel. Indeed, for the case of an electroabsorption modulator we have $a = \alpha$ and $b(\omega) = 0$, i.e., α represents the pure PM term of the modulating signal in $H_{IM\leftrightarrow PM}(\omega)$. Interestingly, some gain proportional to α can be obtained at specific frequency regions in the small-signal regime, as shown in Figure 2.14(b). The reader should hold on to this information for the following sections.

If we compare this time the IM+PM and IM+PM+FM curves, it is possible to see that FM term will act to reduce the depth of the dips in the channel transfer function, specially for modulation frequencies below the laser-specific frequency f_c. For the case IM+FM, it is possible to see that the dips' depth has been considerably decreased if compared to the other curves and that they have the same location as in the pure IM case, which is quite logical since we

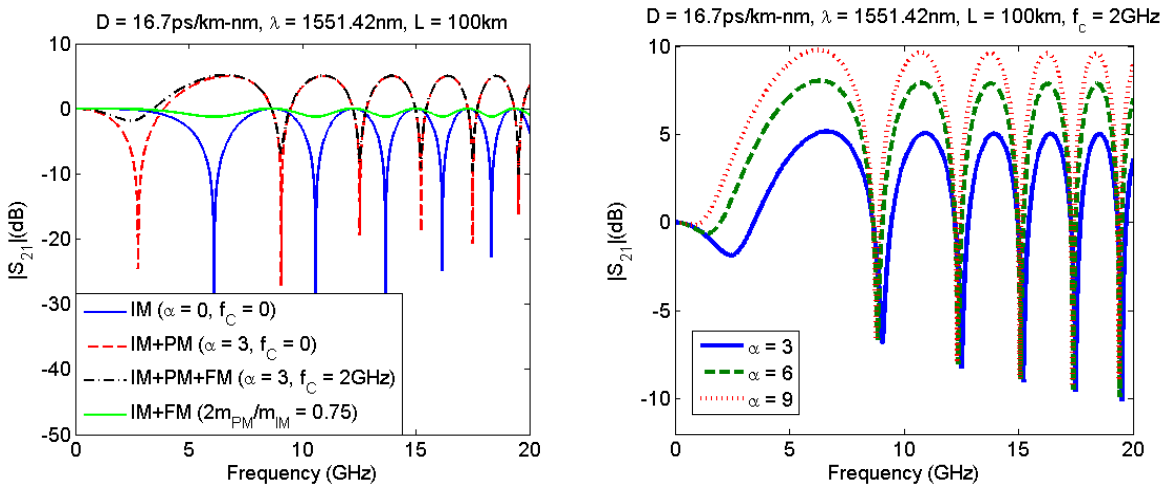

(a) (b)

Figure 2.14: (a) Different SSR single-tone IMDD channel models. (b) Variation of the IM+PM+FM channel response with different values of α .

Table 2.1: Dispersive IMDD SSR channel transfer functions when using lasers as sources.

$H_{IMDD}(\omega)$	Modulation Components	Application
$\lvert\cos(\theta)\rvert$	IM	Unchirped laser
$\lvert\cos(\theta) - \alpha\sin(\theta)\rvert$	IM + PM	EAM or DML with $\omega \gg \omega_C$
$\lvert\cos(\theta) - \sin(\theta)\,\alpha\left(1 - j\frac{\omega_c}{\omega}\right)\rvert$	IM + PM + FM	DML
$\lvert\cos(\theta) - \sin(\theta)\left(j\frac{2m_{PM}}{m_{IM}}\right)\rvert$	IM + FM	SSB modulation if $m_{IM} = 2m_{PM}$

don't have any PM term. The amplitude of the channel response would be completely flat for $2m_{PM}/m_{IM}$ =1.

With the help of the channel transfer function models, we can quite easily determine the fiber and laser characteristics by means of a simple measurement with a network analyzer. For the case of pure PM modulation, the fiber dispersion and the laser's linewidth enhancement factor can still be deduced using only the channel's resonance frequencies, as reported in [27]. However, if the laser has both PM and FM terms, better results are obtained by means of fitting techniques, as described in section 4.2.

2.5.2 Large-signal Regime, Multi-tone Modulation

In the previous sections, we have described the transfer function of an IMDD system after propagation through a single-mode fiber. Even though the presented models managed to include the laser chirp effects for both external and direct modulation cases, they are limited to a single-tone modulation scenario under the small-signal constraint, in which the effects of fiber dispersion and laser chirp are fairly "well-behaved".

In order to conceive a model that would precisely characterize an IMDD OFDM transmission, the consequences of multitone modulation and large signal operation would have to be included in both intensity and phase modulation components of the propagating signal. The large signal modulation of a chirped light source would have then to be studied at the same time in three main axes:

1. the electro-optical conversion and

2. intensity-to-phase coupling at the transmitter side and

3. the squared-law detection after propagation through a dispersive medium at the receiver side.

Such an analysis would also have to consider the particular case of overlapping subcarriers to differentiate between the OFDM modulation and standard Subcarrier Multiplexed (SCM) transmissions. A complete model that addresses all this axes for an OFDM signal has not yet been reported. However, many works concentrate in some of these points separately. In section 4.3 we experimentally address the dynamics of the SNR variation of an IMDD OFDM transmission for different intensity modulation indices and accumulated dispersions in the link.

References

[1] Agilent. *Optimizing Dynamic Range for Distortion Measurements*. URL: http://cp.literature.agilent.com/litweb/pdf/5980-3079EN.pdf (cit. on p. 19).

[2] Anritsu. *Advanced Spectrum Analysis Tools for Microwave Bench Test*. URL: http://www.mechatec.co.kr/upload/pty3/1192246268_0.pdf (cit. on p. 19).

[3] Carls Ferguson, John Drum, and John Krupsky. *Receiver Metrics: Theory and Practice Intermodulation and the 3rd Order Intercept Point*. URL: http://www.google.fr/url?sa=t&rct=j&q=receiver%20metrics%20theory%20and%20practice%20intermodulation%20and%20the%203rd%20order%20intercept%20point&source=web&cd=1&sqi=2&ved=0CB4QFjAA&url=http%3A%2F%2Fwww.w4uoa.net%2FTARCPresentationv14.ppt&ei=sTQ_UL3WBYazhAeE24CIDA&usg=AFQjCNF8VP3-JROq146PXjVCh57MXU4ejA (cit. on p. 19).

[4] Govind P. Agrawal. *Fiber-Optic Communication Systems (Wiley Series in Microwave and Optical Engineering)*. Wiley-Interscience, 2010. ISBN: 0470505117. URL: http://www.amazon.com/Fiber-Optic-Communication-Systems-Microwave-Engineering/dp/0470505117%3FSubscriptionId%3D0JYN1NVW651KCA56C102%26tag%3Dtechkie-20%26linkCode%3Dxm2%26camp%3D2025%26creative%3D165953%26creativeASIN%3D0470505117 (cit. on pp. 21–23, 25, 26).

[5] W.S.C. Chang. *Principles of Lasers and Optics*. Cambridge University Press, 2005. ISBN: 9780521642293. URL: http://books.google.fr/books?id=oYTjNwWC4S4C (cit. on p. 21).

[6] Govind Agrawal. *Nonlinear Fiber Optics, Fourth Edition (Optics and Photonics)*. Academic Press, 2006. ISBN: 0123695163 (cit. on pp. 21, 23).

[7] I.P. Kaminow and T. Li. *Optical Fiber Telecommunications IV*. Optics and Photonics v. 1. Academic Press, 2002. ISBN: 9780123951724. URL: http://books.google.fr/books?id=pAbRHEbLuEwC (cit. on p. 21).

[8] J.C. Campbell. "Recent Advances in Telecommunications Avalanche Photodiodes". In: *Lightwave Technology, Journal of* 25.1 (Jan. 2007), pp. 109 –121. ISSN: 0733-8724. DOI: 10.1109/JLT.2006.888481 (cit. on p. 22).

[9] Wikipedia. *Relative intensity noise*. URL: http://en.wikipedia.org/wiki/Relative_Intensity_Noise (cit. on p. 23).

[10] Gregory E. Obarski and Paul D. Hale. *How to measure relative intensity noise in lasers*. Jan. 1999. URL: http://www.laserfocusworld.com/articles/print/volume-35/issue-5/features/how-to-measure-relative-intensity-noise-in-lasers.html (cit. on p. 23).

[11] Eagleyard Photonics. *Relative Intensity Noise of Distributed Feedback Lasers*. URL: http://www.eagleyard.com/fileadmin/downloads/app_notes/App_Note_RIN_1-5.pdf (cit. on p. 23).

[12] Hamamatsu. *Photodiode Technical Guide*. URL: sales.hamamatsu.com/assets/html/ssd/si-photodiode/index.htm (cit. on p. 23).

[13] Joffray Guillory. "Radio over Fiber for the Future Home Area Networks". PhD thesis. Université de Paris-Est, 2012 (cit. on p. 23).

[14] Thanh Nga Duong. "Etude de Techniques de Modulation Multi-porteuse OFDM pour la Montée en Débit dans le Réseau d'Accès Optique". PhD thesis. Université de Rennes I, 2010 (cit. on p. 23).

[15] Benoît Charbonnier. "Contribution à l'Etude des Systèmes Monocanaux de Transmission de Soliton pour les Réseaux Terrestres". PhD thesis. Ecole National Supérieure des Télécommunications, 1997 (cit. on p. 26).

[16] S.M. Abdur Razzak, Y. Namihira, and F. Begum. "Ultra-flattened dispersion photonic crystal fibre". In: *Electronics Letters* 43.11 (24 2007), pp. 615 –617. ISSN: 0013-5194. DOI: 10.1049/el:20070558 (cit. on p. 27).

[17] A. Ferrando et al. "Designing a photonic crystal fibre with flattened chromatic dispersion". In: *Electronics Letters* 35.4 (Feb. 1999), pp. 325 –327. ISSN: 0013-5194. DOI: 10.1049/el:19990189 (cit. on p. 27).

[18] N.H. Hai et al. "A novel ultra-flattened chromatic dispersion using defected elliptical pores photonic crystal fiber with low confinement losses". In: *Antennas and Propagation Society International Symposium, 2007 IEEE*. June 2007, pp. 2233 –2236. DOI: 10.1109/APS.2007.4395974 (cit. on p. 27).

[19] K. Iiyama, Z. Yamashita, and S. Takamiya. "Design of dispersion flattened photonic crystal fiber with a large core and a concentric missing ring". In: *Fibres and Optical Passive Components, 2005. Proceedings of 2005 IEEE/LEOS Workshop on*. June 2005, pp. 10 –13. DOI: 10.1109/WFOPC.2005.1462092 (cit. on p. 27).

[20] N.Y. Joly et al. "Dispersion-designed high-delta photonic crystal fiber". In: *Lasers and Electro-Optics, 2004. (CLEO). Conference on*. Vol. 1. May 2004, 3 pp. vol.1 (cit. on p. 27).

[21] J.C. Knight et al. "Anomalous dispersion in photonic crystal fiber". In: *Photonics Technology Letters, IEEE* 12.7 (July 2000), pp. 807 –809. ISSN: 1041-1135. DOI: 10.1109/68.853507 (cit. on p. 27).

[22] S.M.A. Razzak et al. "Decagonal Photonic Crystal Fibers with Ultra-Flattened Chromatic Dispersion and Low Confinement Loss". In: *Optical Fiber Communication and the National Fiber Optic Engineers Conference, 2007. OFC/NFOEC 2007. Conference on*. Mar. 2007, pp. 1 –6. DOI: 10.1109/OFC.2007.4348389 (cit. on p. 27).

[23] Lin-Ping Shen, Wei-Ping Huang, and Shui-Sheng Jian. "Design of photonic crystal fibers for dispersion-related applications". In: *Lightwave Technology, Journal of* 21.7 (July 2003), pp. 1644 –1651. ISSN: 0733-8724. DOI: 10.1109/JLT.2003.814397 (cit. on p. 27).

[24] Wang Zhi, Ren Guobin, and Lou Shuqin. "A novel supercell overlapping method for different photonic crystal fibers". In: *Lightwave Technology, Journal of* 22.3 (Mar. 2004), pp. 903 –916. ISSN: 0733-8724. DOI: 10.1109/JLT.2004.824562 (cit. on p. 27).

[25] B. Christensen et al. "Simple dispersion measurement technique with high resolution". In: *Electronics letters* vol. 29, no1 (1993), 132–134 (6 ref.) URL: http://cat.inist.fr/?aModele=afficheN&cpsidt=4512004 (cit. on pp. 30, 32).

[26] Jason D. McKinney. *Measurement of Chromatic Dispersion using the Baseband Radio-Frequency Response of a Phase-Modulated Analog Optical Link Employing a Reference Fiber*. Sept. 2007. URL: http://www.dtic.mil/cgi-bin/GetTRDoc?AD=ADA472284 (cit. on p. 30).

[27] F. Devaux, Y. Sorel, and J.F. Kerdiles. “Simple measurement of fiber dispersion and of chirp parameter of intensity modulated light emitter”. In: *Lightwave Technology, Journal of* 11.12 (Dec. 1993), pp. 1937 –1940. ISSN: 0733-8724. DOI: 10.1109/50.257953 (cit. on pp. 30, 34, 35).

[28] L. Bjerkan et al. “Measurement of laser parameters for simulation of high-speed fiberoptic systems”. In: *Lightwave Technology, Journal of* 14.5 (May 1996), pp. 839 –850. ISSN: 0733-8724. DOI: 10.1109/50.495166 (cit. on pp. 30, 33, 34).

[29] A. Royset et al. “Use of dispersive optical fibre for characterisation of chirp in semiconductor lasers”. In: *Electronics Letters* 30.9 (Apr. 1994), pp. 710 –712. ISSN: 0013-5194. DOI: 10.1049/el:19940505 (cit. on pp. 30, 33, 34).

[30] R.C. Srinivasan and J.C. Cartledge. “On using fiber transfer functions to characterize laser chirp and fiber dispersion”. In: *Photonics Technology Letters, IEEE* 7.11 (Nov. 1995), pp. 1327 –1329. ISSN: 1041-1135. DOI: 10.1109/68.473487 (cit. on pp. 30, 33, 34).

[31] J. Wang and K. Petermann. “Small signal analysis for dispersive optical fiber communication systems”. In: *Lightwave Technology, Journal of* 10.1 (Jan. 1992), pp. 96 –100. ISSN: 0733-8724. DOI: 10.1109/50.108743 (cit. on pp. 30–32).

[32] C. Henry. “Theory of the linewidth of semiconductor lasers”. In: *Quantum Electronics, IEEE Journal of* 18.2 (Feb. 1982), pp. 259 –264. ISSN: 0018-9197. DOI: 10.1109/JQE.1982.1071522 (cit. on p. 31).

[33] M. Joindot and I. Joindot. *Les télécommunications par fibres optiques*. Collection technique et scientifique des télécommunications. Dunod, 1996. ISBN: 9782100027873. URL: http://books.google.fr/books?id=SEeqHAAACAAJ (cit. on p. 31).

[34] T.L. Koch and J.E. Bowers. “Nature of wavelength chirping in directly modulated semiconductor lasers”. In: *Electronics Letters* 20.25 (June 1984), pp. 1038 –1040. ISSN: 0013-5194. DOI: 10.1049/el:19840709 (cit. on pp. 31, 33).

[35] T. L. Koch and R. A. Linke. “Effect of nonlinear gain reduction on semiconductor laser wavelength chirping”. In: *Applied Physics Letters* 48.10 (Mar. 1986), pp. 613 –615. ISSN: 0003-6951. DOI: 10.1063/1.96770 (cit. on p. 31).

[36] G. Meslener. “Chromatic dispersion induced distortion of modulated monochromatic light employing direct detection”. In: *Quantum Electronics, IEEE Journal of* 20.10 (Oct. 1984), pp. 1208 –1216. ISSN: 0018-9197. DOI: 10.1109/JQE.1984.1072286 (cit. on p. 31).

[37] E. Peral and A. Yariv. “Large-signal theory of the effect of dispersive propagation on the intensity modulation response of semiconductor lasers”. In: *Lightwave Technology, Journal of* 18.1 (Jan. 2000), pp. 84 –89. ISSN: 0733-8724. DOI: 10.1109/50.818911 (cit. on p. 31).

[38] E. Peral and A. Yariv. “Large-signal analysis of the effect of dispersive propagation on the intensity modulation response of semiconductor lasers”. In: *Lasers and Electro-Optics, 1999. CLEO ’99. Summaries of Papers Presented at the Conference on*. May 1999, pp. 311 –312. DOI: 10.1109/CLEO.1999.834236 (cit. on p. 31).

[39] A. Villafranca, J. Lasobras, and I. Garces. “Precise characterization of the frequency chirp in directly modulated DFB lasers”. In: *Electron Devices, 2007 Spanish Conference on*. 31 2007-feb. 2 2007, pp. 173 –176. DOI: 10.1109/SCED.2007.384020 (cit. on p. 34).

[40] D.M. Baney and P.B. Gallion. “Power spectrum measurement of a modulated semiconductor laser using an interferometric self-homodyne technique: influence of quantum phase noise and field correlation”. In: *Quantum Electronics, IEEE Journal of* 25.10 (Oct. 1989), pp. 2106 –2112. ISSN: 0018-9197. DOI: 10.1109/3.35722 (cit. on p. 34).

[41] D.M. Baney, P.B. Gallion, and C. Chabran. “Measurement of the swept-frequency carrier-induced FM response of a semiconductor laser using an incoherent interferometric technique”. In: *Photonics Technology Letters, IEEE* 2.5 (May 1990), pp. 325 –327. ISSN: 1041-1135. DOI: 10.1109/68.54694 (cit. on p. 34).

[42] D.M. Baney and W.V. Sorin. “Measurement of a modulated DFB laser spectrum using gated delayed self-homodyne technique”. In: *Electronics Letters* 24.11 (May 1988), pp. 669 –670. ISSN: 0013-5194 (cit. on p. 34).

[43] M. Nazarathy et al. “Spectral analysis of optical mixing measurements”. In: *Lightwave Technology, Journal of* 7.7 (July 1989), pp. 1083 –1096. ISSN: 0733-8724. DOI: 10.1109/50.29635 (cit. on p. 34).

[44] B. Christensen et al. “Detailed mapping of the local IM and FM responses of DFB lasers”. In: *Electronics Letters* 31.10 (May 1995), pp. 799 –800. ISSN: 0013-5194. DOI: 10.1049/el:19950551 (cit. on p. 34).

[45] S. Kobayashi et al. “Direct Frequency Modulation In AlGaAs Semiconductor Lasers”. In: *Microwave Theory and Techniques, IEEE Transactions on* 30.4 (Apr. 1982), pp. 428 –441. ISSN: 0018-9480. DOI: 10.1109/TMTT.1982.1131084 (cit. on p. 34).

[46] J. Binder and U. Kohn. “10 Gbit/s-dispersion optimized transmission at 1.55 /spl mu/m wavelength on standard single mode fiber”. In: *Photonics Technology Letters, IEEE* 6.4 (Apr. 1994), pp. 558 –560. ISSN: 1041-1135. DOI: 10.1109/68.281826 (cit. on p. 34).

Chapter 3

OFDM: Principles, Simulations and Some Results

3.1 Introduction

We have seen in the previous chapter that the major phenomenon limiting the transmission of high bit-rates over a long-reach IMDD PON is the fiber chromatic dispersion. Despite the simplicity of this modulation technique, high bit-rate IMDD OOK systems have to be accompanied by some kind of dispersion compensation technique (either optical or electronic) in order to overcome the frequency-fading characterizing the dispersive optical channel. In this chapter, we describe the principles of Orthogonal Frequency Division Multiplexing, an advanced multi-carrier modulation format that can offer at the same time increased robustness to chromatic-dispersion and enhanced spectral efficiencies while maintaining the simple and cost-effective IMDD approach.

We address the principles of OFDM and analyze the modulation and demodulation procedures of an IMDD OFDM signal. By doing so, not only we manage to highlight the many advantages of this modulation compared to single-carrier approaches but we also provide a detailed step-by-step model that will help understand what is behind the experimental setups shown in Part II. Before addressing the demodulation block, however, we assess the existing types of optical OFDM modulations, including coherent-OFDM and all-optical OFDM and highlight their differences compared to the IMDD solution. We also discuss some interesting techniques used for time and frequency synchronization, which are critical issues in OFDM transmissions. A detailed analysis of the principles of bit and power loading algorithms is also provided to establish the connection between the dispersive IMDD channel frequency response introduced in chapter 2 and the multiuser OFDM approaches that are addressed lately. Finally, we identify some performance parameters that are necessary for evaluating the transmissions.

3.2 OFDM, a Long-standing Friend

OFDM has been first introduced in the late 60's and is a particular case of Frequency-Division Multiplexing (FDM). It is a multicarrier technique that guarantees robustness to the harmful effects of dispersion while allowing an efficient occupation of the available modulation bandwidth of the channel. It has been adopted in many standards including wireline Asymmetric and Very High Bit-rate Digital Subscriber Line (ADSL and VDSL) and Power Line Communications (PLC) as well as wireless Digital Audio Broadcasting (DAB), Wireless Local Area Network (WLAN, IEEE 802.11a/g/n [1–3]), Worldwide Interoperability for Microwave Access (WiMAX) and 3GPP Long Term Evolution (LTE). Table 3.1 recaps on the main characteristics of ADSL and VDSL and Table 3.2 shows several other wireline and wireless standards that use OFDM [4].

Name	Standard(s)	Transmission Mean	First Publication	Frequency Range	Subcarriers	Modulation Scheme	Δf	Maximum Bit-rate
ADSL	ANSI T1.413 ITU G.992.1 ITU G.992.2	twisted pair	ANSI: 1995, 1998 ITU : 1999	US: $25.875 - 138$ kHz DS: $138 - 1104$ kHz	255	Adaptive, up to 15 bits/symbol	4.3125 kHz	US: 1.8 Kb/s DS: 12 Mb/s
ADSL2	ITU G.992.3 ITU G.992.4	twisted pair	2002	US: $25.875 - 138$ kHz DS: $138 - 1104$ kHz				US: 3.5 Mb/s DS: 12 Mb/s
ADSL2+	ITU G.992.5	twisted pair	2003	US: $25.875 - 138$ kHz DS: $138 - 2200$ kHz	511			US: 3.5 Mb/s DS: 24.5 Mb/s
VDSL	ITU G.993.1	twisted pair coaxial cable	2004	US: $2.5 - 3.75$ MHz and $f_x - 12$ MHz DS: $0.138 - 2.5$ MHz and $3.75 - f_x$ MHz	Up to 4095			US: 16 Mb/s DS: 52 Mb/s 85 Mb/s (coax.)
VDSL2	ITU G.993.2	twisted pair coaxial cable	2006	Up to 30 MHz (depends on profile)			4.3125 kHz 8.625 kHz	100 Mb/s

Table 3.1: ADSL and VDSL standards.

Wireline			Wireless	
Name	Standard(s)	Transmission Mean	Name	Standard(s)
DVB-C2	ETSI DVB-C2	Cable TV	WLAN	IEEE 802.11a/g/n HYPERLAN/2
PLC	IEEE 1901	Power line	Digital Radio	DAB/EUREKA 147 DAB+ HD Radio DRM T-DMB ISDB-TSB
G.hn Home Networking	ITU-T G.9960	Coaxial, power line and telephone line	Digital TV	DVB-T ISDB-T
MoCA	MoCA 1.1/2.0	Coaxial	Mobile TV	DVB-H T-DMB ISDB-T MediaFLO
			WPAN-UWB	IEEE 802.15.3a
			Mobile WiMAX	IEEE 802.16e
			MBWA	IEEE 802.20
			Evolved Packet System	LTE

Table 3.2: Wireline and Wireless OFDM standards.

Despite its success in radio-frequency applications, OFDM has only recently started to draw the attention of the optical access network community owing principally to the outstanding advancements in electronics and the increasing demands for higher bit-rates. OFDM appears as one possible solution to cost-effectively provide the long-awaited flexibility that lacks on today's somewhat "rigid" passive optical networks and to allow their evolution towards higher bit-rates, longer transmission distances and increased number of subscribers per PON tree.

In this work, we focus on the IMDD transmission approach which, as previously mentioned, can manage to keep the simplicity and cost-effectiveness of the optical plane by transferring all the "hard work" to the electronics and digital signal processing techniques. The reports on offline SSMF IMDD OFDM transmissions are countless and we should address some of them throughout this work.

As far as the real-time reports are concerned, we can notably name the works summarized in [5]. The authors not only managed to experimentally demonstrate high spectral efficiency transmissions with bit and/or power loading schemes using different emitters (DFB, VCSEL and RSOA) [6–14] but also provided some very interesting results on time-synchronization solutions including cyclic prefix-based [15] and DC subcarrier-based [16] algorithms and even sending the clock reference together with the OFDM signal [17]. The authors have also reported other interesting experimental demonstrations on the WDMA-FDMA-OFDM solution (see section 6.3) [18, 19] and several simulation studies on the use of (R)SOA for colorless operation on WDM-PON architectures [20–22].

Orange Labs has also started its own real-time OFDM endeavor. At the present time, a real-time OFDM platform with bit and power loading capability based on the Levin-Campello algorithm (see section 3.7) has already been demonstrated targeting at least $1Gb/s$ transmissions over $> 50m$ step-index plastic optical fibers (SI-POF) for domestic networks.

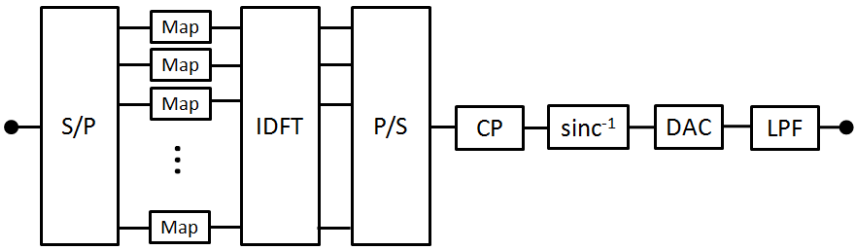

Figure 3.1: OFDM modulator.

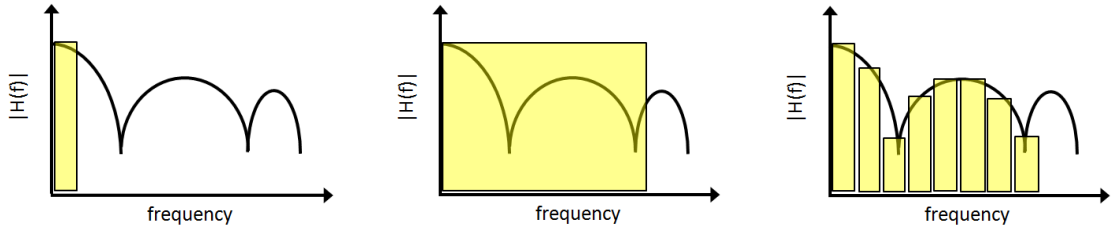

Figure 3.2: Representation of the electrical spectra of single and multi-carrier signals. (a) Low bit-rate SC. (b) High bit-rate SC. (c) High bit-rate MC.

3.3 Transmitter Architecture and Experimental Constraints

Figure 3.1 shows a basic block-diagram of an OFDM transmitter which we detail in the following of this section.

3.3.1 Serial-to-Parallel Conversion: From Single to Multi-carrier Systems

Let us consider the typical case of a single-carrier (SC) transmission in the optical domain: an IMDD NRZ signal that propagates through a SMMF span, such as defined, for instance, in currently deployed GPON ITU-T G.984 [23].

We have seen in section 2.5 that, as far as a frequency-domain analysis is concerned, the dispersive nature of the optical fiber will cause different phase variations on the spectral components of the ODSB signal [24, 25]. When submitted to a square-law detection, such phase variations between the right-side band (RSB) and the left-side band (LSB) of the signal, will translate into a frequency-selective channel whose response will depend on the fiber dispersion and the interaction between the intensity and phase modulation terms arriving from the laser chirp. Indeed, the impulse response of a dispersive fiber results in an undulating transfer function, where the frequency-domain fluctuations are referred to as "frequency selective-fading" [26]. Contrary to the wireless transmission case, in which fast fading may occur due to multipath propagation or shadowing from moving obstacles, the time variations of the optical channel will be very slow thanks to the confined nature of the optical channel.[1].

For low bit-rates and/or short fiber lengths, fiber dispersion will not impose many problems to the transmitted signals as we can see in Figure 3.2(a). Indeed, if we take the example of GPON, $2.5Gbit/s$ downstream transmissions at $1490nm$ and up to $20km$ SSMF are standardized without any kind of dispersion compensation mechanism. However, if we want to increase the bit rate of such a system, it is straightforward to affirm from the time-frequency duality principle that the symbol's duration will decrease and its spectrum will broaden. The signal with a broader spectrum will be more affected by the channel's fading, as represented in Figure 3.2(b).

[1]Here, we assume that the changing on the channel's frequency response due to polarization mode dispersion (PMD) are negligible compared to the chromatic dispersion effects.

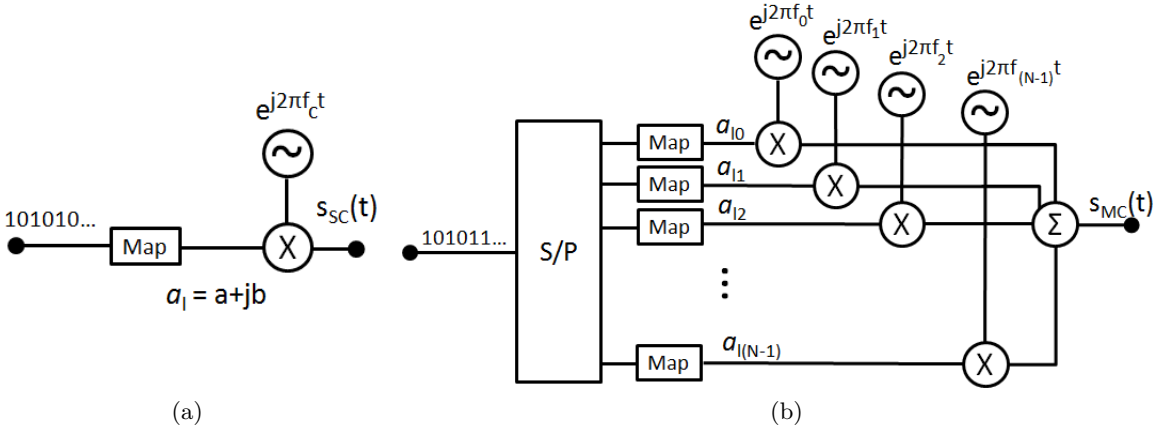

Figure 3.3: Comparison between (a) SC and (b) MC block diagrams.

Actually, such analysis is nothing more than the frequency-domain reciprocal of the phenomenon explained in subsection 2.4.3: the fiber dispersion will cause the information envelope to spread in time and eventually overlap with neighboring pulses, creating what is known as inter-symbol interference (ISI). ISI will be stronger either if the symbols' durations are shorter (high bit-rate signals) and/or if the spreading is wider (higher dispersions or longer fibers).

Despite the fact that very performing equalization techniques exist, the great complexity behind the apparatus needed to revert strong dispersion effects allowed Multi-Carrier Modulation (MCM) approaches to appear as an interesting solution for increasing the bit-rate of a signal submitted to a dispersive channel. In MCM systems, the information is divided into a set of parallel lower-bit-rate sub-channels. Each parallel data sequence then modulates a specific subcarrier. Since each sub-channel has a narrower bandwidth, the frequency components of the signal will be altered by a smoother (ideally flat or quasi-flat) and independent channel component, as depicted in Figure 3.2(c) and this will considerably simplify the frequency equalization procedure on the received signal.

Figures 3.3(a) and (b) show respectively the simplified block-diagrams of single-carrier and FDM modulations. The block "Map" (see section 3.3.3) converts binary data into codewords a_{lk} (for instance, sets of QPSK or 16QAM words) in order to increase the amount of transmitted bits per Hz of the system. The block "S/P" is responsible for the serial-to-parallel conversion.

The MCM signal $s_{MC}(t)$ of figure 3.3(b) is composed of a_{lk} codewords and can be represented by:

$$s_{MC}(t) = \sum_{l=1}^{N_S} \sum_{k=0}^{N-1} a_{lk} e^{j2\pi f_k (t-lT)} u(t-lT) \tag{3.1}$$

where $k = 0, 1, ..., N-1$ indicates the subcarrier (i.e., frequency) index, l the symbol (i.e., time) index, N the number of subcarriers, N_S the number of symbols, T the symbol duration, f_k the frequency of the k-th subcarrier and $u(t)$ the pulse shaping function defined as:

$$u(t-lT) = \begin{cases} 1, & 0 < t - lT \leq T \\ 0, & otherwise \end{cases} \tag{3.2}$$

Actually, an optical WDM system is strictly a FDM approach whose subcarriers are centered at some hundreds of THz and separated according to a specific wavelength grid. For instance, we have a $20nm$ separation in ITU-T's G.694.2 Coarse WDM (CWDM) [27] whereas smaller values (100, 50 and $25GHz$) are defined in ITU-T's G.694.1 Dense WDM (DWDM) [28]. In this work, we concentrate on the MCM approach whose subcarriers are multiplexed in the electric

signal [2]. As far as an optical point-to-multipoint transmission is concerned, this consists of an extremely interesting approach because it allows for sub-wavelength granularity when sharing the system's resources between several users of the network. More details on the subject are given in section 3.8.

3.3.2 Orthogonal FDM: Bringing the Subcarriers Close Together

In conventional FDM systems, the subcarriers' separation Δf should be chosen by taking into account the cost-effectiveness of the filters used to separate the information on each frequency. The complexity and cost of such filters are directly related to the their sharpness or roll-off and, as a consequence, a FDM transceiver will be as cost-effective as the inter-carrier separation constraints are relaxed and the overall occupied bandwidth is large.

However, large bandwidths can represent a huge disadvantage principally when the spectrum is not a virtually infinite resource, which is the case for instance of wireless systems . The beauty of OFDM is that the subcarriers can be overlapped allowing an increase of the transmission's spectral efficiency and yet don't generate any kind of inter-carrier interference (ICI) thanks to the mathematical principle of orthogonality.

In Figure 3.4(b) we can see that by "orthogonal" we actually mean that Δf is chosen so that the maximum of one subcarrier will always coincide with a null of all other subcarriers. Mathematically, the principle can be formalized by the following relation:

$$\frac{1}{T}\int_0^T s_p(t)s_q^*(t)dt = \delta_{pq} = \begin{cases} 0, & p \neq q \\ 1, & p = q \end{cases} \tag{3.3}$$

which states that the signal $s_p(t)$ is orthogonal to $s_q(t)$ over a period T. If $s_p(t)$ and $s_q(t)$ are two adjacent subcarriers of an OFDM signal, then:

$$\frac{1}{T}\int_0^T s_p(t)s_{p+1}^*(t)dt = \frac{1}{T}\int_0^T e^{j2\pi f_p t}e^{-j2\pi f_{p+1}t} = \frac{1}{T}\int_0^T e^{j2\pi t\Delta f}dt = \delta_{pq} \tag{3.4}$$

which holds if:

$$\Delta f = f_p - f_{p+1} = \frac{1}{T} \tag{3.5}$$

Actually, the orthogonality condition still holds for any pair of subcarriers f_p and f_q if:

$$f_p - f_q = \frac{m}{T} \tag{3.6}$$

when m is an integer, meaning that it is possible to guarantee mutual orthogonality between all subcarriers thus avoiding any ICI, at least ideally. An OFDM signal is mathematically described by imposing the orthogonality condition expressed in (3.5) to (3.1). We will see in subsections 3.5.2 and 3.5.3 however that in a real OFDM systems, precise frequency and time synchronization techniques must be used to avoid degradation due to the lost of orthogonality between subcarriers.

It is possible to render OFDM more robust to ICI by changing the pulse shaping function to a different filter such as the raised cosine function [29]. Indeed, the rectangular pulse shaping function represented in 3.2 generates subcarrier spectra with significant side-lobes extending over a broad frequency range (the Fourier Transform of $u(t)$ gives a $sinc(f)$).

[2] We adopt the word "subcarrier" to refer to the electrically multiplexed components and "carrier" to refer to the optical wavelength.

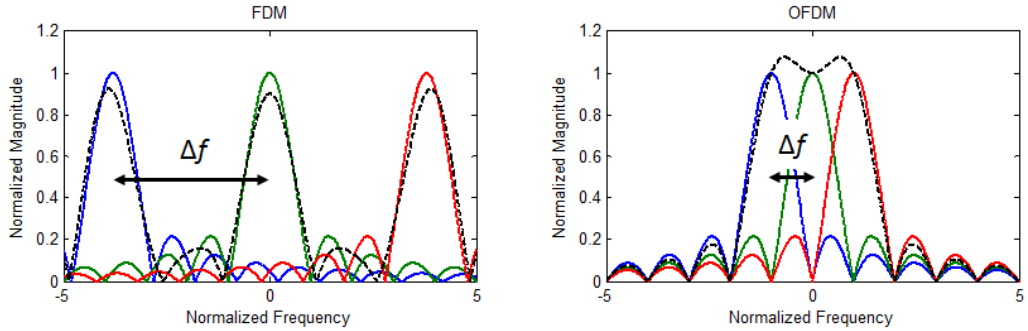

Figure 3.4: Frequency domain comparison between FDM and OFDM.

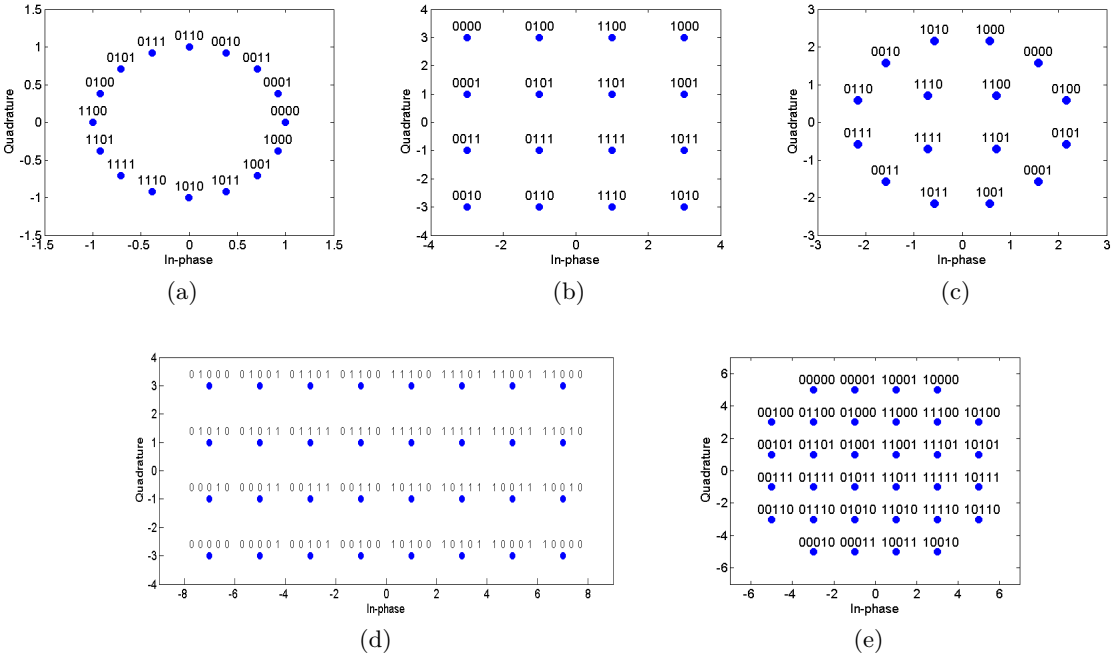

Figure 3.5: (a) Gray-mapped 16PSK. (b) Gray-mapped 16QAM. (c) 16APSK. (d) Gray-mapped rectangular 32QAM. (e) Cross 32QAM.

3.3.3 Mapping Bits to Increase the Spectral Efficiency Even More

We have mentioned in section 3.3.1 that it was common to associate a complex number or codeword to a sequence of b bits in order to increase the spectral efficiency of the transmitted (O)FDM signal. The symbols or codewords of a constellation are represented in the In-Phase vs Quadrature plan according to its real and imaginary components respectively. If the alphabet of a constellation has a total of M possible codewords, then each word will represent a specific combination of $b = log_2 M$ bits.

There are several ways to map a sequence of bits into a constellation, the most known of which are Phase-Shift Keying (PSK) and Quadrature-Amplitude Modulation (QAM) as shown in the examples (a) and (b) of Figure 3.5. Other examples of constellations include the APSK constellations shown in 3.5(c). More constellations can be found in [26, 30].

The choice of a particular constellation depends on several factors such as the SNR limitations of the system, the desired simplicity on the generation and detection of a symbol, the Hamming distance [3] and the robustness to phase jitter or imperfect clock recovery [31]. In general, the BER performance for a fixed SNR will be as good as the Euclidean distance between adjacent

[3]The Hamming distance is the number of different bits between one symbol and its neighbors.

symbols of a constellation is large which, on the other hand, tends to increase the Peak-to-Average Ratio (PAPR) of the signal. Even though PSK constellations are generally easier to implement, QAM constellations show better BER performances by offering a considerable SNR advantage for transmissions over Additive White Gaussian Noise (AWGN) channels [32].

It is relatively simple to create Gray-mapped QAM symbols when b is an even number by dissociation of the I and Q components. Indeed, they can be treated as individual Pulse Amplitude Modulation (PAM) components. An intuitive and also simple approach when b is odd consists of separating the group of b bits into $\frac{b+1}{2}$ bits for the I component and $\frac{b-1}{2}$ for the Q component (or vice-versa) and proceeding similarly as with the squared constellation, in which case we generate a rectangular constellation as shown 3.5(d). In annex B we address the procedure of generating squared and rectangular Gray-mapped constellations from an ordinary binary sequence.

Even though rectangular constellations are easy to implement, in [31] the authors demonstrate that cross-shaped constellations can offer some interesting advantages. This more symmetric structure has some major drawbacks if compared to the rectangular QAM namely the more complex implementation, the changing in the maximum-likelihood decision regions (which are no longer rectangular; the quadrature and in-phase components are not independent anymore) and the impure Gray-mapping. Still, they are capable of allowing at least $1dB$ SNR gain if compared to rectangular QAM, smaller peak and average power requirements and a lower signal set dynamic range. If we look more closely at Figure 3.5(e), we will see that not all symbols have a Hamming distance equal to one. Indeed, it is not possible to perfectly Gray-map a cross-shaped constellation and a certain penalty in the performances should be introduced due to this fact. This penalty is known as Gray mapping penalty (G_p) and indicates the average number of bit-differences per adjacent decision region. Another important parameter is the peak Gray penalty (G_{pk}) defined as the maximum number of bit-errors per single symbol threshold error over the entire constellation. An acceptable impure Gray mapping has $G_p \sim 1$ and $G_{pk} = 2$. The user is referred to [33] for an interesting comparison between different mappings and labelings for 128QAM.

Even though it interesting to mathematically generate a certain constellation from a sequence of bits, it is usually less computationally complex to use look-up tables instead. In this work, the look-up tables approach has been preferred over the mathematical generation approach since its computation proved to be much faster. Also, we choose cross-shaped constellation over the rectangular constellation approach due to its previously mentioned advantages.

3.3.4 Substituting the Oscillators by an (Inverse) Discrete Fourier Transform

We can infer from section 3.3.2 that one of the challenges behind the realization of the first OFDM modulators was the need of several local oscillators and filters, each one associated to a specific subcarrier. The complexity of such an architecture would undoubtedly escalate to an unimplementable level if the number of subcarriers was greatly increased to minimize the dispersion effects of the channel. Furthermore, when compared to ordinary FDM, the strict conditions on the spacing Δf that would guarantee orthogonality between subcarriers could complicate the modulator implementation even more.

These are the reasons why OFDM failed to achieve much success until early seventies when a group of researchers [34] proposed an idea that would allow the dawn of this solution in a new era of communication systems. Interestingly, the authors demonstrated that it was possible to generate an OFDM signal by means of an Inverse Discrete Fourier Transform (IDFT). To clarify their finding, let us concentrate on the equation of a single OFDM symbol $s_l(t)$:

$$s_l(t) = \sum_{k=0}^{N-1} a_k e^{j2\pi f_k t} \tag{3.7}$$

The analogue OFDM signal $s_l(t)$ shown in 3.7 can also be represented by a digital correspondent version with, let's say, Q samples over the time interval $0 < t \leq T$:

$$s_l[n] = \sum_{k=0}^{N-1} a_k e^{j2\pi f_k \frac{nT}{Q}} \tag{3.8}$$

with n being the sample number. By imposing the orthogonality condition, it is possible to say that:

$$f_k = f_0 + k\Delta f = f_0 + \frac{k}{T} \tag{3.9}$$

with f_0 being the frequency of the first subcarrier ($k = 0$). If Q is chosen to be exactly N and if f_0 equals zero (meaning that the first subcarrier is actually a DC level), then equation 3.8 leads to:

$$s_l[n] = \sum_{k=0}^{N-1} a_k e^{j\frac{2\pi kn}{N}} = IDFT\{a_k\} \tag{3.10}$$

which turns out to be exactly the IDFT of the input words a_k. Equation 3.10 shows that an analog OFDM signal of duration T can be represented by a correspondent digital signal with N samples defined by applying an IDFT to the words a_k. The first subcarrier is also known as the DC subcarrier and is generally set to zero. The signals $s_l[n]$ and $s_l(t)$ are directly related one to another by a digital-to-analog/analog-to-digital conversion procedure. This very convenient property makes it possible to substitute the bank of filters and oscillators of Figure 3.3(b) by a digital device capable of realizing an IDFT followed by a Digital-to-Analog Converter (DAC) that will allow retrieving $s(t)$.

One other point that has also boosted the digital OFDM approach was the development of very-low-complexity DFT algorithms, also know as Fast Fourier Transform algorithms. For instance, the radix-2 Cooley-Tukey (I)FFT algorithm can enable a complexity reduction from $O\left(N^2\right)$ to $O\left(\frac{N}{2} log_2 N\right)$ if compared to naïve (I)DFT algorithms. More details on the most used Fast-Fourier Transform algorithms may be found in [35].

If the use of IFFT in the OFDM transmission chain has proved to be quite useful for current wireless and wireline OFDM systems in which the needed sampling ratios are relatively slow, it also implies one major limitation when an optical OFDM PON transceiver is concerned due to the need of higher sampling ratio converters. Indeed, since the potential bandwidths on the optical channel are considerably higher, the costs of the needed converters to allow dealing with high bandwidth signals may increase to prohibitive levels. The debate on whether Moore's conjuncture still be valid for the following years thus allowing the decrease of the prices of high-sampling ratio devices in a near future is still open in the optical community. In section 7.3, we propose a solution to circumvent the cost limitations imposed by high sampling ratio converters in OFDM PON transceivers.

3.3.5 Appending a Cyclic Prefix

In many OFDM systems, it is usual to add a cyclic prefix (CP) in the transmitted signal. It consists of prefixing the time-domain signal with a part of its end. The prefixing has three main purposes:

- Act as a guard interval to remove any residual ISI on the received OFDM symbol:

If the CP is at least as long as the maximum delay on the dispersive channel, then any residual spreading due to an insufficient number of subcarriers will fall into the portion of the signal that contains a redundant part of the transmitted information. We can extract this portion and still

guarantee that the remaining of the signal did not suffer from any overlapping with adjacent symbols.

- Allow simple channel estimation for equalization in the frequency domain:

The main interest of using a copy of the OFDM signal instead of any other kind of guard interval (for instance a sequence of zeros) is that it allows the initially linear convolution between the channel's impulse response and the time-domain signal to mimic a circular convolution [36]. Indeed, the eigendecomposition of a circulant matrix representing a time-invariant channel will give us its frequency response coefficients. In other words, this enables the simple calculation of the channel's frequency response used to recover the transmitted information by means of an equalization procedure. The transmission will respect:

$$Y_k = H_k X_k + n_k \tag{3.11}$$

where X_k, Y_k, H_k and n_k are respectively the transmitted and received frequency domain signals, the channel frequency response and noise on the $k - th$ subcarrier.

Frequency Domain Equalization (FDE) not only manages to offer a simpler solution to correct the channel response if compared to conventional Time Domain Equalization (TDE), since we replace the convolutions by simple multiplications, but it also suits very well the OFDM transmission due to the FFT/IFFT blocks that are inherently necessary at the transceivers. For more details on FDE, please refer to subsection 3.5.4.

- Improve DFT time-window synchronization at the receiver and reduce ICI:

The cyclic prefix can also be used for matters of time synchronization. By proper correlation techniques, it is possible to find the exact beginning of one OFDM symbol thanks to the repetition of some samples in the signal. This procedure helps setting the appropriate FFT window parameters at the receiver-side. In subsection 3.5.2 we detail the cyclic prefix-based FFT window synchronization procedure used in our OFDM demodulator.

3.3.6 Filter to Remove Periodic Replicas

It is well known that the digital-to-analog conversion process will generate an analog signal consisting of periodically repeated copies of the Fourier Transform of the original digital signal centered at multiples of the sampling frequency F_S of the DAC. However, as long as this sampling frequency respects the Nyquist-Shanon sampling theorem, i.e., $F_S \geq 2BW$, with BW being the signal bandwidth, such replicas will not overlap and the signal will not suffer any degradations coming from aliasing [37, 38].

Despite the fact that in such case the replicas won't affect the transmitted signal, they may disturb the received signal depending on the Analog-to-Digital Converter (ADC) sampling ratio since the same phenomenon is also expected in the analog-to-digital conversion. It is convenient then to eliminate the replicas after digital-to-analog conversion by means of a low-pass filter with width $\frac{F_s}{2}Hz$. In order to accommodate the roll-off of the filter, it is possible to oversample the signal such that $F_S > 2BW$. Other way to achieve the same result is by zeroing some subcarriers on the high-frequency edge of the OFDM signal.

3.3.7 Using Pre-emphasis to Correct DAC's *sinc* Filtering

The digital to analog conversion is done with a conversion signal $c(t)$. The analog signal at the output of the DAC is constructed by reproducing, for each sample of the input signal, a replica of $c(t)$ with an amplitude proportional to the sample value during the sampling interval $\Delta t = \frac{1}{F_S}$:

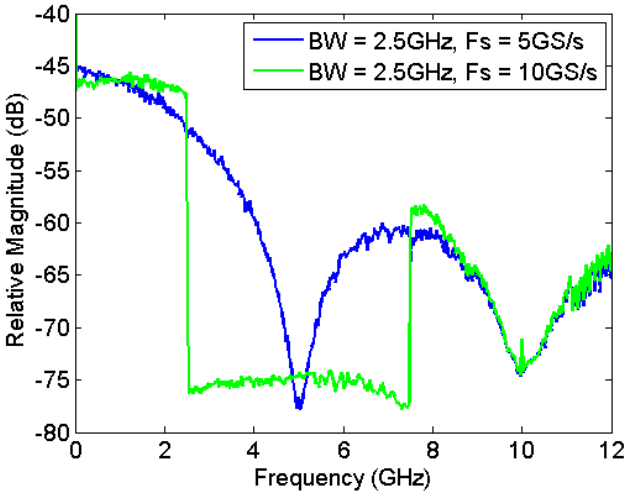

Figure 3.6: Sinc profile induced on the signal spectrum in the digital-to-analog conversion.

$$s(t) = \sum_{n=-\infty}^{\infty} s[n]c(t - n\Delta t) \tag{3.12}$$

Equation 3.12 shows that the analog signal spectrum will be affected by the Fourier transform of $c(t)$. However, if the conversion signal has the form:

$$c_{ideal}(t) = \frac{sin\,(\pi F_s t)}{\pi F_s t} \tag{3.13}$$

corresponding to an ideal conversion function, then the analog signal can be reproduced without distortion [37, 38]. The ideal $c(t)$ is a step function in the frequency domain occupying the $-\frac{F_s}{2}$ to $\frac{F_S}{2}$ span and with amplitude Δt. Unfortunately, such filtering function is not causal and thus cannot be implemented in a real system. The principle of the standard conversion signal of real-world DACs consists instead of holding each sample value during the sampling interval Δt:

$$c_{practice}(t) = \begin{cases} 1, & 0 \leq t \leq \Delta t \\ 0, & otherwise \end{cases} \tag{3.14}$$

This method is called zero-order hold. The main drawback of such an approach is that the analog signal spectrum will be distorted by the Fourier Transform of $c_{practice}(t)$, i.e.:

$$C_{practice}(f) = sinc\left(\frac{f}{F_s}\right) \tag{3.15}$$

This can be noticed in Figure 3.6 which shows the spectrum of the analogue $2.5GHz$ signal after the DAC (and before the low-pass filter) sampled at 5 and $10GS/s$. One way to skirt this effect is by pre-distorting the signal with a filter whose response is equal to the inverse of $C_{practice}\,(f)$.

3.3.8 Scale Signal to Desired Voltage Levels

The DAC generates an electrical signal that is restricted to a certain maximum peak-to-peak voltage (typical values of peak-to-peak voltages are between $0.5V$ and $1V$). This parameter characterizes not only the signal's power at the output of the DAC but also the clipping phenomenon that may happen in the digital-to-analog conversion.

Indeed, if ever the amplitude of the digital signal exceeds the maximum Vpp of the DAC, the digital-to-analog conversion will generate a clipped version of the original signal. This will induce an unwanted noise in the transmitted symbols.

According to the Central Limit Theorem [39, 40], the voltage distribution of the time-domain OFDM signal is Gaussian and the probability of generating a strong peak will be directly proportional to the number of subcarriers and the mapping used in each of them. Indeed, the OFDM signal PAPR depends on the random symbols transmitted in each subcarrier and how they combine with each other to generate the time-domain signal. Figure 3.7 shows the typical histogram of a purely-real OFDM signal[4]. Note that the time-domain OFDM signal is indistinguishable from a Gaussian noise.

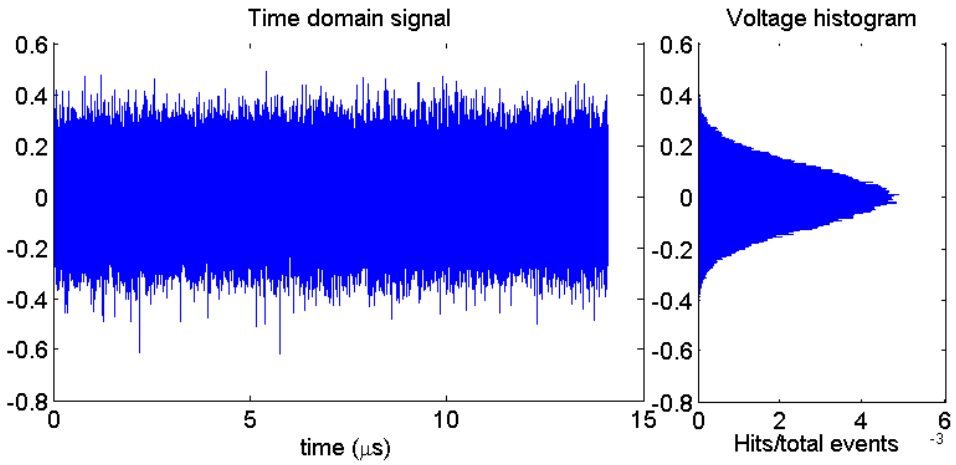

Figure 3.7: Typical OFDM signal and its voltage distribution.

The digital OFDM signal power is given by:

$$P_{OFDM} = \frac{\overline{s\left(t\right)^2} - \left(\overline{s\left(t\right)}\right)^2}{Z} \tag{3.16}$$

with Z being the output impedance of the DAC.

In order to benefit the most from the maximum amplitude of the DAC without clipping the signal, an optimal scaling factor that maximizes the mean RF power and minimizes the clipping noise on the signal must be found as shown in Figure 3.8 so that the events in which the signal's amplitude exceeds the DAC's maximum Vpp are not very frequent.

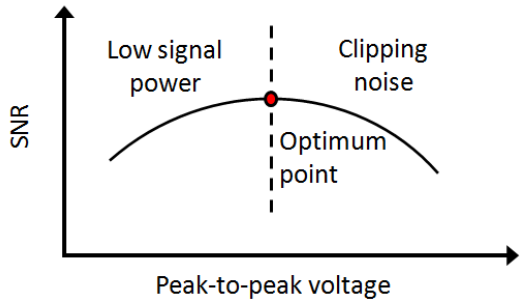

Figure 3.8: Compromise between clipping-induced noise and RF power on digital-to-analog conversion.

[4]The principles of purely-real and complex OFDM signals are addressed in section 3.4.

Let SF be a scaling factor that will change the amplitude of the digital OFDM signal before digital-to-analog conversion. The target power of the scaled OFDM signal constrained to the maximum peak-to-peak voltage (Vpp_{max}) of the DAC is:

$$P_{target} = \left(\frac{1}{2}\frac{Vpp_{max}}{SF}\right)^2 \tag{3.17}$$

To perform the rescaling on the original signal, we simply need to do:

$$s_{rescaled}(t) = s(t)\sqrt{\frac{P_{OFDM}}{P_{target}}} \tag{3.18}$$

Figure 3.9 shows an analysis of the variation of Vpp with SF for different modulations and numbers of data subcarriers. The OFDM signal is a baseband real-valued $6GHz$ signal (please refer to section 3.4). Each point consists of an averaged Vpp over 50 iterations and in each iteration, we find the Vpp over $6M$ OFDM symbols, with M being the alphabet of a M-QAM mapping. The factor 6 has been empirically chosen to assure that the constellations of each subcarrier have been completely filled with all their possible codewords. The constellations' mean powers are normalized and the maximum Vpp of the DAC in this analysis is $1V$. Dashed lines indicate the values of SF under which the signal would be clipped. Figure 3.10 summarizes the results of Figure 3.9 by showing the approximate values of SF for which the mean Vpp is $1V$.

A better way to analyze the effects of OFDM's PAPR is by using the Complementary Cumulative Distribution Function (CCDF) of PAPR, which shows the probability that the PAPR exceeds a particular value. Actually, in our experiments, we do an equivalent analysis by estimating, from the signal's time-domain voltage histogram, the CCDF of the Vpp and using it to infer the probability of exceeding the maximum Vpp imposed by our DAC.

The reader should notice, however, that the digital version of the OFDM signal in which such verification is done may not include the true maximum of the analog signal after the conversion. Indeed, the peaks may occur between the discrete samples [41, 42] and this would generate a false estimation if ever those values are used for matters of RF optimization on other components after the DAC such as an electrical amplifier or even a laser. Nonetheless, we can keep the analysis on the digital domain under the condition that the signal is oversampled. In [41] the authors propose an oversampling ratio of 2 whereas in [42] a ratio of 4 is suggested for means of PAPR investigation using the digital signal.

In our experiments, the optimization of the signal's power is done in two steps. In the first step, we use the electrical back-to-back configuration connecting the DAC directly to the ADC to estimate the value of SF for which we optimize our transmission regarding the clipping effects on the digital-to-analog conversion. For evaluating the performances, we generally use the values of bit-rate after optimization with a bit and power loading algorithm (please refer to section 3.7). The second step on the RF optimization procedure considers the signal after the DAC. To find the optimal powers at the inputs of other components such as an electrical amplifier or even a laser, we do a similar analysis (see section 5.2) based on an extensive research for the optimum operation point. The SF factor in the digital-to-analog conversion is however fixed at an optimum value according to the measurements done in the previous step.

In subsection 3.3.10, we introduce some techniques used to reduce the peak-to-average power ratio (PAPR) of an OFDM signal, which is one of its main drawbacks if compared to the single-carrier approach.

3.3.9 Digital-to-analog Conversion

We have seen that the digital-to-analog conversion consists of creating an electrical signal from a sequence of discretized samples. The first important parameter that might come to mind when

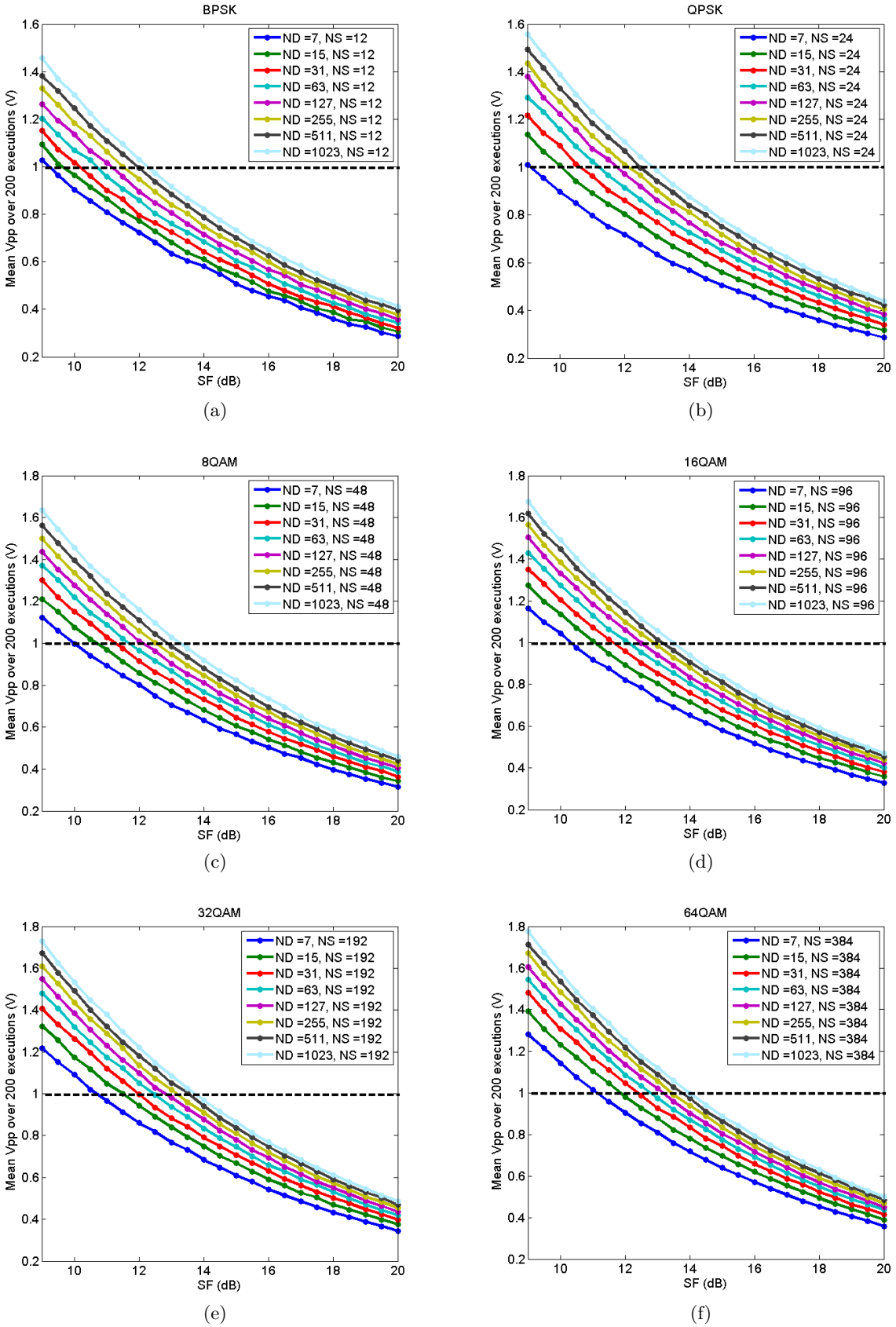

Figure 3.9: Vpp variation with SF. (a) BPSK. (b) QPSK. (c) 8QAM. (d) 16QAM. (e) 32QAM. (f) 64QAM. ND is the number of data subcarriers and NS is the number of OFDM symbols.

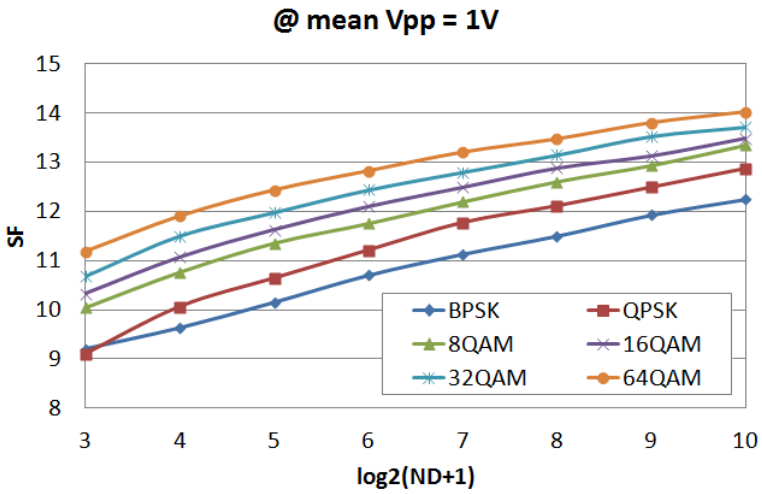

Figure 3.10: Approximate values of SF for guaranteeing 1Vpp.

we think of digital to analog conversion is the sampling ratio of the converter since it is directly related to the maximum signal bandwidth with which the transmitter can deal.

However, there are other important characteristics that must be taken into account when evaluating the digital-to-analog conversion. In fact, the conversion consists of two separate actions: quantization and sampling. Consequently, other than the sampling ratio, the effective number of bits (ENOB), which characterizes the DAC's vertical resolution, appears as a very important design parameter.

Actually, real-world converters are affected by noise, non-linear distortions and offset errors. In addition, most high-speed converters consist of separate slower devices combined to achieve higher overall performances. It is then important to consider an effective performance for the overall system so that an accurate characterization of the transmission in terms of quantization noise can be assured. The interesting point of the ENOB compared to the theoretical resolution of a converter is that it depends on the SNR, i.e., it is directly related to noise and non-linearity distortions that affect the conversion. Some very useful information about the measurement of the effective number of bits of a converter can be found in [43].

Another important parameter is the DAC's maximum peak-to-peak voltage. If on the one hand, a low resolution implies increased quantization noise in the transmitted signal, a low peak-to-peak level requires the use of optical amplifiers to provide for an appropriate RF power before modulating the laser. Despite the fact that electrical amplifiers with low levels of noise (LNA) do exist it should be taken into consideration that they still represent a considerably high percentage of the total electrical consumption of a transceiver. Other extremely important characteristic is the DAC's operation frequency range. Indeed, it is very unlikely that the frequency response of high-speed converters follows a flat profile over the whole of its analog bandwidth up to half the maximum sampling ratio. In some cases, we should expect pronounced roll-offs making the DAC's 3dB bandwidth much lower than previewed, even after correction with the $sinc^{-1}$ pre-emphasis filter. The higher the analog bandwidth of the DAC, the less it will degrade the signal spectrum.

There exists a compromise between sampling ratio and resolution of the converters as can be evidenced in Table 3.3 which shows the parameters of some commercially available DACs or Arbitrary Waveform Generators (AWG) from different vendors.

Vendor	Sampling Rate (GS/s)	Resolution (bits)	Reference
Fujitsu[i]	65	8	-[ii]
Fujitsu[i]	12	14	MB86066
Tektronix[i]	1.2	14	AWG5000
Tektronix[i]	24[iii]	10	AWG7000
Agilent[i]	0.512	16	N5106A
Agilent[i]	12(8)	12(14)	M8190A
Siglent[i]	0.125	14	SDG1000
Signadyne[iv]	0.5	16	PXE-AOU-H0001/2
Fluke[i]	0.1	12	291/292/294
Keithley[i]	0.125	14	3390
BK Precision[i]	0.1	14	4075
GWInstek[i]	0.2	16	AFG-3000
Texas Instruments[v]	1.5	16	DAC34SH84

[i] AWG
[ii] press release
[iii] interleaved mode
[iv] FPGA-based analog output
[v] DAC

Table 3.3: Some commercially available DAC.

3.3.10 PAPR Limitations

The limitation imposed by the PAPR is maybe the most commonly remembered disadvantage of OFDM when compared to SC techniques. In order to avoid nonlinear distortions coming from the chain's components, whether they are electrical or optical, the RF power of the OFDM may have to be considerably decreased to reduce the clipping effects on the signal.

As seen in subsection 3.3.8, from the Central Limit Theorem, the voltage of the time-domain OFDM signal follows a Gaussian distribution and the peaks will be generated according to the way the random symbols on each frequency (subcarrier) interfere with each other. We have also seen that the PAPR was directly proportional to the number of subcarriers and the mapping used on each of them and that a good figure of merit for evaluating its influence was the probability of one peak extrapolating a certain maximum value.

Indeed, we have concluded that a compromise between the clipping noise generated when the signal power is increased and the SNR degradation when the signal power is reduced had to be found. Actually, this approach, known as hard-clipping, is the simplest way of skirting the effects of a high PAPR in OFDM signals. Other interesting techniques exist such as the selective mapping and the asymmetrical clipping of the signal [44–46].

In the selective mapping, the symbols that modulate each subcarrier are changed so that the resulting time-domain signal has a smaller PAPR. Such modifications can be done in different ways. For instance, certain symbols of the constellations can be prohibited or the subcarriers can be scrambled at the IFFT block in a random or deterministic fashion [47]. Other very interesting approaches consist of using the Golay Complementary Sequences and the DFT-precoding with Hermitian symmetry.

In [48], the authors developed a coding scheme capable of providing low PAPR and good error correction capabilities. The provided theory yields PSK Golay sequences as unions of cosets of the classical Reed-Muller codes. 16QAM Golay complementary sequences have later

been demonstrated in [49]. Other interesting reports on the subject can be found in [50–53].

As far as the DFT-precoding technique [54] is concerned, a real-valued baseband OFDM signal is created by adding a FFT block before the IFFT, as shown in Figure 3.11. The interesting point of the DFT-precoded approach is that the voltage distribution of the time-domain signal becomes more "squared" (Figure 3.12), allowing thus the increase of the signal power and consequently considerable gain in terms of SNR.

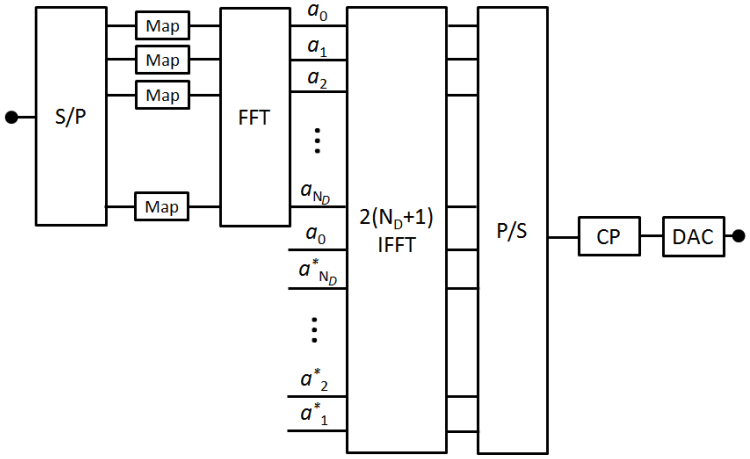

Figure 3.11: Block diagram of OFDM transmitter with DFT-precoding.

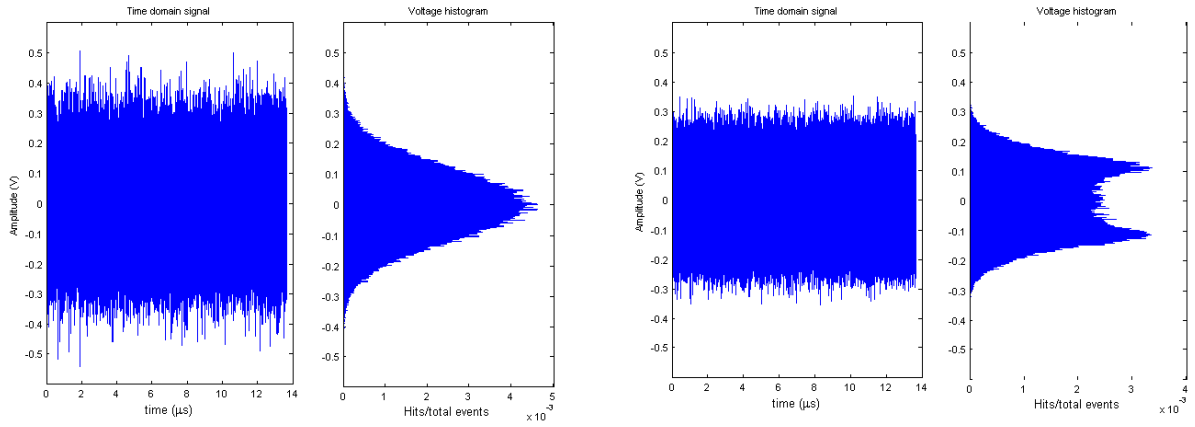

(a) (b)

Figure 3.12: Voltage distributions of (a) standard OFDM signal and (b) DFT-precoded OFDM signal.

The asymmetrically-clipped OFDM approach consists of hard-clipping the original bipolar OFDM signal so that only its positive values are kept and an unipolar signal is generated. Indeed, the authors demonstrate that if only the odd subcarriers are modulated, then all the noise generated by the clipping will fall into the even (unmodulated) subcarriers and the clipping will consequently have no effects on the transmission. Despite the fact that this method allows a considerable gain in terms of SNR and an optical power efficiency approximately $8dB$ better than conventional optical OFDM [44], the main disadvantage is that the spectral efficiency of the transmission is halved. In addition, to completely benefit from the laser's linear regime operation, the laser bias current has to be reduced. By doing so, we reduce the ratio between optical

DC term and modulation component, allowing then an improvement in terms of robustness to Optical Signal-to-noise Ratio (OSNR) degradations. However, we also decrease the laser's emitted power and 3-dB bandwidth (see subsection 2.3.2). These drawbacks would have a direct impact on the maximum achievable split-ratio and throughput of a passive optical network.

Even though we have realized some experiments using the asymmetrically clipped and selective mapping with random scrambling techniques, the results have not been conclusive. The use of Golay complementary sequences includes knowledge on different coding schemes and is beyond the scope of this work. We are currently investigating the performances of DFT-precoded OFDM but the final conclusions have not yet been drawn and are thus kept as perspectives for future works. In our experimental setups, we make use of the hard-clipping method which is realized by finding the best compromise between signal power and clipping noise on the components.

3.3.11 Signal Parameters

At this point, we are capable of calculating the OFDM signal parameters. The number of samples per OFDM symbol is:

$$N = (N_{IFFT} + N_{CYP})\, S_{ov} \tag{3.19}$$

with N_{IFFT} being the number of inputs of the IFFT block, N_{CYP} the number of samples of the cyclic prefix and S_{ov} the oversampling factor given by:

$$S_{ov} = \frac{F_s}{F_{Nyquist}} = \frac{F_s}{2BW} \tag{3.20}$$

where $F_s \geq 2BW$ is the DAC's sampling rate and $F_{Nyquist} = 2BW$ is the minimum sampling rate necessary to correctly convert a digital signal with baseband bandwidth BW to the analog domain. The number of inputs of the IFFT block depends on whether the signal is a real (with Hermitian symmetry) or complex-valued (used with further IQ upconversion) baseband signal:

$$\begin{aligned} N_{IFFT}^{Hermit} &= 2\,(N_D + 1) \\ N_{IFFT}^{IQ} &= N_D + 1 \end{aligned} \tag{3.21}$$

with N_D being the number of data subcarriers (pilot tones, if used, included). The +1 term in 3.21 accounts for the DC subcarrier. The OFDM symbol duration can be trivially found through:

$$T_s = \frac{N}{F_s} = \frac{N_{IFFT}}{2BW} + \frac{N_{CYP}}{2BW} = T_u + T_g \tag{3.22}$$

T_u and T_g are the useful symbol and guard period durations respectively. Finally, the signal bit rate is:

$$R = \frac{\sum_{k=1}^{N_D} b_k}{T_s} \tag{3.23}$$

where b_k is the number of bits/symbol associated to the constellation of the k-th subcarrier. The cyclic prefix can also be defined as a percentage of the total symbol duration:

$$gi_{\%} = 100\left(\frac{T_g}{T_s}\right) = 100\left(\frac{N_{CYP}}{N_{IFFT} + N_{CYP}}\right) \tag{3.24}$$

and we can also find the separation between subcarriers:

$$\Delta f = \frac{2BW}{N_{IFFT}} \tag{3.25}$$

3.4 Different Flavors of Optical OFDM

Before we get further into the details of the OFDM receiver, it is important to comment on the different existing OFDM architectures in the optical domain. In [29], the author brings a very clear and interesting analysis on the subject which we try to detail a little more here. After this section, the reader will be able to situate these optical approaches by comparing them to the "purely electronic method" used in all existing OFDM standards.

Basically, there exists three types of optical OFDM modulations. The first one is the Directly-Detected OFDM (DD-OFDM) and the simplest way of transmitting a signal using this scheme is by the intensity modulation of the light source. This is the same modulation method specified in current and following generations (NG-PON1) of passive optical networks. In the second modulation approach, known as Coherently-Detected OFDM (CO-OFDM), the information is transmitted using an optical IQ modulator which allows the modulation of both intensity and phase of the optical carrier. Finally, in the last type of OFDM modulation called All-Optical OFDM the subcarriers are directly created and transmitted in the optical domain (and not electronically, as in the precedent methods) by means of a wavelength comb and a group of coherent receivers.

As far as next generation PON systems are concerned, the IMDD approach allied to simple digital signal processing techniques can represent a significant advantage in terms of costs thanks to its simplicity and the ease of implementation with mature optical components. Though efforts to conceive cost-effective coherent transponders have been made recently [55], the coherent approach still needs a more complex optical design if compared to IMDD and this may represent a serious limitation for the subscriber premises equipment. While All-Optical OFDM holds the records in terms of throughput of optical OFDM systems [56], its complexity and costs make them a prohibitive solution for the optical access networks context. At the present time, the All-Optical OFDM approach is only considered for long-haul networks.

In this section, we describe the three techniques but maintain the focus on the IMDD approach, which is the main subject of this work.

3.4.1 Directly Detected OFDM

As far as the spectrum of the optical OFDM signal is concerned, the DD approach can be used in two distinct ways. The first one consists of creating an Optical Double-Side Signal (ODSB) through the modulation of a Directly Modulated Laser (DML) or a continuous-wave (CW) laser combined with an intensity External Modulator (EM) or a reflective device such as an RSOA or an R-EAM-SOA. Despite its simplicity, the main disadvantage of the ODSB approach is that the beating of the side-bands upon direct detection will generate a frequency selective channel due to the dispersion of the optical fiber and the consequent phase variations which are imposed to the signal, as discussed in sections 2.4.3 and 2.5.

One very simple alternative to circumvent this problem consists of adapting the subcarriers' power and mapping with specific bit and power loading algorithms, as we will see in section 3.7. Its also possible to reverse the dispersive channel response by means of an Electronic Dispersion Compensation (EDC) [57] mechanism. However, the filter design of an EDC will certainly become very complex for large values of accumulated dispersions in the link. We can also think of Dispersion Managed Fibers (DMF) to put off the dispersion effects by means of special fibers with negative dispersion coefficients (see section 7.2). Even though this approach is quite common in submarine systems, it would most certainly not be used with an already deployed network due to the civil-engineering investments that would be necessary for changing the existing fibers. Still in the optical domain, some types of holey fibers (see previous chapter) are robust to dispersion but they still didn't reach commercial maturity.

Another solution to prevent the effects of dispersion upon direct detection consists of generating an Optical Single-Side Band (OSSB) signal. The main advantage of an OSSB signal is

that the phase variations induced by the dispersion will only provoke a rotation of the received OFDM constellations, which can be easily corrected with an equalizer [41, 58]. If the optical subcarrier is sent along with the OSSB signal, then both optical signal and optical carrier will have the same polarization and phase, allowing then the direct detection at the receiver [59].

We describe both approaches in the following of this subsection.

3.4.1.1 ODSB DD-OFDM

IMDD is the simplest of all modulation approaches. An electronically generated OFDM signal is used to directly modulate the polarization current of a light source which converts the signal to the optical domain. Since we only use intensity variations of the light to transmit the information, the signal needs to be purely real-valued.

There are three ways of generating such real-valued OFDM signal. The first one consists of electrically up-converting the complex base-band signal generated after the IFFT to a central frequency f_{RF} through I/Q mixing. In this scheme, we need one DAC for the quadrature component and one DAC for the in-phase component of the OFDM time-domain signal (Figure 3.13(a)).

The same process can be realized numerically if the signal is previously oversampled, as depicted in Figure 3.13(b). While numerical up-conversion enables using only one DAC because the real signal is created before digital-to-analog conversion, the great advantage of electrical up-conversion is that it allows using DACs with smaller sampling ratios, which can be extremely interesting in terms of costs of the customer premisses equipment.

Finally, the third way of generating the real-valued OFDM signal is through Hermitian symmetry of the inputs of the IFFT block. The Hermitian symmetry condition creates a real-valued baseband OFDM signal by imposing an IFFT with $2(N_D + 1)$ inputs (N_D being the number of data subcarriers without considering the DC subcarrier) whose symbol arrangement respects:

$$\begin{cases} a_k = a^*_{2(N_D+1)-k} \\ a_0 = a_{N_D+1} = 0 \end{cases} , \; k = 1, 2, ..., N_D \tag{3.26}$$

Indeed, if we remember that $e^{j\frac{2\pi n(N-1)}{N}} = e^{-j\frac{2\pi n}{N}}$, then it is possible to re-write equation 3.10 as:

$$s_l[n] = a_o + a_1 e^{j\frac{2\pi n}{N}} + a_2 e^{j\frac{2\pi 2n}{N}} + ... + a_{N-2} e^{-j\frac{2\pi 2n}{N}} + a_{N-1} e^{-j\frac{2\pi n}{N}} \tag{3.27}$$

If equation 3.26 holds, then the signal is purely real and has the form:

$$s_l[n] = 2\sum_{k=0}^{N_D} d_k cos\left(\theta_k + \frac{2\pi kn}{N_D}\right) \tag{3.28}$$

where d_k and θ_k are respectively the modulus and phase of the symbol a_k in the subcarrier k. One of the advantages of this approach over the electrical up-conversion is that the system will not suffer from any kind of I/Q unbalancing neither on the transmitter nor on the receiver side. Nevertheless, its main drawback is a reduction in the spectral efficiency of the signal since half the inputs of the IFFT are not used to carry useful information. Figure 3.13(c) shows the block diagram of the baseband OFDM approach. Notice that the module of the OFDM signal spectrum is symmetric with respect to the DC level ($f = 0$).

One of the disadvantages of the IMDD approach is that great part of the signal's energy will be placed at the optical carrier because of the generally high values needed to properly bias the light source. This should increase the vulnerability of the signal to OSNR degradations [29]. However, it has been shown in [41, 58, 60] that the optical IMDD OFDM performances can be improved by optimizing the relation between the DC component and the signal's side band

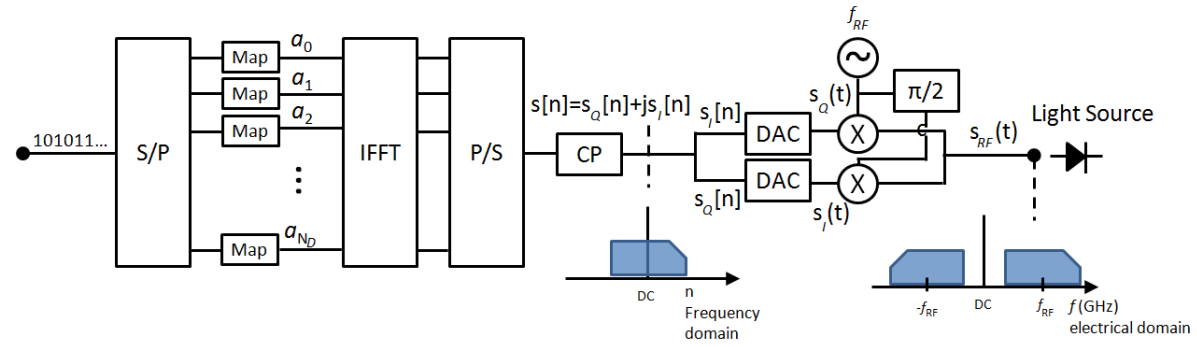

(a)

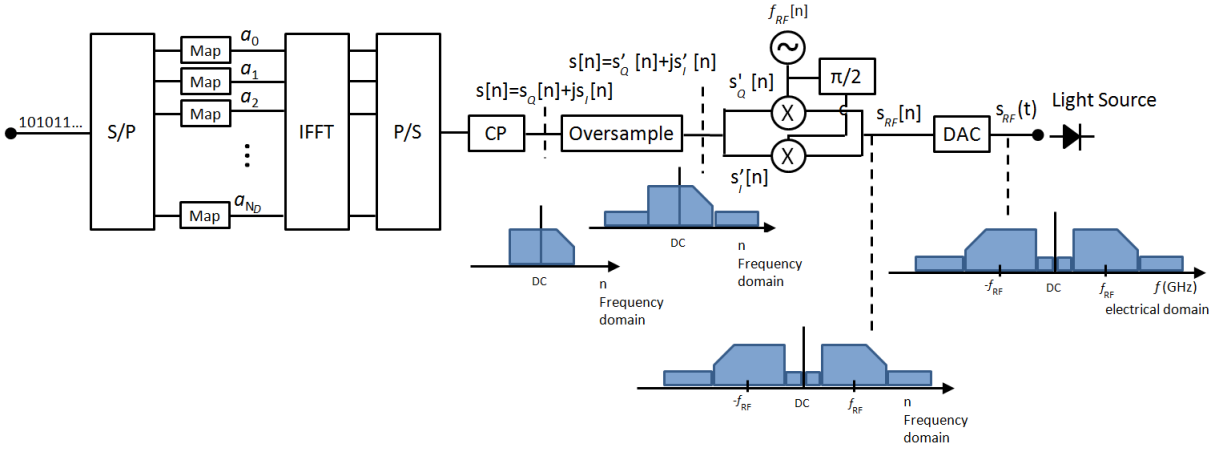

(b)

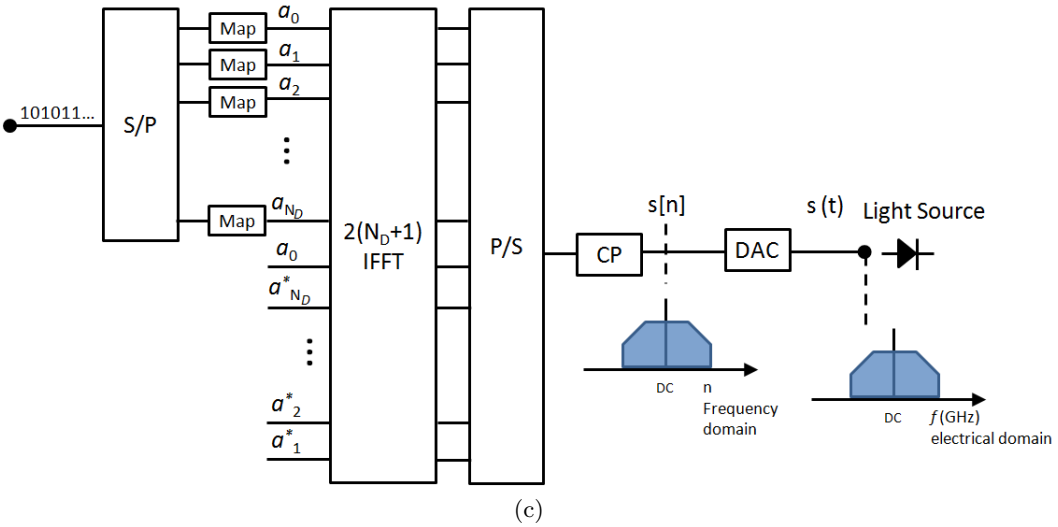

(c)

Figure 3.13: (a) Electrically up-converted OFDM. (b) Numerically up-converted OFDM. (c) Baseband OFDM.

power. More details on the experimental optimization of the signal's parameters are discussed in part II.

3.4.1.2 OSSB DD-OFDM

We have identified four different ways of enabling a DD-OSSB OFDM transmission. The first one consists of using an Optical Band-Pass Filter (OBPF) or an interleaver to filter out one of the side-bands of the optical signal generated through intensity modulation [41, 58, 60–62]. In order to relax the optical filter constraints (and consequently its costs), we can shift the OFDM signal from the DC level by means of an electrical up-conversion so that a less steep filter function can be used. The drawback of this solution is the decrease of the spectral efficiency of the system. Other drawback of this approach is that the optical subcarrier power is significantly reduced, causing the intermixing of OFDM subcarriers upon direct-detection to give rise to significant distortions that will affect majorly the low-frequency subcarriers [41, 58, 60].

The second approach consists of inducing the chirp effects on the source to the IM+FM state, as seen in section 2.5. In this case, instead of keeping the laser in continuous mode operation, it is intensity modulated together with the external modulator. The external modulator has a strong IM component and the laser is developed to have an almost pure FM component.

The third alternative consists of directly generating the OSSB using a dual-drive Mach-Zehnder Modulator (MZM). The signal and its Hilbert transform are fed into the arms of the quadrature biased MZM and the optical signal is then directly detected at the receiver [63–65]. This approach is also known as Compatible SSB Modulation and its great advantage is to have a higher spectral efficiency when compared to the optically filtered signal solution.

Finally, we may also mention the Virtual Single Sideband (VSSB) OFDM approach [66, 67] in which an RF tone is inserted at the left-most subcarrier for remote beating at the receiver side. The complex-valued baseband signal is then fed into an optical IQ modulator; the original subcarrier is suppressed and a new carrier generated thanks to the RF tone appears at the left-side of the signal spectrum, allowing the direct detection at the receiver side.

3.4.2 CO-OFDM and All-Optical OFDM

In CO-OFDM, not only we can use the whole optical field parameters (amplitude, phase and frequency) to transmit information but also the optical carrier doesn't need to be sent along with the signal. An OSSB signal created using either an optical I/Q modulator (Figure 3.14(a), after [42]) or an optical filter (Figure 3.14(b), after [42]) can be detected if there exists a local oscillator at the receiver-side. The great advantage of not sending the optical subcarrier is that it allows ameliorating the receiver's sensitivity [41, 58, 60] and allocating more energy to the side-band, thus assuring a higher robustness to OSNR degradations [29].

Even though CO-OFDM can propitiate better performances in terms of spectral efficiency, sensitivity and robustness against dispersion (the signal is intrinsically OSSB) , its main drawback is the increased complexity in the transceiver design if compared to conventional IMDD OFDM [42]. A coherent receiver is implemented with a local laser used as an oscillator, an optical hybrid and a pair of balanced photodiodes [29, 42]. An optical phase-locked loop and polarization scrambler are required to control the phase and polarization of the LO. Also, low-linewidth lasers are preferred at both transmitter and receiver sides to reduce the phase noise of the oscillator [59]. More details of the coherent detection procedure can be found in [42].

The common point between DD-OFDM and CO-OFDM is that they keep the signal creation at the electronic plan. In All-optical OFDM, however, the IFFT and FFT operations are transferred to the optical domain. The subcarriers are directly generated through a phase-locked wavelength comb, separated and individually modulated by several optical I/Q modulators. Then, the wavelengths are recombined, transmitted and demodulated with the help of a group of coherent receivers.

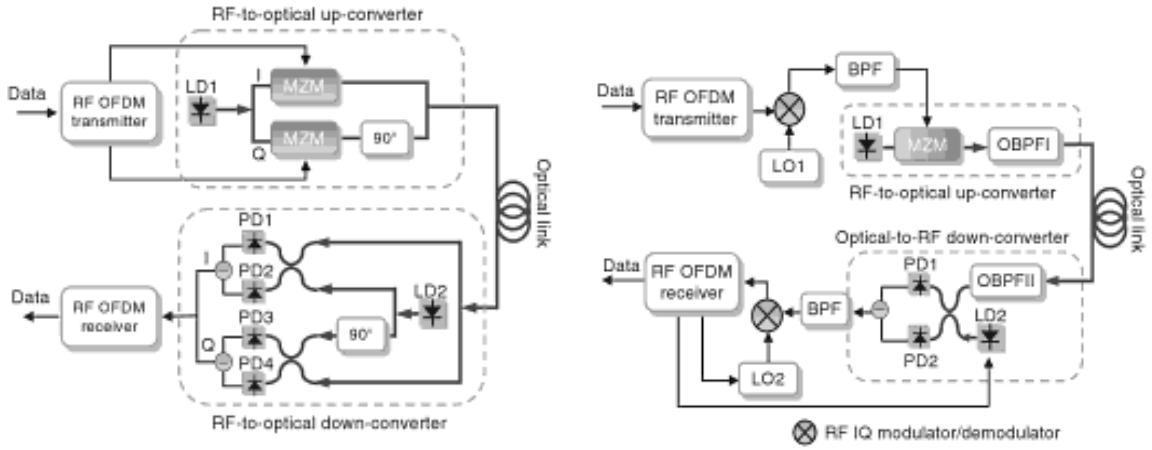

Figure 3.14: (a) Homodyne CO-OFDM. (b) Heterodyne CO-OFDM.

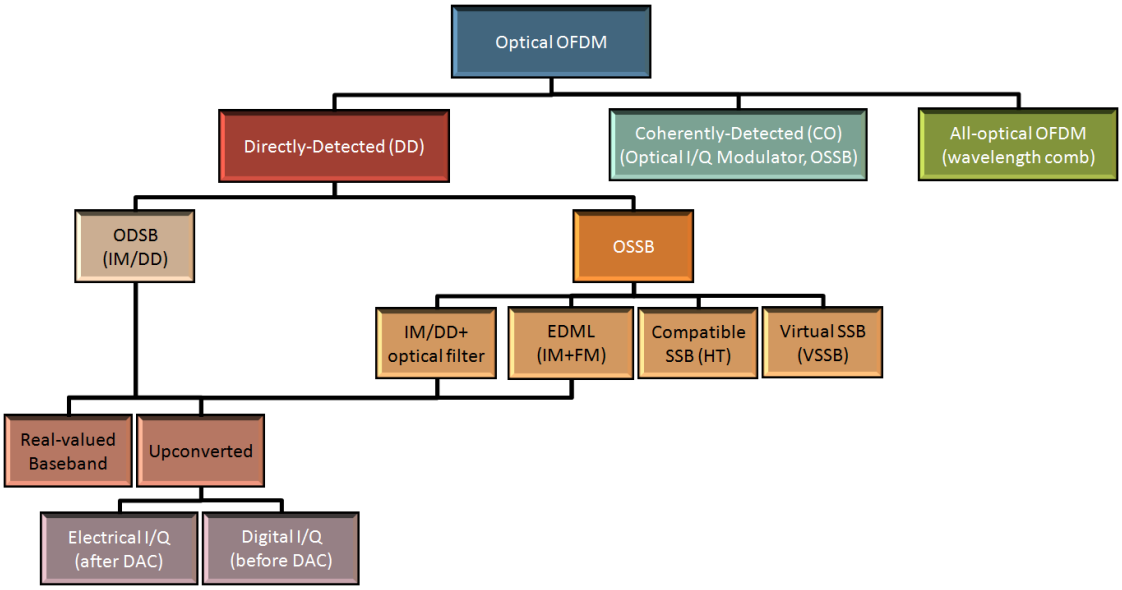

Figure 3.15: Different optical OFDM approaches.

All-optical OFDM has the advantage of being more spectrally efficient compared to conventional WDM. Indeed, a much lower frequency guard band is necessary between subcarriers (in this case, optical carriers) to avoid interference between adjacent channels. Actually, we may say that All-optical OFDM stands for CWDM or DWDM in the optical domain as OFDM stands for FDM in the electrical domain. More details on the optical IFFT and FFT architectures can be found in [56]. At 26Tb/s, All-optical OFDM currently holds the record throughput amongst all OFDM modulation approaches in the optical domain.

Figure 3.15 summarizes the different sorts of optical OFDM modulation.

3.5 Receiver Architecture and Experimental Constraints

In this section, we address the OFDM receiver architecture. We focus on the equalization and time and frequency synchronization approaches, which are by far the most critical aspects of the signal demodulation.

Figures 3.16(a)-(c) depict the ideal OFDM demodulators for the baseband and upconverted ODSB IMDD OFDM approaches, which can be trivially implemented by analogy with the

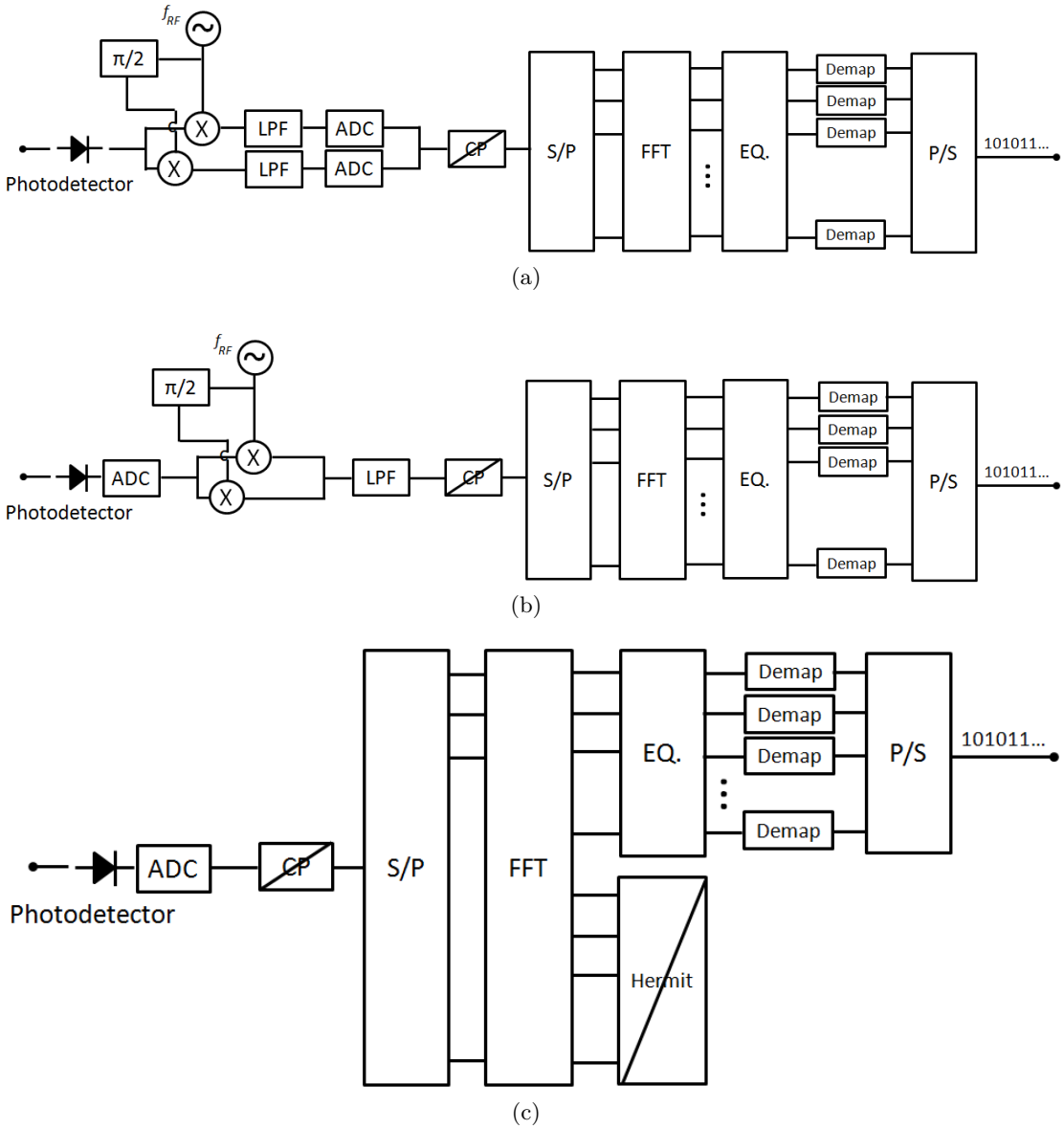

Figure 3.16: Different receiver architectures for the optimal transmission: (a) Electrically down-converted OFDM. (b) Numerically down-converted OFDM. (c) Baseband OFDM.

modulators shown in section 3.3.

The received optical signal is first converted from the optical to the electrical domain by means of a square-law detection at the photodiode. If the original electrical OFDM signal was upconverted at the transmission, we then proceed to a downconversion to baseband, which can be realized either electrically or numerically if done respectively before or after digitization by an ADC. Next, we remove the cyclic prefix and perform the FFT to retrieve the transmitted symbols. We should also remove the FFT outputs used for Hermitian symmetry purposes if the transmitted signal is a real-valued baseband signal.

Then, an equalizer is used to reverse the channel's frequency response. Remember from section 3.3.1 that thanks to the parallel transmission of the information using several subcarriers, the channel response on each subcarrier is approximately flat (the signal is robust to dispersion) and the equalization can be easily implemented by means of a simple multiplication of the received data in each subcarrier by a complex number, i.e., an one-tap filter. Such coefficients can be found for instance by means of a probing signal that can be used to estimate the channel thanks to the insertion of the cyclic prefix (see section 3.3.5). Finally, we proceed to the demap-

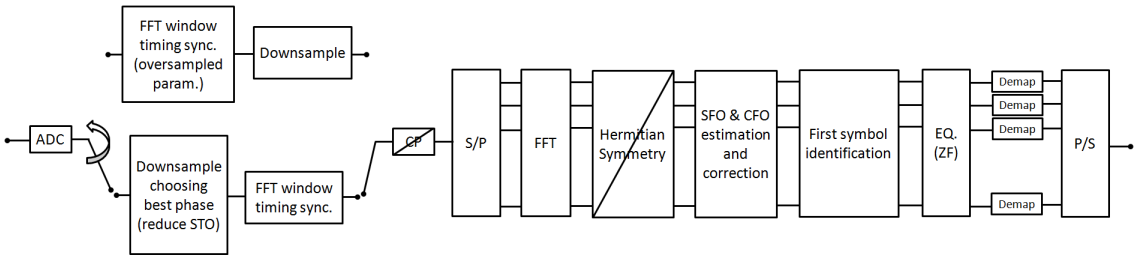

Figure 3.17: Receiver architectures for the non-optimal transmission for the Baseband OFDM approach.

ping of the symbols that will allow retrieving the received binary data after parallel-to-serial conversion.

Unfortunately, the ideal OFDM transmission is far from the reality of an experimental setup. For instance, a drifting of only a small percentage in the sampling frequencies of the DAC or ADC may considerably degrade the performances of the transmissions. Also, since the transmitter and receiver do not share the same clock reference, some kind of time synchronization technique must be used to align the symbols before the FFT and to retrieve the beginning of the transmitted sequence. Furthermore, I/Q unbalancing coming from an imperfect transposition of the signal will also impose some serious limitations on the system.

Since an OFDM signal is extremely sensitive to time and frequency synchronization issues [42], additional care should be taken at the receiver-side to allow the proper functioning of the system. In this section, we detail each step of the demodulation block diagram shown in Figure 3.17 and detail some techniques used in our experimental setups to overcome time and frequency synchronization issues.

3.5.1 Analog to Digital Conversion

Analog to digital conversion consists of creating a discrete time sampled quantity from a continuous electrical signal. Likewise to the digital to analog conversion, the ADC sampling ratio must be higher than twice the signal's bandwidth according to the Nyquist-Shannon theorem.

The analog-to-digital conversion procedure will also generate replicas of the received signal spectrum around the multiples of the ADC sampling ratio which is why it is very important to use the low-pass filters in the transmitter side [37, 38]. Indeed, if the replicas are not removed in the transmitter side, they can fall within the signal's bandwidth depending on the receiver's sampling ratio, thus deteriorating the transmission.

It is quite usual to configure the ADC to oversample the signal at the receiver side. This procedure is very interesting for matters of time synchronization since it enables reducing the Sample Timing Offset (STO, refer to section 3.5.2). In addition, oversampling can also be used for matters of filtering of the signal since it allows the use of a steeper function, implemented in the digital domain. If the signal is oversampled at the receiver side, an additional block must be added in the demodulator so that the signal's bandwidth can be properly filtered before demodulation.

The important characteristics of an ADC are its sampling ratio, vertical resolution, analog bandwidth and sensitivity, the last one being measured in mV/div. Table 3.4 lists some of the most performing commercially available ADC (Digital Storage Oscilloscopes) at the present time.

3.5.2 Time Synchronization

In a real transmission, the emitter and receiver do not share the same clock reference. As a consequence, some sort of synchronization technique should be adopted so that the symbols at

Vendor	Sampling Rate (GS/s)	Resolution (bits)	Reference
Fujitsu	65	8	CHAIS, 2nd gen.
Tektronix	100[i]	11[ii]	DSA73304D
Tektronix	40[i]	8	TDS6124
Agilent	40	8	DSO1308A
Agilent	2	14	U1083A
Rohde & Schwarz	20[i]	>7	RTO1044
Texas Instruments	3.6	12	ADC12D1800

[i] two-channel operation
[ii] with averaging

Table 3.4: Some commercially available ADC.

the receiver-side are correctly aligned before FFT.

The most intuitive way of doing so is by using a known sequence that can be detected by means of a correlation procedure. For an offline transmission, however, this approach risks being somewhat time-consuming since several symbols are treated at a time in each acquisition of the DSO. In addition, the complexity of such procedure is directly proportional to the sampling rate of the signal, meaning that a sample-by-sample search can get considerably slow depending on the bandwidth of the signal.

One way of accelerating the time-synchronization procedure is by dividing it into two steps. In the first step, we find the first beginning of one symbol in the received sequence, independently of its position regarding the transmitted data. This is done thanks to the cyclic prefix with which it is possible to detect the repetition of a group of samples on a signal. Once the cyclic-prefix based synchronization has finished, we can directly proceed to the FFT.

Indeed, despite the fact that at this stage we still do not have any information about the first transmitted symbol (the t_0 of our transmission), all symbols are already delimited and ready for demodulation. After demodulation, we can proceed to a symbol-by-symbol search (which is faster than a sample-by-sample search) to identify the first symbol and finish the synchronization procedure. The first symbol identification can also be performed by means of a pseudorandom binary sequence (PRBS). Indeed, the PRBS generates independent values that are similar to real random sequences and which start to repeat after a certain number of bits.

3.5.2.1 FFT Windowing Synchronization

Let's suppose that the OFDM cyclic prefix has N_{CYP} samples. The first step of the time-synchronization can be performed after the analog-to-digital conversion by searching in the received signal two resembling groups of samples sized N_{CYP} each and separated by $N - N_{CYP}$ samples, with N being the length of the OFDM symbol.

If we call these groups D, for the N_{CYP} starting samples and F for the N_{CYP} ending samples as depicted in Figure 3.18, then a good resemblance function can be found by means of a parameter p defined by:

$$p(m) = \frac{1}{\sum_{l=1}^{N_{CYP}} |D_m(l) - F_m(l)|}$$
$$m = 1, 2, ..., N + N_{CYP} \tag{3.29}$$

Starting from the first sample of the acquired signal we right-shift the groups D and F by one sample for each value m of p. Thereby, we only need $m = N + N_{CYP}$ values to assure that

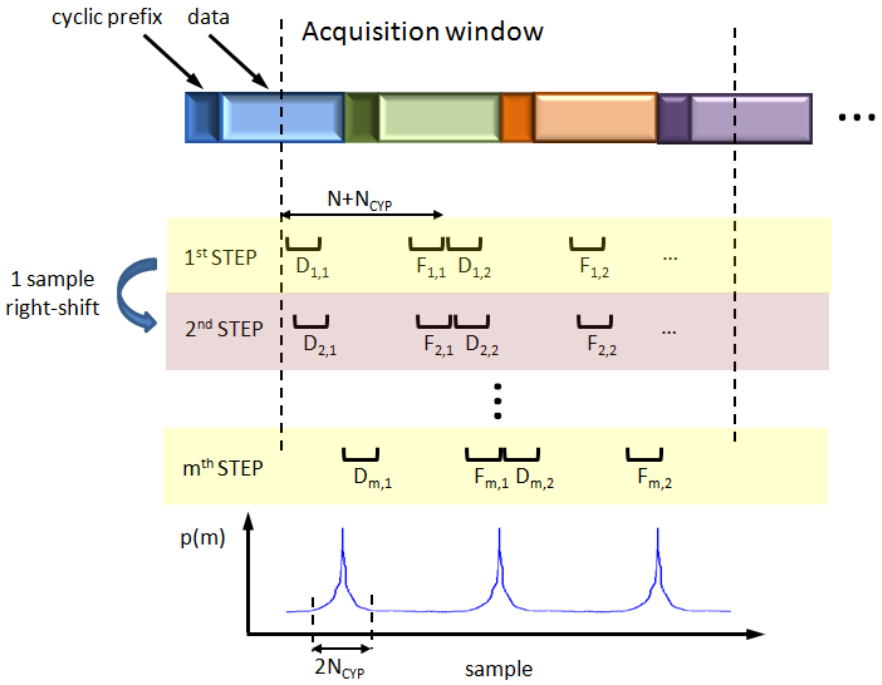

Figure 3.18: CP-based FFT timing-window synchronization.

we will find at least one beginning of a symbol on the acquired signal. Whenever the group of samples D resembles F, the sum over the N_{CYP} samples on the denominator of $p(m)$ tends to zero and $p(m)$ tends to infinite. The peak on $p(m)$ will then mark the beginning of a symbol.

Figure 3.19(a) shows an example of FFT window sync based on CP with $N = 256$ and $N_{CYP} = 64$. If we had extended $p(m)$ over all samples of the acquired signal, we would have seen a sequence of peaks corresponding to the number of symbols in the acquisition window of the DSO. It is important to remark, however, that those peaks would have different profiles. The reason for this is that we are correlating different OFDM symbols containing independent data sets. The correlation output is then a random variable whose standard deviation is proportional to the number of samples over which it is performed, i.e., the ratio between the lengths of the signal and the cyclic prefix [68]. As a consequence, using this technique with an OFDM signal with reduced number of subcarriers (and consequently a small number of samples per symbol) may not allow an appropriate detection.

To better estimate the position of the first symbol, it is possible to take the average value over several S consecutive estimations of $p(m)$, the main disadvantage of which is the increase in the calculation time of the algorithm:

$$\bar{p}(m) = \frac{1}{s}\sum_{s=1}^{S}\left(\frac{1}{\sum_{k=1}^{N_{CYP}}|D_{m,s}(k) - F_{m,s}(k)|}\right) \tag{3.30}$$

as represented by the red line in Figure 3.19(b). In our experimental work, we usually set S to be 10% of the total number of transmitted symbols.

Figure 3.20 shows the variation of $p(m)$ with the lengths of the cyclic prefix of an OFDM signal. In these examples, the useful OFDM symbol has 512 samples. It is a bandbase purely real signal with 255 data subcarriers.

It is clear from Figure 3.20 that the quality of the synchronization is directly related to the ratio between the size of the cyclic prefix and the overall number of samples of the OFDM

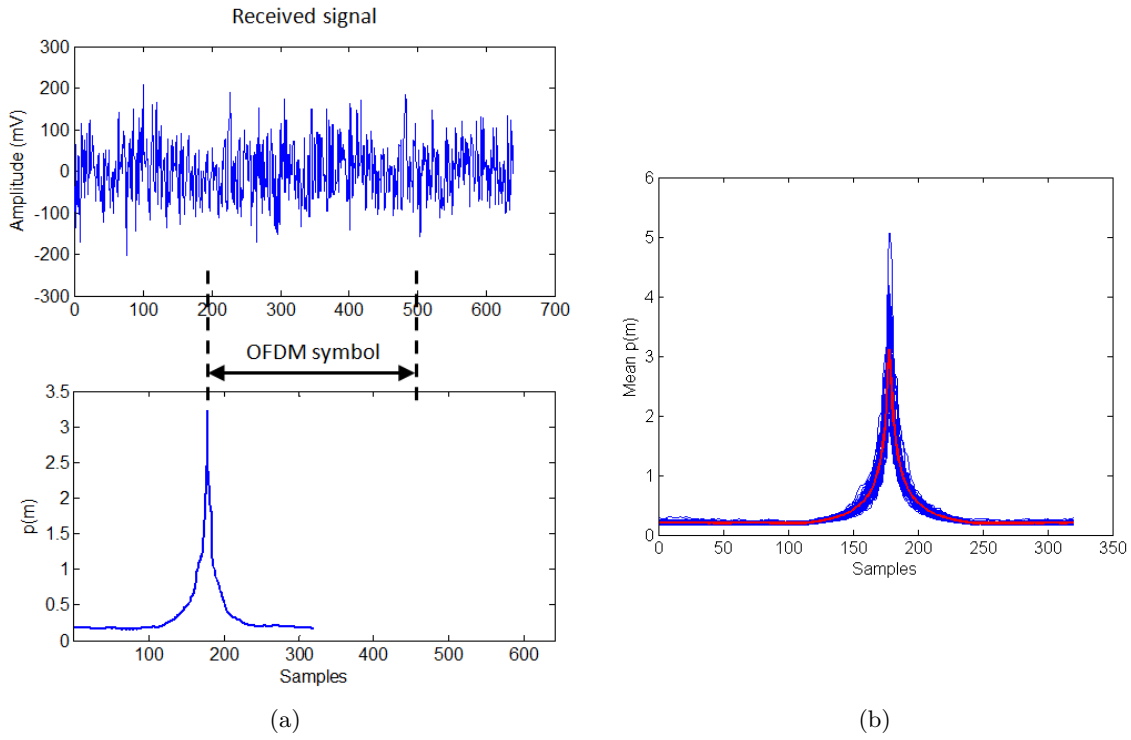

(a) (b)

Figure 3.19: (a) Detection of the first beginning of an OFDM symbol. (b) Mean p(m).

symbol. For instance, when $N_{CYP} = 8$, $p(m)$ becomes very noisy and the synchronization peak is not much higher than the rest of the signal whereas when $N_{CYP} = 128$, the correlation function generates a higher peak and consequently a better estimation of the beginning of a symbol.

The reader should remember, however, that a large cyclic prefix implies a diminution in the net bit-rate of the transmission. Indeed, N_{CYP} must be chosen by searching for the optimum compromise between the quality of the time-synchronization procedure and the system's throughput. The total latency of the channel arriving from any residual dispersion should also be taken into account when choosing N_{CYP} for reducing the effects of ISI.

Other point that needs attention is that even after the cyclic prefix based synchronization, the transmission may still present a slight degradation arriving from the phase difference between the DAC and ADC sampling instants. This is because the FFT window correlation works so that the most resembling sequences are found on a certain digital sequence that has not been sampled with the same timing reference as that of the analog to digital converter. Here, we call Sample Timing Offset the phase offset between the sampling instants of DAC and ADC happening regardless of the FFT window synchronization. STO will cause the rotation of the received symbols [69] but this is easily corrected by means of an equalizer. However, it also induces ICI, which tends to be stronger on high frequency subcarriers.

To circumvent the degradations caused by STO, we can oversample the signal at the receiver side. For instance, if the oversampling ratio between ADC and DAC is 4, it is possible to select 1 over 4 samples on a single sampling interval in the downsampling procedure before synchronizing the signal. This allows choosing the best "starting point" on the received signal, i.e., the set off samples allowing to generate the smallest sampling phase offset between DAC and ADC after the cyclic prefix-based synchronization. Other solution consists of proceeding to time-synchronization before downsampling the signal. In this case, the number of samples per symbol and size of the cyclic prefix have to be translated to the oversampled scenario, as shown in Figure 3.17. This solution, however, becomes complicated if the oversampling ratio is not an integer value. The higher the oversampling ratio at the receiver side, the easier it is to skirt the

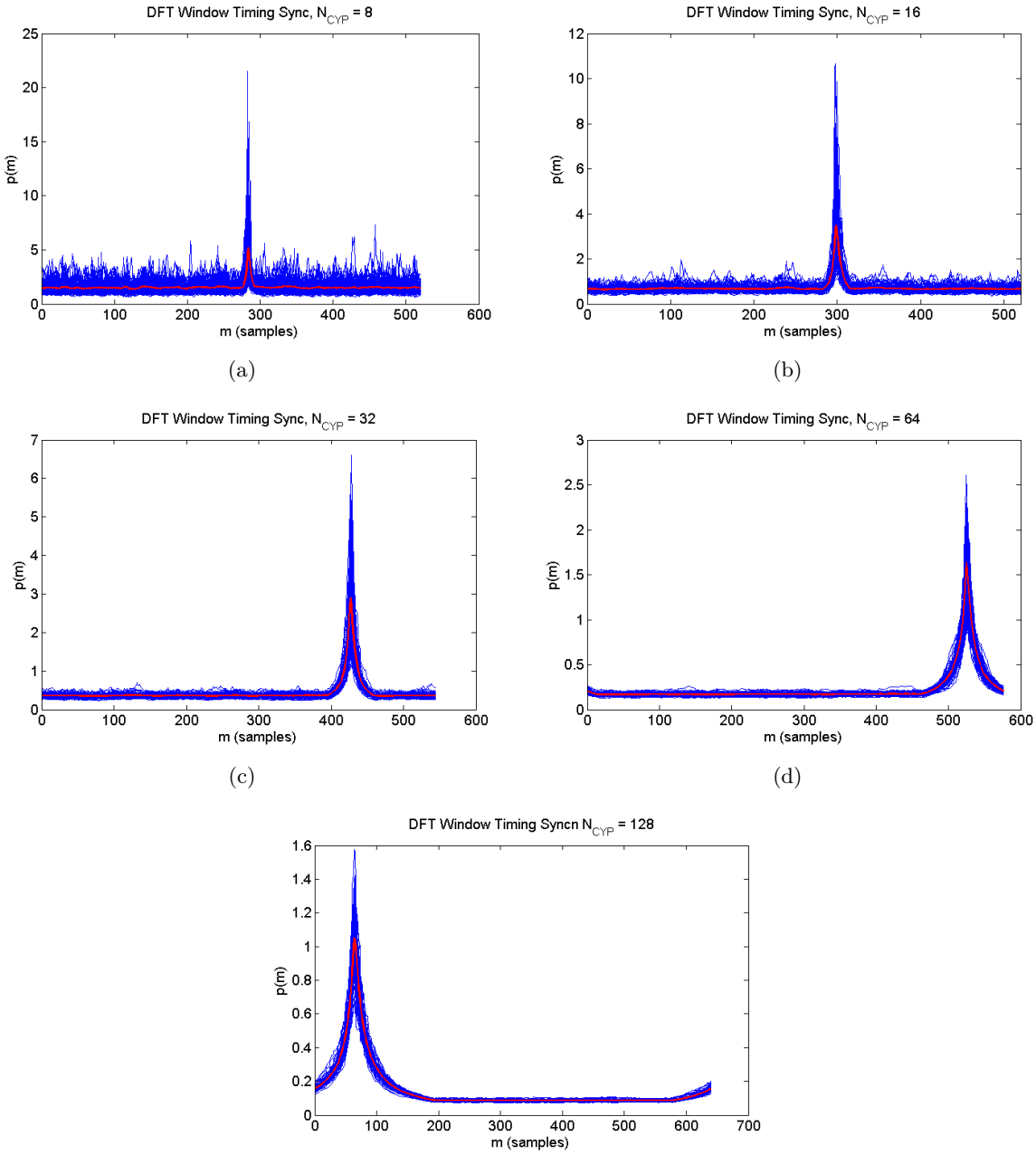

Figure 3.20: $p(m)$ for different sizes of N_{CYP}. (a)$N_{CYP} = 8$. (b)$N_{CYP} = 16$. (c)$N_{CYP} = 32$. (d)$N_{CYP} = 64$. (e)$N_{CYP} = 128$.

degradations imposed by STO. However, it is important to remember that the sampling ratio of the converters is one of the most constraining parameters as far as the costs of the PON-OFDM transceivers is concerned, principally at the ONU side.

Once the beginning of an OFDM symbol has been found, we need only to find the first symbol of the transmitted sequence so that some transmission performance parameters can be calculated. Indeed, since we are dealing with an offline transmission, if we want to precisely infer some parameters such as the real BER[5], then we need to locate the very first OFDM symbol on the received frame.

3.5.2.2 First symbol identification

Thanks to the cyclic prefix-based synchronization, we were able to properly determine the limits of all acquired symbols in the received time-domain OFDM signal. Despite the fact that at this point we still don't have any information concerning the first symbol, we can still proceed to the FFT block and then retrieve the constellations on each subcarrier.

The detection of the first symbol shares the same principle of the cyclic prefix-based correlation. However, since the received symbols are already well demarcated, the procedure may be done on a symbol-by-symbol basis. Indeed, we compare each received symbol with a reference symbol known by the receiver:

$$q(s) = \frac{1}{\sum_{x,x\in s} |ref_x - symb_{x,s}|} \tag{3.31}$$

Here, we are correlating a reference symbol ref to different symbols s of the acquired data by evaluating the sum of the samples x composing both sequences. The correlation principle is once again very simple. Once we find our first symbol (reference), the denominator of $q(s)$ tends to zero and $q(s)$ tends to infinite.

To find the first symbol, we need then to extend s to at least N_s symbols, with N_s being the total number of sent symbols. In our experiments, the DSO acquisition window is always set to get at least two times the total number of transmitted symbols, i.e., $2N_s$. We should point out that the reference sequence need not to be necessarily one single OFDM symbol and we can use several concatenated symbols to improve the correlation profile of $q\,(s)$. Figure 3.21 illustrates the principle of the algorithm.

3.5.2.3 Burst mode synchronization

The DFT window synchronization technique based on the cyclic prefix is very well suited for continuous signals. However, if the transmission is realized by means of bursts of data (please refer to section 6.2), then instead of searching the beginning of a symbol, we actually need to find the intervals in which there is a transmission.

In other words, we need to be capable of differentiating the useful data from the idle moments in the acquired signal. This seemingly trivial problem gave rise to a series of specialized algorithms to detect the data packets on a burst transmission. Indeed the clock and data recovery (CDR) is one of the crucial issues of NRZ transmissions beyond $10Gb/s$. Actually, since the receiver does not collect information continuously, high speed TDMA receivers must be able to correctly synchronize the signals despite the idle periods on the transmission. We have had the opportunity to test one of such receivers. The results are presented in annex D.

One possible way to detect a data burst on a transmission is by searching the variations on the energy of the received signal. In the sliding-window (SW) approach, we calculate the signal energy within a specific interval representing the window size, which is chosen to be equal to

[5]Here we use the word real to differentiate the measured BER from the BER that can be estimated from the EVM.

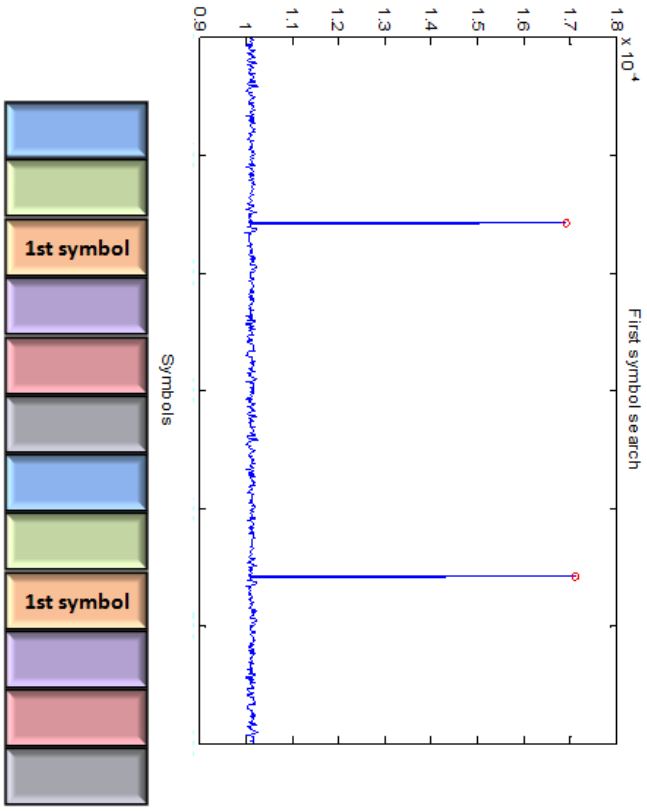

Figure 3.21: Detection of reference symbol.

the burst duration. Starting from the first sample of the received signal, the procedure is then repeated by sliding the window sample-by-sample until it falls exactly on a data burst:

$$p_{SW}(m) = p_{W_1}(m) = \overline{r(m:m+L)^2} - \left(\overline{r(m:m+L)}\right)^2 \tag{3.32}$$

where $r(n)$ is the received time domain OFDM signal and L is the size of the window in samples. Other similar algorithm consists of using an additional window with the size of an idle period. Whenever the first window (W_1) falls exactly on a burst and the second window (W_2) falls on an idle period, the energies within W_1 and W_2 are respectively maximized and minimized (at this point, the energy in W_2 corresponds to the noise power). The ratio between the energies calculated within the first and second windows is then maximized, generating a peak on:

$$p_{DSW}(m) = \frac{p_{W_1}(m)}{p_{W_2}(m)} \tag{3.33}$$

This method is called double-sliding-window (DSW). Figures 3.22(a) and (b) illustrate the principle of the SW and DSW algorithms. For more details on these techniques, please refer to [70, 71].

The great disadvantage of the SW and DSW methods is that they are very complex in terms of computation. Indeed, since they are based on a sample-by-sample search, the detection of the data packets can take a considerable amount of time depending on the size of the acquisition window and sampling frequency of the DSO. In this case, a direct search for a reference symbol or group of symbols generally consists of a faster approach.

3.5.3 Frequency Synchronization

We have seen in the previous subsection that time-synchronization is a crucial issue on the demodulation of an OFDM signal because the transmitter and the receiver do not share the

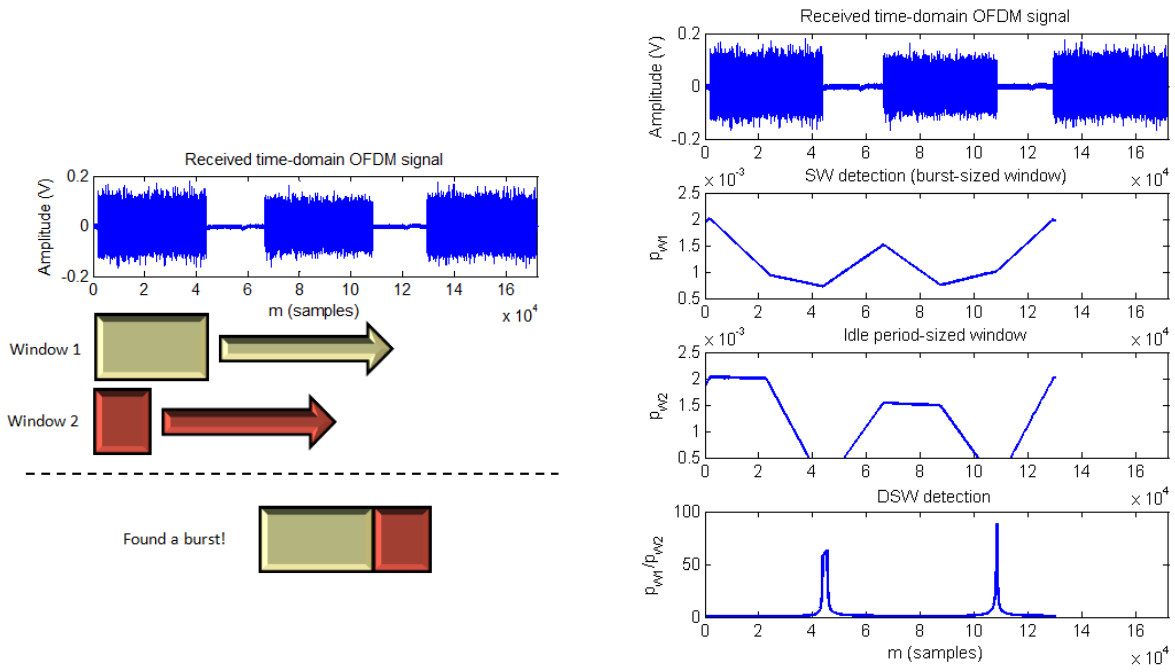

(a) (b)

Figure 3.22: (a) Burst Mode detection with using SW and DSW. (b) Burst identification functions.

same clock reference. Thanks to the cyclic prefix, we can correctly align the FFT window thus reducing the degradations arriving from a wrong delimitation of the symbols. We have also seen that if we wanted to estimate some performance parameters then the cyclic prefix-based synchronization could be complemented by a second step in which the first transmitted symbol is identified based on a reference sequence known by the receiver.

Other pesky source of impairments on a real OFDM system arrives from an imprecise frequency synchronization. Frequency synchronization impairments can be divided into two categories, the first of which is Carrier Frequency Offset (CFO). CFO arrives when there is a misalignment between the RF frequencies of the local oscillators at the transmitter and receiver sides when the signal is in the upconverted configuration (see Figures 3.13(a) and (b)). CFO will cause a wrong down-conversion of the OFDM signal to baseband and its effects are twofold [72, 73]:

- Since the LO offset will result in a wrong frequency shift of the signal spectrum, the FFT will no longer be aligned with the peaks of the received frequency-domain *sinc* pulses of the signal. This results in ICI due to the loss of the orthogonality between subcarriers.
- The transmitted constellations will suffer a phase and module variation in the time-domain which will be constant over all subcarriers.

The other type of frequency-domain impairment arrives from the errors in the sampling frequencies of the transmitter and receiver converters. This is known as Sampling Frequency Offset (SFO) and can result in severe degradation of the transmitted signal, specially for small inter-carrier separations. SFO occurs primarily due to the tolerances of the quartz oscillators and temperature variations of the converters which slightly deviate the sampling intervals of the received signal from their correct values [74, 75]. SFO has two main effects:

- The constellations will suffer a specific phase and module variation in the time-domain. This variation, contrary to the one provoked by CFO, will be proportional to the subcarrier index, being stronger on the subcarriers farthest away from the center of the signal spectrum.
- The signal's SNR will degrade due to ICI arriving from the loss of the orthogonality between subcarriers. Indeed, the time-domain signal observed in the FFT window of the receiver may wander away from its ideal position; if the converters' sampling ratio is too fast or too slow compared to the ideal values, the signal will drift by some samples thus inflecting additional noise to the demodulated signal.

For an interesting explanation and thorough mathematical demonstration of those effects, please refer to [72–76]. Both CFO and SFO can be estimated by analyzing the variation of the phases of the received constellations in time. If we introduce the relative carrier frequency error ε_C and the relative sampling frequency error ε_S as:

$$\varepsilon_C = \frac{CFO}{\Delta f} \tag{3.34}$$

$$\varepsilon_S = \frac{SFO}{F_S} \tag{3.35}$$

with Δf being the separation between adjacent subcarriers and F_S the original sampling rate of the signal, then it is possible to quantify the phase difference between two successive symbols as:

$$\Delta\Phi = 2\pi\left(\varepsilon_C + k\varepsilon_S\right) \tag{3.36}$$

with k being the subcarrier index. Note that the SFO effect will be as dangerous as the spacing between subcarriers is small. We should then expect some serious degradation with a high number of subcarriers on a small signal bandwidth.

The estimation and correction of the time-domain phase variation can be done after the FFT block and before the first symbol identification routine. To illustrate the method, let us consider a practical case of electrical back-to-back experiment in which we transmit 300 OFDM symbols. In this example, we connect the Arbitrary Waveform Generator (AWG) directly to the Digital Sampling Oscilloscope (DSO). The bandbase OFDM signal has 127 subcarriers (256 inputs at the IFFT, with Hermitian symmetry), 16 samples of cyclic prefix per OFDM symbol, $5GHz$ bandwidth and is transmitted by the AWG at $12GS/s$. All subcarriers are QPSK mapped and have the same power. The signal is scaled according to the DAC's maximum Vpp with a scaling factor of $13dB$. At the receiver, it is digitized at $40GS/s$ by the DSO and time synchronized before FFT.

Figure 3.23(a) shows the constellations retrieved at the receiver side after FFT for three different subcarriers ($k = 2, 60, 90$). The DSO acquisition window was more than 2 times longer than the necessary for acquiring the 300 OFDM symbols, which resulted in more than one extra copy of the initial sequence (734 acquired OFDM symbols).

Since the constellations show all the transmitted symbols of each subcarrier, we can easily notice the effects of CFO and SFO by analyzing, on each subcarrier, how much the symbols have been circularly spread. This phenomenon is stronger for higher subcarrier indexes, as anticipated by equation 3.36. Figure 3.23(b) shows the symbols phase variation in time for each of the three subcarriers. To estimate the CFO and SFO, the slope of that curve must be determined and then eliminated.

To do so, we first need to reduce all the four phases of the received $\hat{a}_{lk}$ symbols to one single phase φ_{lk} :

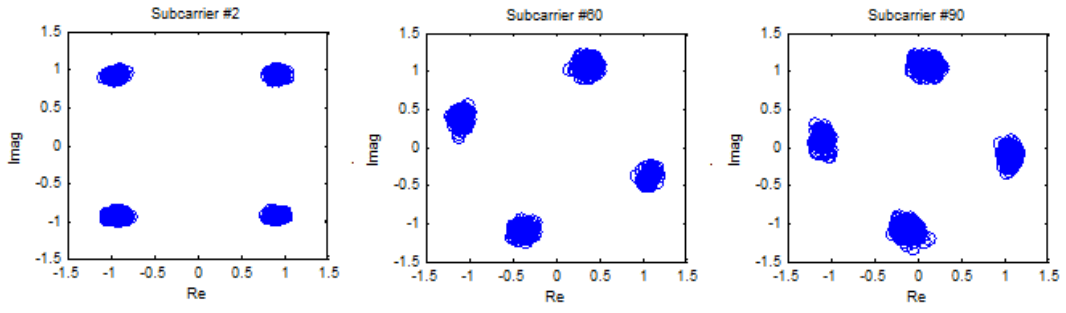

(a)

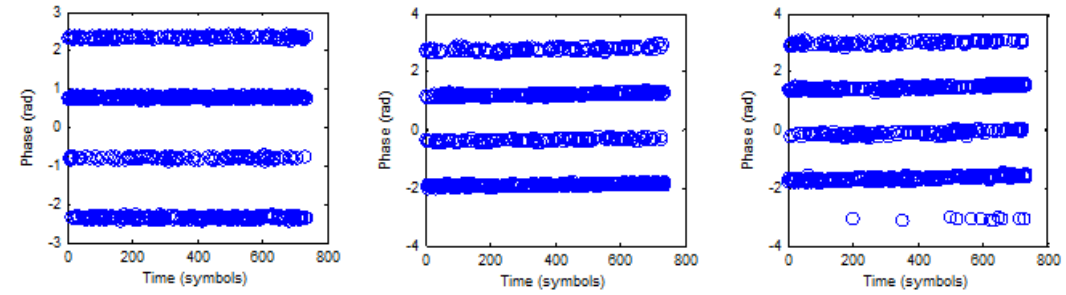

(b)

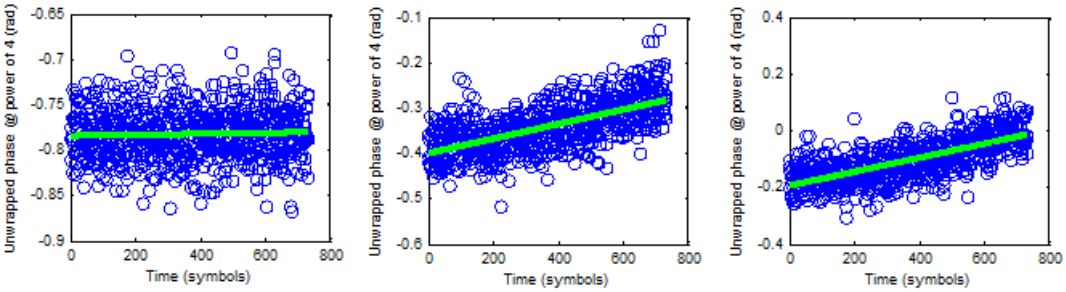

(c)

Figure 3.23: SFO and CFO estimation procedure, visualization of subcarriers 2, 60 and 90. (a) Constellations. (b) Time variation of the symbols's phases. (c) φ_{lk} and corresponding fitting.

$$\varphi_{lk} = \frac{\angle \hat{a}_{lk}^4}{4} \tag{3.37}$$

For each subcarrier k , the variation of φ_{lk} in time can be represented by a first order polynomial that respects:

$$\varphi_{lk} = \varphi_k(l) = \rho_k l + \varsigma_k \tag{3.38}$$

with ρ_k being the slope of the curve which will help retrieving the SFO and CFO, l the time domain index of each symbol and ς_k the phase variation imposed by the channel's frequency response.

Since ς_k represents only the phase variation in the frequency domain, it can be corrected later with an equalizer and shall not impose any problems at this stage. Fig 3.23(c) shows φ_{lk} and a linearly fitted curve used to calculate the parameters ς_k and ρ_k of the three subcarriers according to equation 3.38.

Finally, after finding φ_{lk} for all subcarriers, it is possible to plot ρ_k as a function of the subcarrier's index, which allows us to retrieve ε_S and ε_C using equation 3.36. The procedure is

shown in Figure 3.24(a). Here, another linear fitting has been done and ε_S and ε_C have been estimated to $0.42ppm$ and $0.27ppm$ respectively.

Once ε_S and ε_C have been found, a post-FFT SFO and CFO phase correction is done simply by multiplying the received constellations $\hat{a}_{lk}$ by a factor F_{phase} :

$$F_{phase} = e^{-j2\pi l(k\varepsilon_S+\varepsilon_C)} \tag{3.39}$$

Figure 3.24(b) shows the corrected symbols on subcarriers 2, 60 and 90. Notice that the corrected phases no longer vary in the time-domain, which makes the constellations less spread on each subcarrier. Notice also that the channel's phase response ς_k has not been compensated and each subcarrier constellation presents a certain rotation.

SFO and CFO also induce a variation in the amplitude of the received constellations. Such variation can be corrected by multiplying the received symbols by a correction factor that obeys [74, 75]:

$$F_{amplitude} = \left(\frac{N_D^2 \sin\left(\frac{\pi\varepsilon_C}{N_D}\right) \sin\left(\frac{\pi k\varepsilon_S}{N_D}\right)}{\sin\left(\pi\varepsilon_C\right) \sin\left(\pi k\varepsilon_S\right)} \right)^l \tag{3.40}$$

Generally, the attenuation $\frac{1}{F_{amplitude}}$ imposed by the SFO and CFO is very close to 1 and can therefore be neglected [72, 73].

At this point, we should concern some attention to the phase unwrapping problem. Because of the cyclic nature of the $arctan$ function, φ_{lk} will be wrapped modulo 2π, i.e., it will be limited to the interval $[-\pi, +\pi]$. This will create a phase ambiguity that will generate discontinuities in the form of $2n\pi$, $n = 1, 2, ...$ jumps whenever the phase is outside this range. The wrapped phase with jumps cannot be used to estimate the values of ρ_k and ς_k since it will generate an incorrect linear fitting. A phase unwrapping routine is then necessary.

The unwrapped phase is the instance of the phase function in which those jumps are removed to ensure that the curve is continuous. Intuitively, we can perform the phase unwrapping quite easily by computing the absolute values of the phase differences between two adjacent points, verifying if they are bigger than π and then compensating them with $\pm 2\pi$ if so.

The real problem arrives when those jumps are masked by phase noise, as seen in Figure 3.25. The effects of a wrong unwrapping on a noisy phase will propagate to the whole set of values and accumulate the errors of the phase unwrapping routine [77]. We need then to implement a phase unwrapping algorithm capable of dealing with low values of SNR.

One possible way to detect phase jumps on a noisy signal is to extend the searching procedure. Instead of limiting the search to adjacent points, we can actually iteratively look up for discontinuities by comparing one point to several other neighboring points. For instance, if a phase jump between samples 1 and 2 at one first evaluation is not found due to phase noise, we can still find it by analyzing the phase differences between samples1 and 3 or 1 and 4 for instance. The biggest problem of this approach is an increased computational complexity. The algorithm complexity can be considerably reduced by analyzing only a few subcarriers instead of the whole set of subcarriers of the OFDM signal. Indeed, if equation 3.36 holds, we don't need to unwrap all subcarriers to infer the values of ε_S and ε_C and so, the carriers with worst SNR, i.e., the ones whose unwrapping would take more time, can be avoided. Figure 3.26(a) shows the result of ε_S and ε_C fitting using only the first 32 subcarriers of the signal. For a formal mathematical description of the phase unwrapping problem, please refer to [78]. For other phase unwrapping solutions, refer to [79, 80].

Figure 3.26(b) shows an histogram of the estimated values of SFO over several iterations of our program in electrical back-to-back. The SFO has a Gaussian distribution whose mean can be used for correcting the frequency impairments of signals that are not necessarily QPSK modulated, which is the case, for instance, after implementing a bit and power loading algorithm. Other way of estimating the SFO and CFO is by using a group of pilot subcarriers. Indeed,

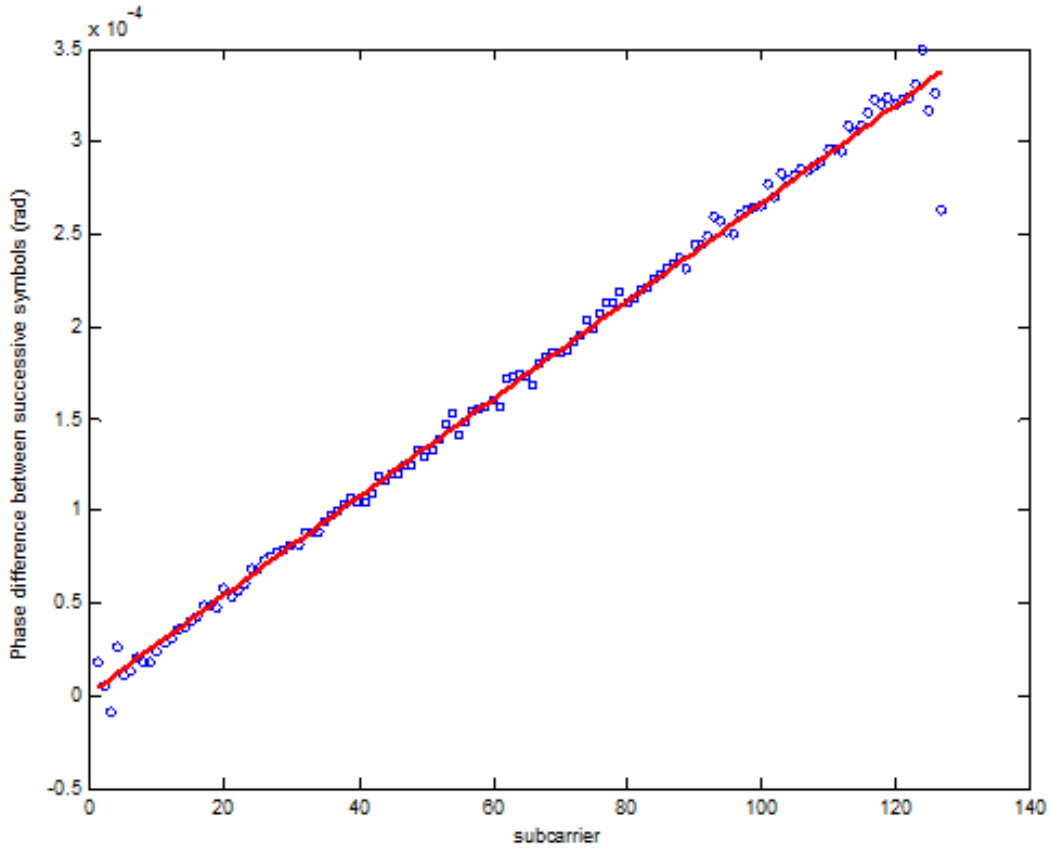

(a)

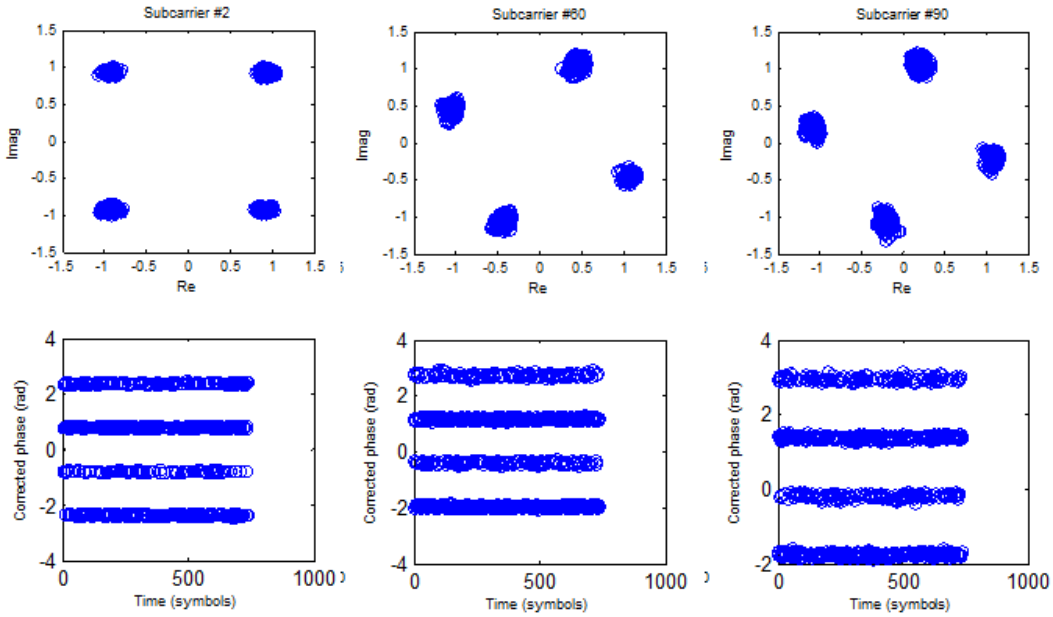

(b)

Figure 3.24: (a) Estimation of ε_S and ε_C. (b) Symbols after post-FFT SFO and CFO correction

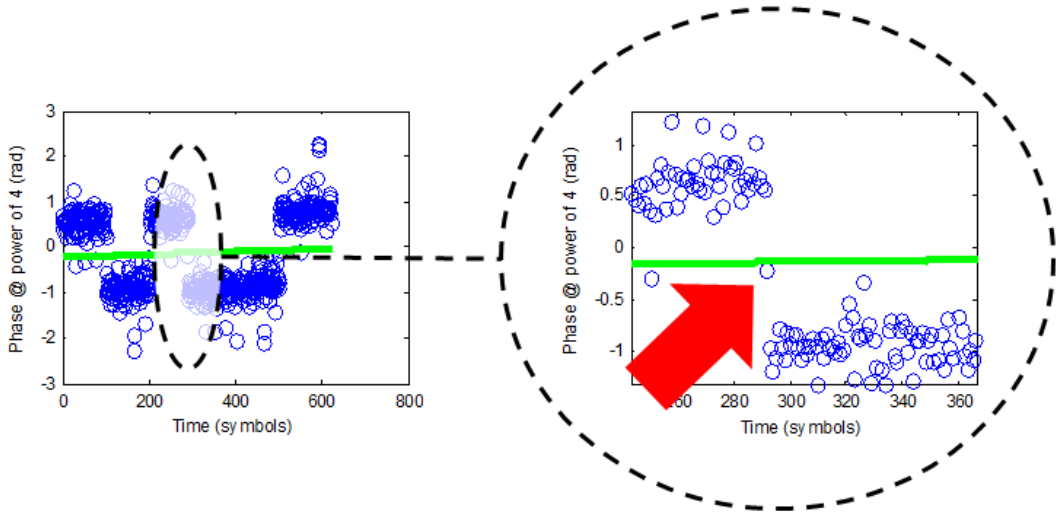

Figure 3.25: Influence of noise in the phase unwrapping.

even if the other subcarriers are mapped with higher level constellations, the pilot tones can be QPSK mapped and the CFO and SFO can still be inferred by means of a linear fitting.

It is worth mentioning that the estimations of SFO and CFO may present small fluctuations within the same acquisition window. Indeed, we have experimentally verified it by separating the acquired time domain signal into two or three parts and by doing an individual estimation for each part. The problem of increasing the granularity of the SFO and CFO estimations, i.e., reducing the number of symbols over which they are done, is that it will imply a less precise linear fitting in the phase difference between successive symbol versus subcarrier curve. Actually, due to phase noise, the more symbols we use to find φ_{lk}, the better the estimation will be.

3.5.4 Channel Estimation and Equalization

Any transmission mean can be thought of as a combination of two effects: the deterministic[6] response imposed by the channel and the random changes introduced by the noise. To reconstruct the signal that was transmitted, the receiver must be capable of reverting the channel response and ideally minimizing the impacts of channel noise. This procedure, known as equalization, is an essential step on the recovery of a signal [69].

We have seen in section 2.5 that an advanced equalization solution becomes indispensable with increasing bit-rates and transmission ranges in optical SC IMDD transmissions due to the typical frequency-selective response of the channel arriving from the ODSB nature of the signal, the interaction between fiber dispersion and laser chirp and the squared-law detection at the receiver side. Different dispersion compensation techniques have also been discussed such as the electronic dispersion compensation, dispersion managed fibers (DMF) and photonic fibers, side-band filtering with optical band-pass filters and coherent transmissions by means of optical IQ modulators. The great advantage provided by OFDM is that the parallelization of the data stream into a set of lower bit-rate channels causes each subcarrier to be affected by a quasi-flat frequency response thus guaranteeing robustness to chromatic dispersion. In section 3.3.5 we have also seen that thanks to the cyclic prefix extension, the linear convolution between the channel's impulse response (CIR) and the time-domain signal could mimic a circular convolution thus allowing a much simpler estimation of the channel's effect, in the frequency domain.

As far as these two points are concerned, it is straightforward to affirm that a cyclic-prefixed OFDM signal has the potential to transform an ISI channel into a set of parallel Additive White Gaussian Noise (AWGN) channels needing a much simpler equalization scheme [29].

[6] Actually, if the channel presents aleatory variations, it can be also be characterized by means of a probabilistic model.

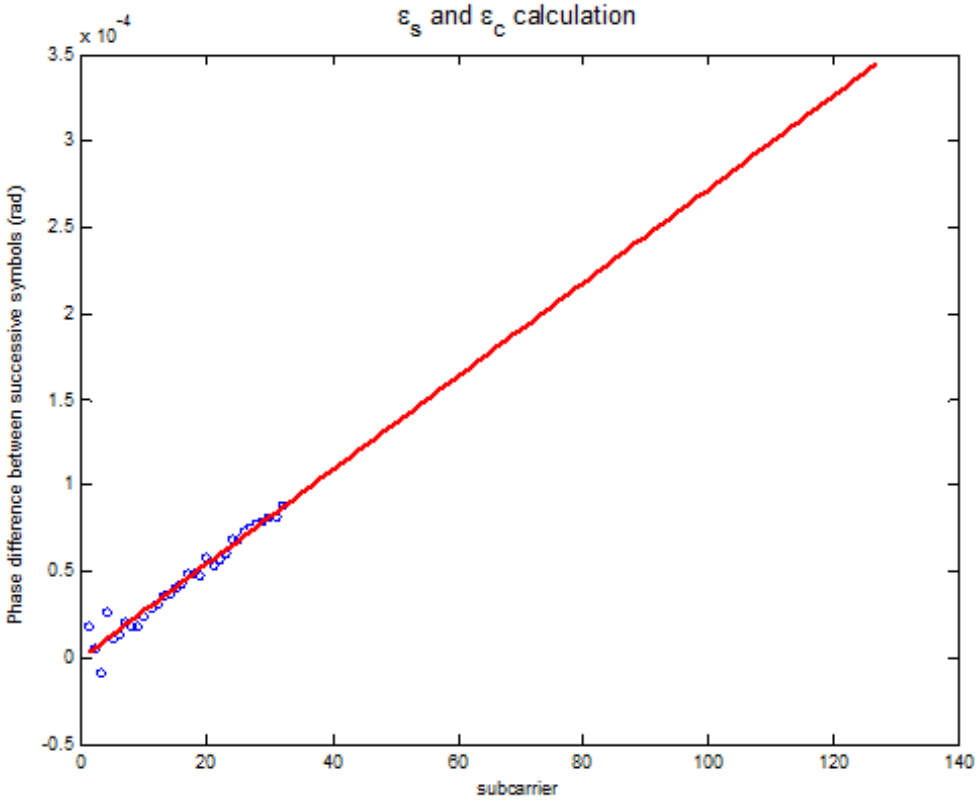

(a)

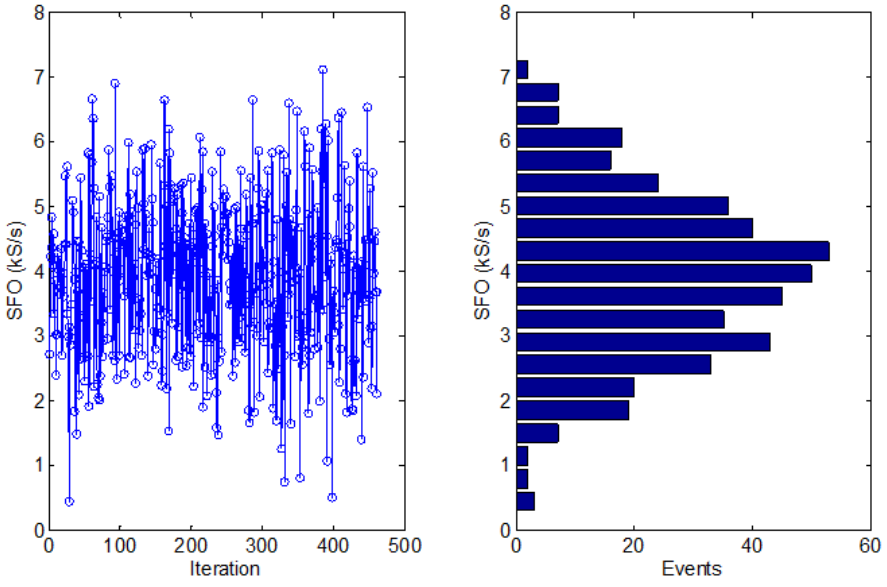

(b)

Figure 3.26: (a) Fitting only on the first 32 subcarriers to find ε_S and ε_C. (b) SFO histogram.

Indeed, the complex time-domain equalization that would be needed to revert the channel's response on a high-bit rate, long range single-carrier transmission can be replaced by a much simpler equalization procedure in the frequency domain with a multicarrier signal. Indeed, the equalization can be done with a single-tap filter, i.e., by simply multiplying the data on each subcarrier by a complex number representing the inverse of the channel's frequency response. Actually, the presence of the IFFT and FFT blocks on the OFDM transmission chain renders FDE quite an intuitive approach.

3.5.4.1 Zero Forcing Equalization

The equalization procedure that is adopted in our experimental works is very simple and holds up to two suppositions: i) the receiver has full awareness of the transmitted data and ii) the channel does not vary in time.

While in wireless transmissions the time variations of the channel frequency response are related to the velocity of the mobile device (Doppler frequency effect) [81], in our case they come from the frequency mismatch in the converter's sampling ratio and the central carrier's frequency. The time-invariance assumption is then only valid thanks to a previous SFC/CFO estimation and correction stage in our demodulation block (see subsection 3.5.3). In addition, since the channel is considered to be flat over the reduced frequency span occupied by each subcarrier, the symbols can be easily equalized in the frequency domain with an array of complex coefficients, one per subcarrier, representing the inverse of the channel's frequency response. The time-invariance of the channel also allows all acquired symbols to be corrected with the same set of coefficients.

Given that the receiver knows which symbols X_k have been sent in the transmission, the simplest approach that comes to mind for estimating the channel's frequency response on each subcarrier k from the received symbols Y_k is:

$$H_k^{ZF-LE} = \frac{Y_k}{X_k} \tag{3.41}$$

This is known as the Zero-Forcing (ZF) or Least Square (LS) estimator [82]. Despite its simplicity, the great disadvantage of such approach is the fact that it ignores the channel's noise term $\tilde{n_k} = n_k/X_k$. Indeed, we have seen in section 3.3.5 that the received signal could be expressed as $Y_k = H_k X_k + n_k$ thanks to the use of a cyclic extension. This means that whenever the subcarrier's SNR is low, the ZF equalizer will not only revert the channel's frequency response but will also amplify the noise component. In [42], the authors demonstrate, however, that the noise can be averaged down and the ZF channel estimation can be considerably enhanced by taking the mean of H_k^{ZF} over several training symbols.

Figures 3.27(a) shows an example of ZF channel estimation in the optical back-to-back configuration. Each red point represents one estimation with a specific training symbol and the blue line is the averaged estimation. The low and high frequency arrows highlight the different noise levels on the signal's bandwidth ($5GHz$).

Since we have already corrected the time-domain variation of the received constellations caused by SFO and STO, we may assume that the "colored" noise that we see in Figure 3.27(a) is actually arriving from the components used in our chain. Notice that the notion of frequency-dependent noise applies for the signal as a whole but each subcarrier individually witnesses a white Gaussian noise channel. Figure 3.27(b) shows the equalized constellation.

The equalization procedure in 3.41 uses a set of training symbols to deduce the channel frequency response and is referred to as Linear Equalization (LE). Other structures however exist such as the Decision Feedback Equalizer (DFE), which instead of using a known sequence of symbols, estimates the channel frequency response using a reference $\hat{Y_k}$ taken after a decision (demapping) on the received constellations. For each subcarrier k:

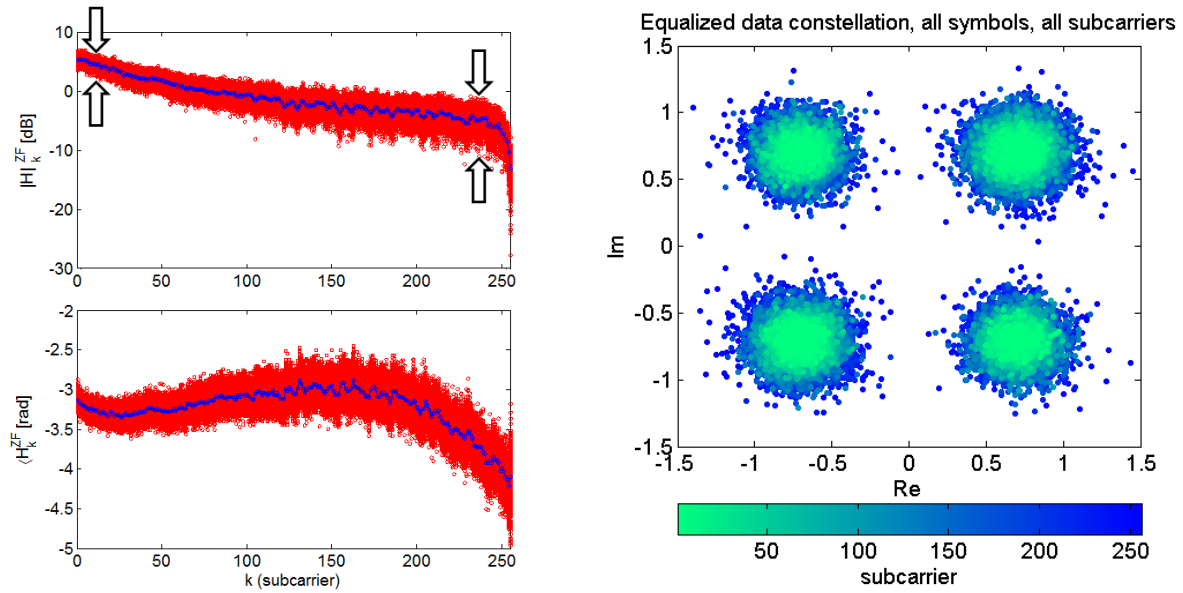

(a) (b)

Figure 3.27: (a) Example of ZF channel frequency response estimation. (b) Example of constellation after equalization.

$$H_k^{ZF-DFE} = \frac{Y_k}{\hat{Y}_k} \tag{3.42}$$

The great disadvantage of the DFE is the error propagation in case of a wrong decision made from Y_k [83, 84].

After the equalization, the estimated noise variance can be easily found from the mean of the error over the N_S equalized transmitted OFDM symbols:

$$\sigma_k^2 = \frac{1}{N_S} \sum_{l=1}^{N_S} |Y_{lk} - X_{lk} H_k|^2 \tag{3.43}$$

Assuming that the noise distribution on each subcarrier is Gaussian, σ_k^2 has to be averaged over at least 269 symbols in order to provide a good estimation [69].

3.5.4.2 Other Equalization Criteria

Other approaches more performing than ZF exist. Actually, the ZF is optimized to minimize ISI but ignores the noise on the channel [69]. In the Minimum Mean-Square Error estimator (MMSE), the channel coefficients are chosen so that the noise variance of the subcarrier set is minimized. It supposes however that the noise power density and the channel's correlation function are known variables [42, 82].

We may also mention the maximum likelihood criteria (ML), which contrary to the other approaches truly aims to maximize the probability of correct decisions on the received symbols [69]. We should note however that, strictly speaking, the ML is basically a sequence estimation solution and not a conventional equalizer.

In addition, some interesting algorithms exist that address the case of a channel whose frequency response varies in time. They are able to track down the changes in the channel conditions and adapt the equalizer coefficients accordingly. We can mention for instance the Least Mean Square (LMS) or the Recursive Least Squares (RLS or Kalman/Godard) approaches, which can be used either with the help of a set of training symbols or in a decision directed

fashion. Blind adaptation can also be adopted and in this case the equalizer is optimized based on the statistics of the received data. Note that in our experiments, these approaches could have been used to correct at the same time the channel's frequency response and the changes caused by SFO, CFO and STO provided that the algorithm's adaptation pace was fast enough to track down the variations of the channel in time.

Another benefit of the adaptive approaches is that they can also be used to infer the channel coefficients without necessarily dealing with closed-form equations such as the ones used for instance with the ZF or MMSE equalizers. For example, let us consider the training sequence-based LMS approach. The LMS algorithm can be implemented by means of an initial estimation of the equalization coefficients per subcarrier $G_{0,l}$ that is iteratively updated on a symbol-by-symbol basis so that the error $e_{l,k}$ between the transmitted sequence and the equalized symbols is minimized. The update of the channel coefficients is characterized by a weight factor μ that states its speed of convergence and the quality of the estimation:

$$\begin{aligned} e_{l,k} &= X_{l,k} - G_{l,k}Y_{l,k} \\ G_{l+1,k} &= G_{l,k} + \mu X^*_{l,k} e_{l,k} \end{aligned} \tag{3.44}$$

Figures 3.28(a) and (b) show respectively the LMS block diagram and the convergence of the mean squared error of the equalized data with different weight factors. $G_{0,l}$ was set to 1 for all subcarriers. The user is referred to [69] for a very detailed explanation of different equalization approaches.

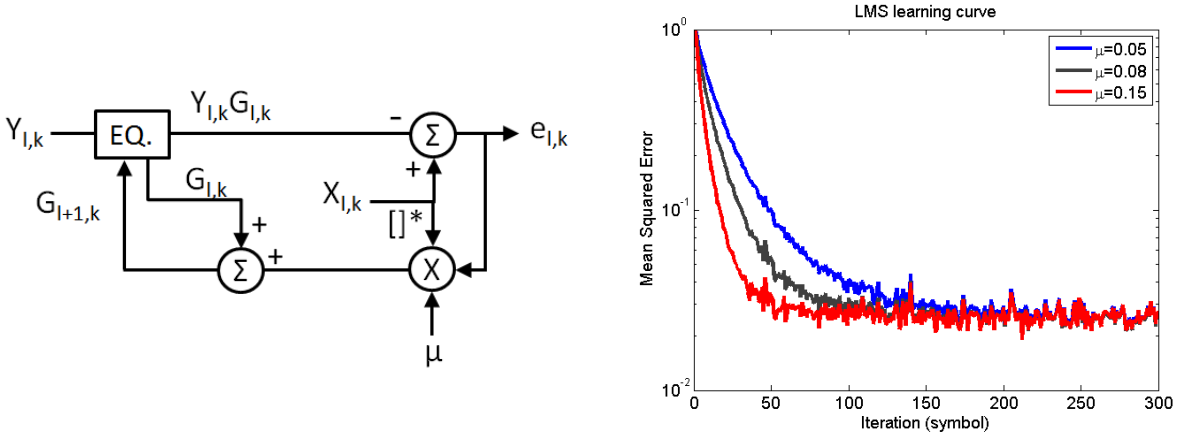

(a) (b)

Figure 3.28: (a) Training sequence-based LMS block diagram. (b) Convergence of channel coefficients with different values of μ.

3.5.4.3 SC-FDE vs OFDM

In some reports, the use of single carrier transmissions with frequency domain equalization (SC-FDE) has been identified as an alternative to OFDM due to its better performances in terms of peak-to-average power ratio and sensibility to time and frequency synchronization issues. Indeed, if implemented with appropriate cyclic prefixing, the SC-FDE should not show higher complexity than a typical OFDM transmission block; the single difference between these approaches is that in SC-FDE the IFFT is placed at the receiver side [29].

However, OFDM has one huge advantage if compared to SC-FDE which is being capable of providing an extra dimension in terms of sharing of the resources of the network between several users. Indeed, the sub-wavelength granularity allowed by OFDM's subcarrier sharing capability can be very interesting in point-to-multipoint architectures, as we will see in section

3.8. For more details on SC-FDE, please refer to [85, 86]. A good comparison between SC-FDE and OFDM regarding their sensitivities to CFO, SFO and IQ imbalance can be found in [87].

3.6 Transmission Performance Metrics

Before proceeding to the presentation of some bit and power loading algorithms, let us take a moment to recap on the performance parameters that can be used to evaluate an OFDM transmission. Besides the typical bit error rate (BER), other indicators may be extremely useful to evaluate the channel impacts on each subcarrier, namely the symbol error rate (SER), the error vector magnitude (EVM) and the signal to noise ratio (SNR). The relations provided in this section are based on two conditions:

1. the number of transmitted symbols is much higher than the alphabet of the constellations, i.e., $N_s \gg 2^{b_k}$ and
2. the noise distribution is supposed Gaussian on each subcarrier.

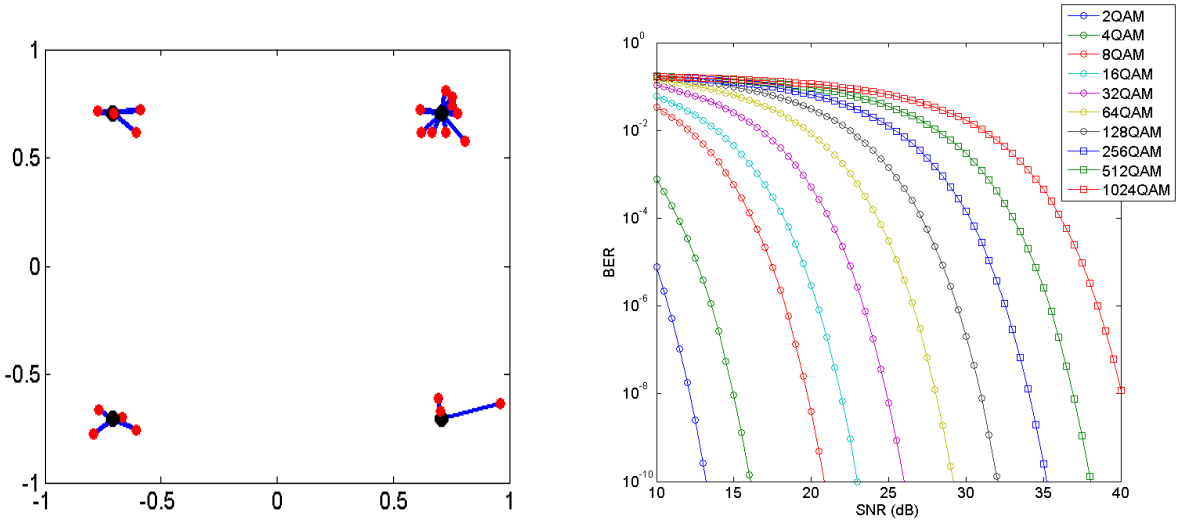

(a) (b)

Figure 3.29: (a) Examples of error vectors. (b) BER evolution with SNR for squared gray-coded QAM constellations and BPSK.

EVM is a measurement of the distance between a received symbol and its expected position and quantifies the spreading of the symbols around the ideal constellation points. Figure 3.29(a) shows an example with several error vectors (blue lines) on a QPSK constellation connecting the received symbols (red circles) to the transmitted symbols (black circles). To facilitate the calculation of EVM, we normalize the constellations so that the mean square amplitude (energy) of any mapping alphabet equals one. Table 3.5 shows the normalization coefficients (nc) for different constellations. The EVM is defined as the root-mean-square (RMS) value of the difference between received and expected symbols and is averaged over a group of symbols larger than the constellation alphabet. It is given as a percentage of the average power per symbol of the constellation:

$$EVM_{k,\%}^{RMS} = 100\sqrt{\frac{1}{p_k N_s}\sum_{l=1}^{N_s} n_{Q,l}^2 + n_{I,l}^2} \tag{3.45}$$

where $n_{Q,l}$ and $n_{I,l}$ are the normalized noise quadrature and in-phase components of the symbol l in subcarrier k given by the difference between received and reference symbols and p_k is the power

Constellation	b (bits/symbol)	nc
BPSK	1	1
QPSK	2	$\sqrt{2}$
cross 8QAM	3	$\sqrt{6}$
16QAM	4	$\sqrt{10}$
cross 32QAM	5	$\sqrt{20}$
64QAM	6	$\sqrt{42}$
cross 128QAM	7	$\sqrt{82}$
256QAM	8	$\sqrt{170}$
cross 512QAM	9	$\sqrt{330}$
1024QAM	10	$\sqrt{682}$

Table 3.5: Normalization coefficients for different constellations.

of the normalized ideal constellation [88]. The reader should notice that the EVM measurement also depends on whether the reference symbols are the real transmitted symbols, in which case the calculation is referred to as data-aided, or the symbols after demapping, in which case the calculation is nondata-aided. Whilst the second method is generally used in real-world receivers it may represent a rather optimistic evaluation.

Indeed, for very noisy channels, the EVM calculation based on a demapped version of the received symbols may lead to associating it to a wrong reference which is closer to the received symbol than the real transmitted symbol. In [89], the authors demonstrate that both methods can be used to infer about the system's BER for BER values as low as 10^{-2} in AWGN channels using mappings up to 64QAM. Despite the fact that we have implemented both approaches in our transmission chain, we hold on to the data-aided solution.

The SNR can be directly found from the EVM with:

$$SNR_{k,dB} \approx 10\log_{10}\left(\frac{1}{\left(\frac{EVM_{k,\%}^{RMS}}{100}\right)^2}\right) \tag{3.46}$$

and the BER for the squared, Gray coded QAM constellations can also be derived [88]:

$$\begin{aligned} BER_k \cong \tfrac{2}{b_k}\left(1-\tfrac{1}{\sqrt{2^{b_k}}}\right) erfc\left(\frac{1}{\left(\frac{EVM_{k,\%}^{RMS}}{100}\right)}\sqrt{\frac{3}{2\left(2^{b_k}-1\right)}}\right) = \\ \tfrac{4}{b_k}\left(1-\tfrac{1}{\sqrt{2^{b_k}}}\right) Q\left(\frac{1}{\left(\frac{EVM_{k,\%}^{RMS}}{100}\right)}\sqrt{\frac{3}{\left(2^{b_k}-1\right)}}\right), \quad b_k = 2,4,6,... \end{aligned} \tag{3.47}$$

with $Q(x)$ being the tail probability function of the Gaussian distribution and $erfc(x)$ the complementary error function, also know as the complementary Gauss error function. $Q(x)$ and $erfc(x)$ are defined as:

$$Q(x) = \frac{1}{\sqrt{2\pi}}\int_x^\infty e^{-\frac{u^2}{2}}du \tag{3.48}$$

$$erfc(x) = \frac{2}{\sqrt{\pi}}\int_x^\infty e^{-u^2}du \tag{3.49}$$

and related through:

$$\begin{array}{lll} Q(x) = \frac{1}{2} erfc\left(\frac{x}{\sqrt{2}}\right) & , & Q^{-1}(x) = -\sqrt{2} erfc^{-1}(2x) \\ erfc\left(\frac{x}{2}\right) = 2Q\left(\frac{x}{\sqrt{2}}\right) & , & erfc^{-1}(x) = -\frac{1}{\sqrt{2}} Q^{-1}\left(\frac{x}{2}\right) \end{array} \tag{3.50}$$

We should remark that equation 3.47 supposes that one symbol error caused by the noise will translate into only 1 out of b_k erroneous bit. This assumption is only true if the constellation is Gray mapped and if the subcarriers' SNR is high enough to avoid any event of a symbol error generating two or more erroneous bits, in which case we have[7]:

$$SER_k \approx b_k BER_k \tag{3.51}$$

For the BPSK mapping, the BER can be trivially described by:

$$BER_k = \frac{1}{2} erfc\left(\frac{1}{\left(\frac{EVM_{k,\%}^{RMS}}{100}\right)}\right),\ b_k = 1 \tag{3.52}$$

The SER variation with the EVM can be directly found with 3.51:

$$SER_k = 2\left(1 - \frac{1}{\sqrt{2^{b_k}}}\right) erfc\left(\frac{1}{\left(\frac{EVM_{k,\%}^{RMS}}{100}\right)}\sqrt{\frac{3}{2\left(2^{b_k}-1\right)}}\right),\ b_k = 2,4,6,... \tag{3.53}$$

For the BPSK, $SER_k = BER_k$, as expected. Equation 3.53 can be approximated by [90, 91]:

$$SER_k \cong 4Q\left(\sqrt{\frac{3SNR_{k,linear}}{\left(2^{b_k}-1\right)}}\right) = 2erfc\left(\sqrt{\frac{3SNR_{k,linear}}{2\left(2^{b_k}-1\right)}}\right) \tag{3.54}$$

The reader will find in [92] more precise equations relating the BER and SER with the SNR for squared and rectangular QAM constellations as well as the equivalent formulae for the M-PSK mapping. Other approximations considering a Gray mapped constellation over an AWGN channel can also be found in [93, 94].

Up to this point, we have supposed squared M-QAM constellations for all performance parameters. An equivalent analysis for the cross M-QAM constellations is therefore necessary. In [31, 95] the authors propose an approximate expression for the BER calculation:

$$BER_k = \frac{G_p\left(4 - \frac{6}{\sqrt{2^{b_k+1}}}\right)}{2b_k} erfc\left(\frac{d}{\sqrt{N_0}}\right),\ b_k = 5,7,9,... \tag{3.55}$$

where G_p is the Gray penalty (see section 3.3.3), $2d$ is the minimum distance between adjacent symbols in the constellation and $N_0/2$ is the two-sided noise power spectral density. In [95], the authors derive the exact BER computation for cross M-QAM constellations which is further extended to Rayleigh channels. The equations of the BER are found with an intricate bit-per-bit error calculation.

A simpler relation is given though in [69] for both square and cross QAM constellations:

$$SER_k = 2\left(1 - \frac{1}{2\left\lceil 2^{\frac{b_k}{2}-1}\right\rceil}\right) erfc\left(\sqrt{\frac{SNR_{k,linear}}{P}}\right) \tag{3.56}$$

[7]The energy per bit-to-noise power-spectral-density ratio E_b/N_0 is related to the energy per symbol-to-noise power-spectral-density ratio E_s/N_0 through $E_s/N_0 = log_2(M)E_b/N_0$.

with P being the average symbol power of the constellation. The values of P can be found from nc in Table 3.5 through:

$$P = nc^2 \tag{3.57}$$

Again, if we assume that 3.51 is true, then:

$$BER_k = \frac{2}{b_k}\left(1 - \frac{1}{2\left\lceil 2^{\left(\frac{b_k}{2}-1\right)}\right\rceil}\right) erfc\left(\sqrt{\frac{SNR_{k,linear}}{P}}\right) \tag{3.58}$$

For matters of simplicity, in this work we assume that the equations ruling the squared M-QAM constellations are also valid for the cross M-QAM constellations. By making this assumption, we find practically the same results as with 3.58 and the estimated BER from the measured EVM converge pretty well to the real measured BER after demapping of the symbols. Figure 3.29(b) shows the evolution of the BER with the SNR for different constellations.

The reader will find in [96] an exact expression for the star-16QAM. In [97], the authors claim a general algorithm that yields to the exact BER and SER calculations for arbitrary sets of symbols in a constellation and arbitrary bit-to-symbol mapping in AWGN channels.

3.7 Adaptively-Modulated OFDM

We have seen that a huge gain in terms of spectral efficiency could be provided by OFDM compared to ordinary FDM thanks to the orthogonality principle. Actually, the transmission's spectral efficiency can be further optimized thanks to the use of adaptive algorithms with which the mapping and power of each subcarrier can be individually optimized according to the channel characteristics.

Since the optical channel is considered to slowly vary in time, the great interest of the bit and power loading algorithms is that they allow a considerable gain in terms of performance vis-a-vis the selective frequency response of the IMDD optical channel. Indeed, not only they enable privileging frequency spans that are more favorable to the transmission but they also avoid that the subcarriers that are submitted to a worst SNR degrade the overall performance of the signal. In this section, we focus on the rate and margin adaptive bit and power loading solutions.

3.7.1 SNR Gap to Capacity

According to the Shanon-Hartley theorem [98–100], the channel capacity C, i.e., the maximum amount of error-free information that can be transmitted with infinite complexity, can be defined as:

$$C = \log_2(1 + SNR) \tag{3.59}$$

If we isolate b_k in 3.54, we will find:

$$b_k = \log_2(M) = \log_2\left(1 + \frac{SNR_{k,linear}}{\frac{1}{3}\left[Q^{-1}\left(\frac{SER_k}{4}\right)\right]^2}\right) = \log_2\left(1 + \frac{SNR_{k,linear}}{\frac{2}{3}\left[erfc^{-1}\left(\frac{SER_k}{2}\right)\right]^2}\right) \tag{3.60}$$

If we define a new variable Γ_k:

$$\Gamma_k = \frac{1}{3}\left[Q^{-1}\left(\frac{SER_k}{4}\right)\right]^2 = \frac{2}{3}\left[erfc^{-1}\left(\frac{SER_k}{2}\right)\right]^2 \tag{3.61}$$

then:

$$b_k = \log_2\left(1 + \frac{SNR_k}{\Gamma_k}\right) \tag{3.62}$$

which is very similar to 3.59. Γ_k is called the SNR gap to capacity of subcarrier k and can be though of as a penalty associated to a specific SER that avoids the transmission of reaching a perfect error-free regime in which $log_2\left(1 + SNR_k\right)$ ($\Gamma_k = 1$ or 0dB) bits are transmitted per subcarrier with infinite complexity.

Indeed, forward error correcting codes (FEC) can be used to reduce this gap and thus increase the target pre-FEC bit error rate allowed in a transmission. Some very powerful codes are able to reach a gap of about $0,7dB$ [101] but the price to be payed is a reduction in the net bit-rate of the system.

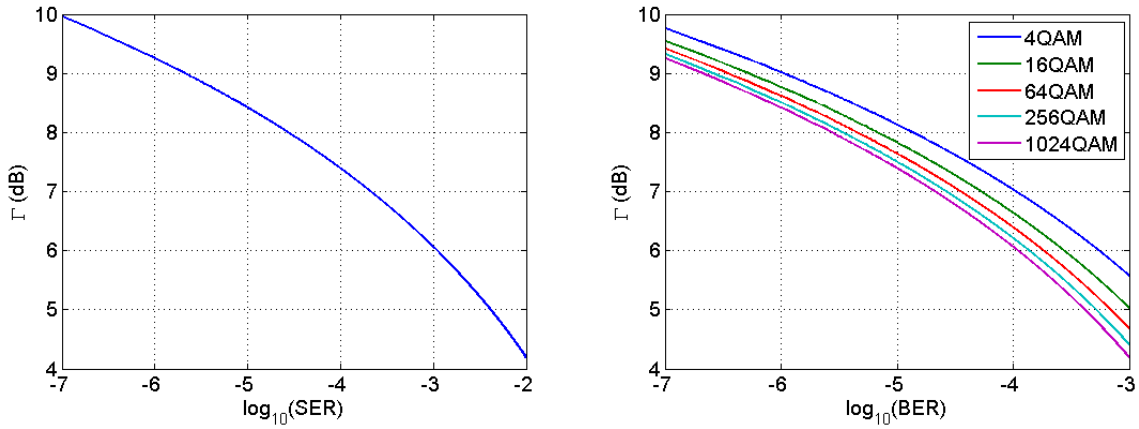

(a) (b)

Figure 3.30: (a) Gap variation with SER. (b) Gap variation with BER.

Figures 3.30 (a) and (b) show respectively the gap variation with the SER and BER adopting the simplification in 3.51. We should remember that this relation is only valid for squared Gray-mapped QAM constellations whose SNR is high enough to avoid more than one erroneous bit per erroneous symbol.

In [102] the authors consider an approximation in which a fixed value of Γ_k per BER (and not SER) is considered to simplify the analysis so that $\Gamma_k = \Gamma$. Table 3.6 shows some of these values. Note that in this case we are neglecting that fact that the gap variation with the BER depends on the mapping scheme and that the relations between gap and BER for cross constellations are different from those used with square constellations. In [90], an approximation for the gap is derived for M-PSK.

3.7.2 The Water-filling Solution

The SNR of each subcarrier can be defined as:

$$SNR_k = g_k\varepsilon_k = \frac{|H_k|^2\varepsilon_k}{\sigma_k^2} \tag{3.63}$$

where $g_k = \frac{|H_k|^2}{\sigma_k^2}$ is the channel's gain coefficient, ε_k is the energy of each subcarrier, $|H_k|$ is the absolute value of the channel's frequency response and σ_k^2 is the noise variance.

$\log_{10}(BER)$	$\Gamma(dB)$
-7	9.5
-6	8.8
-5	7.8
-4	6.6
-3	5.0

Table 3.6: Approximated SNR gap to capacity values for different BER

The loading algorithms were developed to determine the group of values of b_k and ε_k based on an initial set of constraints. Basically, they can be divided into two dual approaches:

- Rate Adaptive (RA) algorithms, which search to maximize the amount of transmitted bits subject to a total available energy constraint:

$$\begin{aligned} max \quad & \sum_{k=1}^{N_D} b_k \\ s.t. \quad & \sum_{k=1}^{N_D} \varepsilon_k = E \end{aligned} \tag{3.64}$$

- Margin Adaptive (MA) algorithms, which search to minimize the amount of transmitted energy subject to a fixed bit-rate constraint:

$$\begin{aligned} min \quad & \sum_{k=1}^{N_D} \varepsilon_k \\ s.t. \quad & \sum_{k=1}^{N_D} b_k = R \end{aligned} \tag{3.65}$$

Both RA and MA algorithms consist of solving a convex optimization problem for which there exists an optimal solution. They start by defining the problems using the Lagrange multipliers method[8] an the relation shown in 3.62:

$$\mathcal{L}_{RA}(\varepsilon_k, \lambda_{RA}) = \sum_{k=1}^{N_D} b_k + \lambda_{RA}\left(\sum_{k=1}^{N_D} \varepsilon_k - E\right) = \sum_{k=1}^{N_D} log_2\left(1 + \frac{g_k \varepsilon_k}{\Gamma}\right) + \lambda_{RA}\left(\sum_{k=1}^{N_D} \varepsilon_k - E\right) \tag{3.66}$$

$$\mathcal{L}_{MA}(\varepsilon_k, \lambda_{MA}) = \sum_{k=1}^{N_D} \varepsilon_k + \lambda_{MA}\left(\sum_{k=1}^{N_D} b_k - R\right) = \sum_{k=1}^{N_D} \varepsilon_k + \lambda_{MA}\left(\sum_{k=1}^{N_D} \log_2\left(1 + \frac{g_k \varepsilon_k}{\Gamma}\right) - R\right) \tag{3.67}$$

where $\mathcal{L}_{RA}(\varepsilon_k, \lambda_{RA})$ and $\mathcal{L}_{MA}(\varepsilon_k, \lambda_{MA})$ are the RA and MA Lagrange functions and λ_{RA} and λ_{MA} are the RA and MA Lagrange multipliers respectively. If the solution of the problem is a maximum (minimum) for the original constrained problem, then there exists a $\lambda_{RA}(\lambda_{MA})$ such that $\varepsilon_k, \lambda_{RA}$ $(\varepsilon_k, \lambda_{MA})$ is a stationary point for the Lagrange function $\mathcal{L}_{RA}$ $(\mathcal{L}_{MA})$. In other words, the gradient of $\mathcal{L}_{RA}$ $(\mathcal{L}_{MA})$ in those points should be zero:

$$\nabla \mathcal{L}_{RA/MA}(\varepsilon_k, \lambda_{RA/MA}) = 0 \tag{3.68}$$

The partial derivatives in $\lambda_{RA/MA}$ will give the initial RA/MA constraints:

$$\sum_{k=1}^{N_D} \varepsilon_k - E = 0 \tag{3.69}$$

[8]The reader is referred to [103] for an intuitive and detailed analysis of the Lagrange multiplier optimization method.

$$\sum_{k=1}^{N_D} b_k - R = 0 \tag{3.70}$$

If we remember that $\ln(x) = \log_2(x)\ln(2)$ and if we assume that the symbol period is fixed, it is possible to deduce that:

$$\frac{\partial \mathcal{L}_{RA}(\varepsilon_k, \lambda_{RA})}{\partial \varepsilon_k} = 0 \therefore \frac{\Gamma}{g_k} + \varepsilon_k = -\frac{1}{\lambda_{RA}\ln(2)} = constant \tag{3.71}$$

$$\frac{\partial \mathcal{L}_{MA}(\varepsilon_k, \lambda_{MA})}{\partial \varepsilon_k} = 0 \therefore \frac{\Gamma}{g_k} + \varepsilon_k = -\frac{\lambda_{MA}}{\ln(2)} = constant \tag{3.72}$$

Meaning that in both problems, the solution will take the form of:

$$\frac{\Gamma}{g_k} + \varepsilon_k = K = constant \tag{3.73}$$

Equation 3.73 is also known as the "water-filling" (WF) solution. Indeed, the analogy is clearer when we represent Γ/g_k and ε_k as in Figure 3.31 and imagine the curve of the inverted signal-to-noise ratio as a bowl being filled with energy (water) to a constant line [102, 104]. The water-filling algorithms are also known as "greedy algorithms" [105] since they consist of allocating more energy (more bits) to the subcarriers with a better channel gain and less energy (less bits) to the subcarriers with a worst channel gain. In general, the principle can be resumed by this very interesting metaphor presented in [104] in which it is compared to "a tax collector taking money and reapportioning it to those who can best use it to improve the collective good of all".

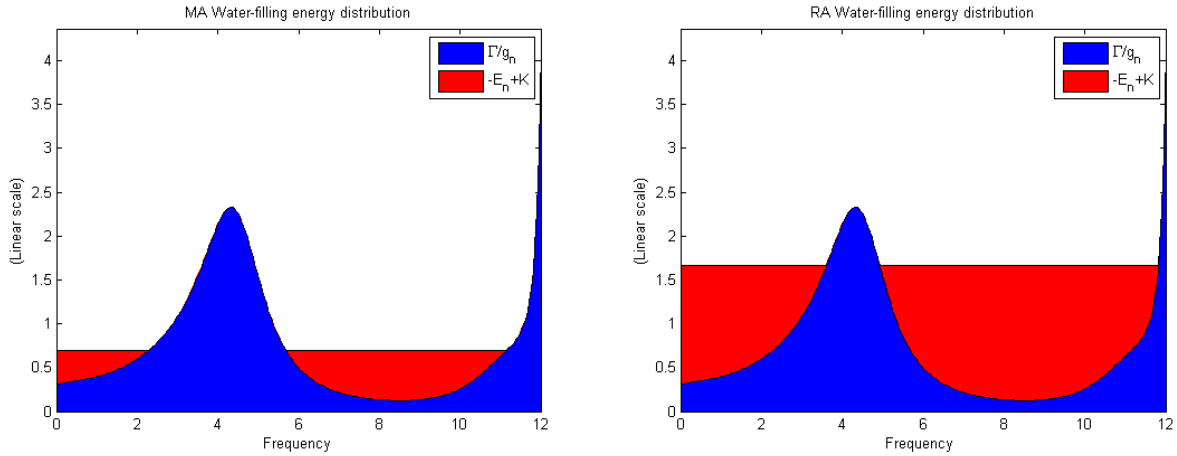

(a) (b)

Figure 3.31: (a) MA water-filling solution. (b) RA water-filling solution..

The algorithms for retrieving the solution of equations 3.73 and 3.69 (or 3.70) are discussed in details in [102, 104]. Basically, there are two ways of solving the set of N_D+1 linear equations: either by matrix inversion or by recursively changing the number of used subcarriers until the all values of ε_k are non-negative. The computational complexity of the last approach is directly related to the required sorting procedure of the channel coefficients.

Figures 3.32(a) and (b) show respectively an example of the MA and RA bit and power distribution per subcarrier according to the water-filling solution. The channel frequency response was generated using the IM+PM+FM IMDD model proposed in section 2.5 which was then

adapted with a low-pass filter corresponding to the roll-off of one of the laser/photodiode couples used in our experimental work. SSMF length is $40km$ and the laser's wavelength and chirp parameters α and f_c are respectively $1544nm$, 2.8 and $2.1GHz$. Fiber dispersion coefficient is $D = 16.7ps/km - nm$. The noise variance of 0.1 is constant over the $12GHz$ bandwidth of the signal and $\Gamma = 5dB$. The mean constellation powers have been normalized to the unity. The target bit-rate for the MA approach is $10Gb/s$ and $N_D = 255$.

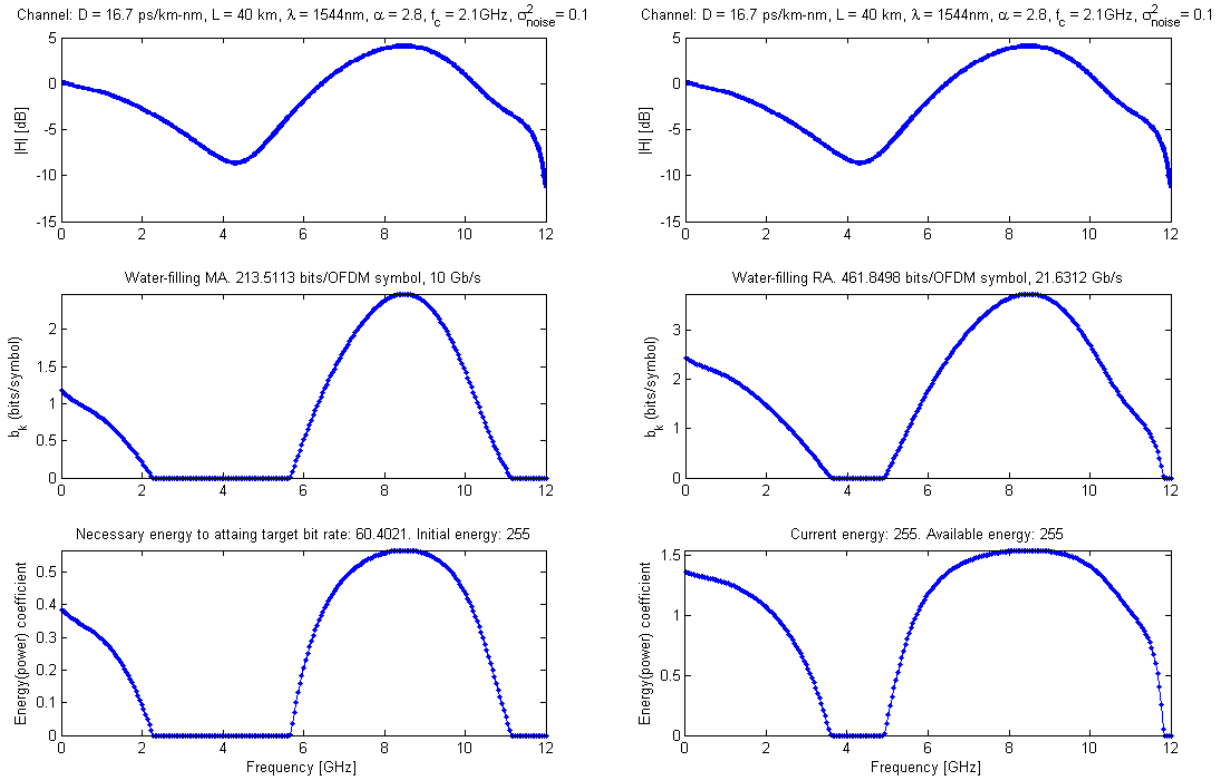

(a) (b)

Figure 3.32: Water-filling (a) MA and (b) RA bit and power distribution.

3.7.3 Loading Algorithms with Integer b_k

As we have seen in the previous subsection, the optimal solution of the water-filling RA and MA algorithms may produce any $b_n \in \mathbb{R}$ and this can complicate the implementation of the OFDM encoder and decoder [102, 104]. Alternative quasi-optimal loading algorithms have been conceived to address this issue by constraining b_k to integer values. In this section, we will discuss six of these algorithms: Levin-Campello's and Chow's classical RA and MA and other RA and MA solution developed by us.

3.7.3.1 Chow's bit and power loading algorithm

In early 90's, P. Chow demonstrated that an ON/OFF energy distribution, whenever used in the same or nearly the same frequency bands as the water-filling solution, would allow approximating the optimal water-filling results. From this discovery, he conceived the first step (Chow's Primer) of his bit and power loading algorithm which is used in both his RA and MA approaches. After

Chow's Primer, the group of subcarriers will contain non-integer b_k. This issue is solved at a second step by rounding b_k and correspondingly adapting ε_k.

More details on Chow's algorithm implementation can be found in [102, 104, 106]. Figure 3.33 shows a typical set of results after the first and second steps of Chow's MA and RA approaches. The parameters are the same as the ones presented in Figure 3.32 and the granularity β of the allowed constellations is $1bit/symbol$.

Note that the saw-tooth profile of the energy coefficients is a direct consequence of assigning the same mapping to subcarriers with different channel gains. Indeed, in order to attain the same BER performances over a group of subcarriers with the same mapping, the channel variations should be compensated with an adequate energy coefficient. Note also that the resulting needed energy and bit-rate of Chow's MA and RA solutions approximate very well the optimal WF results shown in Figure 3.32.

3.7.3.2 Levin-Campello's bit and power loading algorithm

Another very interesting bit and power loading algorithm is the one proposed by J. Campello and H. Levin. Levin-Campello's algorithm (LCA) basic concept is that any additional information should be transported in the subcarrier that would require the least "effort" to do so. Such effort is translated as incremental and decremental energies e_k^+ and e_k^-:

$$e_k^+ = \varepsilon_k(b_k + \beta) - \varepsilon_k(b_k) = \frac{\Gamma}{g_k} 2^{b_k+\beta} \left(1 - 2^{-\beta}\right) \tag{3.74}$$

$$e_k^- = \varepsilon_k(b_k) - \varepsilon_k(b_k - \beta) = \frac{\Gamma}{g_k} 2^{b_k} \left(1 - 2^{-\beta}\right) \tag{3.75}$$

Similarly to Chow's algorithm, LCA MA and RA approaches also share a common first step, known as "Efficientizing". Starting from any group of b_k, a bit-distribution is said to be efficient when there is no movement of a bit from one subcarrier to another that reduces the total energy $\sum \varepsilon_k$ of the OFDM symbol. LCA's Efficientizing step replaces one bit-distribution with another closer to the efficient through single-information unit changes between subcarriers [102] until no more changes can be done.

Figure 3.34(a) shows the bit and power distribution after LCA Efficientizing for the example presented in section 3.7 and starting from a QPSK mapping ($b_k = 2$) over all subcarriers. Note that at the end of this step, the efficient energy distribution won't necessarily be the same as the one imposed by the RA energy constraint. Equivalently, the associated bit-rate won't necessarily be the same as the one imposed by the MA bit-rate constraint. Note also that the amount of bits per OFDM symbol hasn't changed; indeed, those bits have just been allocated differently through the subcarriers.

An additional step is then necessary in order to adapt the total OFDM symbol bit-rate (energy) to the MA's (RA's) constraint. The second step of LCA is known as "B-tight" for the MA approach and "E-tight" for the RA approach. E-tightness implies that no additional unit of information can be carried by the OFDM signal without violating the total energy constraint. Equivalently, B-tightness will change the allocation of bits per subcarrier until the bit-rate constraint is satisfied. Figures 3.34(b) and (c) show respectively the final LCA MA and RA results after B-tightness and E-tightness of the bit distribution. More details on the implementation of the LCA can be found in [42, 102, 104].

3.7.3.3 Our own adaptive algorithm (LA-RA/LA-MA)

Until now, we have considered an approximation in which the gap parameter for a specific BER is fixed independently of the mapping that is used. Here, we propose a more precise analysis in which the gap is chosen individually for each subcarrier according to its SNR. In order to

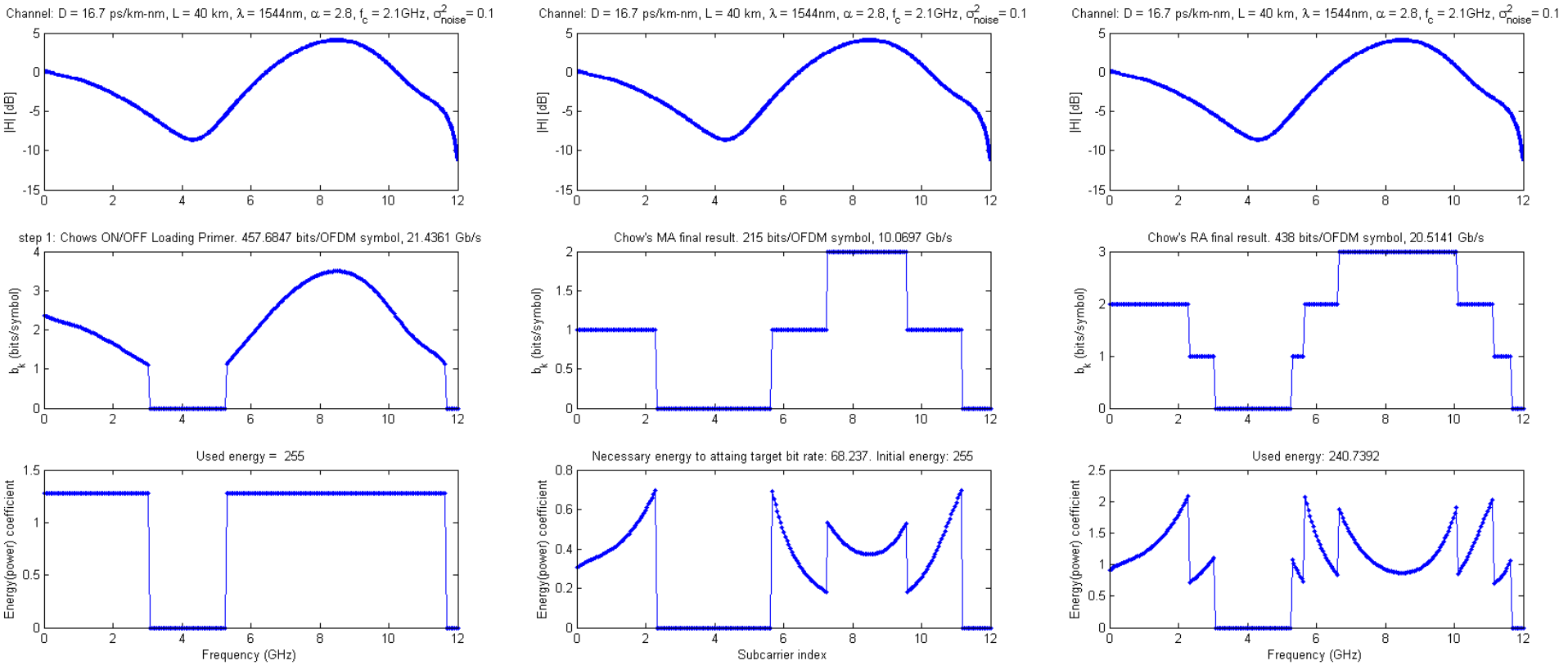

(a) (b) (c)

Figure 3.33: (a) Bit and power distribution after Chow's Primer. (b) Chow's MA final result. (c) Chow's RA final result.

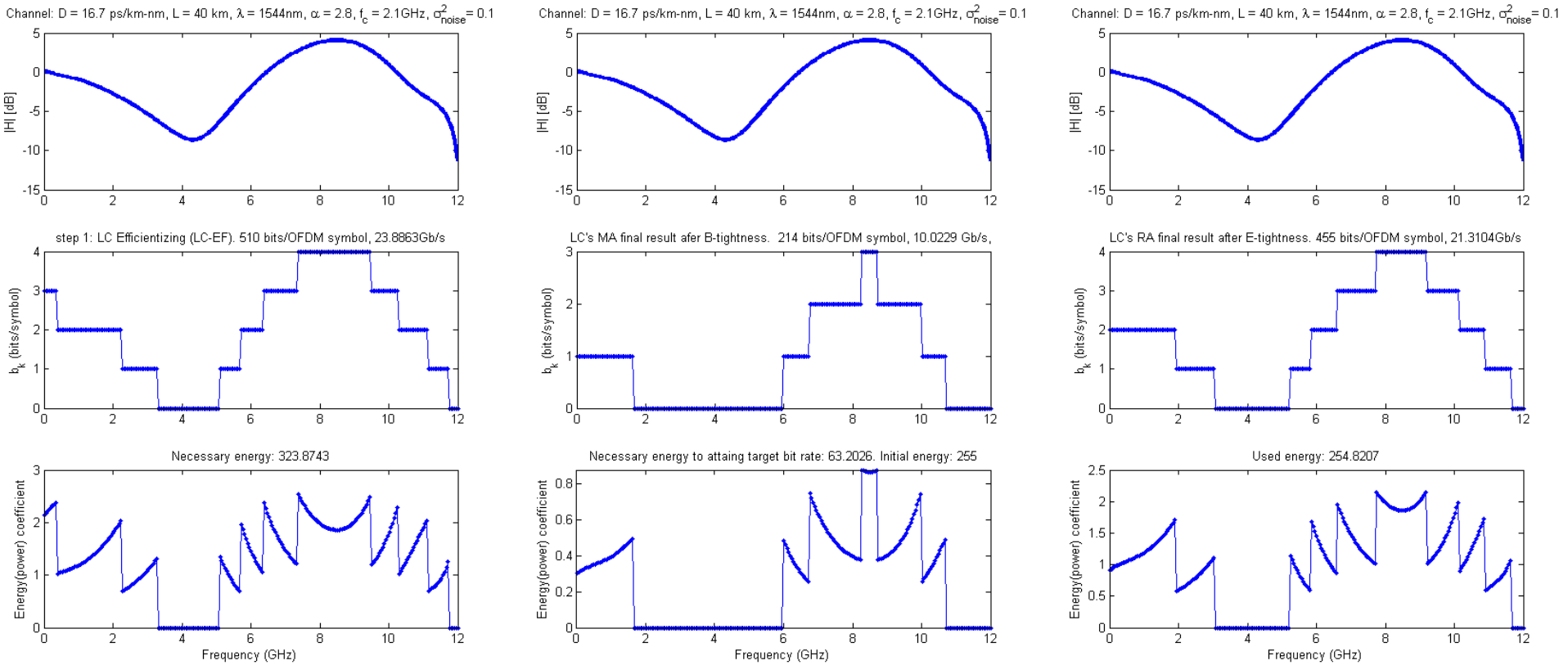

(a) (b) (c)

Figure 3.34: (a) Bit and power distribution after LCA Efficientizing. (b) LCA's MA final result. (c) LCA's RA final result.

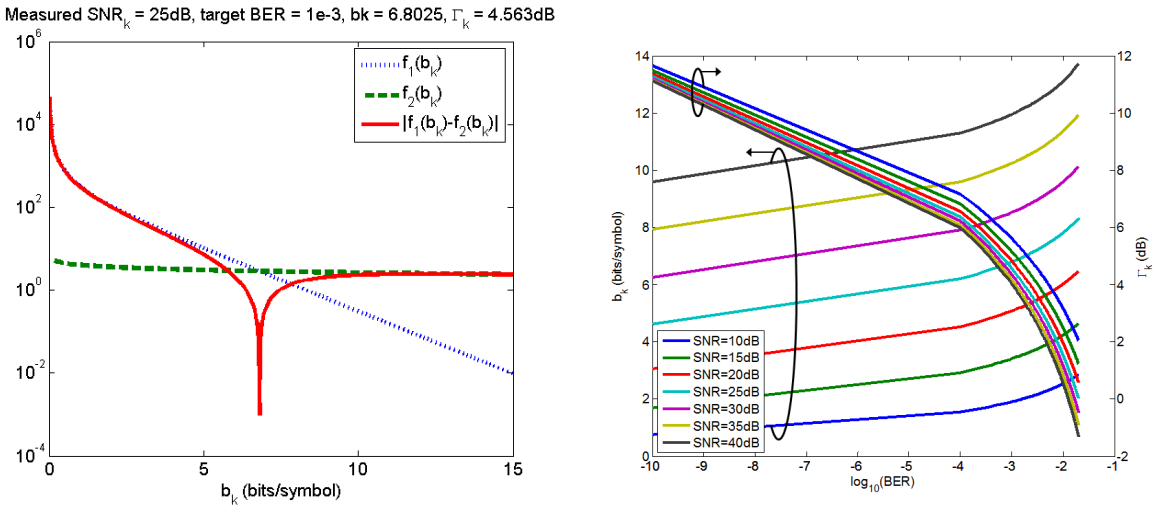

(a) (b)

Figure 3.35: (a) Example showing $f_1(b_k)$, $f_2(b_k)$ and $f_3(b_k)$. (b) Variation of Γ_k and b_k with the target BER with different values of SNR.

facilitate the identification of our solution when comparing it to other approaches, let us call the algorithm "LA", for the author's initials.

Let us isolate Γ_k in 3.62 and recall 3.61 :

$$\Gamma_k = f_1(b_k) = \frac{SNR_k}{2^{b_k} - 1} \tag{3.76}$$

$$\Gamma_k = f_2(b_k) = \frac{2}{3}\left(erfc^{-1}\left(\frac{BER_k b_k}{2}\right)\right)^2 \tag{3.77}$$

Notice that we are still considering the approximation in which we use of the square constellation relation to all constellations. Also, we are supposing Gray mapped symbols with a high enough SNR (see section 3.6). If we define:

$$f_3(b_k) = |f_1(b_k) - f_2(b_k)| \tag{3.78}$$

then we can find the exact value of Γ_k and b_k for a specific SNR and target BER by searching the minimum of $f_3(b_k)$. Figure 3.35(a) shows an example with $SNR = 25dB$ and target BER $= 10^{-3}$.

The first step of our algorithm consists of using such analysis to find a specific Γ_k and b_k for each subcarrier according to its SNR and target BER. Figure 3.35(b) shows the variation of Γ_k and b_k with the target BER with different values of SNR. As expected, for a fixed BER, the higher the SNR of the subcarrier, the higher the number of bits per symbol that it can transport and the smaller the SNR gap to capacity.

Since the b_k that are found after the first step of the algorithm are not necessarily integers, we then round it to the nearest integer and calculate the equivalent energy using 3.62 and 3.63. Then, in a third step, we proceed to either Campello's E-tight or B-tight depending if the loading approach that we define is RA or MA to finally impose the energy or bit-rate constraint. Figure 3.36 shows the three steps of our algorithm in the RA and MA approaches for the same example presented in section 3.7. Notice that in this particular example the signal energy has already converged to a value that is very close to the power constraint after the second step and thus the third step of the algorithm does not change the bit and power allocation of the subcarriers.

In Figure 3.37, we compare the six algorithms presented in this section in their RA and MA versions. We can notice that LCA is the solution that better approximates the optimal WF

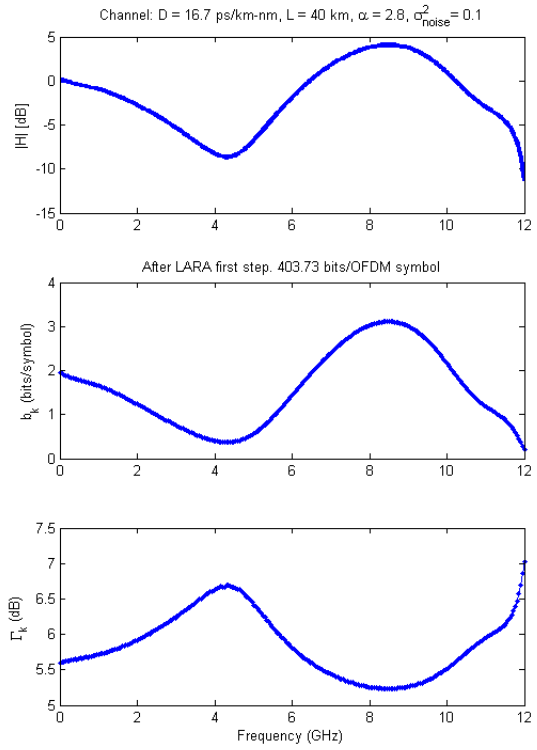

(a)

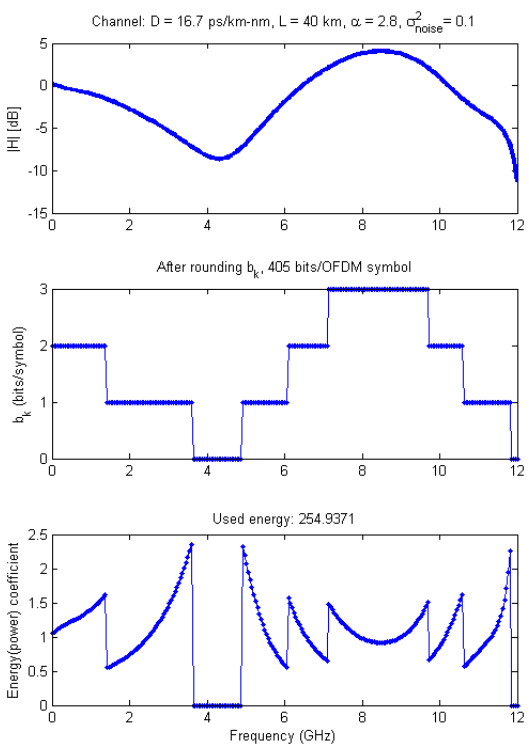

(b)

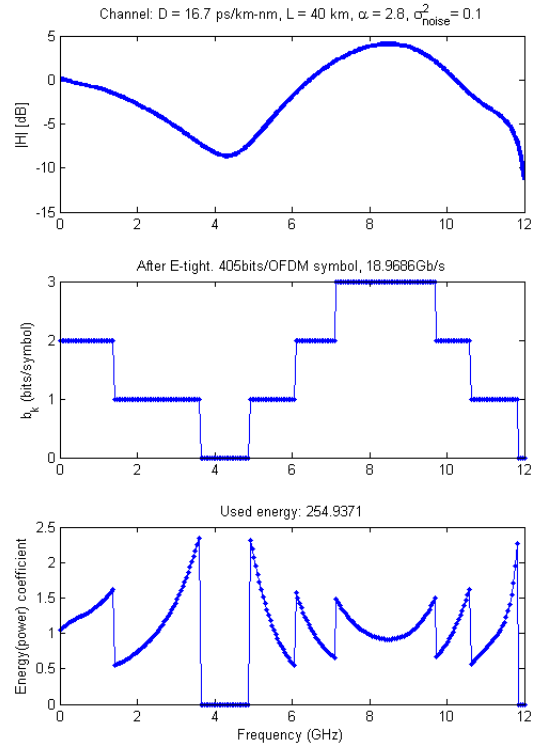

(c)

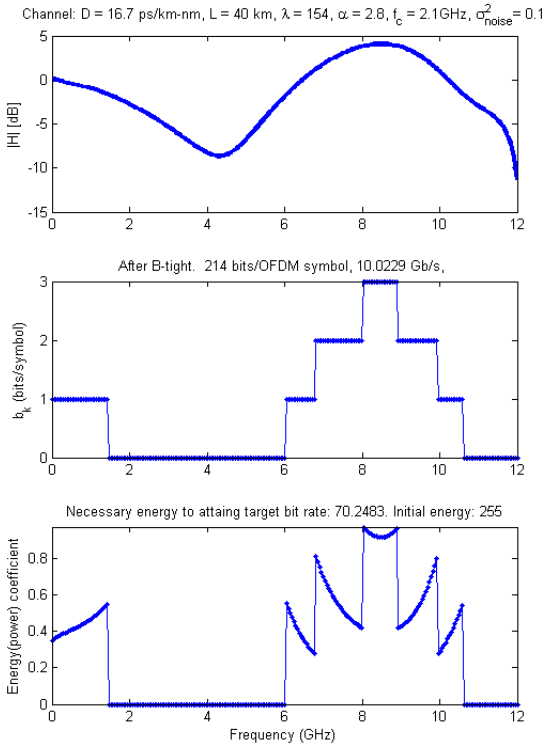

(d)

Figure 3.36: (a) Bit gap distribution after first step. (b) Rounded bit distribution and equivalent energy distribution after second step. (c) LA-RA's final result after E-tight in third step. (d) LA-MA's final result after B-tight in third step

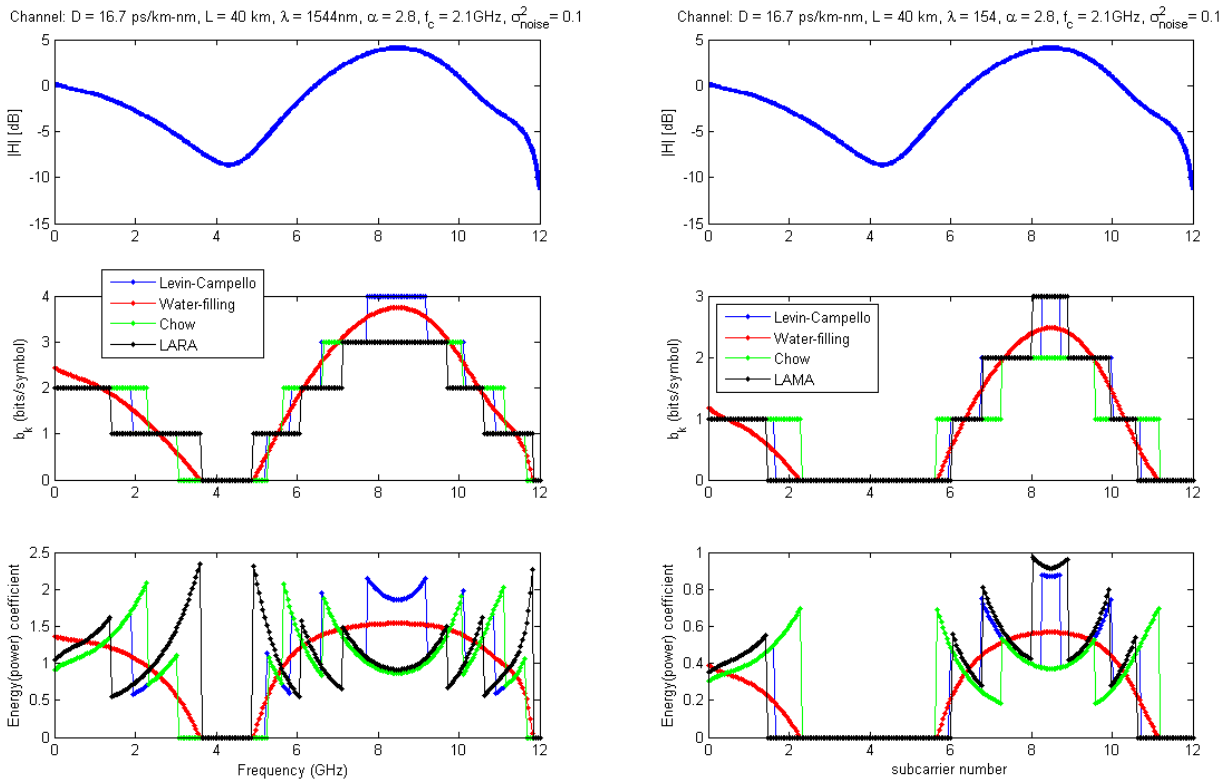

(a) (b)

Figure 3.37: Comparison between WF, LC, Chow and LA algorithms in the (a) RA and (b) MA approaches.

solution. In addition, we can see that using the precise values of gap in the LA has caused a slight penalty in the form of a decrease in the transmitted bit-rate for the RA solution and an increase in the necessary energy to attain the target bit-rate for the MA solution if compared to the other integer b_k solutions.

3.7.3.4 Practical LC-RA example

Let us now show a practical example of implementation of the LC-RA algorithm over $40km$ SSMF fiber.

We transmit a real-valued baseband OFDM signal with $6GHz$ bandwidth sampled at $12GS/s$ and 10 bits resolution. An electrical $6GHz$ low-pass filter is placed after the AWG to remove the signal replicas centered at the multiples of the DAC's sampling ratio and a pre-emphasis filter is digitally implemented to compensate the *sinc* response due to the digital-to-analog conversion. The number of data subcarriers is 255 ($N_{IFFT} = 512$) and 32 samples are used as cyclic prefix. We send 300 OFDM signals and the signal scaling factor is $13dB$. At the receiver, the signal is captured at $40GS/s$ by the DSO with an 8 bits resolution. The DSO's acquisition window is such that the system's parameters can be calculated over 600 symbols, i.e., the 300 symbols repeated one time. The signal is demodulated according to the block diagram shown in Figure 3.17.

In the first iteration of our program, we send a probing signal in which all subcarriers are QPSK mapped and have the same power coefficient. We are then able to estimate the SNR and BER per subcarrier based on the EVM measurements using the equations shown in subsection

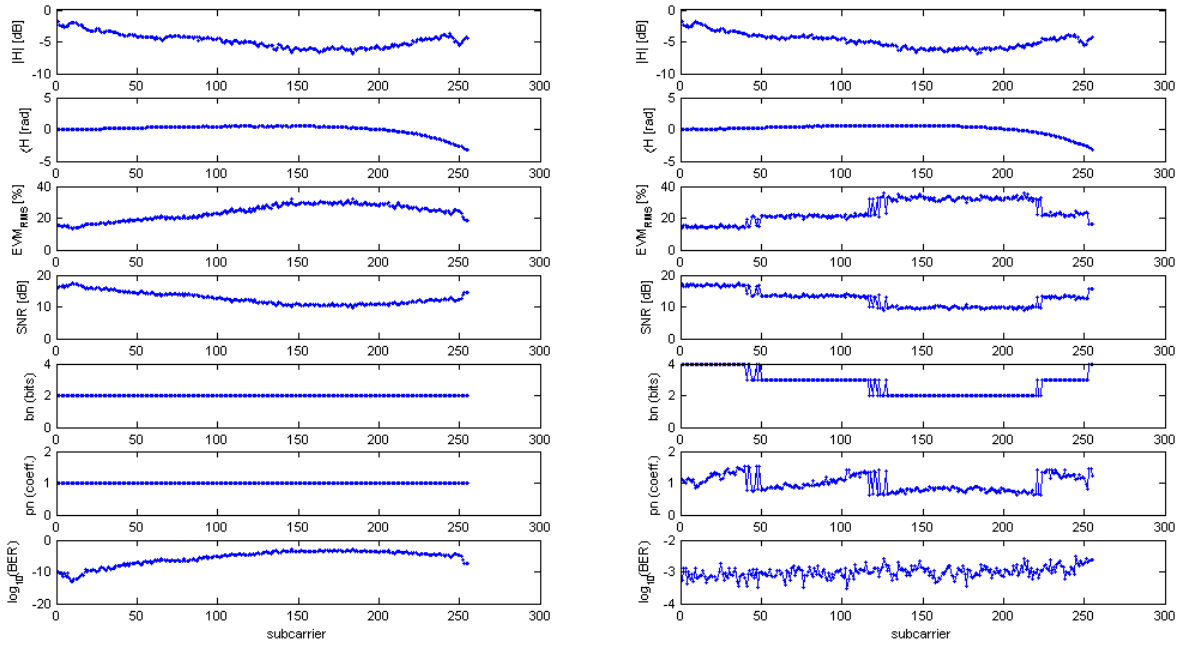

(a) (b)

Figure 3.38: Transmission parameters (a) before and (b) after LC-RA.

3.6. The SNR is used as an input for the LC-RA algorithm that optimizes the mapping and power of the subcarriers so that the average BER of the signal over all subcarriers converges to 10^{-3}. Figures 3.38(a) and (b) show respectively the subcarriers parameters before and after LC-RA. Notice that the measured EVM and estimated SNR will have some sort of step-like profile which varies as a function of the mapping of the subcarriers after bit and power loading.

3.7.3.5 Other bit and power loading algorithms

Many other bit and power loading algorithms have been proposed by different authors. In [107], a low-complexity algorithm which maximizes the transmission bit-rate based on look-up tables is proposed for wireless channels. The algorithm's complexity is greatly reduced if compared to Chow's approach by assigning sets of boundary values for g_k according to each mapping level (b_k). Indeed, the proposed algorithm represents quite a direct solution if we carefully observe Figures 3.33 and 3.34. The table can be easily adjusted according to the channel's variations in time. Another slightly more complex rate adaptive solution for the wireless scenario is proposed in [108] that does not need sorting the channel's coefficients.

In [109], a constant power allocation is assumed over all subcarriers for an unfixed target BER. The solution is quite interesting for systems in which the transmitted power has to obey a certain spectral mask that leaves almost no room for power loading configurations. The authors show that relaxing the constant BER constraint allows maintaining a negligible performance loss if compared to the ideal water-filling solution.

In [110], the authors show a detailed complexity analysis between their bit and power loading algorithm and optimal bit-filling and bit-removal algorithms for the wired ADSL scenario. They exploit the subchannel gain-to-noise ratio to calculate a channel representative bit-allocation profile and then use multiple bits-insertions or removals until the convergence to target bit-rate is obtained. Still in the ADSL domain, [111] proposes an algorithm for systems that have constraints arriving from spectral compatibility specifications both in terms of total and peak

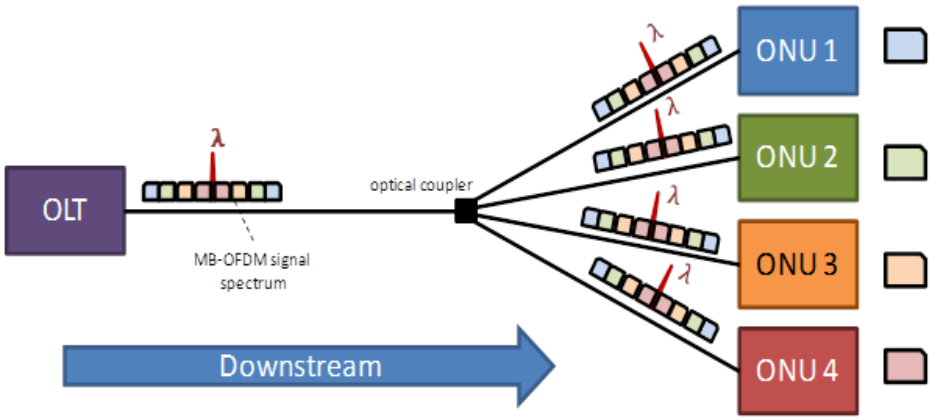

Figure 3.39: MB-OFDM PON.

powers per subcarriers. Other examples of reduced complexity algorithms are presented in [112, 113].

A very interesting power consumption analysis of bit loading algorithms is made in [114]. By swiching the focus of the discussion from the complexity and computation efficiency to the energy consumption and required chip area, the authors manage to give some very interesting parameters related to the practical implementation of different solutions for a "energy conscient wireless systems". The authors conclude that algorithms with lower theoretical complexity may apparently consume more chip area and energy.

In section 7.3, we propose an algorithm in which both the bit rate and power constraints are used to minimize the bandwidth occupied by the OFDM signal. This solution is referred to as bandwidth-adaptive OFDM.

3.8 Multiuser Approaches with OFDM

We have seen in this chapter that one of the greatest advantages of OFDM if compared to SC modulations was the fact that it allowed the creation of an extra dimension when sharing the resources of the network. Indeed, the subcarrier allocation to different users provides sub-wavelength granularity and can be used together with other conventional multiplexing approaches such as TDM and WDM.

However, the frequency domain multiplexing will face different challenges depending on the architecture of the PON and whether it is used on a downstream or upstream transmission. In part II, we assess those limitations and comment on different architectures that can be implemented using OFDM. For the moment, let us consider the simplest scenario. Let us take a single-wavelength IMDD downstream transmission as shown in Figure 3.39. Each ONU receives the whole OFDM signal spectrum but chooses only the subcarriers to which it has been associated. Each user will have a specific channel frequency response depending on how far he is situated from the central. The frequency attribution per ONU can consist of either a group of adjacent subcarriers as shown in Figure 3.39 or sparsely distributed subcarriers. Let us call the first and second approaches Multiband OFDM (MB-OFDM) and Sparsely-Distributed OFDM (SD-OFDM) respectively.

If we first consider the MB-OFDM approach, then the maximum bit-rate (or minimum total energy) can be achieved independently for all subscribers by applying one of the bit and power loading algorithms described in section 3.7 on each frequency band. Figure 3.40(a) shows a typical example of a MB-OFDM approach. Three subscribers (ONU 1, 2 and 3) located at 40, 60 and 80km from the central are assigned each with a group of 85 adjacent subcarriers (1-85 to ONU 1, 86-170 to ONU 2 and 171-255 to ONU 3). We use the LC-RA separately on

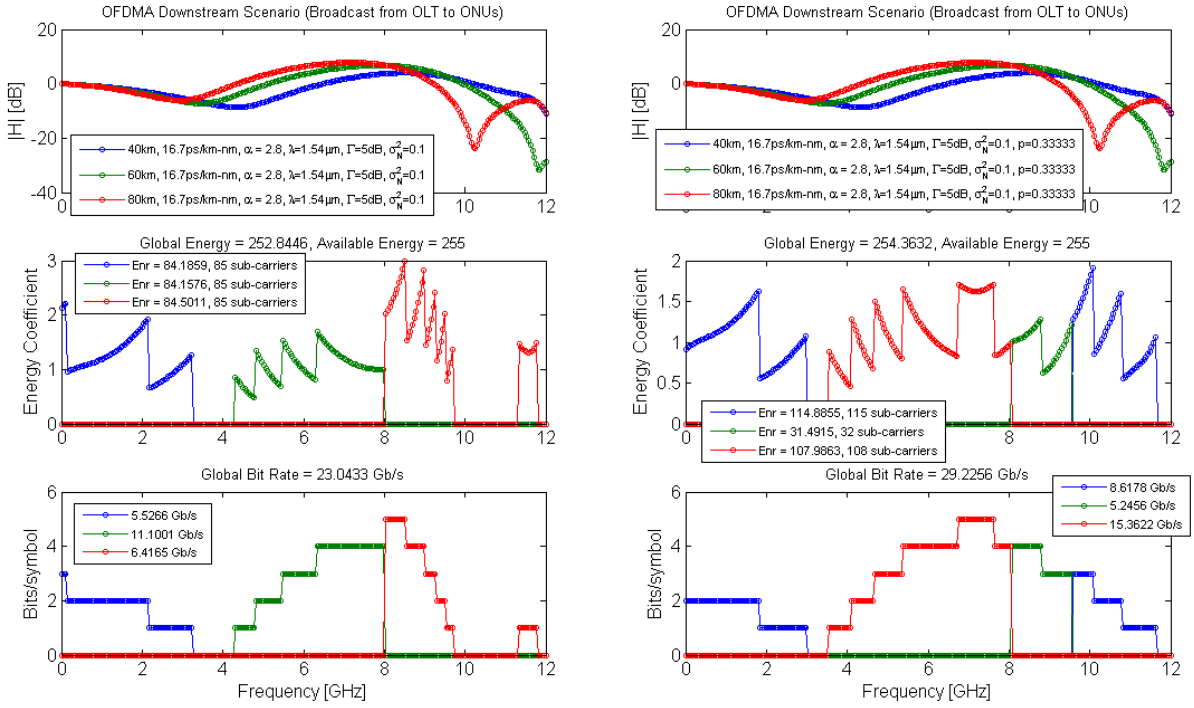

(a) (b)

Figure 3.40: Rate Adaptive Levin-Campello solution for the (a) MB-OFDM and (b) SD-OFDM multiuser approaches.

each frequency band to maximize the bit-rate of each user according to his channel frequency response. For matters of simplicity, in this example all users have the same fiber dispersion coefficient, noise variance and target BER. In addition, since it is a downstream transmission, all frequency responses share the same wavelength and chirp parameters of the OLT laser. Figure 3.40 also shows the frequency responses and bit and power allocation of the three ONUs.

One of the advantages of the MB-OFDM approach is that it can be quite simply implemented. At the ONU side we can have either of these solutions:

- Each ONU's ADC has a high sampling rate and is thus capable of receiving the whole set of subcarriers sent by the OLT. In this case, the selection of its frequency band is optimally realized in the digital domain [115].
- Each ONU selects its frequency band through IQ mixing in the electrical domain.

The advantage of the IQ mixing approach is that with the help of tunable local oscillators, each band can be electrically downconverted while maintaining the ONU's ADC at relatively low sampling ratios. Not only such an approach is interesting in terms of costs of implementation but it may also allow increasing the signal's quality since the ADC's sampling ratio is inversely proportional to the maximum achievable vertical resolution as seen previously in this work.

In addition, the evolution of chipsets including the whole apparatus needed for downconversion (phase shifters, mixers, local oscillators and photodetectors) on the same wafer [55, 116] can offer MB-OFDM a substantial benefit in terms of market maturity. The same cost-effectiveness argument, however, falls down for frequency ranges over $20GHz$ due to the still prohibitive costs of local oscillators that are tunable in this range. Other disadvantages of this solution if compared to the first one is the likely presence of IQ imbalancing and the effects of the electrical components bandwidth on the signal.

While MB-OFDM succeeds to offer a simple-to-implement and cost-effective multiuser approach, it fails to exploit its full potential. Actually, if the resource (i.e. the frequency bands) assignment is fixed or if they are arbitrarily chosen, it will most certainly result in an inefficient allocation of subcarriers per user. Consequently, in order to maximize the performances of the multicarrier system as a whole, a joint subcarrier, bit and power loading algorithm is necessary to optimally allocate and configure the subcarriers of the different ONU according to their channel responses. This is the principle of SD-OFDM. Indeed, not only should we consider the different channel responses, but also the different requirements of the subscribers in terms of target BER, noise margins, and coding schemes.

In [117], the authors divide this problem into two categories. The first one is called "broadcast" and can be used in our example of downstream transmission. It imposes a single energy constraint to the whole set $\mathcal{U}$ of subscribers. The second category, called "multiple access", refers to the upstream transmission and is characterized by the fact that each subscriber has its own energy constraint. However, we will see in section 6.3 that this approach cannot be implemented in a real IMDD PON upstream transmission.

The RA SD-OFDM problem can be formalized by the following equations:

$$max_{S_u,\varepsilon_{u,k}} \sum_{u=1}^{\mathrm{U}} p_u \sum_{k\in S_u} b_{u,n} = \sum_{u=1}^{\mathrm{U}} p_u \sum_{k\in S_u} log_2\left(1+\frac{\varepsilon_{u,k} g_{u,k}}{\Gamma_u}\right) \tag{3.79}$$

$$s.t.: \sum_{u=1}^{\mathrm{U}} \sum_{k\in S_u} \varepsilon_{u,k} \leqslant \varepsilon_{tot},\ Broadcast \tag{3.80}$$

$$s.t.: \sum_{k\in S_u} \varepsilon_{u,k} = \varepsilon_{tot}\ \forall u \in \mathcal{U},\ Multiple\ Access \tag{3.81}$$

$$\begin{gathered} S_u \cap S_{u'} = 0,\ \forall u \neq u' \\ \varepsilon_{u,k} \geq 0,\ \forall u \in \mathcal{U},\ \forall k \in \mathcal{K} \end{gathered} \tag{3.82}$$

$$\sum_{u=1}^{\mathrm{U}} p_u = 1 \tag{3.83}$$

where p_u and S_u are respectively the priority coefficient and the set of subcarriers associated to the subscriber u. $\varepsilon_{u,k}$ and $g_{u,k}$ are the power and channel gain coefficient of the subcarrier k in the group u and Γ_u is the SNR gap to capacity of the subscriber u. Even though equations 3.79 to 3.83 seem quite complicated at a first glance, a very simple analysis of the SD-OFDM problem can be made if we analyze them one by one. Actually, the main objective of the problem is to find the right energies and mappings that maximize the weighted sum of each subscriber´s bit-rate (equation 3.79). This maximization is subjected either to a global (broadcast approach, equation 3.80) or individual (multiple access approach, equation 3.81) energy constraint. Equations 3.82 guarantee that each subcarrier is assigned to only one user and that no subcarrier is set to a negative energy. In addition, each subscriber has its own gap Γ_p and channel coefficients $g_{p,k}$.

For the specific case in which all users have the same priority, i.e. $p_u = 1/U\ \forall u$, the solution is simplified: the bit rate is maximized by assigning the subcarriers according to the best weighted channel gain coefficient $\frac{g_{u,k}}{\Gamma_u}$. Figure 3.40(b) shows the same example as proposed for the MB-OFDM reviewed in the Broadcast SD-OFDM approach. The SD-OFDM approach provided an increase of more than 20% on the global bit-rate compared to the MB-OFDM approach.

However, one of the main disadvantages of SD-OFDM compared to MB-OFDM is that each user must be aware of the whole bandwidth of the signal since his subcarriers can be potentially assigned anywhere in the spectrum. To do so, they will need high sampling ratio ADC which could imply a significant increase in the cost of the transceiver. Other difficulty that comes with a sparse subcarrier assignment is that the users must be very well synchronized in the frequency-domain to allow a proper selection of the subcarriers. On the other hand, MB-OFDM constraints

in terms of frequency synchronization between users can be easily solved if an appropriate guard interval is chosen between the frequency bands.

For a historical overview of the reports on the broadcast and multiple access problems, please refer to [117].

3.9 Conclusions

We have addressed in this chapter the main functions related to the OFDM modulation and demodulation block diagrams. Let us now recap on the most important points presented.

As far as the modulator is concerned, we have seen that each OFDM subcarrier could be modulated by a specific constellation. Several types of constellations exist, each with its own pros and cons and we have then chosen the squared and cross QAM constellations due to their better SNR performances. We have also seen that the group of local oscillators and filters needed for the modulation of each subcarrier could be substituted by computationally-efficient IFFT algorithms and that the OFDM subcarriers could be closer to each other thanks to the orthogonality principle, thus guaranteeing higher spectral efficiencies than conventional FDM. The importance of the cyclic prefix for matters of channel estimation, time synchronization and for offering robustness to residual dispersion has also been addressed in this chapter.

We have later seen that it was judicious to add a low-pass filter after the DAC to remove periodic replicas of the analog signal centered at the multiples of the sampling rate and that it was interesting to compensate the *sinc* response arriving from the digital-to-analog conversion. Finally, we have talked about the importance of scaling the OFDM signal according to the AWG's peak-to-peak voltage range so that an optimum point is found in which the signal's RF power is maximized and the noise arriving from the clipping in the DAC is minimized.

Before detailing the demodulation procedure, we addressed the different OFDM modulation solutions in the optical domain with a focus on the intensity modulation and direct detection, which is investigated in this thesis for its simplicity and cost-efficiency. We have described the advantages of the different IMDD solutions including the use of either a purely-real baseband signal with Hermitian symmetry or the electrically (or digitally) upconverted versions of a complex-valued baseband signal.

As far as the demodulator is concerned, we have payed special attention to time and frequency domain synchronization techniques, which are critical elements of any OFDM transmission. We have seen that the time-domain synchronization was constituted of two steps, the first one based on a cyclic-prefix identification and the second one based on the search of the first symbol. For the frequency synchronization, we have presented a solution based on the verification of the rotation in time of the symbols of each subcarrier to correct the EVM degradations caused by SFO and CFO. We have also addressed some channel estimation techniques and we have presented the metrics for evaluating the quality of an OFDM transmission.

In the last part of the chapter, we have reviewed the water-filling principle allowing to change the modulation and power of each subcarrier so that an optimized transmission is obtained. We have seen Campello's and Chow's Rate Adaptive and Margin Adaptive algorithms for integer number of bits per symbol per subcarrier and we have even presented one bit-loading solution of our own to address the problems of bit-rate maximization and power minimization. Finally, we have introduced a multi-user bit and power loading algorithm which can be extremely useful in the PON context for offering subcarrier granularity when sharing the resources of the network among different ONUs.

The implementation of the modulation and demodulation block diagrams constituted a fundamental step of this thesis and this is why we have dedicated a considerable part of this memoir to the subject. Each and every solution regarding the different points addressed in this chapter passed through an extensive and exhaustive verification by means of transmissions in the electrical domain before we could proceed to the optical experimental setups that will be shown in

the following of this work.

The reasons for such precautions become clear when we consider the interpretation of certain transmission results. It is essential that the modulation and demodulation functions are sufficiently trustworthy to guarantee that

- the degradations arriving from an imperfect OFDM modulation/demodulation are not mistaken with the physical phenomena arriving from the optical transmission and
- that the program is enough stable to allow the needed repeatability in the results.

We should remember, however, that even though our "home made" OFDM modulator/demodulator has continuously evolved during these three years of work, there will always exist new implementable ideas which have the potential to improve it and are thus worth of testing.

References

[1] IEEE. *IEEE 802.11a: Wireless LAN*. Medium Access Control (MAC) and Physical Layer (PHY) specifications, High-speed Physical Layer in the 5 GHz Band. URL: `http://standards.ieee.org/getieee802/download/802.11a-1999.pdf` (cit. on p. 40).

[2] IEEE. *IEEE 802.11g: Wireless LAN*. Medium Access Control (MAC) and Physical Layer (PHY) specifications, Amendment 4: Further Higher Data Rate Extension in the 2.4 GHz Band. URL: `http://standards.ieee.org/getieee802/download/802.11g-2003.pdf` (cit. on p. 40).

[3] IEEE. *IEEE 802.11n: Wireless LAN*. Medium Access Control (MAC) and Physical Layer (PHY) specifications, Amendment 5: Enhancements for Higher Throughput. URL: `http://standards.ieee.org/getieee802/download/802.11a-1999.pdf` (cit. on p. 40).

[4] Wikipedia. *Orthogonal frequency-division multiplexing*. URL: `http://en.wikipedia.org/wiki/OFDM` (cit. on p. 40).

[5] J.M. Tang et al. "Real-time optical OFDM transceivers for PON applications". In: *Optical Fiber Communication Conference and Exposition (OFC/NFOEC), 2011 and the National Fiber Optic Engineers Conference*. Mar. 2011, pp. 1 –3 (cit. on p. 42).

[6] E. Giacoumidis et al. "Performance optimization of adaptive loading algorithms for SMF-based optical OFDM transceivers". In: *Networks and Optical Communications (NOC), 2011 16th European Conference on*. July 2011, pp. 56 –59 (cit. on p. 42).

[7] R.P. Giddings et al. "Colourless real-time optical OFDM end-to-end transmission at 7.5Gb/s over 25km SSMF using 1GHz RSOAs for WDM-PONs". In: *Optical Fiber Communication (OFC), collocated National Fiber Optic Engineers Conference, 2010 Conference on (OFC/NFOEC)*. Mar. 2010, pp. 1 –3 (cit. on p. 42).

[8] R.P. Giddings et al. "Experimental demonstration of colourless real-time end-to-end optical OFDM transmission at 7.5Gb/s over 25km SSMF using a 1GHz RSOA". In: *Future Network and Mobile Summit, 2010*. June 2010, pp. 1 –6 (cit. on p. 42).

[9] R.P. Giddings et al. "Experimental Demonstration of Real-Time Optical OFDM Transmission at 7.5 Gb/s Over 25-km SSMF Using a 1-GHz RSOA". In: *Photonics Technology Letters, IEEE* 22.11 (June 2010), pp. 745 –747. ISSN: 1041-1135. DOI: `10.1109/LPT.2010.2045493` (cit. on p. 42).

[10] R.P. Giddings et al. "Experimental demonstration of record high 11.25Gb/s real-time end-to-end optical OFDM transceivers for PONs". In: *Future Network and Mobile Summit, 2010*. June 2010, pp. 1 –13 (cit. on p. 42).

[11] R.P. Giddings et al. “Demonstration of real-time multi-gigabit optical OFDM modems for access networks”. In: *Communications and Photonics Conference and Exhibition (ACP), 2009 Asia*. Nov. 2009, pp. 1 –2 (cit. on p. 42).

[12] E. Hugues-Salas et al. “First experimental demonstration of low-cost VCSEL-intensity modulated end-to-end real-time optical OFDM signal transmission at 11.25Gb/s over 25km SSMFs”. In: *Optical Fiber Communication Conference and Exposition (OFC/NFOEC), 2011 and the National Fiber Optic Engineers Conference*. Mar. 2011, pp. 1 –3 (cit. on p. 42).

[13] X.Q. Jin et al. “End-to-end real-time demonstration of 128-QAM-encoded optical OFDM transmission with a 5.25bit/s/Hz spectral efficiency over IMDD systems”. In: *Optical Fiber Communication (OFC), collocated National Fiber Optic Engineers Conference, 2010 Conference on (OFC/NFOEC)*. Mar. 2010, pp. 1 –3 (cit. on p. 42).

[14] X.Q. Jin et al. “Experimental Demonstrations and Extensive Comparisons of End-to-End Real-Time Optical OFDM Transceivers With Adaptive Bit and/or Power Loading”. In: *Photonics Journal, IEEE* 3.3 (June 2011), pp. 500 –511. ISSN: 1943-0655. DOI: 10.1109/JPHOT.2011.2154380 (cit. on p. 42).

[15] X.Q. Jin et al. “First experimental demonstration of end-to-end real-time optical OFDM symbol synchronization using subtraction and Gaussian windowing in 25km SMF IMDD systems”. In: *Optical Communication (ECOC), 2010 36th European Conference and Exhibition on*. Sept. 2010, pp. 1 –3. DOI: 10.1109/ECOC.2010.5621544 (cit. on p. 42).

[16] R.P. Giddings and J.M. Tang. “Real-time experimental demonstration of a versatile optical OFDM symbol synchronisation technique using low-power DC offset signalling”. In: *Optical Communication (ECOC), 2011 37th European Conference and Exhibition on*. Sept. 2011, pp. 1 –3 (cit. on p. 42).

[17] R.P. Giddings and J.M. Tang. “World-first experimental demonstration of synchronous clock recovery in an 11.25Gb/s real-time end-to-end optical OFDM system using directly modulated DFBs”. In: *Optical Fiber Communication Conference and Exposition (OFC/NFOEC), 2011 and the National Fiber Optic Engineers Conference*. Mar. 2011, pp. 1 –3 (cit. on p. 42).

[18] X.Q. Jin and J.M. Tang. “First experimental demonstration of real-time optical OFDMA PONs with colorless ONUs and adaptive DBA”. In: *Optical Fiber Communication Conference and Exposition (OFC/NFOEC), 2012 and the National Fiber Optic Engineers Conference*. Mar. 2012, pp. 1 –3 (cit. on p. 42).

[19] X.Q. Jin and J.M. Tang. “Experimental Investigations of Wavelength Spacing and Colorlessness of RSOA-Based ONUs in Real-Time Optical OFDMA PONs”. In: *Lightwave Technology, Journal of* 30.16 (Aug. 2012), pp. 2603 –2609. ISSN: 0733-8724. DOI: 10.1109/JLT.2012.2204725 (cit. on p. 42).

[20] J.L. Wei, A. Hamie, and J.M. Tang. “Optimization and comparison of the transmission performance of RSOA/SOA intensity-modulated optical OFDM signals for WDM-PONs”. In: *Optical Fiber Communication (OFC), collocated National Fiber Optic Engineers Conference, 2010 Conference on (OFC/NFOEC)*. Mar. 2010, pp. 1 –3 (cit. on p. 42).

[21] J.L. Wei et al. “Wavelength reused bidirectional adaptively modulated optical OFDM transmission in colourless WDM-PONs”. In: *Optical Communication (ECOC), 2010 36th European Conference and Exhibition on*. Sept. 2010, pp. 1 –3. DOI: 10.1109/ECOC.2010.5621459 (cit. on p. 42).

[22] J.L. Wei et al. “SOA intensity modulator-enabled colourless transmission of adaptively modulated optical OFDM signals for WDM-PONs”. In: *OptoElectronics and Communications Conference, 2009. OECC 2009. 14th.* July 2009, pp. 1 –2. DOI: 10.1109/OECC.2009.5214084 (cit. on p. 42).

[23] ITU-T. *ITU-T G.984.1: Gigabit-capable passive optical networks (GPON): General characteristics.* Telecommunication Standardization Sector. URL: http://www.itu.int/rec/T-REC-G.984.1-200803-I/en (cit. on p. 43).

[24] Govind Agrawal. *Nonlinear Fiber Optics, Fourth Edition (Optics and Photonics).* Academic Press, 2006. ISBN: 0123695163 (cit. on p. 43).

[25] Govind P. Agrawal. *Fiber-Optic Communication Systems (Wiley Series in Microwave and Optical Engineering).* Wiley-Interscience, 2010. ISBN: 0470505117. URL: http://www.amazon.com/Fiber-Optic-Communication-Systems-Microwave-Engineering/dp/0470505117%3FSubscriptionId%3D0JYN1NVW651KCA56C102%26tag%3Dtechkie-20%26linkCode%3Dxm2%26camp%3D2025%26creative%3D165953%26creativeASIN%3D0470505117 (cit. on p. 43).

[26] L. Hanzo and T. Keller. *OFDM and MC-CDMA: a primer.* John Wiley, 2006. ISBN: 9780470030073. URL: http://books.google.fr/books?id=7A8fAQAAIAAJ (cit. on pp. 43, 46).

[27] ITU-T. *ITU-T G.694.2: Spectral grids for WDM applications: CWDM wavelength grid.* Telecommunication Standardization Sector, Dec. 2003. URL: http://www.itu.int/rec/T-REC-G.694.2-200312-I/en (cit. on p. 44).

[28] ITU-T. *ITU-T G.694.1: Spectral grids for WDM applications: DWDM frequency grid.* Telecommunication Standardization Sector, June 2002. URL: http://www.itu.int/rec/T-REC-G.694.1-200206-I/en (cit. on p. 44).

[29] N. Cvijetic. “OFDM for Next Generation Optical Access Networks”. In: *Lightwave Technology, Journal of* PP.99 (2011), p. 1. ISSN: 0733-8724. DOI: 10.1109/JLT.2011.2166375. URL: http://ieeexplore.ieee.org/stamp/stamp.jsp?tp=&arnumber=6004799 (cit. on pp. 45, 58, 59, 61, 76, 80).

[30] Lifang Li, D. Divsalar, and S. Dolinar. “Iterative demodulation and decoding of coded non-square QAM”. In: *Military Communications Conference, 2003. MILCOM 2003. IEEE.* Vol. 1. Oct. 2003, 84 –89 Vol.1. DOI: 10.1109/MILCOM.2003.1290082 (cit. on p. 46).

[31] J. Smith. “Odd-Bit Quadrature Amplitude-Shift Keying”. In: *Communications, IEEE Transactions on* 23.3 (Mar. 1975), pp. 385 –389. ISSN: 0090-6778. DOI: 10.1109/TCOM.1975.1092806 (cit. on pp. 46, 47, 83).

[32] J.G. Proakis and M. Salehi. *Digital communications.* McGraw-Hill, 2008 (cit. on p. 47).

[33] Ravi Mahadevappa and Stephen ten Brink. *Comparison of 128QAM mappings/labelings for 802.11n.* Realtek Semiconductors. Nov. 2003. URL: http://www.google.fr/url?sa=t&rct=j&q=comparison+of+128QAM+mappings%2Flabelings+for+802.11n&source=web&cd=1&sqi=2&ved=0CB4QFjAA&url=https%3A%2F%2Fmentor.ieee.org%2F802.11%2Fdcn%2F03%2F11-03-0825-00-000n-11-03-0825-00-000n-comparison-128qam-mappings-and-labelings.ppt&ei=kTg_UNK9MY6R0QWkqYGoAg&usg=AFQjCNEzz2ORvNlV_q8oSV7iSZsd-VCILg (cit. on p. 47).

[34] S. Weinstein and P. Ebert. “Data Transmission by Frequency-Division Multiplexing Using the Discrete Fourier Transform”. In: *Communication Technology, IEEE Transactions on* 19.5 (Oct. 1971), pp. 628 –634. ISSN: 0018-9332. DOI: 10.1109/TCOM.1971.1090705 (cit. on p. 47).

[35] M. Kunt, G. Granlund, and M. Kocher. *Traitement de l'information*. Collection technique et scientifique des télécommunications v. 1. Presses Polytechniques et Universitaires Romandes, 1991. ISBN: 9782880742072. URL: http://books.google.com.br/books?id=OhwLaAEACAAJ (cit. on p. 48).

[36] D. Tse and P. Viswanath. *Fundamentals of wireless communication*. Cambridge University Press, 2005. ISBN: 9780521845274. URL: http://books.google.fr/books?id=66XBb5tZX6EC (cit. on p. 49).

[37] A.V. Oppenheim and R.W. Schafer. *Discrete-time signal processing*. Prentice-Hall signal processing series. Prentice Hall, 2010. ISBN: 9780131988422. URL: http://books.google.com.br/books?id=mYsoAQAAMAAJ (cit. on pp. 49, 50, 64).

[38] J.A. Rodríguez, J.B. Mariño, and A. Moreno. *Tratamiento digital de la señal: Una introducción experimental*. Politecnos comunicaciones. E, 1999. ISBN: 9788483012925. URL: http://books.google.com.br/books?id=WtC78IhiNBYC (cit. on pp. 49, 50, 64).

[39] Wikipedia. *Central Limit Theorem*. URL: http://en.wikipedia.org/wiki/Central_limit_theorem (cit. on p. 51).

[40] Hua Yu, Min Chen, and Gang Wei. "Distribution of PAR in DMT systems". In: *Electronics Letters* 39.10 (May 2003), pp. 799 –801. ISSN: 0013-5194. DOI: 10.1049/el:20030500 (cit. on p. 51).

[41] A.J. Lowery, Liang Bangyuan Du, and J. Armstrong. "Performance of Optical OFDM in Ultralong-Haul WDM Lightwave Systems". In: *Lightwave Technology, Journal of* 25.1 (Jan. 2007), pp. 131 –138. ISSN: 0733-8724. DOI: 10.1109/JLT.2006.888161 (cit. on pp. 52, 59, 61).

[42] W. Shieh and I. Djordjevic. *OFDM for Optical Communications*. Electronics & Electrical. Academic Press/Elsevier, 2009. ISBN: 9780123748799. URL: http://books.google.fr/books?id=ViPrzMHnY8EC (cit. on pp. 52, 61, 64, 78, 79, 89).

[43] Andrew Schaefer. *The Effective Number of Bits (ENOB) of my R&S Digital Oscilloscope*. Tech. rep. Rohde & Schwarz, 2011. URL: http://www2.rohde-schwarz.com/file_15829/ENOB_Technical_Paper_1ER03_1e.pdf (cit. on p. 54).

[44] J. Armstrong and A.J. Lowery. "Power efficient optical OFDM". In: *Electronics Letters* 42.6 (Mar. 2006), pp. 370 –372. ISSN: 0013-5194. DOI: 10.1049/el:20063636 (cit. on pp. 55, 56).

[45] J. Armstrong and B.J.C. Schmidt. "Comparison of Asymmetrically Clipped Optical OFDM and DC-Biased Optical OFDM in AWGN". In: *Communications Letters, IEEE* 12.5 (May 2008), pp. 343 –345. ISSN: 1089-7798. DOI: 10.1109/LCOMM.2008.080193 (cit. on p. 55).

[46] J. Armstrong et al. "SPC07-4: Performance of Asymmetrically Clipped Optical OFDM in AWGN for an Intensity Modulated Direct Detection System". In: *Global Telecommunications Conference, 2006. GLOBECOM '06. IEEE*. 27 2006-dec. 1 2006, pp. 1 –5. DOI: 10.1109/GLOCOM.2006.571 (cit. on p. 55).

[47] Laia Nadal et al. "Low Complexity Bit Rate Variable Transponders Based on Optical OFDM with PAPR Reduction Capabilities". In: *Proceedings of 17th European Conference on Network and Optical Communications (NOC 2012) & 7th Conference on Optical Cabling and Infrastructure (OC&I 2012)*. 2012 (cit. on p. 55).

[48] J.A. Davis and J. Jedwab. "Peak-to-mean power control and error correction for OFDM transmission using Golay sequences and Reed-Muller codes". In: *Electronics Letters* 33.4 (Feb. 1997), pp. 267 –268. ISSN: 0013-5194. DOI: 10.1049/el:19970205 (cit. on p. 55).

[49] C. Rossing. “Golay complementary sequences for OFDM with 16-QAM”. In: *Information Theory, 2000. Proceedings. IEEE International Symposium on*. 2000, p. 331. DOI: 10.1109/ISIT.2000.866629 (cit. on p. 56).

[50] J.A. Davis and J. Jedwab. “Peak-to-mean power control in OFDM, Golay complementary sequences, and Reed-Muller codes”. In: *Information Theory, IEEE Transactions on* 45.7 (Nov. 1999), pp. 2397 –2417. ISSN: 0018-9448. DOI: 10.1109/18.796380 (cit. on p. 56).

[51] J.A. Davis and J. Jedwab. “Peak-to-mean power control in OFDM, Golay complementary sequences and Reed-Muller codes”. In: *Information Theory, 1998. Proceedings. 1998 IEEE International Symposium on*. Aug. 1998, p. 190. DOI: 10.1109/ISIT.1998.708788 (cit. on p. 56).

[52] F. Fiedler and J. Jedwab. “How Do More Golay Sequences Arise?” In: *Information Theory, IEEE Transactions on* 52.9 (Sept. 2006), pp. 4261 –4266. ISSN: 0018-9448. DOI: 10.1109/TIT.2006.880024 (cit. on p. 56).

[53] F. Fiedler, J. Jedwab, and M.G. Parker. “A Framework for the Construction ofGolay Sequences”. In: *Information Theory, IEEE Transactions on* 54.7 (July 2008), pp. 3114 –3129. ISSN: 0018-9448. DOI: 10.1109/TIT.2008.924667 (cit. on p. 56).

[54] M. Sung. “DFT-Precoded Coherent Optical OFDM With Hermitian Symmetry for Fiber Nonlinearity Mitigation”. In: *Lightwave Technology, Journal of* 30 (2012), pp. 2757–2763 (cit. on p. 56).

[55] B. Charbonnier, N. Brochier, and P. Chanclou. “(O)FDMA PON over a legacy 30dB ODN”. In: *Optical Fiber Communication Conference and Exposition (OFC/NFOEC), 2011 and the National Fiber Optic Engineers Conference*. Mar. 2011, pp. 1 –3 (cit. on pp. 58, 97).

[56] D. Hillerkuss et al. “26 Tbit/s Line-rate Super-channel Transmission Utilizing All-optical Fast Fourrier Transform Processing”. In: *Nature Photonics* 5 (2011), pp. 364–371 (cit. on pp. 58, 62).

[57] D. Torrientes et al. “10Gbit/s for next generation PON with electronic equalization using un-cooled 1.55um directly modulated laser”. In: *Optical Communication, 2009. ECOC ’09. 35th European Conference on*. Vol. 2009-Supplement. Sept. 2009, pp. 1 –2. URL: http://ieeexplore.ieee.org/search/srchabstract.jsp?tp=&arnumber=5395701&openedRefinements%3D*%26filter%3DAND%28NOT%284283010803%29%29%26searchField%3DSearch+All%26queryText%3Dtorrientes (cit. on p. 58).

[58] A.J. Lowery, Liang Du, and J. Armstrong. “Orthogonal Frequency Division Multiplexing for Adaptive Dispersion Compensation in Long Haul WDM Systems”. In: *Optical Fiber Communication Conference, 2006 and the 2006 National Fiber Optic Engineers Conference. OFC 2006*. Mar. 2006, pp. 1 –3. DOI: 10.1109/OFC.2006.216072 (cit. on pp. 59, 61).

[59] D. Qian et al. “10 Gbit/s WDM-SSB-OFDM transmission over 1000 km SSMF using conventional DFB lasers and direct-detection”. In: *Electronics Letters* 44.3 (31 2008), pp. 223 –225. ISSN: 0013-5194. DOI: 10.1049/el:20083157 (cit. on pp. 59, 61).

[60] Arthur Lowery and Jean Armstrong. “Orthogonal-frequency-division multiplexing for dispersion compensation of long-haul optical systems”. In: *Opt. Express* 14.6 (Mar. 2006), pp. 2079–2084. DOI: 10.1364/OE.14.002079. URL: http://www.opticsexpress.org/abstract.cfm?URI=oe-14-6-2079 (cit. on pp. 59, 61).

[61] J.L. Wei, X.Q. Jin, and J.M. Tang. “The Influence of Directly Modulated DFB Lasers on the Transmission Performance of Carrier-Suppressed Single-Sideband Optical OFDM Signals Over IMDD SMF Systems”. In: *Lightwave Technology, Journal of* 27.13 (July 2009), pp. 2412 –2419. ISSN: 0733-8724. DOI: 10.1109/JLT.2008.2010718 (cit. on p. 61).

[62] J.L. Wei et al. “Wavelength-Offset Filtering in Optical OFDM IMDD Systems Using Directly Modulated DFB Lasers”. In: *Lightwave Technology, Journal of* 29.18 (Sept. 2011), pp. 2861 –2870. ISSN: 0733-8724. DOI: 10.1109/JLT.2011.2163057 (cit. on p. 61).

[63] Brendon J. Schmidt, Arthur J. Lowery, and Jean Armstrong. “Experimental Demonstrations of 20 Gbit/s Direct-Detection Optical OFDM and 12 Gbit/s with a Colorless Transmitter”. In: *Optical Fiber Communication Conference and Exposition and The National Fiber Optic Engineers Conference*. Optical Society of America, 2007, PDP18. URL: http://www.opticsinfobase.org/abstract.cfm?URI=OFC-2007-PDP18 (cit. on p. 61).

[64] M. Schuster et al. “Spectrally Efficient Compatible Single-Sideband Modulation for OFDM Transmission With Direct Detection”. In: *Photonics Technology Letters, IEEE* 20.9 (May 2008), pp. 670 –672. ISSN: 1041-1135. DOI: 10.1109/LPT.2008.918911 (cit. on p. 61).

[65] Matthias Schuster et al. “Spectrally Efficient OFDM-Transmission with Compatible Single-Sideband Modulation for Direct Detection”. In: *Optical Communication (ECOC), 2007 33rd European Conference and Ehxibition of* 1 (Sept. 2007), pp. 1 –2 (cit. on p. 61).

[66] Wei-Ren Peng et al. “Experimental Demonstration of 340 km SSMF Transmission Using a Virtual Single Sideband OFDM Signal that Employs Carrier Suppressed and Iterative Detection Techniques”. In: *Optical Fiber communication/National Fiber Optic Engineers Conference, 2008. OFC/NFOEC 2008. Conference on*. Feb. 2008, pp. 1 –3. DOI: 10.1109/OFC.2008.4528409 (cit. on p. 61).

[67] Wei-Ren Peng et al. “Experimental demonstration of 1600 km SSMF transmission of a generalized direct detection optical virtual SSB-OFDM system”. In: *Optical Communication, 2008. ECOC 2008. 34th European Conference on*. Sept. 2008, pp. 1 –2. DOI: 10.1109/ECOC.2008.4729136 (cit. on p. 61).

[68] ANÍBAL LUIS INTINI. *Orthogonal Frequency Division Multiplexing for Wireless Networks*. Tech. rep. UNIVERSITY OF CALIFORNIA SANTA BARBARA, 2000. URL: http://www.create.ucsb.edu/ATON/01.01/OFDM.pdf (cit. on p. 66).

[69] P. Golden, H. Dedieu, and K.S. Jacobsen. *Fundamentals of DSL Technology*. Taylor & Francis, 2005. ISBN: 9780849319136. URL: http://books.google.fr/books?id=m77kZl71gysC (cit. on pp. 67, 76, 79, 80, 83).

[70] Ang Ken Li, Yew Kuan Min, and V. Jeoti. “A study of frame timing synchronization for WiMAX applications”. In: *Intelligent and Advanced Systems, 2007. ICIAS 2007. International Conference on*. Nov. 2007, pp. 440 –443. DOI: 10.1109/ICIAS.2007.4658425 (cit. on p. 70).

[71] J.E. Salt and H.H. Nguyen. “Performance analysis of a frame detection algorithm for burst mode communications”. In: *Wireless Communications and Networking Conference, 2004. WCNC. 2004 IEEE*. Vol. 1. Mar. 2004, 571 –576 Vol.1. DOI: 10.1109/WCNC.2004.1311609 (cit. on p. 70).

[72] M. Speth et al. “Optimum receiver design for OFDM-based broadband transmission .II. A case study”. In: *Communications, IEEE Transactions on* 49.4 (Apr. 2001), pp. 571 –578. ISSN: 0090-6778. DOI: 10.1109/26.917759 (cit. on pp. 71, 72, 74).

[73] M. Speth et al. “Optimum receiver design for wireless broad-band systems using OFDM. I”. In: *Communications, IEEE Transactions on* 47.11 (Nov. 1999), pp. 1668 –1677. ISSN: 0090-6778. DOI: 10.1109/26.803501 (cit. on pp. 71, 72, 74).

[74] M. Sliskovic. “Carrier and sampling frequency offset estimation and correction in multicarrier systems”. In: *Global Telecommunications Conference, 2001. GLOBECOM ’01. IEEE*. Vol. 1. 2001, 285 –289 vol.1. DOI: 10.1109/GLOCOM.2001.965124 (cit. on pp. 71, 72, 74).

[75] M. Sliskovic. “Sampling frequency offset estimation and correction in OFDM systems”. In: *Electronics, Circuits and Systems, 2001. ICECS 2001. The 8th IEEE International Conference on*. Vol. 1. 2001, 437 –440 vol.1. DOI: 10.1109/ICECS.2001.957773 (cit. on pp. 71, 72, 74).

[76] P.J. Voltz et al. “Frequency Domain Re-Sampler for Clock Sampling Offset in MIMO ODFM Systems”. In: *Vehicular Technology Conference, 2006. VTC-2006 Fall. 2006 IEEE 64th.* Sept. 2006, pp. 1 –5. DOI: 10.1109/VTCF.2006.120 (cit. on p. 72).

[77] Salah A. Karout et al. “Two-dimensional phase unwrapping using a hybrid genetic algorithm”. In: *Appl. Opt.* 46.5 (Feb. 2007), pp. 730–743. DOI: 10.1364/AO.46.000730. URL: http://ao.osa.org/abstract.cfm?URI=ao-46-5-730 (cit. on p. 74).

[78] Caroline Lacombe, Gilles Aubert, and Laure Blanc-Féraud. *Mathematical Statement to one dimensional Phase Unwrapping: a Variational Approach*. 2002. URL: http://hal.inria.fr/I3S/inria-00072067 (cit. on p. 74).

[79] Zahi Nadim Karam. *Computation of the One-Dimensional Unwrapped Phase*. Jan. 2006. URL: http://www.rle.mit.edu/dspg/documents/karammastersthesis.pdf (cit. on p. 74).

[80] Leslie Ying. “Phase Unwrapping”. In: *Wiley Encyclopedia of Biomedical Engineering*. John Wiley & Sons, Inc., 2006. ISBN: 9780471740360. DOI: 10.1002/9780471740360.ebs1356. URL: http://dx.doi.org/10.1002/9780471740360.ebs1356 (cit. on p. 74).

[81] Ye Geoffrey Li, Jr Cimini L.J., and N.R. Sollenberger. “Robust channel estimation for OFDM systems with rapid dispersive fading channels”. In: *Communications, 1998. ICC 98. Conference Record. 1998 IEEE International Conference on*. Vol. 3. June 1998, 1320 –1324 vol.3. DOI: 10.1109/ICC.1998.683039 (cit. on p. 78).

[82] J.-J. van de Beek et al. “On channel estimation in OFDM systems”. In: *Vehicular Technology Conference, 1995 IEEE 45th*. Vol. 2. July 1995, 815 –819 vol.2. DOI: 10.1109/VETEC.1995.504981 (cit. on pp. 78, 79).

[83] S.U.H. Qureshi. “Adaptive equalization”. In: *Proceedings of the IEEE* 73.9 (Sept. 1985), pp. 1349 –1387. ISSN: 0018-9219. DOI: 10.1109/PROC.1985.13298 (cit. on p. 79).

[84] S. Qureshi. “Adaptive equalization”. In: *Communications Magazine, IEEE* 20.2 (Mar. 1982), pp. 9 –16. ISSN: 0163-6804. DOI: 10.1109/MCOM.1982.1090994 (cit. on p. 79).

[85] N. Benvenuto and S. Tomasin. “On the comparison between OFDM and single carrier modulation with a DFE using a frequency-domain feedforward filter”. In: *Communications, IEEE Transactions on* 50.6 (June 2002), pp. 947 –955. ISSN: 0090-6778. DOI: 10.1109/TCOMM.2002.1010614 (cit. on p. 81).

[86] D. Falconer et al. “Frequency domain equalization for single-carrier broadband wireless systems”. In: *Communications Magazine, IEEE* 40.4 (Apr. 2002), pp. 58 –66. ISSN: 0163-6804. DOI: 10.1109/35.995852 (cit. on p. 81).

[87] F. Horlin and A. Bourdoux. “Comparison of the sensitivity of OFDM and SC-FDE to CFO, SCO and IQ imbalance”. In: *Communications, Control and Signal Processing, 2008. ISCCSP 2008. 3rd International Symposium on*. Mar. 2008, pp. 111 –116. DOI: 10.1109/ISCCSP.2008.4537202 (cit. on p. 81).

[88] R.A. Shafik, S. Rahman, and AHM Razibul Islam. “On the Extended Relationships Among EVM, BER and SNR as Performance Metrics”. In: *Electrical and Computer Engineering, 2006. ICECE ’06. International Conference on*. Dec. 2006, pp. 408 –411. DOI: 10.1109/ICECE.2006.355657 (cit. on p. 82).

[89] R. Schmogrow et al. “Error Vector Magnitude as a Performance Measure for Advanced Modulation Formats”. In: *Photonics Technology Letters, IEEE* 24.1 (Jan. 2012), pp. 61 –63. ISSN: 1041-1135. DOI: 10.1109/LPT.2011.2172405 (cit. on p. 82).

[90] Ana Garcia-Armada. “SNR gap approximation for M-PSK-Based bit loading”. In: *Wireless Communications, IEEE Transactions on* 5.1 (Jan. 2006), pp. 57 –60. ISSN: 1536-1276. DOI: 10.1109/TWC.2006.1576527 (cit. on pp. 83, 85).

[91] Sumanth Jagannathan. “Interference and Outage Optimization in Multi-user Multi-carrier Communication Systems”. PhD thesis. Stanford University, 2008 (cit. on p. 83).

[92] Mathworks. *Bit Error Rate (BER) R2012a Documentation, Communications System Toolbox*. URL: http://www.mathworks.fr/help/toolbox/comm/ug/bsvzixi.html (cit. on p. 83).

[93] Seong Taek Chung and A.J. Goldsmith. “Degrees of freedom in adaptive modulation: a unified view”. In: *Communications, IEEE Transactions on* 49.9 (Sept. 2001), pp. 1561 –1571. ISSN: 0090-6778. DOI: 10.1109/26.950343 (cit. on p. 83).

[94] A.J. Goldsmith and Soon-Ghee Chua. “Variable-rate variable-power MQAM for fading channels”. In: *Communications, IEEE Transactions on* 45.10 (Oct. 1997), pp. 1218 – 1230. ISSN: 0090-6778. DOI: 10.1109/26.634685 (cit. on p. 83).

[95] P.K. Vitthaladevuni, M.-S. Alouini, and J.C. Kieffer. “Exact BER computation for cross QAM constellations”. In: *Wireless Communications, IEEE Transactions on* 4.6 (Nov. 2005), pp. 3039 –3050. ISSN: 1536-1276. DOI: 10.1109/TWC.2005.857997 (cit. on p. 83).

[96] Xiaodai Dong, N.C. Beaulieu, and P.H. Wittke. “Error probabilities of two-dimensional M-ary signaling in fading”. In: *Communications, IEEE Transactions on* 47.3 (Mar. 1999), pp. 352 –355. ISSN: 0090-6778. DOI: 10.1109/26.752813 (cit. on p. 84).

[97] L. Szczecinski et al. “Exact evaluation of bit- and symbol-error rates for arbitrary 2-D modulation and nonuniform signaling in AWGN channel”. In: *Communications, IEEE Transactions on* 54.6 (June 2006), pp. 1049 –1056. ISSN: 0090-6778. DOI: 10.1109/TCOMM.2006.876853 (cit. on p. 84).

[98] R. V. L. Hartley. *Transmission of Information*. ., 1928. URL: http://www.dotrose.com/etext/90_Miscellaneous/transmission_of_information_1928b.pdf (cit. on p. 84).

[99] C.E. Shannon and Institute of Radio Engineers. *Communication in the presence of noise*. Institute of Radio Engineers, 1949. URL: http://books.google.fr/books?id=6P3HHAAACAAJ (cit. on p. 84).

[100] C.E. Shannon and W. Weaver. *The mathematical theory of communication*. Illini books. University of Illinois Press, 1964 (cit. on p. 84).

[101] C. Berrou, A. Glavieux, and P. Thitimajshima. “Near Shannon limit error-correcting coding and decoding: Turbo-codes. 1”. In: *Communications, 1993. ICC 93. Geneva. Technical Program, Conference Record, IEEE International Conference on*. Vol. 2. May 1993, 1064 –1070 vol.2. DOI: 10.1109/ICC.1993.397441 (cit. on p. 85).

[102] John M. Cioffi. “EE379A: Digital Communications - Signal Processing and EE379C: Advanced Digital Communications”. Stanford University Class Reader. URL: http://www.stanford.edu/group/cioffi/ee379a/ (cit. on pp. 85, 87–89).

[103] Denis Auroux. *Lagrange Multipliers*. MIT. URL: http://www.academicearth.org/lectures/lagrange-multipliers (cit. on p. 86).

[104] T. Starr et al. *Understanding digital subscriber line technology*. Prentice Hall communications engineering and emerging technologies series vol. 1. P, 1999. ISBN: 9780137805457. URL: http://books.google.fr/books?id=gQ5TAAAAMAAJ (cit. on pp. 87–89).

[105] Morgan Hill CA Dirk Hughes-Hartogs. “Ensemble modem structure for imperfect transmission media”. Patent US 4731816 (US). Mar. 15, 1988. URL: http://www.patentlens.net/patentlens/patent/US_4731816/en/ (cit. on p. 87).

[106] P.S. Chow, J.M. Cioffi, and J.A.C. Bingham. “A practical discrete multitone transceiver loading algorithm for data transmission over spectrally shaped channels”. In: *Communications, IEEE Transactions on* 43.234 (Feb. 1995), pp. 773 –775. ISSN: 0090-6778. DOI: 10.1109/26.380108 (cit. on p. 89).

[107] Joonsuk Kim, Jiunn-Tsair Chen, and J.M. Cioffi. “Low complexity bit mapping algorithm for multi-carrier communication systems with fading channels”. In: *Universal Personal Communications, 1998. ICUPC ’98. IEEE 1998 International Conference on*. Vol. 2. Oct. 1998, 927 –931 vol.2. DOI: 10.1109/ICUPC.1998.733645 (cit. on p. 95).

[108] J. Dulj, Z. Ilic, and A. Bazant. “Efficient power allocation algorithm for OFDM systems”. In: *Electrotechnical Conference, 2004. MELECON 2004. Proceedings of the 12th IEEE Mediterranean*. Vol. 2. May 2004, 425 –428 Vol.2. DOI: 10.1109/MELCON.2004.1346955 (cit. on p. 95).

[109] Yaniv George and Ofer Amrani. “Constant-Power Bit Loading for Multicarrier Systems: BER-Allocation”. In: *Wireless Personal Communications* 64 (4 2012). 10.1007/s11277-010-0209-z, pp. 625–645. ISSN: 0929-6212. URL: http://dx.doi.org/10.1007/s11277-010-0209-z (cit. on p. 95).

[110] N. Papandreou and T. Antonakopoulos. “A new computationally efficient discrete bit-loading algorithm for DMT applications”. In: *Communications, IEEE Transactions on* 53.5 (May 2005), pp. 785 –789. ISSN: 0090-6778. DOI: 10.1109/TCOMM.2005.847141 (cit. on p. 95).

[111] E. Baccarelli, A. Fasano, and M. Biagi. “Novel efficient bit-loading algorithms for peak-energy-limited ADSL-type multicarrier systems”. In: *Signal Processing, IEEE Transactions on* 50.5 (May 2002), pp. 1237 –1247. ISSN: 1053-587X. DOI: 10.1109/78.995090 (cit. on p. 95).

[112] A. Mahmood and J.C. Belfiore. “An efficient algorithm for optimal discrete bit-loading in multicarrier systems”. In: *Communications, IEEE Transactions on* 58.6 (June 2010), pp. 1627 –1630. ISSN: 0090-6778. DOI: 10.1109/TCOMM.2010.06.0800482 (cit. on p. 96).

[113] Li-ping Zhu et al. “Computationally Efficient Optimal Discrete Bit Allocation for Medium and High Target Bit Rate DMT Transmissions”. In: *Communications, 2007. ICC ’07. IEEE International Conference on*. June 2007, pp. 6408 –6412. DOI: 10.1109/ICC.2007.1060 (cit. on p. 96).

[114] O. Hammami and M.A. Yusuf. “Bit loading algorithms: Circuit area, energy consumption and theoretical complexity”. In: *Microelectronics (ICM), 2009 International Conference on*. Dec. 2009, pp. 340 –345. DOI: 10.1109/ICM.2009.5418613 (cit. on p. 96).

[115] A. Gharba et al. “Multi-band power allocation in AMOOFDM high data rate NG-PON downlink transmission direct modulation of linear laser”. In: *Optical Fiber Communication (OFC), collocated National Fiber Optic Engineers Conference, 2010 Conference on (OFC/NFOEC)*. Mar. 2010, pp. 1 –3 (cit. on p. 97).

[116] B. Charbonnier et al. “Silicon Photonics for Next Generation FDM/FDMA PON”. In: *J. Opt. Commun. Netw.* 4.9 (Sept. 2012), A29–A37. DOI: 10.1364/JOCN.4.000A29. URL: http://jocn.osa.org/abstract.cfm?URI=jocn-4-9-A29 (cit. on p. 97).

[117] Y.G. Li and G.L. Stuber. *Orthogonal Frequency Division Multiplexing for Wireless Communications*. Signals and Communication Technology. Springer, 2006. ISBN: 9780387290959 (cit. on pp. 98, 99).

Part II

Details on Personal Contributions: Potentialities of OFDM for Next Generation PON, an Experimental Analysis

Chapter 4

IMDD Channel Characterization

4.1 Introduction

The objective of this chapter is twofold. Firstly, we want to validate the IMDD channel models presented in section 2.5 by means of experimental chirp estimations on different light-sources. We propose a fast and simple method for doing so which is based on the channel $|S_{21}|$ measurements done with a network analyzer and a fitting procedure with a high-performance algorithm. The comprehension of the dynamics of the channel response will help us understand the limitations of the transmission as far as the interplay between the fiber chromatic dispersion and the parasitic laser chirp is concerned. Such "frequency-domain comprehension" will give a very useful tool to infer about the propagation of signals that do not have a time-domain representation as simple as ordinary OOK signals.

Since this analysis is based on a single modulation carrier, in the following section we try to better understand the effects of the channel on OFDM signals which, in addition, do not necessarily obey the small-signal constraint. We show that the dispersion and chirp induced distortions caused at long fiber spans impose some changing in the transmitted signal power in order to optimize the system's performances. This investigation provides the answers for a phenomenon that has constantly been noticed in our experimental transmissions through long-reach PON.

4.2 Fiber and Chirp Estimation using the Downhill-Simplex Algorithm

In this section we detail one procedure to estimate the fiber dispersion coefficient and laser chirp parameters based on the measurements done with a network analyzer. The method consists of fitting the measured channel response with a mathematical model which describes the dispersive IMDD channel seen in section 2.5, until a group of parameters that allows a minimum level of resemblance between model and measurement is found. Figure 4.1 shows one example of estimation in which the IM+PM+FM model has been used to characterize a DFB laser model from EM4. The measurement has been done over $100km$ and the estimated parameters are $D = 16.52ps/km{\cdot}nm$, $\alpha = 3.8$ and $f_C = 6.46GHz$. The laser's central wavelength is $1551.42nm$.

The first approach that might come to mind when we think of creating a fitting algorithm is the brute-force method. Indeed, it is relatively simple to test several combinations of possible values for the parameters and then take the one that generates the channel response that gives the closest result to the measurement. For instance, we could try generating several theoretical curves with $D \in [15 : 0.5 : 19]\, ps/km - nm$, $\alpha \in [1 : 0.25 : 5]$ and $f_C \in [0 : 0.05 : 7]\, GHz$ but this would require the algorithm a total of 21573 iterations. The algorithm's complexity will scale with the needed level of precision and the degree of uncertainty of each parameter.

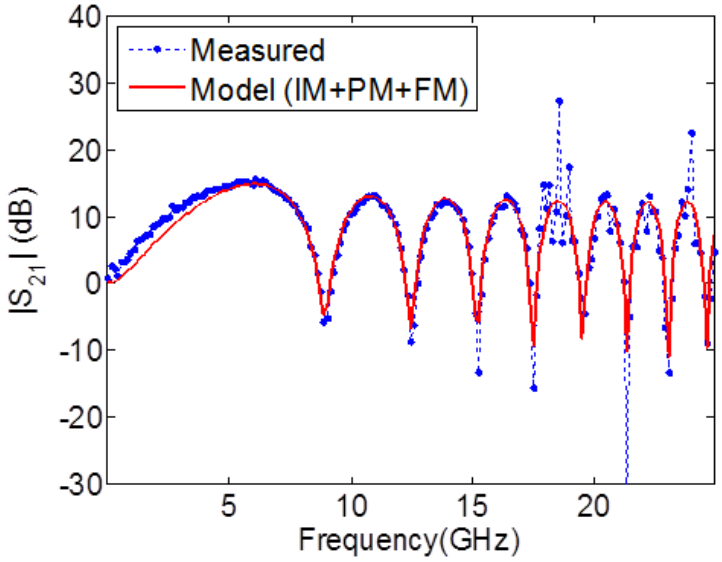

Figure 4.1: Example of channel frequency response fitting on a DFB laser.

A faster way of realizing the same task is by means of an optimization algorithm. In this work, we have chosen the Nelder-Mead algorithm, also known as the Downhill Simplex algorithm, which is detailed in the following.

4.2.1 The Downhill Simplex Algorithm

Let us take as an example the case of a linear curve $f_{exp}(x) = a_{exp}x + b_{exp}$ that has been experimentally measured and which we want to fit to a theoretical model $f_{theo}(x) = a_{theo}x + b_{theo}$ such that $f_{exp}(x)$ converges to $f_{theo}(x)$ and the parameters a_{exp} and b_{exp} can be estimated. Let us define a function $m(x) = f_{exp}(x) - f_{theo}(x)$ which measurements the degree of similarity between $f_{exp}(x)$ and $f_{theo}(x)$. One possible way of converging $f_{exp}(x)$ and $f_{theo}(x)$ is by minimizing the constant $M = \overline{|m(x)|}$ representing the mean value of $m(x)$ taken over x.

Let us also define a simplex: it is a n-dimensional polytope which is the convex hull of its $n+1$ vertices, with n being the number of parameters which we want to estimate. In our example, since we want to estimate a_{exp} and b_{exp}, $n = 2$ and the simplex is a triangle. If we had to estimate 1 variable, it would be a line in a 1-dimensional space; for 3 variables it would be a tetrahedron in the 3-dimensional space and so forth. The relation between the n-dimensional space and the number of parameters that we want to estimate becomes clearer if we take a look at Figure 4.2(a) which evidences one of the great advantages of the Simplex method: the fact that it has a vivid geometrical interpretation [1].

Here we have two axes representing the possible values of a_{theo} and b_{theo}. The point $(a_{theo}, b_{theo}) = (a_{exp}, b_{exp})$ represents the case for which $f_{exp}(x) = f_{theo}(x)$. In this figure, we can also see a non-degenerate Simplex S_0 consisting of the triangle $\Delta A_0 B_0 C_0$, with $A_0 = (a_{A,0}, b_{A,0})$, $B_0 = (a_{B,0}, b_{B,0})$, $C_0 = (a_{C,0}, b_{C,0})$. Each vertex of the Simplex is associated to a value $M_{A/B/C,0}$. For instance:

$$M_{A,0} = \overline{abs\left(f_{exp}(x) - f_{theo}(x)\,|_{a_{theo}=a_{A,0}, b_{theo}=b_{A,0}}\right)} \tag{4.1}$$

To carry out the algorithm, we first need to find the vertex that has the worst (highest) value of M. This information serves to decide among four possible actions that will help constructing a second Simplex in the following iteration of the algorithm. These actions are expansion, reflection, 1-dimensional contraction and multiple contraction. The procedure is then iteratively

[1] Naturally, a visualization in the $\mathbb{R}^{n>3}$ would be impossible.

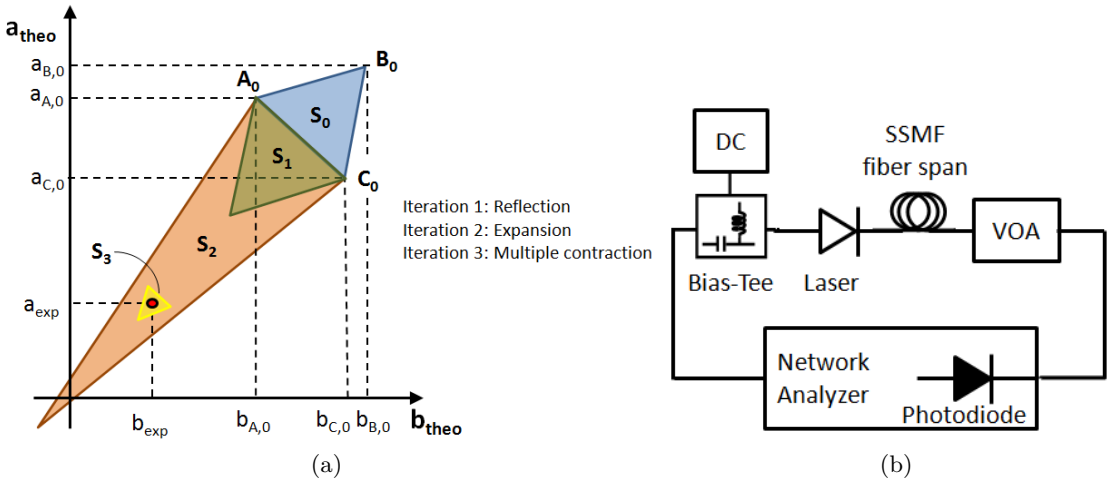

(a) (b)

Figure 4.2: (a) Visualization of the simplex algorithm principle. (b) Experimental setup.

repeated until the centroid of one Simplex is near enough the point (a_{exp}, b_{exp}). In the example of Figure 4.2(a), the simplexes S_1, S_2 and S_3 associated to the first, second and third iterations of the program have been found respectively by means of the reflection, expansion and multiple contractions operations. The centroid of the simplex S_3 represents a point $(a_{centroid,3}, b_{centroid,3})$ for which $f_{exp}(x)$ is fairly similar to $f_{theo}(x)$ and M is minimized. The reader is referred to [1] for the details on the iterative choice of a new Simplex.

4.2.2 Particularities and Precautions on the Estimations

4.2.2.1 Subtracting the Optical Back-to-back Contribution

The equations seen in section 2.5 represent exclusively the IMDD channel response, which is characterized by the fiber dispersion and the laser chirp characteristics. It is necessary then to exclude the optical back-to-back measurement from those realized with an optical fiber before fitting the measure to the theoretical curve. This means that for one dispersion/chirp estimation we actually need two $|S_{21}|$ experimental curves. Figure 4.3 shows one example of the procedure.

It also interesting to keep the same mean power at the photodiode in both measurements. If the same power is kept, the subtraction of the back-to-back measure from the fiber measure will result a channel curve starting at $0dB$. If not, the power difference between back-to-back and fiber measurements will have to be compensated by an extra parameter that will be responsible for vertically shifting the channel frequency response. This procedure, which is apparently simple, can actually be very problematic since the network analyzer's start frequency is generally limited to some tenths of MHz. Indeed, low-frequency noise generated by an injudicious experimental measurement can induce a wrong vertical shift, thus contributing to a bad parameter estimation.

4.2.2.2 Fixing as Many Parameters as Possible

One particularity of the equations that characterize a dispersive IMDD optical channel is the fact that they do not have a unique solution. In other words, there exist different groups of parameters with which it is possible to approximate the measured channel's frequency response.

For instance, a dispersion of $1700ps/nm$ can be obtained either with a fiber length $L = 100km$ and dispersion coefficient $D = 17ps/km \cdot nm$ or with $L = 106.25km$ and $D = 16ps/km \cdot nm$. In this case, the algorithm could converge to either of the solutions depending on the initial simplex, since both combinations of parameters give the same $D \times L$ product. It would be

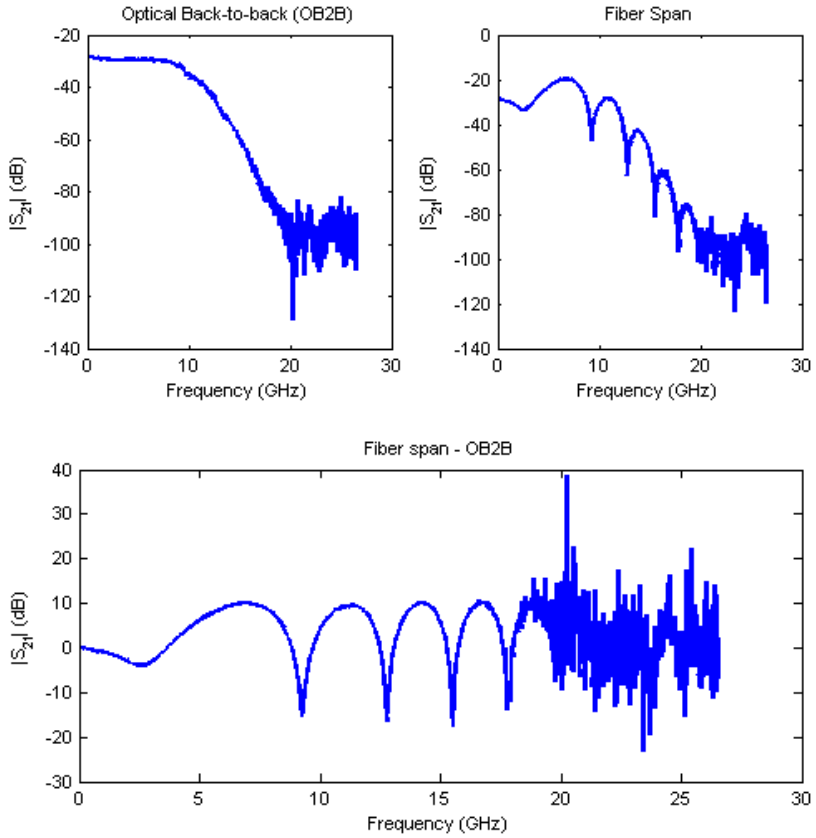

Figure 4.3: Optical back-to-back, fiber and final $|S_{21}|$ measured with a network analyzer.

virtually impossible to determine which combination is really representative of the experimental measurement.

That is why it is extremely important to fix as many parameters as possible before proceeding to the fitting itself. For instance, the central wavelength can be easily deduced with an Optical Spectrum Analyzer (OSA) and the exact fiber length can be found with the help of an Optical Time Domain Reflectometer (OTDR). Other very helpful measurement is that of the fiber dispersion coefficient variation with the wavelength. With the fiber dispersion measurement in hands, we can either fix the parameter D to find only the laser's chirp parameters or use it to check if the algorithm has converged to a plausible dispersion coefficient value if the user decided to fit it as well. Figure 4.4 shows a measurement of fiber dispersion coefficient done with an Anritsu/NetTest FD440 Portable Chromatic Dispersion Test Set.

4.2.2.3 Privileging Lower Frequency Fitting

If the low-frequency limitation of the network analyzer makes it important to align the mean optical power levels in the back-to-back and fiber measurements, the high-frequency limitation of the optical components also requires some extra care in the fitting. Indeed, as we can see in Figure 4.3, the laser's and photodiode's bandwidth limitation will make $|S_{21}|$ to be noisier in higher frequencies.

Since our "similarity parameter" M between model and measurement takes into account a mean over all frequencies, it is interesting to give different weights for different frequency spans to reduce the influence of those noisier values on the fitting:

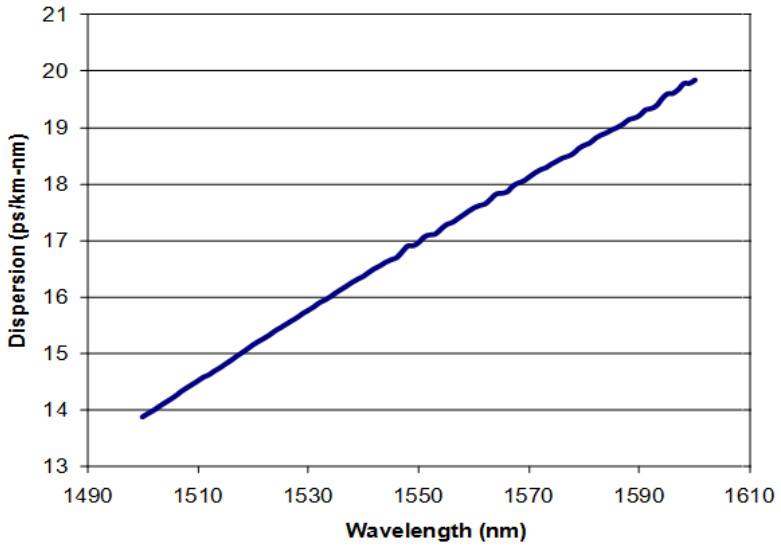

Figure 4.4: Fiber dispersion coefficient variation with the wavelength.

$$M = \frac{\sum_{p=1}^{P} M_p}{\sum_{p=1}^{P} w_p}, \text{ with}$$
$$M_p = w_p \left(\overline{abs\left(f_{exp}\left(x\right) - f_{theo}\left(x\right)\right)} \right), \; x \in p \tag{4.2}$$

Here, we have divided the frequency span into P parts, each one of which is attributed to a specific weight factor w_p. For instance, we can made the fitting between 0 and $2GHz$ to have a higher influence on M than the one from 20 to $25GHz$ simply by attributing to it a higher weight coefficient.

4.2.3 Applications with Different Light Sources

Figures 4.5(a) to (h) show some examples of parameter estimation for different kinds of single-longitudinal-mode light sources. Here, we use the IM+PM+FM IMDD frequency response model expressed by equation 2.28:

$$H_{IMDD}\left(\omega\right) = |\cos\left(\theta\right) - \sin\left(\theta\right)\alpha\left(1 - j\frac{\omega_c}{\omega}\right)|$$

Reduced fiber lengths have been privileged in some measurements due to low mean optical power of the components. Different frequency spans have also been chosen according to the emitters' bandwidth. All parameters have been estimated, including the sources' chirp parameters and wavelengths, the fiber's dispersion coefficient and length and finally the vertical shift parameter used to correct the difference between the mean optical power at the input of the network analyzer in both measurements. The simplex fitting will then occur in $\mathbb{R}^6$. The fact of knowing the source's wavelength, fiber length and fiber dispersion coefficient helped setting the most appropriated initial simplexes.

Even though Figures 4.5(a) to (e) all represent a same class of laser, the variations on the channel frequency response according to the components' specific chirp parameters are remarkable. For instance, the influence of the adiabatic chirp parameter is very clear when we analyze the position of the first dip of the channels. Despite the fact that lasers (a) and (c) have approximately the same α parameter, the adiabatic chirp frequency plays an important role on the dips depths, principally at lower frequencies. Indeed, in (c), f_c is so high that the first dip

occurs only at $8.6GHz$. The influence on the lobes' height is also quite noticeable. For instance, the maximum of the channel frequency response increases by approximately $6.5dB$ when we pass from an $\alpha = 2.85$ on laser (a) to $\alpha = 4.57$ on laser (b). The parameter also has a strong influence on the dips' positions, as already mentioned in Part II.

Interestingly, the same model also served to estimate the parameters of other kinds of light sources, namely two externally modulated lasers and a RSOA+FBG. While the α parameter of (g) is much smaller than those of the DFB lasers, the adiabatic chirp parameter contributed to a pronounced reduction in the first dip of its channel frequency response. The EAM prototype from MODULE project and shown in Figure 4.5(h) was specially conceived to have a very small transient chirp. Indeed, its α parameter is approximately zero and the frequency response converges to that of a light source having a pure IM component. That's why all lobes present the same height. Finally, the very same mathematical model and fitting method could be used to characterize the RSOA+FBG [2] shown in Figure 4.5(f). We can see that the RSOA+FBG presents the highest α parameter of all sources.

4.3 Dispersion-induced Distortions in IMDD OFDM

Even though the IMDD channel models managed to give a fairly good characterization of the laser chirp for both external and direct modulations, they are limited to a single-tone modulation scenario under the small-signal constraint. In such case, the effects of fiber dispersion and laser chirp on the channel frequency response are fairly "well-behaved".

In order to conceive a model that would precisely characterize an IMDD OFDM transmission, the consequences of multitone modulation and large signal operation would have to be included in both intensity and phase modulation components of the propagating signal. The large signal modulation of a chirped light source would have then to be studied at the same time in three main axes, as we have mentioned earlier in this thesis:

1. the electro-optical conversion and
2. intensity-to-phase coupling at the transmitter side and
3. the squared-law detection after propagation through a dispersive medium at the receiver side.

Such an analysis would also have to consider the particular case of overlapping subcarriers to differ the OFDM modulation from standard SCM (Subcarrier Multiplexed) transmissions. A complete model that addresses all this axes for an OFDM signal has not yet been reported. However, many works concentrate in some of these points separately.

The effects of harmonic and intermodulation distortions arriving from nonlinear electro-optical conversion of a multi-tone signal were thoroughly studied both theoretically and experimentally [3–8]. In [9] and [10], a similar report is provided, this time also considering the frequency modulation term arriving from the laser chirp, but under a small-signal assumption.

In [11], the author investigates the consequences of dispersion-induced distortions on a chirped source in the large-signal regime and submitted to a single-tone modulation. It is shown that a harmonic distortion proportional to the accumulated chromatic dispersion in the link can be potentiated due to the spectrally rich nature of the phase modulation component in the LSR. The analysis does not include, however, predictions on multitone transmissions and nonlinear variations of the intensity and phase modulation components at the emitter-side.

Some very interesting results are however derived in [12, 13]. The authors introduce a large-signal IMDD channel model and show that the enhancement on the channel's frequency response obtained with a chirped laser under the small-signal assumption can indeed be suppressed if the intensity modulation index is too high due to the direct effect that such intensity modulation will have on the phase modulation term.

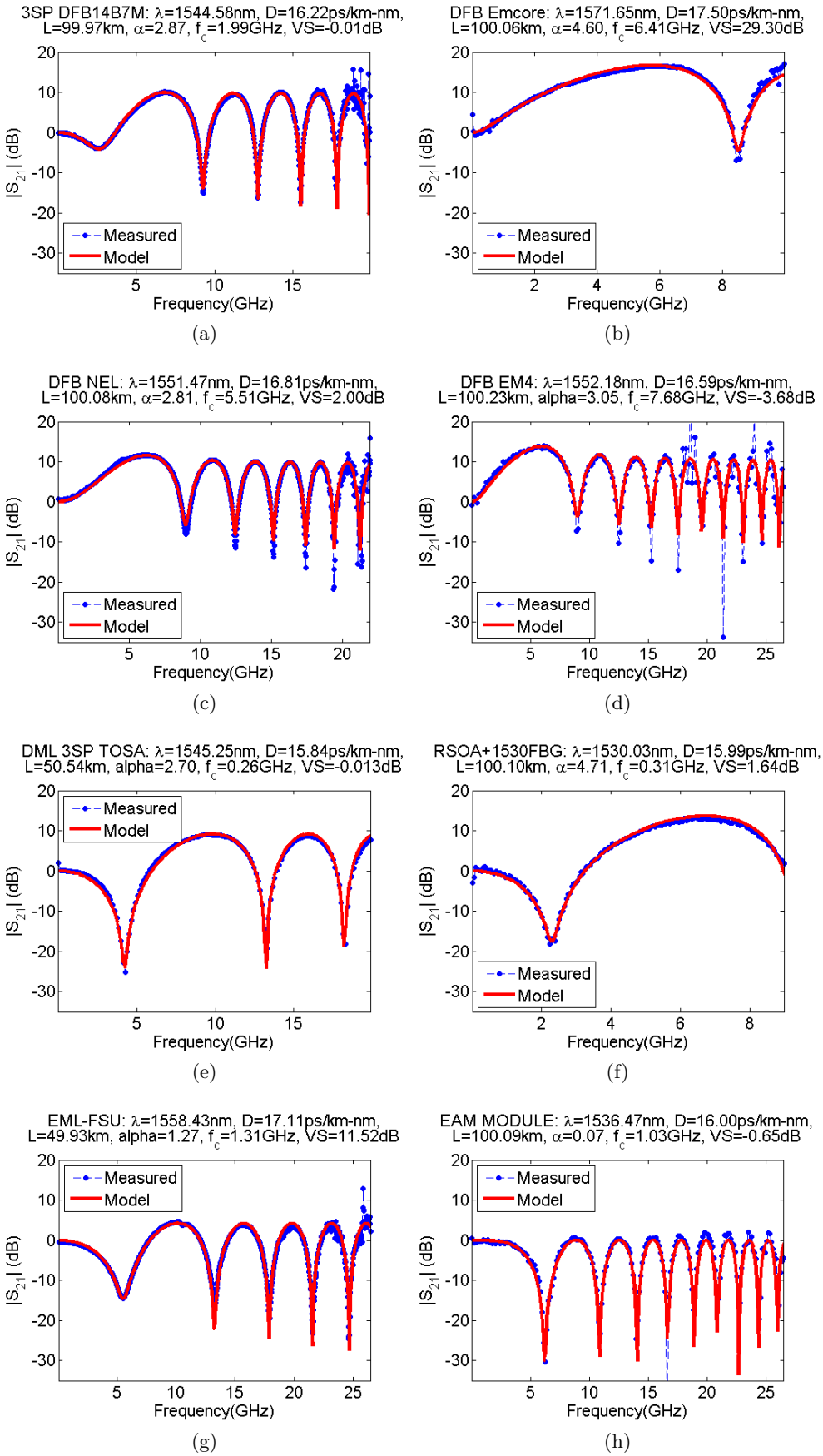

Figure 4.5: (a) DFB 3SP 14B7M butterfly package. (b) DFB EMCORE 1995YY-A-DI-1570-FA. (c) DFB NEL NLK5C5EBKA. (d) DFB EM4 E0037751. (e) DFB 3SP TOSA package. (f) RSOA + 1530nm FBG. (g) EAM FSU-684sea-7. (h) EAM MODULE

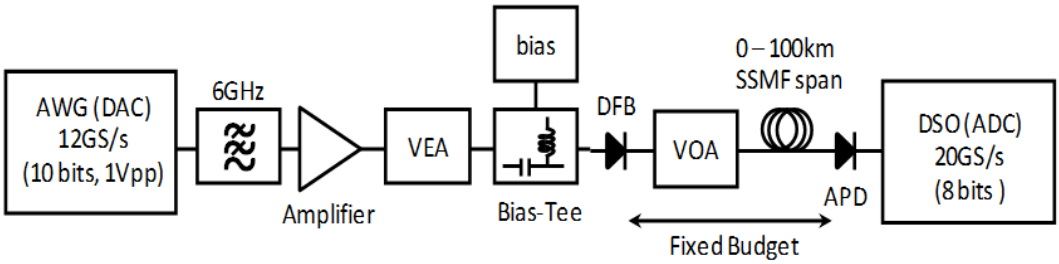

Figure 4.6: Experimental setup.

In this section, we experimentally address the dynamics of the SNR variation of an IMDD OFDM transmission for different intensity modulation indices and accumulated dispersions in the link. To some extent, we confirm the effects reported in [11–13] and highlight the importance of the optimization of the signal's modulation index for a specific fiber length. Owing to the complexity behind the mathematical modeling of the channel, such an experimental investigation proves to be quite useful as far as an optimization of the system's capacity for different fiber configurations is concerned.

4.3.1 Experimental Setup and System Parameters

The experimental setup used in this work is shown in Figure 4.6. The transmitted OFDM signal has 255 data subcarriers and we use Hermitian symmetry (512 inputs IFFT) to generate a purely real baseband signal and avoid I/Q impairments. 32 samples per symbol are used as cyclic prefix and the signal occupies a $5GHz$ baseband bandwidth. For matters of SNR investigation, all subcarriers have the same power and are mapped with QPSK.

The digital OFDM signals are generated with Matlab® and sent to an Arbitrary Waveform Generator (AWG) Tektronix AWG7122B which plays the role of Digital-to-Analog Converter and creates the analog signal at $12GS/s$ with a $10bits$ vertical resolution. The AWG's vertical output is limited to $1Vpp$ and we set a scaling factor of $13dB$ that guarantees that the probability of a peak extrapolating this range is below 0.01%, avoiding thus any clipping noise.

A $6GHz$ low-pass filter is added after the AWG to eliminate the signal replicas generated in digital-to-analogue conversion. The voltage profile of the time-domain OFDM signal follows a Gaussian distribution, as seen in Figure 4.7(a).

The analogue OFDM signal is then amplified by an electrical power amplifier (Picosecond Pulse Labs Model 8001) which is set to an optimal amplification gain, previously deduced in electrical back-to-back measurements. A variable electrical attenuator (VEA) is used to change the intensity modulation indices of the signal. Figure 4.7(b) shows the spectrum of the digital OFDM signal. Figure 4.7(c) shows the spectrum of the analog OFDM signal measured with an Anritsu MS2719B spectrum analyzer after the VEA at maximum RF power.

The bias-tee, which adds the DC component ($135mA$) to the amplified OFDM signal, is integrated in the laser module. The laser is a $15.5GHz$ DFB, model E0037751 from EM4, whose parameters at $135mA$ bias current are listed in Table 4.1.

The signal is then transmitted through different SSMF spans that varied from 0 to $100km$. The optical budget is kept always constant at $29dB$ by means of a variable optical attenuator (VOA). Down-conversion from the optical to the electrical domain is done with an $8GHz$ APD AT10SFA from Picometrix. The $40GS/s$ ADC of the Digital Sampling Oscilloscope Tektronix TDS6124 then digitizes the electrical signal with $8bits$ vertical resolution.

Sampling Frequency Offset between DAC and ADC is in the order of $5KS/s$ and is estimated and corrected after FFT according to the method shown in subsection 3.5.3. Equalization is done after channel estimation with 30 preamble symbols. The same preamble is also used in the second step of the time synchronization procedure for first symbol identification, after a cyclic

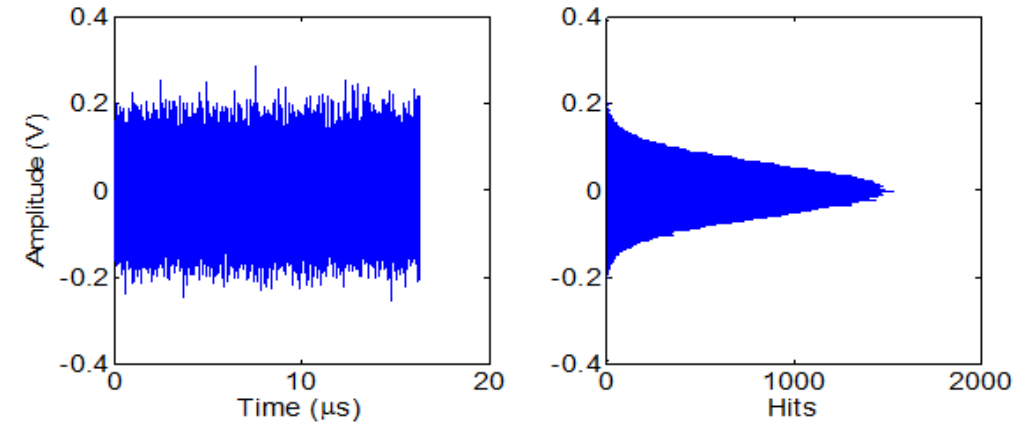

(a)

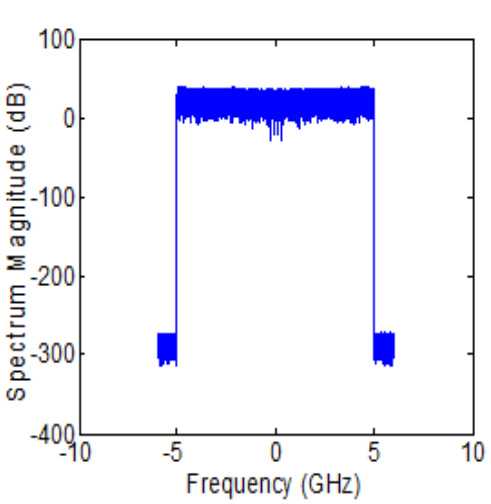

(b)

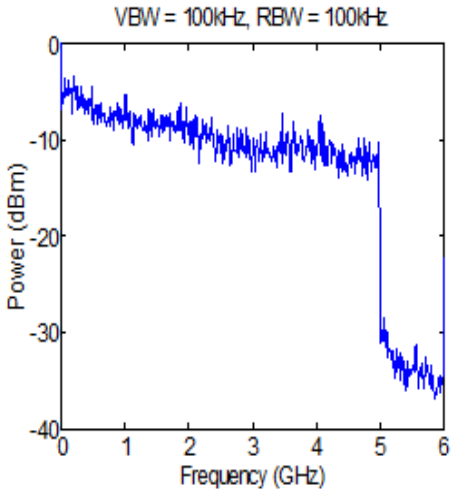

(c)

Figure 4.7: Digital OFDM signal in the (a) time domain with characteristic Gaussian voltage distribution. (b) Digital OFDM signal spectrum. (c) Analog OFDM signal spectrum after VEA.

Symbol	Quantity	Value
BW_{3dB}	$3dB$ bandwidth	$15.5GHz$
λ_c	Central wavelength	$1551.42nm$
$\Delta\lambda_{3dB}$	FWHM	$0.05nm$
P_o	Mean optical power	$12.3dBm$
α	Linewidth enhancement factor	3.3
f_c	Adiabatic chirp frequency	$7.83GHz$

Table 4.1: Laser Parameters @$135mA$ and 25^oC

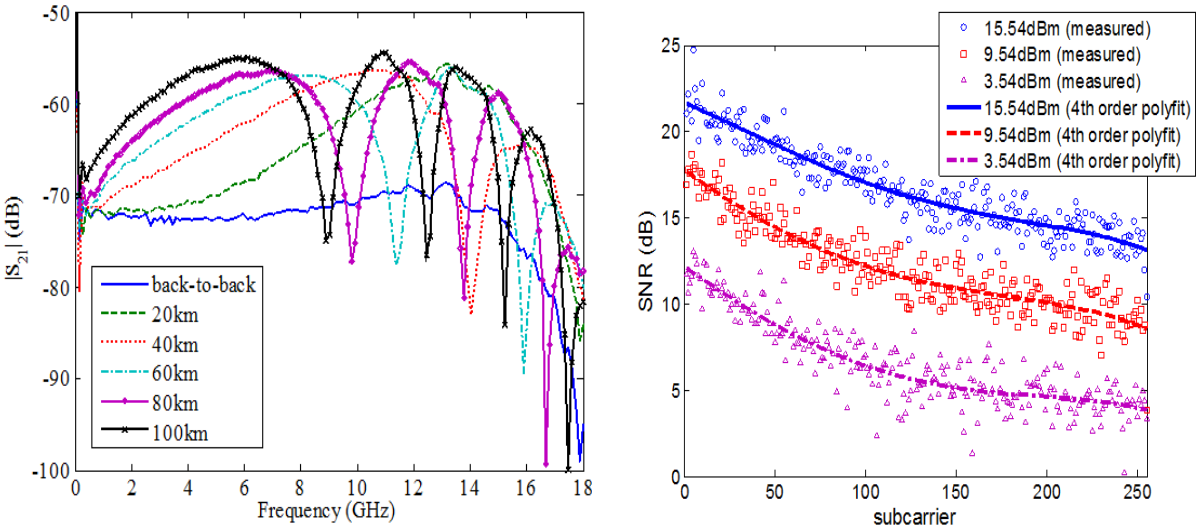

(a) (b)

Figure 4.8: (a) Channel frequency responses for different lengths of fiber. (b) Subcarriers' SNR measurement in optical back-to-back for different modulation powers.

prefix-based DFT window synchronization process (see subsection 3.5.2). The received digital signal is then post-processed with Matlab and some performance parameters are then inferred over 300 symbols.

The laser small-signal chirp parameters estimation is shown in Figure 4.5(d). Figure 4.8(a) shows the single-tone small signal channel frequency responses for all span configurations. Measurements were done with $0dBm$ RF power and the same optical budget in all cases. As predicted in section 2.5, we can notice a gain in the $0-5GHz$ bandwidth where the signal is located due to the coupling between intensity and phase modulations and the adiabatic and transient chirp characteristics of the laser.

4.3.2 Results and Discussions

In order to inspect the non-linearities arriving from the electro-optical conversion at the emitter, we started our study in the optical back-to-back scenario. Figure 4.8(b) shows the subcarriers' SNR in the optical back-to-back configuration for different modulation powers of the OFDM signal. The SNR measurements have been fitted to 4-th order polynomials to smooth down the curves and facilitate the analysis. As far as the laser nonlinearities in the electro-optical conversion are concerned, the highest RF power should be responsible for the worst scenario, i.e., the one that would cause higher harmonic and intermodulation distortions in the optical signal. It can be seen, however, that the best SNRs are obtained with the highest modulation power, meaning that the laser's electro-optical conversion remains quite linear and the nonlinear distortions at the electro-optical conversion are negligible. In other words, the gain that is provided by the electrical amplifier is not high enough to cause the clipping of the signal at the emitter and we can exclude this hypothesis of the dynamics of the multicarrier, large-signal channel frequency response.

We have carried out the same analysis for different fiber spans. We remind that the optical budget was kept constant at $29dB$ for all cases, meaning that all SNR measurements are subjected to the same losses due to attenuation. Figure 4.9 shows the different SNR vs. subcarrier vs. signal power maps for different fiber lengths, including the previously shown back-to-back case.

From Figure 4.9, we can notice that the optimal RF power configuration varies with the

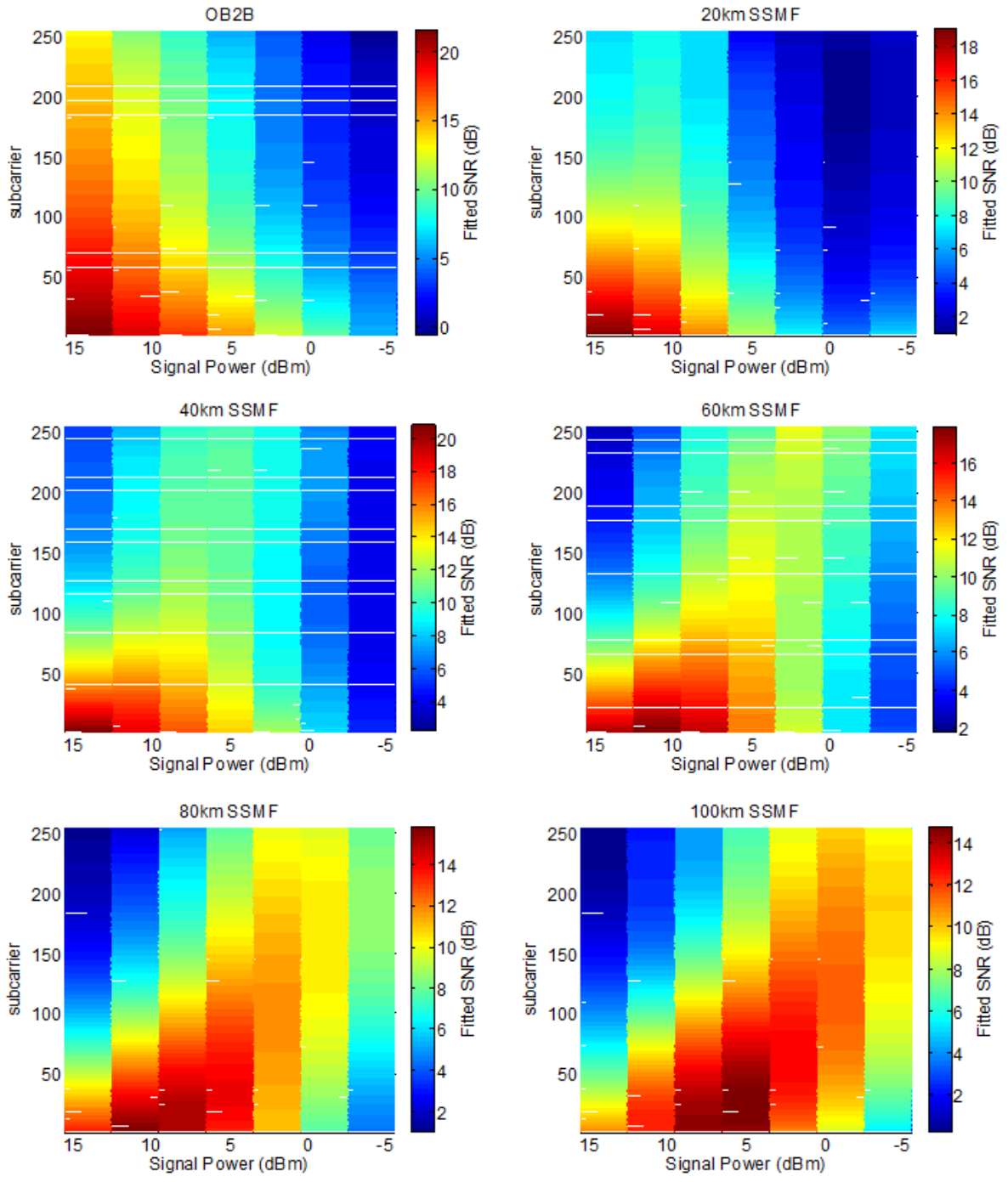

Figure 4.9: SNR maps for different fiber spans. The optical budget is kept at $29dB$ in all cases.

amount of accumulated dispersion in the link. Indeed, if we keep the highest RF power (which in the optical back-to-back configuration allowed for the best SNR) in the $100km$ transmission, the subcarriers' SNR will considerably degrade. Such effect can also be perceived with an evaluation of the OFDM signal in the time and frequency domains. Figures 4.10(a) and (b) show respectively the received time and frequency domain signals in the optical back-to-back and $100km$ SSMF configurations when the highest modulation power is used.

We can see that the voltage distribution remains Gaussian in the optical back-to-back case but the signal is quite distorted in the $100km$ configuration. Indeed, the time domain voltage profile seems to have changed from a Gaussian to a Rayleigh distribution. We may also perceive some pronounced out-of-band products in the signal spectrum shown in Figure 4.10(b), which can be extremely degrading in a multi-band transmission such as shown in section 3.8. In the optical back-to-back measurement, the limits of the signal spectrum remain well demarcated. There may be some harmonic products arriving from the IM component due to nonlinear electro-optical conversion in the laser but these are too small to be evidenced outside the $5GHz$ bandwidth. Intermodulation products may also be present but are indistinguishable from the transmitted signal.

The effects of the PM component will not be seen in optical back-to-back. Without dispersion, the left and right-hand side PM components with respect to the optical carrier will cancel out in the squared detection at the receiver [12]. In this case, the electrical signal at the receiver is composed exclusively of the IM term, even if the PM component exists. However, the fiber chromatic dispersion will generate a phase variation between the PM side bands which will then become detectable at the received electrical signal. In addition, if we admit that we are in the LSR, the Bessel expansion of the PM term will have several harmonics which will generate some pronounced distortions inside and outside the OFDM signal bandwidth. Indeed, this phenomenon has already been reported in [11–13] for single-tone and SCM signals.

In order to exclude other possible causes for this effect such as fiber nonlinear effects or saturation of the detector's Transimpedance Amplifier (TIA), we have repeated the experiment under different conditions.

The distortion phenomenon is still present even with lower mean optical powers at the input of the fiber. We have also stimulated the saturation effect at the TIA by injecting higher powers at the photodiode but the voltage distribution of the signal was characterized by a symmetrically clipped profile which was different from the one shown in Figure 4.10(b). This is a plausible result if we assume that the TIA is preceded by a DC block. We have also conducted the same experiment with a photodiode that was not followed by an electrical amplification stage and we have even simulated the same transmission chain using VPI^{TM} and assuming that all components were perfectly linear. The phenomenon was still present.

To facilitate the conclusions on the results shown in Figure 4.9, let us introduce the concept of multi-carrier SNR [14]. The multi-carrier SNR is a single SNR that characterizes the whole set of subcarriers by an equivalent single-carrier Additive-White-Gaussian-Noise (AWGN) channel capable of achieving the same data rate:

$$SNR_{MC} = \Gamma \left[\left(\prod_{k=1}^{N_D} \left(1 + \frac{SNR_k}{\Gamma} \right) \right)^{\frac{1}{\Gamma}} - 1 \right] \tag{4.3}$$

with N_D being the number of data subcarriers (255) and Γ the SNR gap to capacity, which is set to $5dB$. The multi-carrier SNR represents a good way of characterizing the channel without the use of bit and power loading algorithms. By considering the multi-carrier SNR definition, we can eliminate the subcarrier dimension in our RF optimization analysis. Figure 4.11(a) shows the variation of the SNR_{MC} with the RF power of the modulating OFDM signal for different fiber spans. The parabolic profile of the curves shows that there is an optimal modulation power for which the effects of the PM term of the signal are optimized. Indeed, in such points, we have

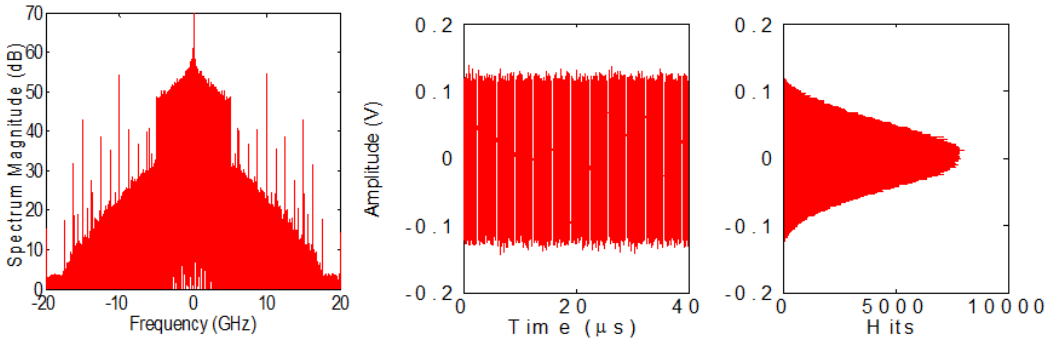

(a)

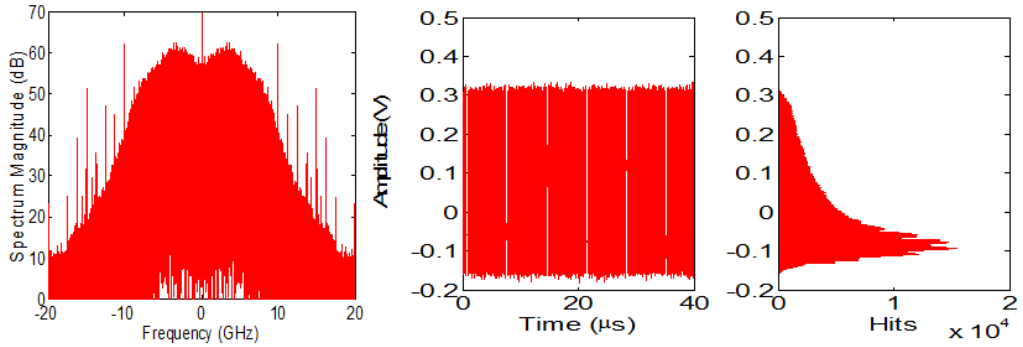

(b)

Figure 4.10: Received time and frequency domain OFDM signal after quadratic detection and propagation through (a) 0 km and (b) 100km SSMF fiber. Here, the highest modulation power is used.

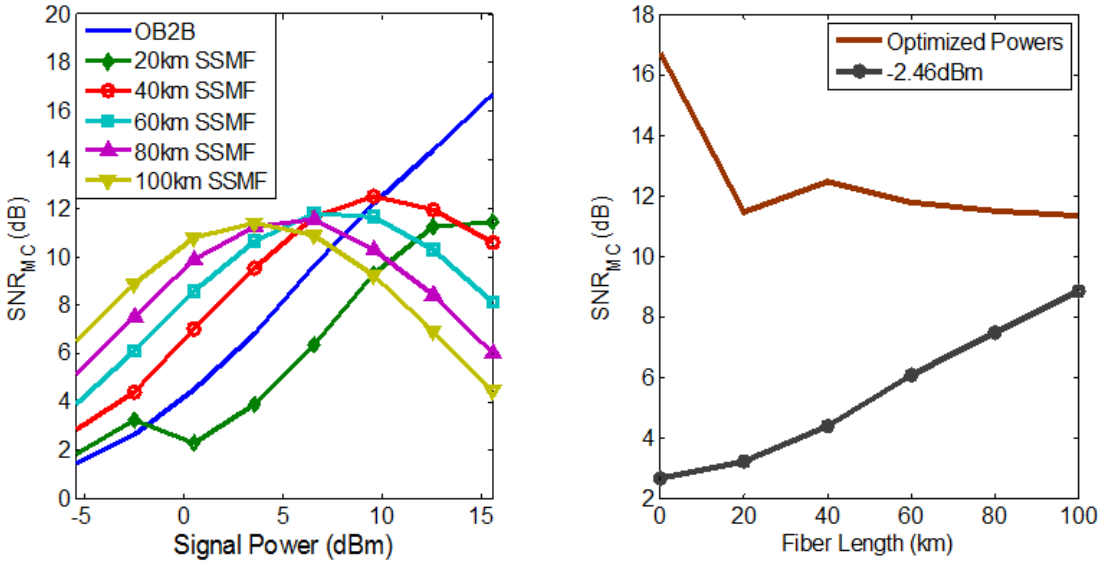

(a) (b)

Figure 4.11: (a) Variation of the multi-carrier SNR with the signal power for different fiber lengths. (b) Comparison between the optimal modulation and the small-signal scenario.

an equilibrium between the gain created by the PM-to-IM conversion in the channel frequency response and the distortions arriving from the laser chirp and fiber dispersion.

This optimal point varies with the accumulated dispersion in the link, highlighting the dependence of the phase modulation component with the product D×L. Figure 4.11(b) shows a comparison between the optimal SNR_{MC} values and the SNR_{MC} for $-2.46dBm$ RF power for different fiber lengths. When the signal RF power is very low, the dynamics of the transmission converge to that of the small-signal single carrier model evidenced in the previous section and confirmed with the measurements shown in Figure 4.8. Indeed, with a small modulating power, we can perceive an improvement of the channel with increasing fiber lengths which is perfectly reasonable since the signal is in the $0-5GHz$ band. The small-signal regime also provides for the smallest out-of-band products. However, the small-signal condition does not manage to offer better results than the optimized RF configurations as far as the in-band SNR is considered.

4.4 Conclusions

We have seen in this chapter that even if the IMDD channel model allowed a fast and efficient way of characterizing the chirp parameters of different types of light sources through fitting with the measurements retrieved with a network analyzer, the OFDM propagation was indeed subjected to more complex phenomena. Due to the laser chirp and the phase variations between the signal side-bands caused by fiber chromatic dispersion, the optimum modulation power at the transmitter-side is characterized by an intricate interference pattern between the signal subcarriers which can lead to pronounced SNR degradation and considerable increase of the out-of-band noise levels of the system. We have then shown the interest of the experimental investigation of the best operation points for different lengths of optical fiber not only for matters of improvement of the quality of the transmission but also for reducing the levels of noise that might affect other users under a MB-OFDM downstream multicarrier approach on a PON.

References

[1] J. A. Nelder and R. Mead. "A simplex method for function minimization". In: *The Computer Journal* 7 (1965), pp. 308–313. URL: http://comjnl.oxfordjournals.org/content/7/4/308.full.pdf (cit. on p. 112).

[2] Qian Déniel et al. "Transmission Jusqu'à 10Gbit/s basée sur un Laser à Cavité Externe Utilisant un RSOA et un Réseau de Bragg Photo-inscrit sur Fibre pour WDM PON". In: *Journées Nationales d'Optique Guidée (JNOG)*. 2012 (cit. on p. 115).

[3] T.E. Darcie, R.S. Tucker, and G.J. Sullivan. "Intermodulation and harmonic distortion in InGaAsP lasers". In: *Electronics Letters* 21.16 (Jan. 1985), pp. 665 –666. ISSN: 0013-5194. DOI: 10.1049/el:19850470 (cit. on p. 115).

[4] J. Helms. "Intermodulation distortions of broad-band modulated laser diodes". In: *Lightwave Technology, Journal of* 10.12 (Dec. 1992), pp. 1901 –1906. ISSN: 0733-8724. DOI: 10.1109/50.202844 (cit. on p. 115).

[5] P. Iannone and T.E. Darcie. "Multichannel intermodulation distortion in high-speed GaInAsP lasers". In: *Electronics Letters* 23.25 (Mar. 1987), pp. 1361 –1362. ISSN: 0013-5194. DOI: 10.1049/el:19870939 (cit. on p. 115).

[6] J. Le Bihan et al. "Bessel function analysis of harmonic distortion in semiconductor lasers". In: *Electronics Letters* 29.10 (May 1993), pp. 834 –835. ISSN: 0013-5194. DOI: 10.1049/el:19930557 (cit. on p. 115).

[7] S.J. Wang and N.K. Dutta. "Intermodulation and harmonic distortion in GaInAsP distributed feedback lasers". In: *Electronics Letters* 25.13 (June 1989), pp. 850 –852. ISSN: 0013-5194. DOI: 10.1049/el:19890573 (cit. on p. 115).

[8] W. Way. "Large signal nonlinear distortion prediction for a single-mode laser diode under microwave intensity modulation". In: *Lightwave Technology, Journal of* 5.3 (Mar. 1987), pp. 305 –315. ISSN: 0733-8724. DOI: 10.1109/JLT.1987.1075517 (cit. on p. 115).

[9] J. Le Bihan and G. Yabre. "FM and IM intermodulation distortions in directly modulated single-mode semiconductor lasers". In: *Quantum Electronics, IEEE Journal of* 30.4 (Apr. 1994), pp. 899 –904. ISSN: 0018-9197. DOI: 10.1109/3.291359 (cit. on p. 115).

[10] G. Yabre. "Interferometric conversion of laser chirp to IM: effect of the interferometer free spectral range on the output nonlinear distortion". In: *Photonics Technology Letters, IEEE* 8.10 (Oct. 1996), pp. 1388 –1390. ISSN: 1041-1135. DOI: 10.1109/68.536664 (cit. on p. 115).

[11] G. Meslener. "Chromatic dispersion induced distortion of modulated monochromatic light employing direct detection". In: *Quantum Electronics, IEEE Journal of* 20.10 (Oct. 1984), pp. 1208 –1216. ISSN: 0018-9197. DOI: 10.1109/JQE.1984.1072286 (cit. on pp. 115, 117, 121).

[12] E. Peral and A. Yariv. "Large-signal theory of the effect of dispersive propagation on the intensity modulation response of semiconductor lasers". In: *Lightwave Technology, Journal of* 18.1 (Jan. 2000), pp. 84 –89. ISSN: 0733-8724. DOI: 10.1109/50.818911 (cit. on pp. 115, 117, 121).

[13] E. Peral and A. Yariv. "Large-signal analysis of the effect of dispersive propagation on the intensity modulation response of semiconductor lasers". In: *Lasers and Electro-Optics, 1999. CLEO '99. Summaries of Papers Presented at the Conference on*. May 1999, pp. 311 –312. DOI: 10.1109/CLEO.1999.834236 (cit. on pp. 115, 117, 121).

[14] T. Starr et al. *Understanding digital subscriber line technology*. Prentice Hall communications engineering and emerging technologies series vol. 1. P, 1999. ISBN: 9780137805457. URL: http://books.google.fr/books?id=gQ5TAAAAMAAJ (cit. on p. 121).

Chapter 5

Downstream Transmission (OLT⇒ONU)

5.1 Introduction

In this chapter we focus on the downstream transmission of a typical IMDD OFDM signal with bit and power loading capabilities. We start by evaluating the transmission performances in terms of bit rate and optical budget with different types of lasers and photodetectors after previously characterizing the components according to the parameters highlighted in chapter 2. We also investigate the use of optical amplification by means of an Erbium Doped Fiber Amplifier (EDFA) and the effects of laser chirp on a multiuser approach allowing sharing the subcarriers among several subscribers. Moreover, we finish this chapter by a comprehensive evaluation of the practical implementation of OFDM for next generation PON under different types of possible architectures and multiplexing approaches.

5.2 Typical Downstream Transmission

Downstream IMDD OFDM transmissions have been extensively investigated previously to this work using different types of light sources, including a DFB laser and low-bandwidth VCSEL [1, 2]. In this section, we show the OFDM performances of a TOSA-packaged DFB laser developed in the framework of project EPOD.

The Transmission Optical Sub-assembly (TOSA) encapsulation has been developed to answer a growing need of miniaturized and thermally-efficient packages on the market. Their small footprint and high heat dissipation capacity are particularly interesting as far as next generation optical networks are concerned. The module evaluated here is shown in Figure 5.1. It consists of the same laser as the one used in the butterfly module 14B7M, also developed in the same project.

5.2.1 Laser Characterization

Fig. 5.2(a) and (b) show respectively the $P \times I$ and electro-optical conversion efficiency curves of the laser at $25°C$. The laser's threshold current is approximately $18mA$ and linear operation region is situated between 20 and $100mA$. The laser's saturation region has been avoided in the $P \times I$ characterization to preserve the prototype. Figure 5.3(a) depicts the laser's frequency responses at $25°C$ and $30°C$ for currents varying from 50 to $90mA$. The laser's $3dB$ bandwidth variation with the bias current is shown in Fig. 5.3(b).

We have also carried out chirp measurements using the method shown in section 4.2 over $50km$ SSMF. Figure 5.4 sums up the evolution of α and f_C for different bias currents. The fittings from which the parameters were estimated can be found in appendix C. It can be seen that α

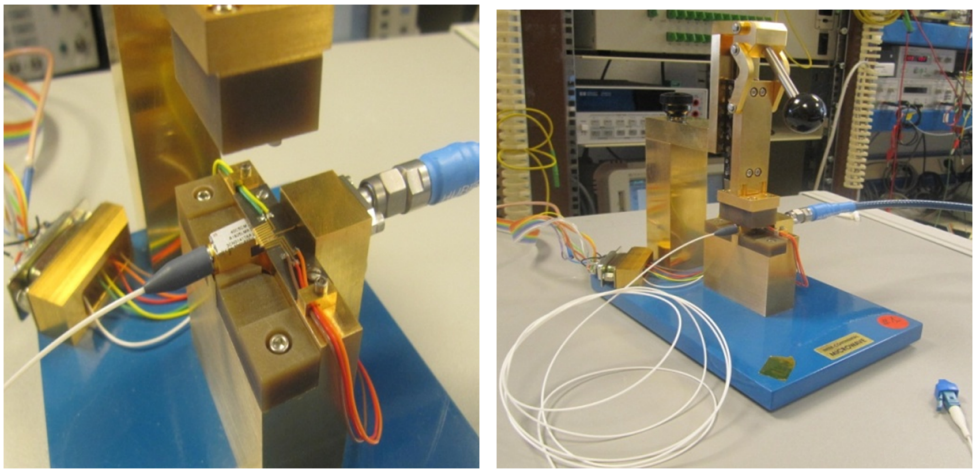

Figure 5.1: Detail on TOSA laser and transmitter set-up.

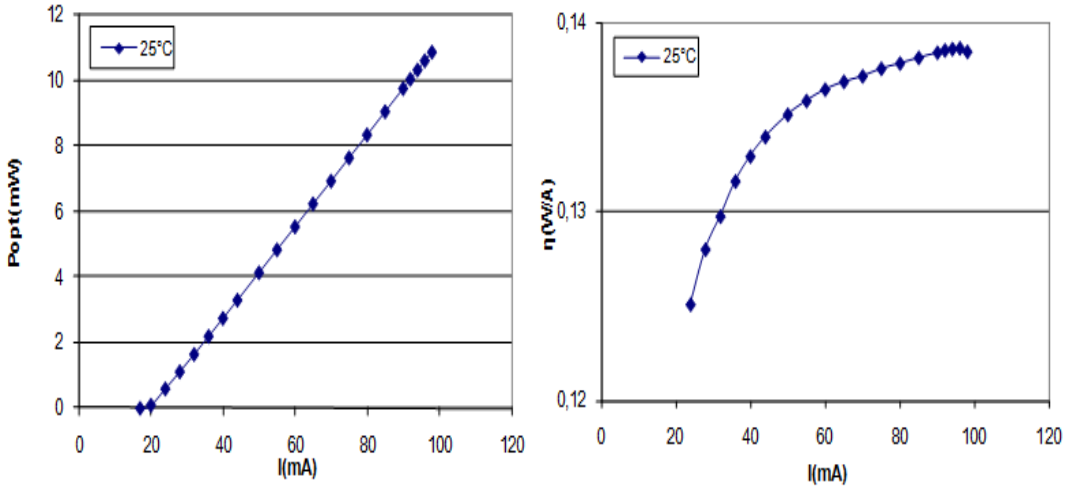

(a) (b)

Figure 5.2: TOSA static characterization. (a) $P \times I$ and (b) electro-optical conversion efficiency curves.

did not vary much over all measurements but is inversely proportional to the bias current. The FM component, related to f_c, remains stable until approximately $65mA$ and starts to increase after that. This fact is easily confirmed by comparing the depths of the first dips in Figure C.1; there is roughly a $10dB$ difference between the first dip levels at 50 and $90mA$ when the laser is controlled at 25^oC.

5.2.2 AMOOFDM Transmissions with PIN and APD

Fig. 5.5 shows the experimental setup used to evaluate the laser's performance under Adaptively Modulated Optical OFDM (AMOOFDM) IMDD modulation. The $12GHz$ OFDM signal is composed of 255 information subcarriers (512 inputs at the IFFT after Hermitian symmetry), 16 samples of cyclic prefix and is sampled at $24GS/s$ at the transmitter side with $10bits$ vertical resolution. The scaling factor is set to $13dB$ and the DAC's maximum peak-to-peak voltage is $1V$. Levin-Campello algorithm is used to optimize the mapping and power level per subcarrier according to the channel frequency response after measurement with a probing signal. An

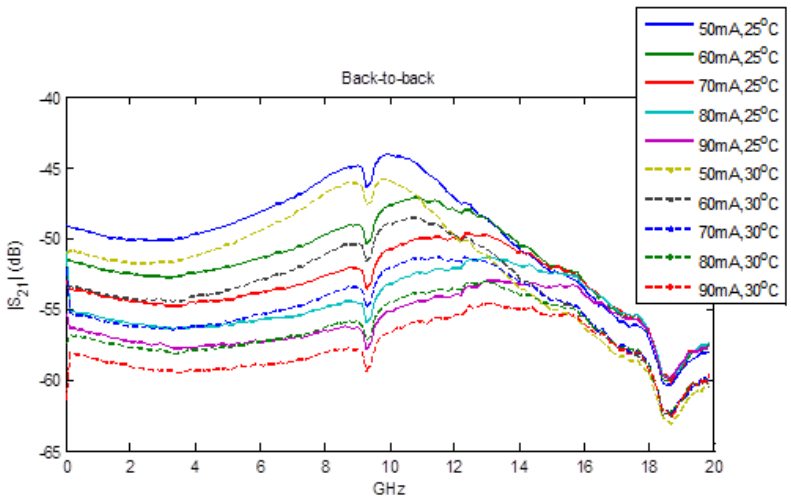

(a)

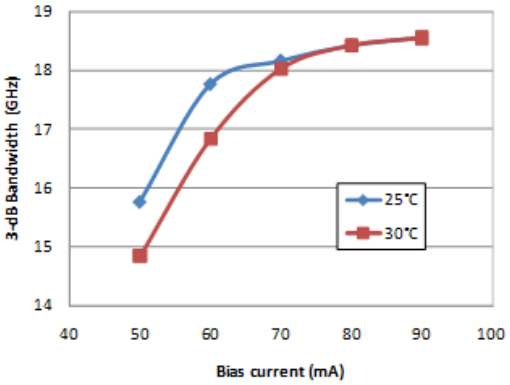

(b)

Figure 5.3: (a) frequency response for different bias currents at 25°C and 30°C. (b)Laser's 3-dB bandwidth evolution with bias current at 25°C and 30°C.

electrical amplifier (kept fixed at an optimized gain value) and an electrical attenuator were used to increase and optimize the power of the signal that directly modulates the laser after proper biasing. At the receiver side, the signal is detected with either a $8GHz$ APD or a $33GHz$ PIN. The ADC acquires the signal at $40GS/s$ and $8bits$ vertical resolution.

The bit rate variation with the optical budget was evaluated in the optical back-to-back configuration and with a $50km$ SSMF span. Fig. 5.6 shows a preliminary bit rate evaluation for different mean optical powers at the inputs of the photodiodes in optical back-to-back. Even with non-optimal values of bias currents and RF powers at the transmitter side, bit rates of up to $35Gb/s$ at $13dB$ optical budget and $31Gb/s$ at $22dB$ optical budget were attained with the PIN and APD photodiodes respectively. This similarity in the maximum bit rates despite the huge differences in the photodetectors' bandwidths, indicates the high influence of the AWG's roll-off to about $8GHz$. In addition, even if the $3dB$ bandwidths of the components serve as a quite good indicative of the performances of the transmission, we should remember that some subcarriers can still be modulated beyond these values thanks to the adaptive bit and power loading algorithm.

The expected gap between the PIN and APD curves is due to the APD's better sensitivity as mentioned in chapter 2. $10Gb/s$ is still feasible after 23 and $34dB$ optical budgets with the PIN and APD photodiodes respectively.

After these first measurements, the laser's operation point is optimized by means of an

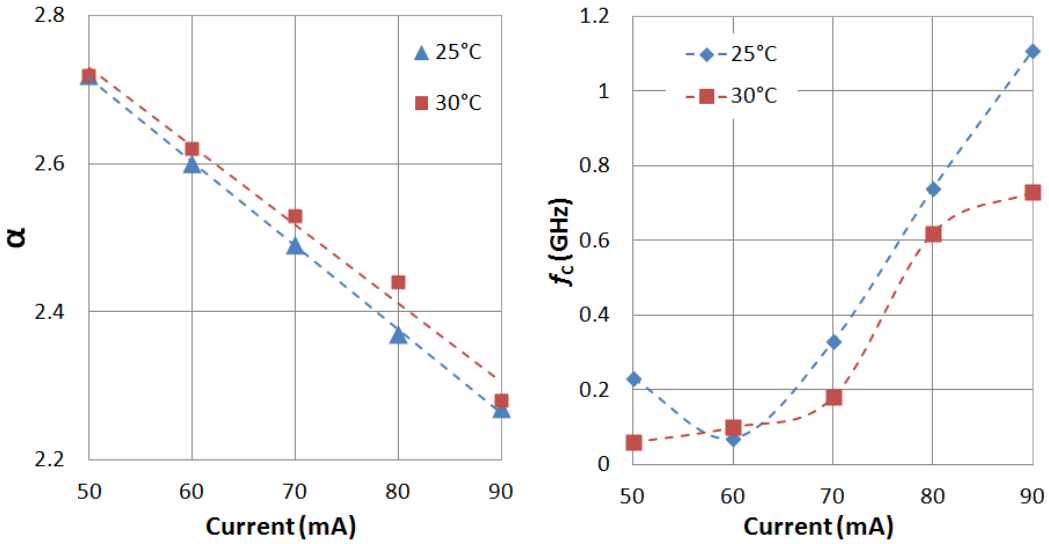

(a) (b)

Figure 5.4: Chirp measurements based on IMDD IM+PM+FM model for different bias currents at (a) $25°C$ and (b) $30°C$.

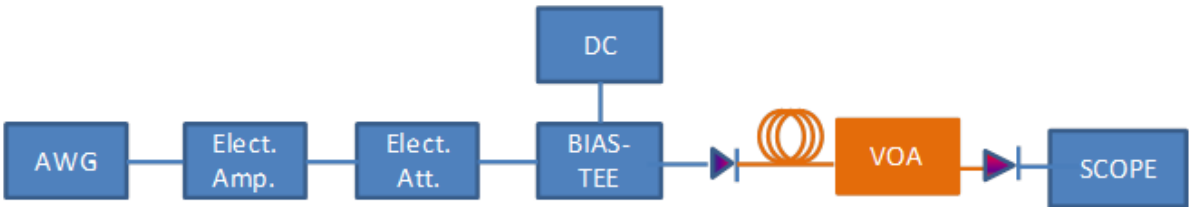

Figure 5.5: Experimental setup used to evaluate TOSA module on IMDD AMOOFDM transmission.

evaluation of the transmission throughput. Figure 5.7(a) shows the optical back-to-back bit-rate cartography for different values of bias currents and RF powers (electrical attenuation values in the VEA) with a fixed mean optical power of $-13dBm$ at the photodiode. By using the optimized bias and RF power values, the maximum bit rates could be increased to $37Gb/s$ and $33Gb/s$ with the PIN and APD photodiodes respectively, as shown in Figure 5.7(b).

Figure 5.8 compares the back-to-back results with the ones found after propagation over $50km$ SSMF. Table 5.1(a) summarizes the optical budgets for $20Gb/s$ and $10Gb/s$ bit-rates after $50km$. If we consider a $3.5dB$ loss per two-stage splitter, this setup would allow either a $10Gb/s$ PON network with 8 or 64 clients (PIN or APD respectively) or a $20Gb/s$ PON with 4 or 8 clients (PIN or APD respectively). It should be noted that an improvement on the bit rate can still be obtained with further optimization of the bias and RF power of the signal, as seen in chapter 4. The penalties due to fiber insertion at 10 and $20Gb/s$ are shown in Table 5.1(b).

We may conclude here that the PIN did not manage to provide better performances when submitted to propagation through a SSMF span despite its higher modulation bandwidth. This is because of its worst sensitivity if compared to the APD. In the next section, we investigate the use of EDFA to increase the optical budgets allowed with PIN photodiodes.

5.3 Optically Amplified OFDM

There are several solutions to extend the optical budgets on PONs. AMOOFDM transmissions with in-line optical amplification have been reported [4] using either an Erbium Doped Fiber Am-

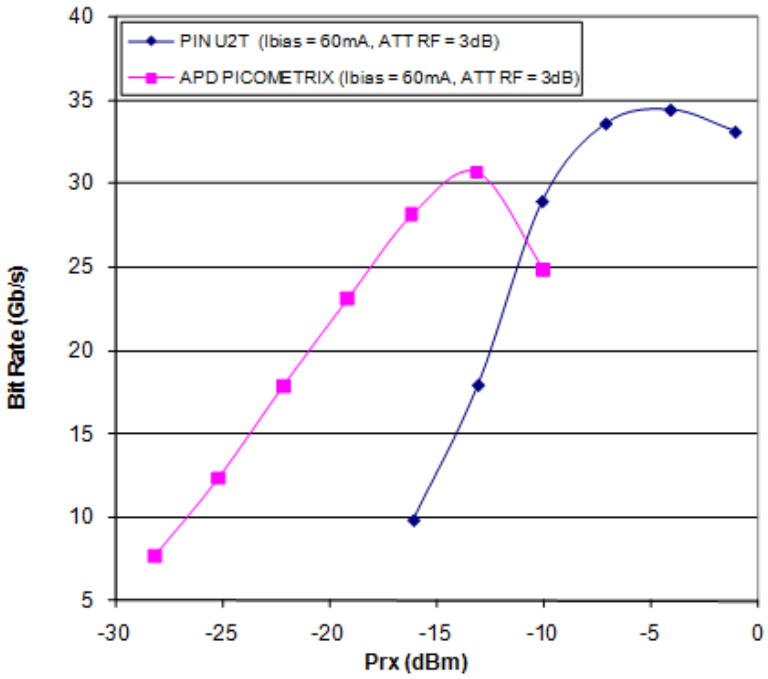

Figure 5.6: Preliminary back-to-back bit rate evaluation with PIN and APD.

$50km$ SSMF	PIN	APD
10Gb/s	23dB	32dB
20Gb/s	18dB	23dB

(a)

Penalty due to $50km$ fiber insertion	PIN	APD
$10Gb/s$	$2.5dB$	$2dB$
$20Gb/s$	$4dB$	$7dB$

(b)

Table 5.1: (a) Optical budgets at 10 and $20Gb/s$ after propagation through $50km$ SSMF. (b) Power penalties at 10 and $20Gb/$s after propagation through $50km$ SSMF

plifier (EDFA) or a Semiconductor Optical Amplifier (SOA) at the local exchange. Despite its worst performances in terms of noise figure (NF) and gain, the SOA presents several advantages over the EDFA namely easy monolithic integration, need of lower operating currents, compactness and capability of operating over a larger wavelength window. An optical budget of $45dB$ over two $10km$ trunks and a bit rate higher than $5Gb/s$ has been successfully demonstrated. By the way, reach extended GPON are standardized under ITU-T G984.6 using either an optical amplifier or an optical-electrical-optical (OEO) converter. Despite a simple implementation, the great disadvantage of the OEO approach is its high electrical consummation.

The use of Raman amplifiers has also been recently reported [3] to allow up to $50km$ bidirectional GPON transmissions with $1:64$ split ratio. The advantage of this approach is maintaining a passive outside plant by using pump lasers deployed at the OLT. However, the laser safety concerns should be increased since high optical powers are needed to stimulate the amplification effect. Furthermore, this is certainly not the most appropriate solution in terms of power consumption.

In this section, we evaluate the use of an EDFA either on the transmitter side (booster mode) or on the receiver side (pre-amplification mode) to increase the performances of an AMOOFDM transmission in the C band. Similarly to [3], we also maintain a passive outside plant but use a safer and "greener" device.

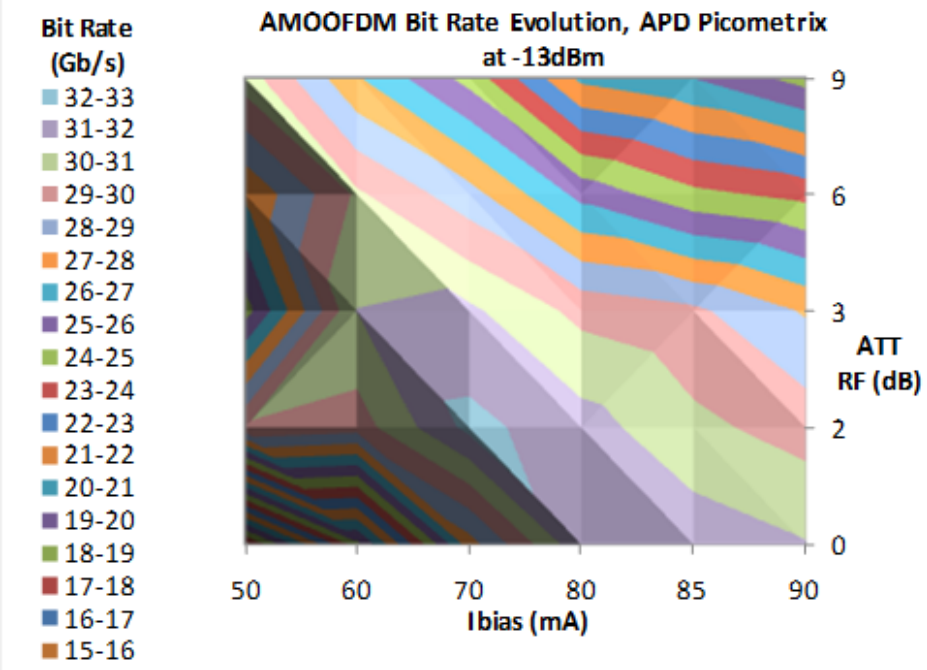

(a)

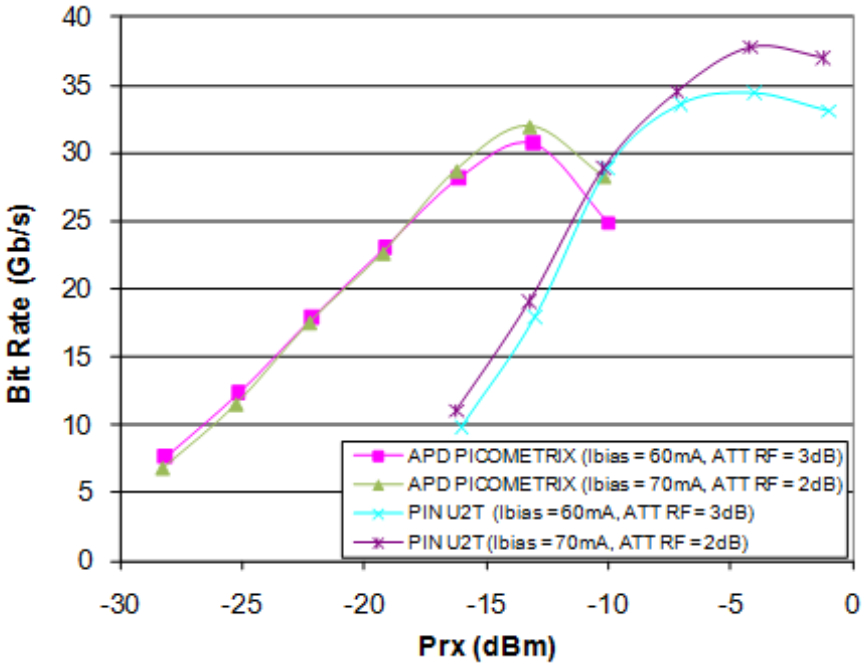

(b)

Figure 5.7: (a) Bias and RF power optimization results in back-to-back transmission. (b) Maximum bit rate increase with optimized values of bias current and RF power.

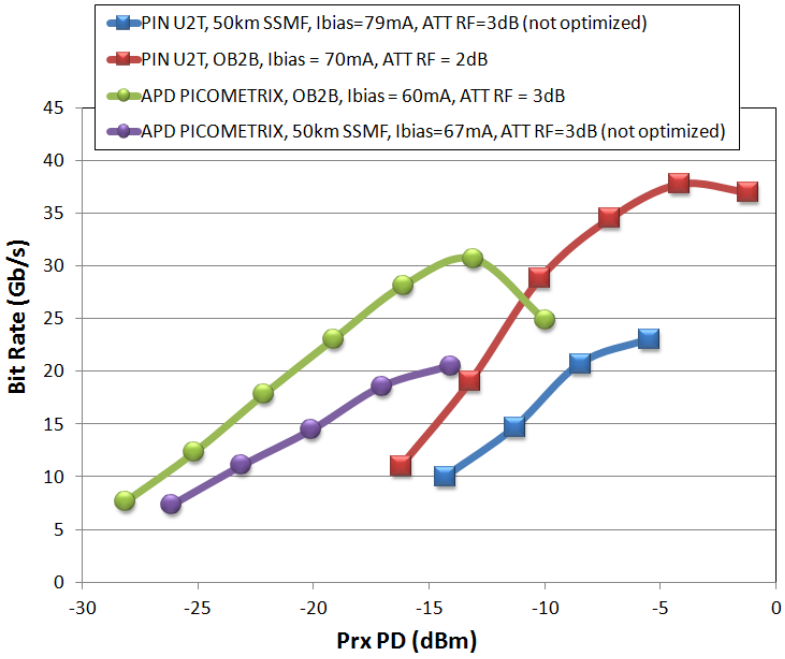

Figure 5.8: Comparison between back-to-back and 50 km SSMF propagation.

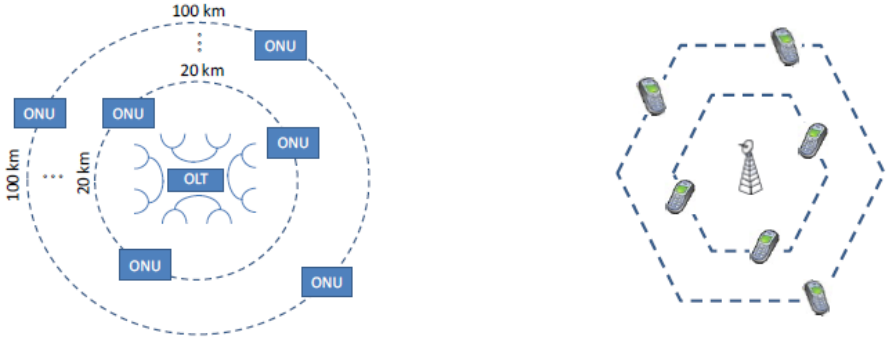

Figure 5.9: Cell-based analysis on Passive Optical Networks and analogy with mobile networks.

We compare the unamplified configuration with the booster and pre-amplified set-ups for fixed split ratios and we investigate the bit rate variation of the system with different SSMF spans. Thus, by keeping the same number of users for all span lengths, it is possible to make an analogy in terms of range and coverage between PON and standard mobile networks, as depicted in Figure 5.9.

5.3.1 Experimental Set-ups

The AMOOFDM are constituted of 255 data subcarriers constituting 512 inputs at the IFFT to generate a real-valued baseband signal through Hermitian symmetry. 8 samples per frame are used as cyclic prefix and each acquisition is composed of 300 symbols. The signal is sampled at $24GS/s$ at the emitter-side. The Levin-Campello algorithm is used to optimize channel capacity for a target BER of 10^{-3}. Figure 5.10 shows a typical output of the transmission program with the modulation level (varying from BPSK up to 128-QAM), BER and EVM per subcarrier as well as the constellation of the subcarrier number 10.

The Arbitrary Waveform Generator is responsible for the digital to analogue conversion with $13dB$ scaling factor and maximum peak-to-peak voltage of $1V$. The power of the signal that modulates the laser and its bias current are respectively optimized between $11.8dBm$ to $7.8dBm$

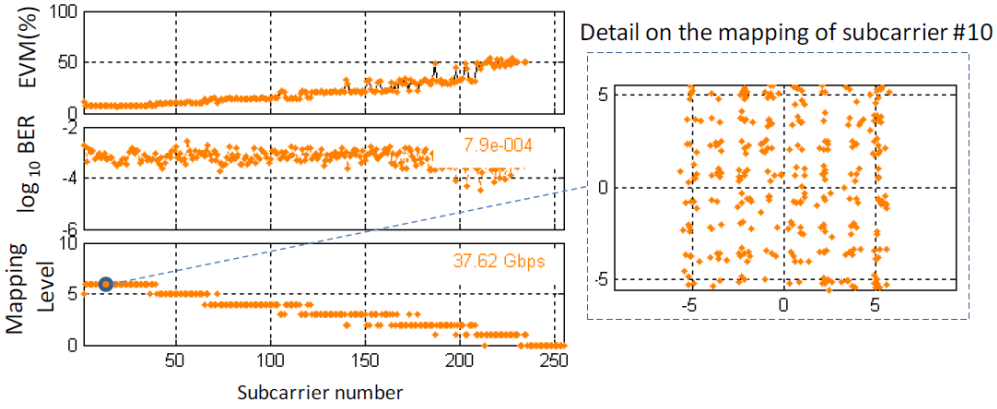

Figure 5.10: Output of the transmission program.

and $90mA$ to $115mA$ according to the fiber length to reduce the dispersion and chirp induced distortions after propagation (see section 4.3). These signals are then used to directly modulate the $17GHz$ butterfly DFB prototype laser model 14B7M developed in the framework of project EPOD. At the receiver side, the optical signal is converted to the electrical domain by a $33GHz$ PIN photodiode from U2T, model XPRV2022A (the same used in the previous section) and finally captured and converted from analogue to digital at $40GS/s$ by the DSO for analysis. A variable optical attenuator (VOA) is set to $17dB$ or $20dB$ before the fiber span to account for 1:32 or 1:64 split ratios respectively[1]. The fiber spans vary from 0 to $100km$. No optical or electrical dispersion compensation technique is used. Figure 5.11(a) shows the experimental set-up for the transmission without optical amplification.

Figures 5.11(b) and (c) show the experimental set-ups of the pre-amplified and booster configurations respectively. In the pre-amplified scenario, an EDFA is placed at the receiver side and is set to Automatic Gain Control mode (AGC) so that its output power is kept constant at $14dBm$. After the EDFA, an attenuator is used to fix the input power of the PIN photodiode at optimal $-1dBm$. For the booster configuration, an attenuator is needed before the EDFA for setting an optimal input power of $2dBm$. Here, the amplifier operation mode is also also AGC and the EDFA's output power is $16dBm$. The noise figure of both amplifiers is $4dB$. The booster and pre-amplifier EDFA differ one from another in their saturation powers (higher in the booster EDFA) and gains (higher in the pre-amplifier).

5.3.2 Results and Discussions

Figures 5.12(a) and (b) show the bit rate variation with the span length for 1:32 and 1:64 split ratios respectively. In Figure 5.12(a), it can be seen that $40Gb/s$ can be attained in back-to-back configuration with 32 subscribers. In the unamplified transmissions, this bit rate falls sharply until $5Gb/s$ after $60km$. At this same length, the boosted and pre-amplified modes allow an increase to $18Gb/s$ and $23Gb/s$ respectively. The booster mode enables a bit rate up to $9Gb/s$ after $80km$ whereas the pre-amplified mode permits the transmission of $10Gb/s$ after $100km$. As far as the 1:64 split ratio is concerned, it can be observed in Figure 5.12(b) that a $2Gb/s$ decrease is imposed in optical back-to-back mode compared to the 1:32 scenario. In addition, the maximum span length attained without amplification decreases to $40km$. After $80km$, the bit rate drops to $4Gb/s$ and $14Gb/s$ in the boosted and pre-amplified modes respectively. The maximum span length attained at 1:64 is $100km$ at which the bit rate is approximately $8Gb/s$.

As far as the bit rate-distance product (BL) on $1:32$ scenario is concerned, maximum values of $1400Gb/s.km$ at $70km$ and $1150Gb/s.km$ at $50km$ are found in the pre-amplified and booster modes respectively. For 64 subscribers, the maximum value of the BL product is $850Gb/s.km$

[1]Here, we consider a more optimistic case than the $3.5dB$ per two-stage splitter previously reported.

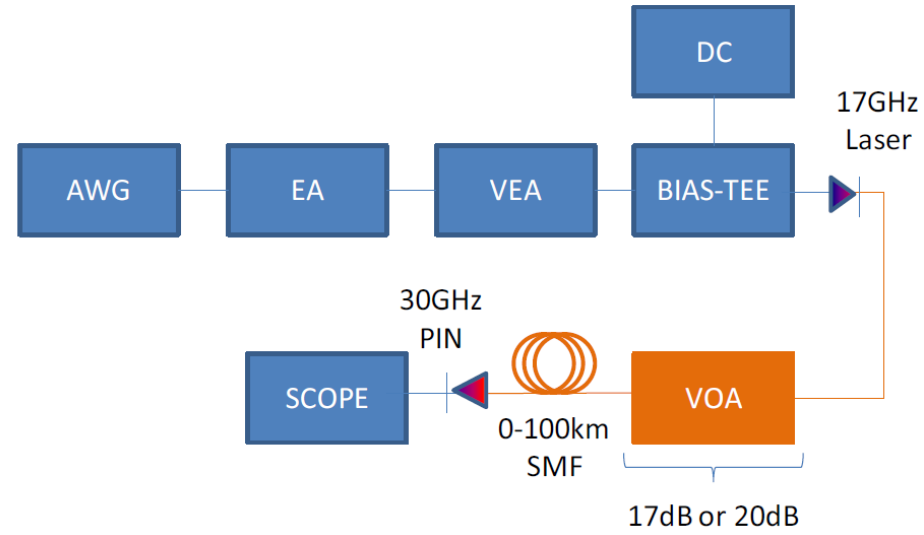

(a)

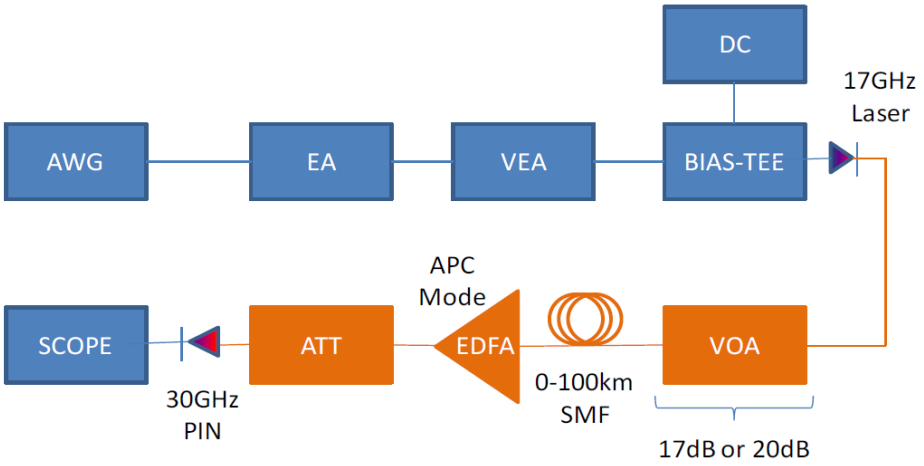

(b)

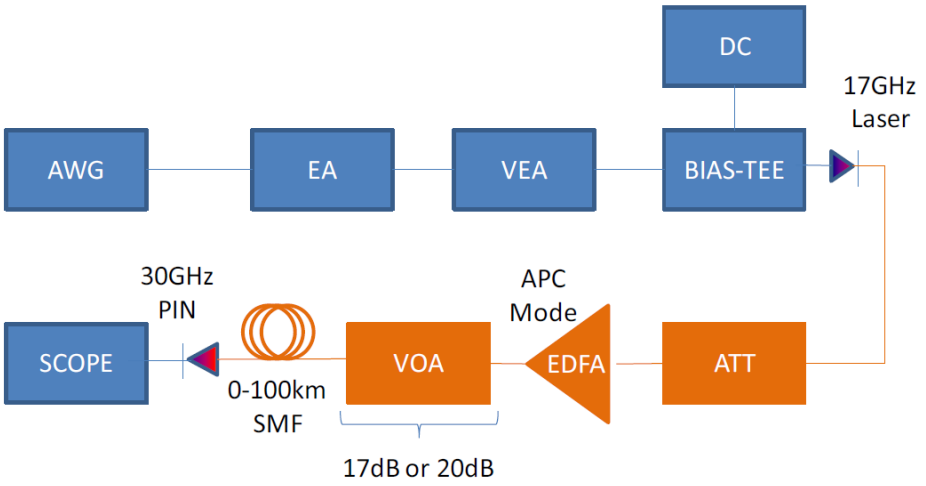

(c)

Figure 5.11: Experimental set-ups for the (a) unamplified transmissions and (b) pre-amplifier and (c) booster modes

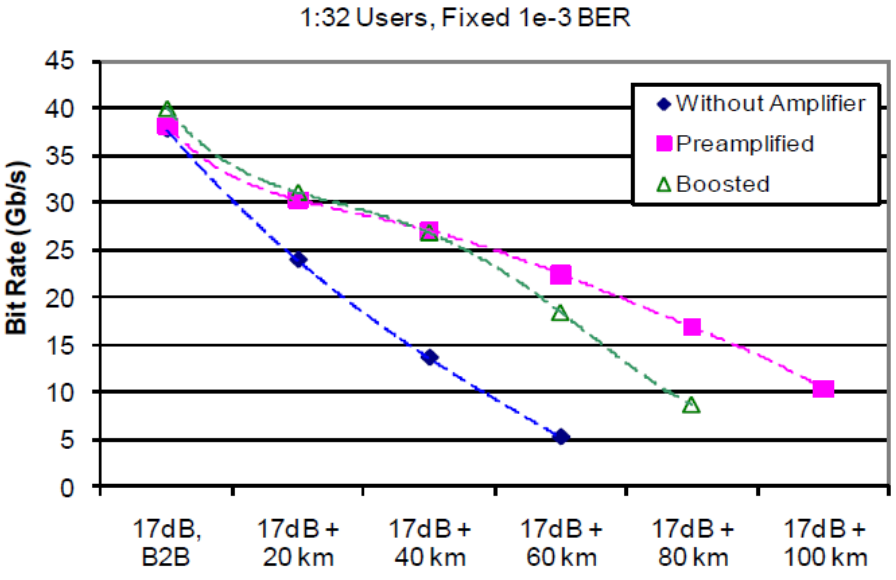

(a)

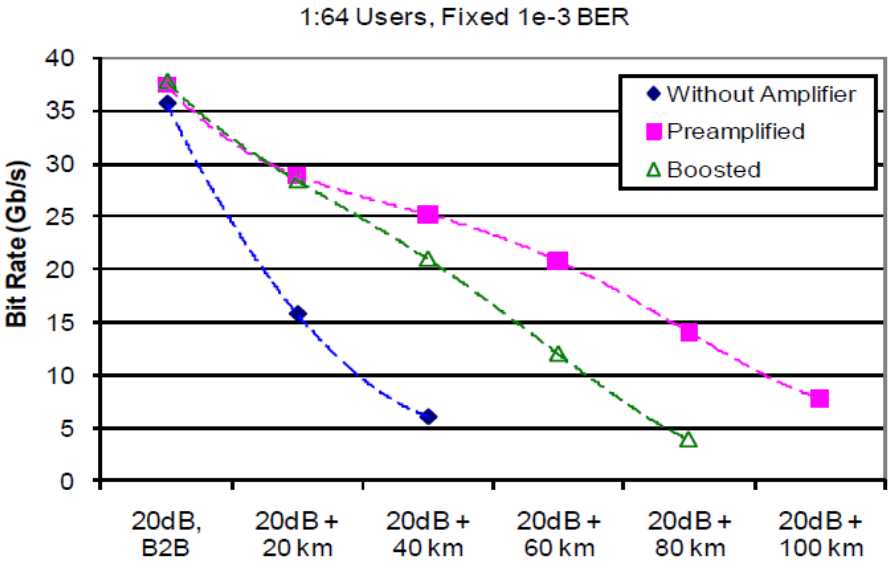

(b)

Figure 5.12: Bit rate evolution with the span length for (a) 1:32 and (b) 1:64 split ratios

at $40km$ in the booster mode and $1250Gb/s \cdot km$ at $60km$ in the pre-amplified mode. Figures 5.13 show the capacity of the transmission for 32 and 64 users respectively.

To conclude, we can see that the pre-amplified scenario presents better performance than the booster solution. When compared to the unamplified configuration, the booster configuration has the advantage of allowing the increase of the optical budget and bit rate with a single EDFA at the OLT. On the other hand, since the pre-amplified configuration offered better performances, it would be an interesting approach if ever the receivers with integrated optical amplifiers become economically reasonable. Table 5.2 sums up the results of the experiment. Global optical budgets are calculated considering a fiber attenuation coefficient of $0.22dB/km$. The booster and pre-amplified AMOOFDM solutions are able to accommodate $20Gb/s$ class B+ (between 13 and $28dB$) and C+ (between 17 and $32dB$) optical budgets respectively.

	Max. bit-rate (32 subsc.)	Max. bit-rate (64 subsc.)	O.B. @$5Gb/s$	O.B. @$10Gb/s$	O.B. @$20Gb/s$
W.O. amplification	$37.7Gb/s$	$35.6Gb/s$	$29dB$	$27dB$	$23dB$
Booster	$40.1Gb/s$	$38.3Gb/s$	$37dB*$	$34dB$	$29dB$
Pre-amplification	$38.2Gb/s$	$37.9Gb/s$	$45dB*$	$40dB$	$33dB$

Table 5.2: Summary of optically amplified OFDM transmissions.

*estimated

5.4 Effects of Laser Chirp in Multiuser OFDM

Up to this point, we have extensively verified the effects of the laser chirp on the frequency response of a dispersive IMDD optical channel. We have managed to investigate the interplay between fiber dispersion and both transient and adiabatic components of the laser chirp which characterizes the frequency selective channel limiting the increase of the system's bit rate-distance product when standard single-carrier modulations are used.

This phenomenon, which translates in the time-domain to the known inter-symbol interference, has been the main motivation behind the efforts to produce low or negative chirp lasers in the last decades. Indeed, we have seen that the number of dips on the channel response was proportional to the amount of accumulated dispersion in the link and that the transient component of the chirp acts in the sense of shifting the channel's dips towards lower frequencies.

We have highlighted the interest of OFDM to transforming such ISI channel on a collection of lower bit-rate AWGN sub-channels thus guaranteeing robustness to chromatic dispersion provided that the number of subcarriers is high enough. Thanks to such robustness, we can actually benefit from a secondary effect of the chirp: the improvement of the channel's frequency response at certain spans due to the phase-to-intensity coupling on the signal.

We start this section by showing the dynamics of the subcarrier allocation over an IMDD transmission using a DML with different fiber spans. We will see that, depending on the frequency location of the signal, higher bit-rates can be obtained at longer fiber spans. Finally, we provide a simulation addressing the changing of the subcarrier allocation according to the chirp parameters of the laser of the OLT in a multiuser SD-OFDM downstream transmission.

5.4.1 Experimental Setup

In order to investigate the effects of the chirp parameter and the span length on the throughput of the transmission, we place our AMOOFDM signal in the 3 to $9GHz$ frequency range. To do so, an IQ modulation scheme similar to what is used in conventional OFDM radio systems was adopted, as shown in Figure 5.14. We must say that the bandwidth limitation of the AWG to $7.5GHz$ served as a motivation to choosing this set-up. A complex AMOOFDM signal (without Hermitian symmetry) having 256 subcarriers and 16 cyclic prefix samples is generated at $6GS/s$

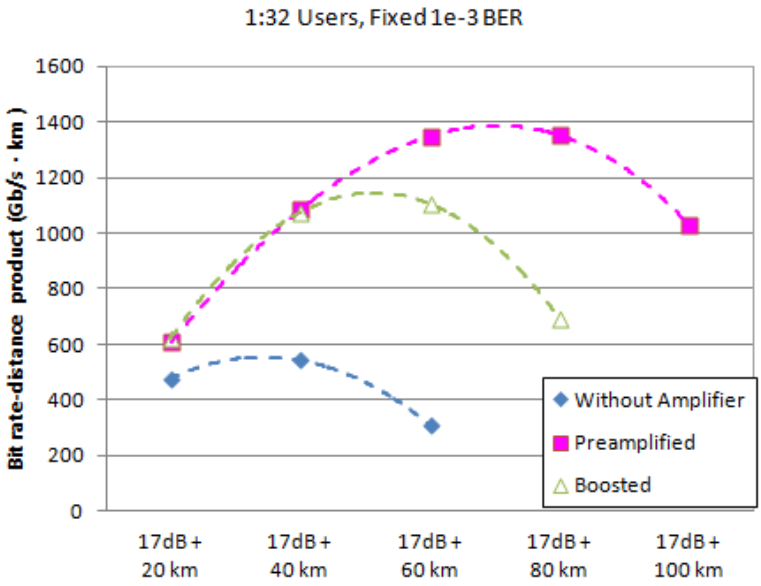

(a)

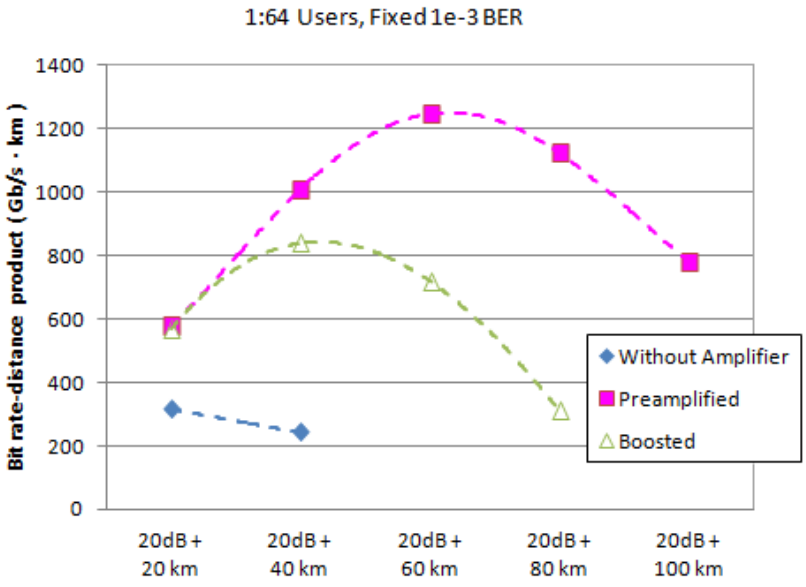

(b)

Figure 5.13: System capacity for (a) 32 and (b) 64 users.

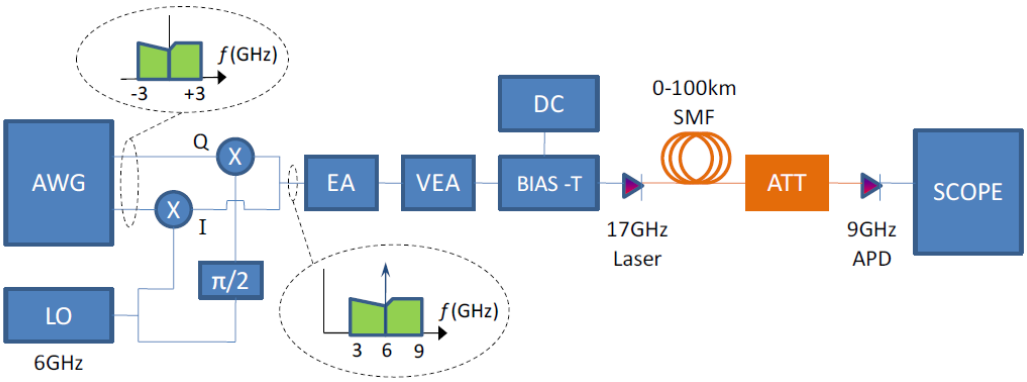

Figure 5.14: Experimental setup.

and oversampled to $12GS/s$. The real and imaginary parts of the signal are then converted from digital to analogue by the AWG at $10bits$ vertical resolution. A Local Oscillator (LO) is used to up-convert the baseband signal to $6GHz$. The LO's power is optimized to $6.8dBm$. An electrical amplifier (EA) and a variable electrical attenuator are used to set the appropriate modulation depth of the upconverted signal before modulating the laser. Once again, we perform an optimization of the signal's RF power, which varied from 8 to $12dBm$ according to the span length.

After proper biasing, the AMOOFDM signal is used to directly modulate the DFB prototype 14B7M which has a bandwidth of $17GHz$ at $3dB$. A SSMF fiber span varying from 0 to $100km$ is then used as dispersive medium. An attenuator is placed before a $8GHz$ APD to fix its input power to $-20dBm$ in all measurement points. The optical budget is consequently fixed to approximately $30dB$. Finally, the photodetector converts the optical signals to the electrical domain and the DSO captures the received signals for offline analysis. The filtering and downconversion at the receiver side are digitally performed. The Levin-Campello algorithm is used to maximize the transmission bit-rate at a target BER of 10^{-3}, which can still provide error-free transmissions with appropriate error correcting schemes.

5.4.2 Results and Discussions

Figure 5.15(a) shows the system's frequency responses with different span lengths. The chirp parameters of the laser are estimated using the Nelder-Mead fitting algorithm to give $\alpha = 2.8$ and $f_c = 1.93GHz$.

Figure 5.15(b) shows the system's bit rate variation with the span length. For the IQ modulation, the bit rate increases at 40, 60 and $80km$ after falling to $7.5Gb/s$ at $20km$. It finally starts to decrease again at $100km$ when approximately $12Gb/s$ is achieved. Figure 5.15(b) also shows the bit rate variation of a baseband $6GHz$ AMOOFDM signal having 255 information subcarriers (512 inputs in the IFFT after Hermitian symmetry), 16 cyclic prefix samples and converted at $12GS/s$. Contrary to the IQ AMOOFDM signal, the baseband bit-rate plunges as the span length increases. Figure 5.15(c) shows an example of the subcarrier's mapping level of the IQ OFDM signal after 20 and $100km$. The subcarriers' mapping (which varied from BPSK to 16QAM), follows the same profile as the frequency response of each span.

5.4.3 Influence of Laser Chirp on a SD-OFDM Downstream Context

We have seen throughout this work that the transient chirp parameter of the laser will play an important role in the positions of the fading dips and in the height of the lobes of an IMDD channel. Also, the adiabatic chirp parameter will change the depths of such dips and can act even to improve the channel responses, as we have seen in the components characterization shown in

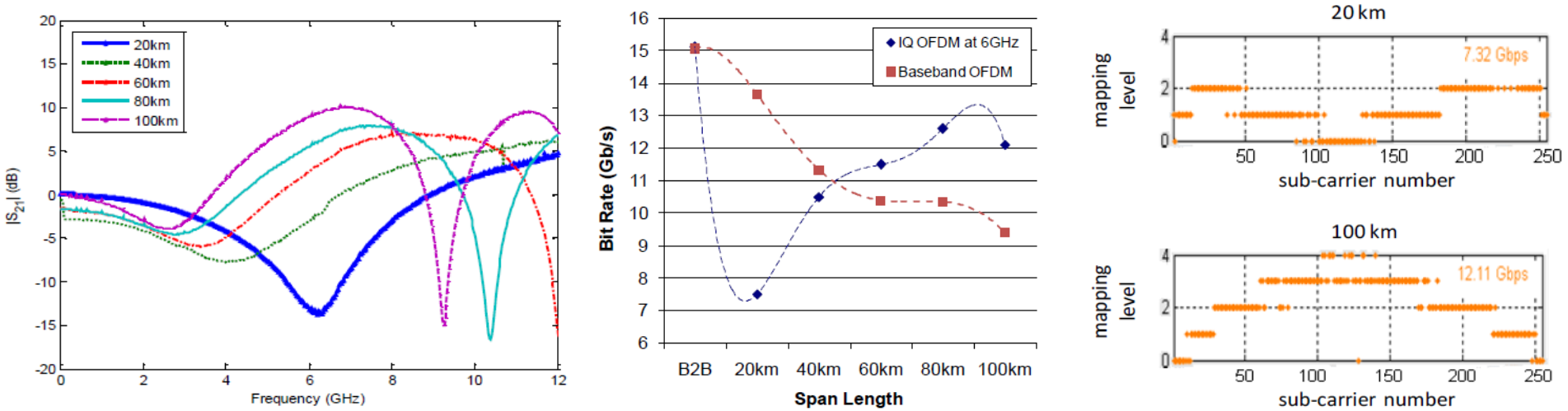

(a) (b) (c)

Figure 5.15: (a) Frequency response variation with the span length. (b) Bit rate variation with span length. (c) Mapping level of IQ OFDM after 20 and 100km.

section 4.2. The laser chirp characteristics can be decisive on the allocation of subcarriers per subscriber on a multiuser passive optical network.

Let us consider the case of a single-wavelength downstream SD-OFDM transmission as seen in section 3.8. Just to recall the principle of the approach, the subcarriers which are allocated to each subscriber of the network are not necessarily adjacent to each other such as it was the case with the MB-OFDM solution. Indeed, the subcarrier allocation is chosen according to the channel response of each user so that the global bit-rate of the optical channel is maximized.

In this simulation, we want to demonstrate the importance of the laser chirp on the subcarrier allocation per user of the PON. To do so, we consider the example of 3 subscribers located at 40, 60 and $80km$ from the central. For matters of simplification, they all have the same optical budget, meaning that the subscribers closer to the OLT have a certain attenuation so that the link losses of all users are matched. Also, all users' converters are capable of dealing with signals between 0 and $12GHz$ and the noise variance σ_N^2 is considered constant over this frequency range.

Fiber dispersion coefficient is considered the same for all users ($D = 16.7ps/km \cdot nm$). The OLT wavelength and f_c are respectively $1.54\mu m$ and $2.1GHz$ and the multiuser RA Levin-Campello algorithm is used to set the allocation of subcarriers per user and their mapping and power levels. All users have the same priority p of accessing the subcarriers and the target mean bit-error rate is 10^{-3}, according to a SNR gap to capacity (Γ) of $5dB$. The OFDM signal is constituted of 255 data subcarriers and we use Hermitian symmetry to generate a real-valued signal occupying the $0 - 6GHz$ bandwidth.

Figure 5.16 shows the different subcarrier allocation for three cases considering different linewidth enhancement factors in the OLT laser: $\alpha = 1, 3$ and 5. We have used the IM+PM+FM IMDD channel model shown in section 2.5 and we have added a low-pass frequency response corresponding to a real measurement done with the 3SP DFB laser model 14B7M and an $8GHz$ APD photodiode used in the previous experiment to render the analysis more real.

It is possible to see from Figure 2.5 that the OLT chirp parameters will play a very important role on the dynamics of the subcarrier allocation of the network. For instance, user 1, which is located at $40km$ from OLT, has passed from 145 to 112 and 91 subcarriers when we changed α from 1 to 3 and finally to 5. The number of subcarriers attributed for each user will evidently have a direct effect on his bit-rate. We can also see that in the theoretical small-signal model, an increase of the α parameter will cause a rise in the overall bit-rate of the channel because it is directly related to the height of the channel's lobes and because the users have exactly the same optical budget. We should recall, however, that the small-signal single-carrier IMDD model was not enough to characterize the chirp and dispersion effects on a multicarrier signal and that a particular optimization of the modulation power at the emitter-side was necessary to reduce the effects of dispersion-induced distortions on the signal (see section 4.3). Consequently, increasing the laser chirp component could degrade the system's SNR, inflecting on the diminution of the maximum achievable throughput.

This analysis raises the question on whether a light source capable of being tuned in chirp could be used to provide different bit-rate dynamics for the network regarding its subscribers. For instance, by changing the OLT laser chirp, it is theoretically possible to increase or decrease the bit-rate of a certain user in the OFDM-PON network. Currently, chirp-tunable light sources are still at a state-of-art level. We have performed some tests on unpackaged DML wafers whose chirp could be changed simply by means of a change of their bias current. The great challenge when comparing those sources, however, was that the variations in the bias levels also influenced the modulation bandwidths and emitted powers of the lasers, which prevented an appropriate experimental investigation of the proposal.

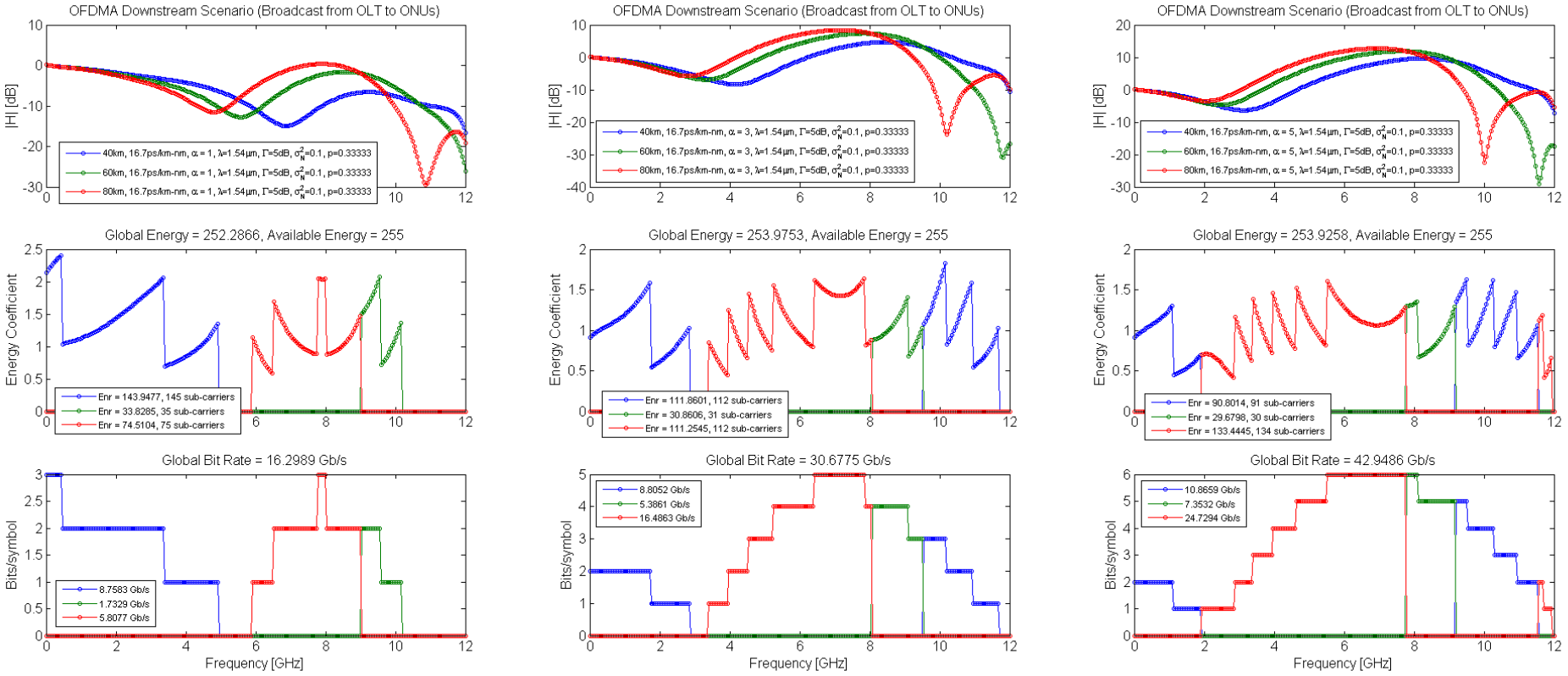

(a) (b) (c)

Figure 5.16: Simulated subcarrier allocation per user in a downstream SD-OFDM approach with different chirp parameters: (a) $\alpha = 1$, (b) $\alpha = 3$ and (c) $\alpha = 5$ at the OLT.

5.5 Considerations about Different Downstream Architectures

We have shown that the IMDD OFDM solution with adaptive bit and power loading capability provides very encouraging results in terms of spectral efficiencies and robustness to chromatic dispersion for future passive optical networks. Some very interesting results have been found using standard 10Gb/s NRZ photodiodes and a miniaturized DML package capable of maintaining an increased performance whilst providing lower power consumption characteristics in terms of temperature control.

We have also seen that the performances of the OFDM transmissions in terms of optical budgets could be considerably improved by means of optical amplification but preserving a passive outside plant. The use of EDFA's in either the OLT or ONU sides allowed $20Gb/s/\lambda$ operation compatible with classes B+ and C+ optical budgets respectively and transmission through up to $100km$ SSMF. Of course, the pre-amplified approach would only be feasible if the costs of the transceivers with integrated optical amplification could offer the economical advantages allowing its implementation at the subscriber side. The booster approach, on the other hand, could be much easily adopted since the costs of the central-side equipment are actually shared amongst all users of the network.

Furthermore, we have seen that the chirp parameter of the OLT laser would influence the subcarrier distribution on a multiuser OFDM PON and we have raised the possibility of using lasers capable of being tuned in chirp to change the bit-rates of the subscribers according to their needs. We have also seen that while the sparse distribution of subcarriers amongst the users allowed the maximization of the capacity per wavelength, it certainly imposed serious economical limitations on the user-side equipment due to the need of high-sampling ratio converters capable of demodulating subcarriers that could potentially be anywhere in the received signal spectrum from the OLT. We have also seen that the simpler but less efficient multi-band approach could allow the use of lower-sampling ratio ADC at the ONU through electrical downconversion of the bandwidths associated to each user. The cost-effectiveness of the MB-OFDM approach would, however, be limited to the desired level of tunability of the LO.

We should remember that the subcarrier allocation capability provided by the OFDM signal could actually benefit from the concurrent use of other sharing techniques such as wavelength and/or time multiplexing. Indeed, since the OFDM modulation allows higher spectral efficiencies if compared to conventional NRZ, the "life expectation" of TDM as far as the clock and data recovery problematic is concerned could be soared to allow higher bit-rates in burst mode operation without demanding complex synchronization solutions at the ONU receiver. Furthermore, the adoption of subcarrier allocation in a time-multiplexed solution would allow the circumvention of a fundamental limitation of Time Division Multiplexing (TDM): the fact the all users have to work at the line-rate even though they might require only a small percentage of that speed. Indeed, the data rate of each user would be defined by the number of subcarrier allocated to it on a burst. In addition, this approach would also allow transmissions to two or more users at the same burst, which is not possible in conventional NRZ-TDM systems. Figures 5.17(a) and (b) show respectively the implementation of SD-OFDM and MB-OFDM solutions with time division multiplexing.

WDM could be easily implementable with OFDM if in a static or quasi-static wavelength configuration by stacking of fixed optical channels. This solution could potentially approximate the core and access network worlds and offer an interesting scalability capability. Figure 5.18 shows an evolution of the MB-OFDM architecture allowing WDM operation by a simple substitution of the first-level coupler by a multiplexer and the use of a wavelength comb at the OLT. Each ONU receives the totality of the optical information transmitted in a certain wavelength but electrically selects only a particular group of subcarriers that has been attributed to it. Note that some extra care might have to be taken in dense WDM approaches due to the out-of-band noise arriving from the dispersion and chirp induced distortions on the OFDM signal. Notice also that the use of an optical amplifier at the central-office would be even more important to

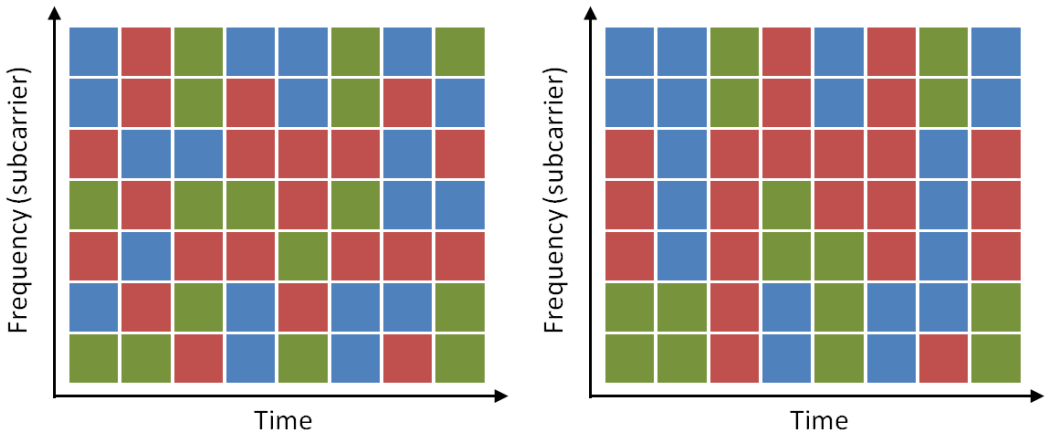

(a) (b)

Figure 5.17: Subcarrier allocation in (a) TDM-SD-OFDM and (b) TDM-MB-OFDM.

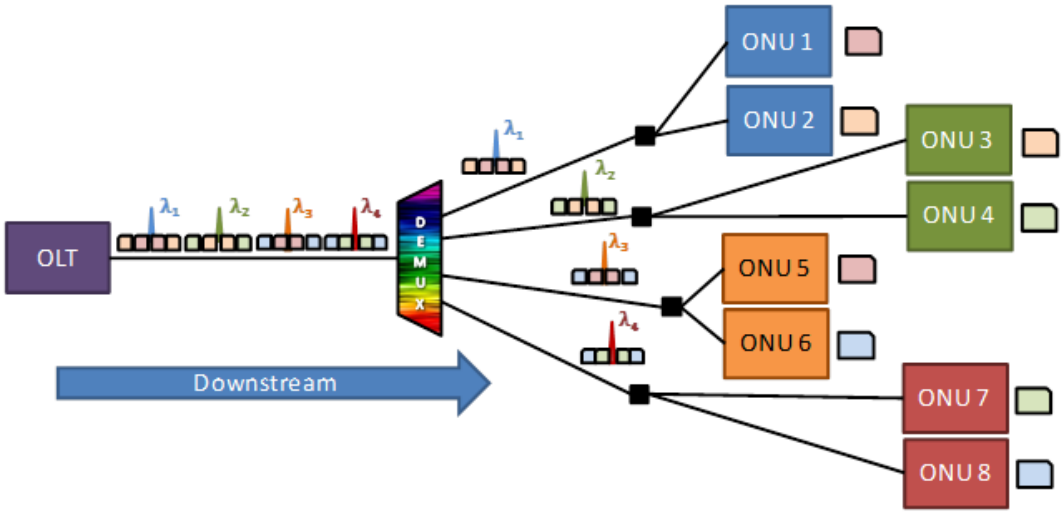

Figure 5.18: WDM-MB-OFDM.

increase the optical budget of the network. Indeed, the high insertion losses of the filtering devices will impose constraints on a network whose optical budget is already tight. In this case, the use of an EDFA at the OLT could impose some limitations due to its limited wavelength operation range. To circumvent this problem, we could either think of a dynamic gain equalizer (DGE), which would probably not be a cost-effective solution for a PON, or use a SOA, which could allow reduced electrical consumption and easy integration on the transceiver's chip board. We could also think of other solutions such as using higher power emitters and/or more sensitive receivers.

References

[1] T. Duong et al. "10Gbit/s transmission over 2.5GHz bandwidth by direct modulation of commercial VCSEL and multi-mode FP lasers using adaptively modulated optical OFDM modulation for passive optical network". In: *Optical Communication, 2008. ECOC 2008. 34th European Conference on*. Sept. 2008, pp. 1 –2. DOI: 10.1109/ECOC.2008.4729294 (cit. on p. 125).

[2] T.N. Duong et al. “Experimental demonstration of 10Gbit/s transmission over 110km SMF by direct modulation of 2 GHz bandwidth DFB laser using Discrete Multi-tone Modulation for Passive Optical Network”. In: *Optical Fiber communication/National Fiber Optic Engineers Conference, 2008. OFC/NFOEC 2008. Conference on*. Feb. 2008, pp. 1 –3. DOI: 10.1109/OFC.2008.4528261 (cit. on p. 125).

[3] D. Nesset, K. Farrow, and P. Wright. “Bidirectional, Raman extended GPON with 50 km reach and 1:64 split using wavelength stabilised pumps”. In: *Optical Communication (ECOC), 2011 37th European Conference and Exhibition on*. Sept. 2011, pp. 1 –3 (cit. on p. 129).

Chapter 6

Upstream Transmissions (ONU⇒OLT)

6.1 Introduction

We have concluded the previous chapter with some considerations about different approaches for sharing the resources in the downstream of a PON. Despite some needed precautions related notably to the costs of the user-side equipment, we have seen that OFDM could outperform currently deployed NRZ solutions in spectral efficiency and robustness to chromatic dispersion. Also, OFDM can be transparently used with wavelength or time multiplexing approaches thus allowing dynamic allocation of the network resources thanks to an additional frequency/subcarrier sharing dimension. Indeed, not only such dynamism could be guaranteed even for a simpler static/quasi-static wavelength plan in WDM-OFDM-PON but it would also solve the main drawback of pure TDM-PON namely the fact that each ONU needs medium access control (MAC) and physical (PHY) layers working at the line-rate even if only a percentage of this line-rate is needed [1, 2].

If the downstream transmissions did not reveal themselves problematic, the major challenge facing future NG-PON2 concerns the upstream transmission. This is because the simple ON/OFF TDMA approach (Figure 6.1) used in current BPON, GPON/GE-PON and XG-PON1/10GE-PON standards will not be capable of providing alone the needed performances for next generations in terms of aggregate bit-rate, distances and number of users per PON tree. The upstream multipoint-to-point transmission might indeed impose a paradigm shift in the network architecture. Some proposed solutions include coherent detection, pure wavelength division multiple access (WDMA) and frequency division multiple access (FDMA).

Pure WDMA using NRZ has been proposed as a solution capable of guaranteeing flexibility and interoperability to the network. The wavelength dimension is added to allow high spectral efficiency in a one-wavelength-per-user basis and since each user has all the resources of an optical carrier, it creates some sort of virtual point-to-point architecture. The major drawback of this solution appears when we try to implement a flexible resource allocation in the network. Indeed, wavelength agility in a network with potentially hundreds of subscribers has never

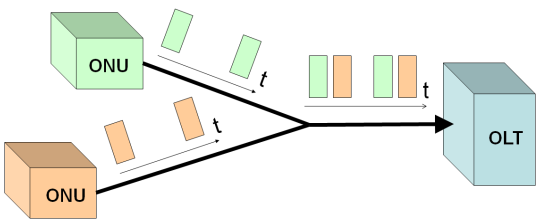

Figure 6.1: TDMA approach.

been seen before in the optical domain. Not only will it impose a great challenge in terms of network operation and control but it will also be dependent on the time that wavelength agnostic components take to mature and provide viable commercial pricing. Indeed, dynamic WDMA requires complex components such as tunable lasers (colored) or colorless devices at the ONU to guarantee agile and unconstrained wavelength allocation per user.

As far as the colored ONU transceivers are concerned, we can imagine for instance the use of cost-reduced versions of standard long-haul transceivers [2] or alternative solutions such as a standard RSOA followed by tunable Fiber Bragg Gratings [3]. The major problem of the colored ONU is the fact that they will need to consume some energy to realize the tuning. That is exactly how the colorless solutions become interesting.

Indeed, the use of a reflective device such as an RSOA or an R-EAM-SOA at the ONU allows the optical carrier to be sent by the OLT [4]. Nevertheless, such an approach faces some challenges as far its implementation in the NG-PON2 is concerned. From a physical point of view, the reflective components are still limited to low emission powers and to the degradations imposed by backscattering. From an operational point of view, the implementation of such solution would force the first operator to bear the whole cost of the installation of the central-side laser array that would be necessary for generating the feeding elements. This would imply an alternative that is far from the desired modular upgradability capability mentioned in chapter 1. In addition, the upcoming operators would be restrained to a fixed set of wavelengths that would not necessarily meet theirs network's needs.

Finally, FDMA appears as another interesting option in which different electrical carriers corresponding to the signals of each ONU are sent over a single wavelength. In this approach, the signals of all ONU can be detected by a single photodiode at the OLT and the legacy infrastructure of the network can remain unchanged. However, an upstream IMDD FDMA scheme with single photodiode and only one wavelength (without polarization control) cannot be implemented due to Optical Beat Interference (OBI) arriving from the square-law detection at the photodiode. It requires then a complementary time or wavelength multiplexing dimension to be used.

In this chapter we investigate both TDMA-OFDM and WDMA-FDMA-OFDM performances and limitations for the upstream PON.

6.2 TDMA-OFDM

In this section, we address for the first time according to our knowledge the transmission of burst mode AMOOFDM signals by direct modulation of two low-bandwidth VCSELs and an APD originally designed for continuous-mode operation. The lasers are not controlled in temperature and represent a very suitable and cost-effective solution for the user-side transceivers. Apart from demonstrating the feasibility of the approach, we also provide an analysis of the effects of unbalancing the losses of two users in the network. We will show that a total bit rate of approximately $5Gb/s$ per user is obtained after $20km$ SSMF and $25dB$ optical budget even when one of the subscribers is submitted to a $9dB$ higher loss compared to the other one.

6.2.1 Experimental Setup

Figure 6.2(a) shows the proposed experimental setup and the OFDM signals after each block of the transmission chain. The OFDM signals generated by an Arbitrary Waveform Generator are composed of two concatenated bursts representing the information sent by each ONU and those are separated by a zero-padding sequence. The same signal is generated in both normal and inverted outputs of a single channel of the AWG and with the help of two ON/OFF electrical switches, it is possible to create two separate bursts that will modulate each one a different laser.

The ON/OFF controlling signals sent to the switches guarantee that during burst 1, the

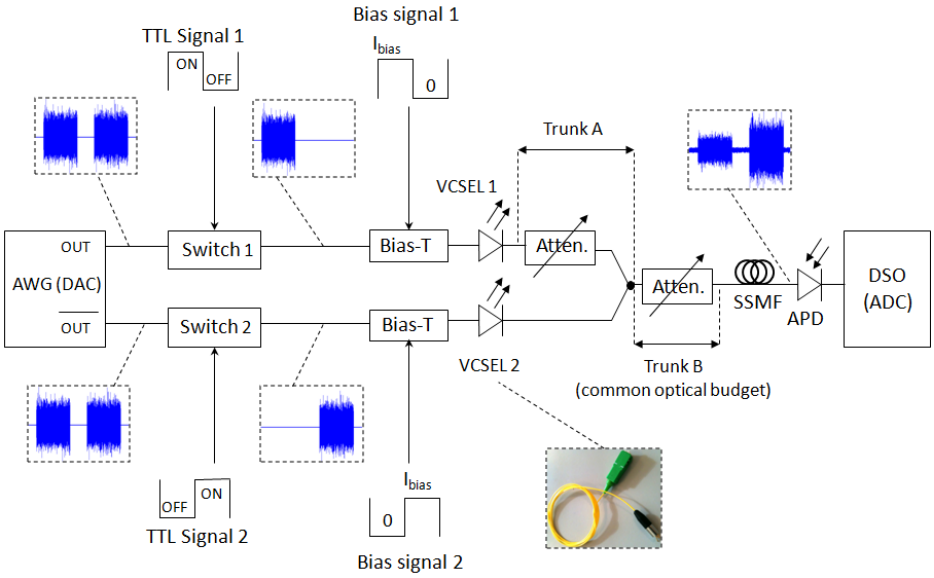

(a)

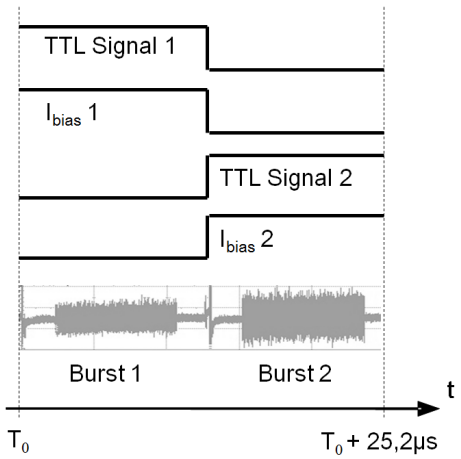

(b)

Figure 6.2: (a) Experimental setup. (b) Clock synchronization for burst generation.

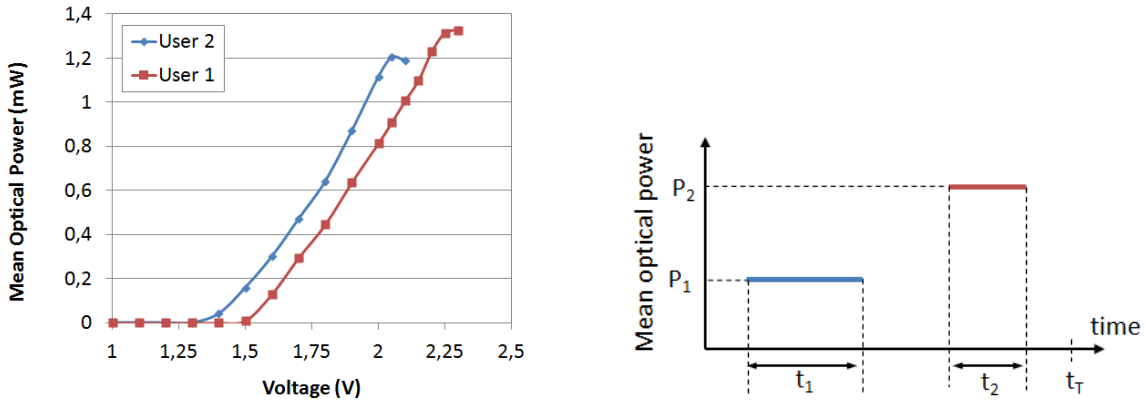

(a) (b)

Figure 6.3: (a) VCSEL $P \times i$ characterization. (b) Illustration of power measurement in power meter.

first switch is turned on and the second switch is turned off and vice-versa. The zero-padding sequence prevents switching inside bursts. Figure 6.2(b) shows the switching signals used to generate the bursts. The bias voltage (Vbias) signal sent to each $1310nm$ VCSEL having $2GHz$ 3dB-bandwidth must match its respective switching control signal so that the laser emits only when the switch is turned on. The controlling and bias signals are generated by two pulse generators. The first one is responsible for the clock reference that is sent to the AWG and to the other pulse generator and thus guarantees the time alignment of the modulating and bias signals.

An attenuator is connected to only one of the users to allow the analysis of the effects of unbalancing user 1 and user 2 optical budgets. A 50/50 coupler assembles both optical bursts into a single optical signal which is transmitted through $20km$ of SSMF. Another attenuator is used to vary the common optical budget of the two users. Finally, after opto-electrical conversion with a $9GHz$ APD, the electrical signal is captured by the DSO for demodulation. An additional step is added at demodulation to invert the bursts associated to the inverted output of the AWG (user 2).

Each burst is composed of 300 symbols. We use 128 sub-carriers, 63 of which carry real data. One sub-carrier contains no power, and the remaining 64 sub-carriers are complex conjugates of the aforementioned sub-carriers and respect Hermitian symmetry. 12 samples per OFDM symbol are used as cyclic prefix and each burst is composed by 42000 samples. 10500 zero-padded samples are inserted before the first burst and after the second burst and other 21000 zero-padded samples are inserted between the bursts. The signal is sampled by the AWG at $5GS/s$. Each AMOOFDM symbol lasts $28ns$ of which $2.4ns$ are occupied by the cyclic prefix. The whole signal (burst 1 + burst 2 + zero-padding) lasts $25.2\mu s$. The Rate Adaptive Levin-Campello algorithm is used independently on each user. The mapping of each sub-carrier varied from BPSK to 64-QAM according to its SNR.

The first switch is turned on from t_0 to $t_0 + 12.6\mu s$ and turned off from $t_0 + 12.6\mu s + \delta$ to $t_0 + 25.2\mu s$, with δ being the time it takes for the pulse generator to go from high to low TTL level. The controlling signal sent to the second switch is the inverse of the one sent to the first switch. At the receiver, synchronization is done independently for each burst using a reference sequence.

Figure 6.3(a) shows the $P \times i$ curves of the lasers. Due to the fact that they had slightly different responses, the bias levels for laser 1 and 2 are $1.92V$ and $1.76V$ respectively. Since the linear conversion range of the emitters were approximately $1V$, we did not use an electrical amplifier in this experiment. The optical attenuation values set to only one of the users (user 1) were $6dB$, $9dB$ and $15dB$ and results are compared to the balanced scenario, when both users

are submitted to the same optical budget.

Before proceeding to the experimental results, we first need to explain the method of calculation of the optical budget of each user using a single power meter located right before the photodiode. Let P_1 and P_2 be the mean optical powers associated to the bursts of users 1 and 2 respectively as shown in Figure 6.3(b). If we admit that mean optical power P_{PM} measured by the power meter is the result of the integration of the received powers over a certain time slot, then:

$$P_{PM} = \frac{P_1 t_1 + P_2 t_2}{t_T} \tag{6.1}$$

where t_1 and t_2 correspond respectively to the periods during which the lasers are biased for modulation by the first and second bursts and t_T is the duration of the whole signal, i.e., both burst plus the zero padding sequence. Since the bursts have the same duration, we may say that $t_1 = t_2 = t_B$ and equation 6.1 reduces to:

$$P_1 + P_2 = P_{PM} \frac{t_T}{t_B} \tag{6.2}$$

If we call $\Delta OB|_{dB} = 10 \log_{10} \left(\frac{P_2}{P_1} \right)$ the difference between the optical budgets of the users in dB related to the attenuation in Trunk A, then:

$$P_2 = P_{PM} \frac{t_T}{t_B} \frac{1}{\left(1 + 10^{\frac{-\Delta OB|_{dB}}{10}} \right)} \tag{6.3}$$

or, in dBm:

$$P_2|_{dBm} = P_{PM}|_{dBm} + 10 \log_{10} \left(\frac{t_T}{t_B} \right) - 10 \log_{10} \left(1 + 10^{\frac{-\Delta OB|_{dB}}{10}} \right) \tag{6.4}$$

From Figure 6.2(b), we can see that $t_T = 2t_B$ and so:

$$P_2|_{dBm} = P_{PM}|_{dBm} + 3 - 10 \log_{10} \left(1 + 10^{\frac{-\Delta OB|_{dB}}{10}} \right) \tag{6.5}$$

The received mean optical power P_1 of user 1 can be trivially found from P_2.

6.2.2 Results and Discussions

Figure 6.4 shows the optical back-to-back bit rate curve as a function of the received power on continuous and balanced burst mode operations for a 10^{-3} target BER. It can be seen that the penalties due to burst mode are negligible.

Figure 6.5(a) shows the bit rate variation with the optical budget in optical back-to-back. The signals outputted by the APD for the different values of attenuation at the trunk A are also shown in the figure. The output powers of lasers 1 and 2 are $-1.2dBm$ and$-1.7dBm$ respectively. As expected, it can be seen that the performance of user 1 worsens as its optical budget is increased by 6, 9 and $15dB$. In addition, despite the fact that the switching of the transmitted bursts always coincides with a zero-padded period, a huge peak can be noticed in the received AMOOFDM signal. This is most probably caused by the switches' transient response and although the peaks are removed during demodulation, they might have induced some distortions at the APD. This is the reason why the curves of user 2 are not always the same for the different values of attenuation on trunk A.

Furthermore, we can notice that the curves of user 1 for the 6, 9 and $15dB$ unbalanced scenarios are flattened in the overshooting region of the photodiode. This limitation may be caused by the combined effects of the saturation of the photodiode by the signal of user 2 and the distortions created by the peaks during switching.

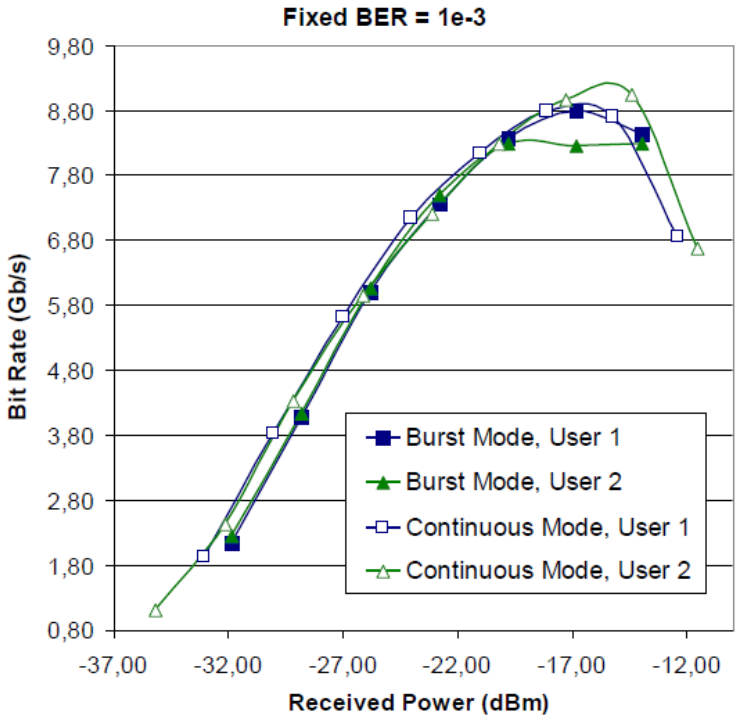

Figure 6.4: Burst mode bit-rate penalties. Optical back-to-back and fixed BER = 10^{-3} .

Figure 6.5(b) shows the BER variation with the optical budget for the balanced and unbalanced scenarios at a fixed bit rate of $5Gb/s$ for each user. Figure 6.5(c) depicts the bit rate variation with the optical budget after $20km$ SSMF for a fixed 10^{-3} BER. We can see that the penalties after introducing the fiber span can be considered negligible. In addition, there are no flattened regions since the photodiode doesn't reach overshooting. Figure 6.5(c) also shows that users 1 and 2 can reach up to $8Gb/s$ each with $16dB$ optical budget for the balanced case. In addition, with $25dB$ optical budget, users 1 and 2 attain more than $4Gb/s$ and $5Gb/s$ respectively on the $9dB$ unbalanced case. Tables 6.1(a) and (b) summarize the results with $20km$ SSMF span for the different scenarios.

The reader should remember that due to the operation near the zero-dispersion wavelength of the fiber, we should not be limited by the selective response of the fiber. Actually, in this particular experiment, the main limitation of the transmissions was indeed the fiber attenuation.

The reader is referred to Appendix D for a similar experiment, this time using a $2.5GHz$ APD.

6.3 WDMA-FDMA-OFDM

The use of frequency division multiple access for the upstream PON can represent an interesting solution to maintain the currently deployed infrastructures and allow demodulation of the signals of several ONUs using a single photodiode at the central office. Indeed, this approach had been widely reported in early nineties under the designation "subcarrier multiplexing (SCM) PON" in which each subscriber would transmit a signal using its own separate optical carrier modulated at a specific electrical subcarrier.

Indeed, the need of an extra dimension (wavelength) becomes clearer if we remind the principles behind the square-law detection at the receiver. Since the photocurrent is proportional to the intensity and thus the square of the received optical field, the mixing taking at the opto-electrical conversion gives rise to interference terms that might result in additional noise on the transmission [5, 6]. These unwanted beat signals (cross-mixing terms) are known as optical beat

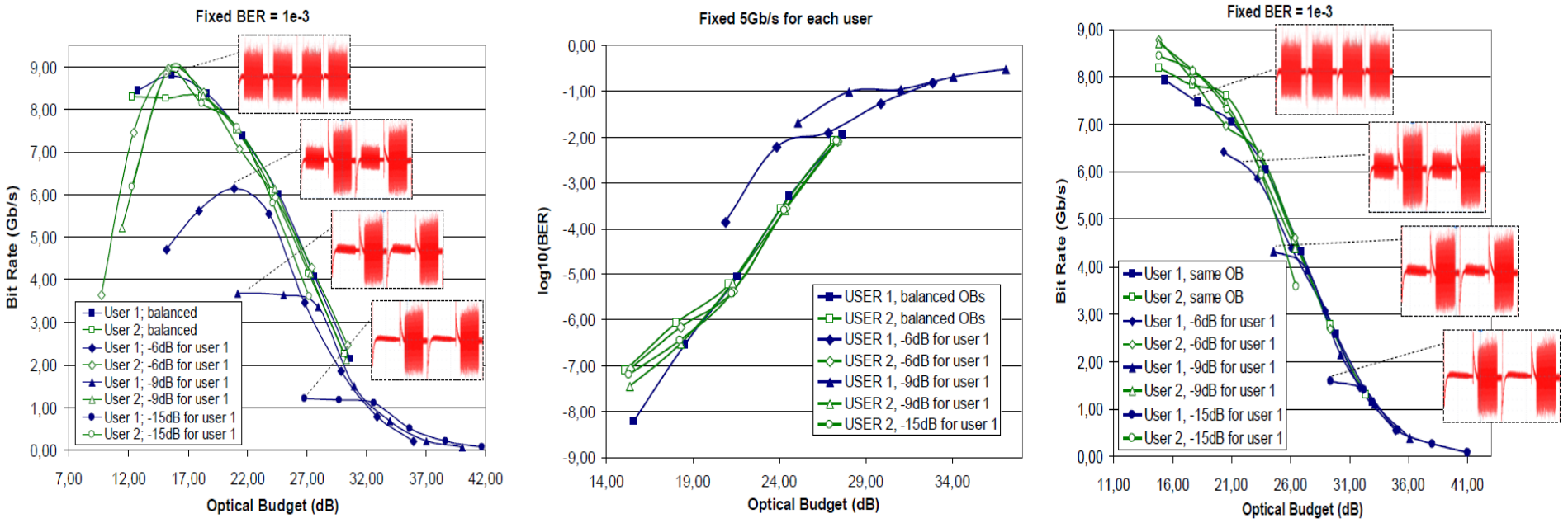

(a) (b) (c)

Figure 6.5: Burst mode optical back-to-back: (a) bit-rate variation with optical budget for fixed BER=10^{-3} and (b) BER variation with optical budget for fixed $5Gb/s$ per user. (c) Burst mode with $20km$ SSMF fiber. Bit-rate variation with optical budget, fixed BER = 10^{-3}.

Configuration Trunk A + Trunk B	$0+16dB$	$0+21dB$	$0+25dB$	$0+30dB$
Optical Budget User 1 (dB)	16	21	25	30
Optical Budget User 2 (dB)	16	21	25	30
Bit-rate User 1 (Gb/s)	7.8	7.0	5.5	2.8
Bit-rate User 2 (Gb/s)	8.0	7.2	5.5	2.8
Mean bit-rate (Gb/s)	7.9	7.1	5.5	2.8

(a)

Configuration Trunk A + Trunk B	$6+15dB$	$9+16dB$	$15+15dB$
Optical Budget User 1 (dB)	21	25	30
Optical Budget User 2 (dB)	15	16	15
Bit-rate User 1 (Gb/s)	6.4	4.2	1.5
Bit-rate User 2 (Gb/s)	8.4	8.0	8.4
Mean bit-rate (Gb/s)	7.4	6.2	4.9

(b)

Table 6.1: $20km$ performances with (a) balanced optical budgets and (b) unbalanced optical budgets.

interference (OBI). For instance, in a transmission with only two ONUs such as depicted in Figure 6.6, the strongest beat interference products are those centered at $\Delta f = f_{o2} - f_{o1}$ with $f_{o1/2}$ being the frequencies of the optical carriers.

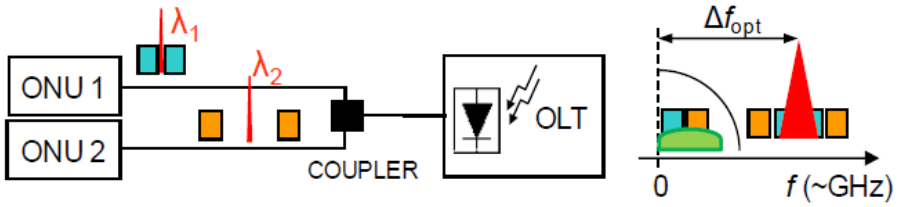

Figure 6.6: Upstream WDMA-FDMA with single photodiode.

Instead of using single electrical subcarriers such as in SCM PON, we can allocate different frequency spans for each user. Actually, the transmission of OFDM signals inside each of these spans, would allow a similar approach to the MB-OFDM seen for the downstream transmissions in the previous chapter.

It can be demonstrated that, in this case, the minimum separation between wavelengths to lessen the effects of OBI is twice the baseband bandwidth of the aggregate of the transmitted signals [7]. A more conservative approach would consist, however, of fixing the separation between wavelengths so that the strongest OBI terms are filtered out by the frequency response of the photodetector, such as depicted in Figure 6.6.

Furthermore, the reader should remember that in order to maintain a cost-effective operation at the user-side, the lasers are, ideally, not controlled in temperature. This means that an extra margin must have to be considered in the wavelengths separation to accommodate the uncertainty of the laser wavelengths arising from temperature variations, different fabrication characteristics and short or long-term changes in the components [8].

We should also remark that in a scenario without stabilization/referencing of the wavelengths, the use of an upstream approach equivalent to the SD-OFDM, in which the subcarriers are sparsely distributed amongst the subscribers, would be absolutely impossible. In fact, not even

the use of a peltier to control the laser's temperature would allow the implementation of such an approach since it would require an extremely high precision mechanism to finely stabilize the laser wavelength and avoid drifting higher than the separation between two OFDM subcarriers.

Based on these points, we dedicate this section to an evaluation of the WDMA-FDMA-OFDM solution. Recently [9], an experimental study of the minimum spacing between adjacent wavelengths on a WDM-FDMA-OFDM architecture with single photodiode has been shown with two Mach-Zehnder modulators. Here, we do a similar analysis, this time with an IMDD approach with adaptive bit/power loading per OFDM subcarrier. We focus on the limiting phenomena specific to direct modulation, namely the laser chirp and fibre dispersion interplay characterizing the channel frequency response and the limitations imposed by spectral broadening of the optical sources on the separation between adjacent wavelengths. We also assess the bit-rate degradation with fiber spans varying from 20 to $100km$.

6.3.1 Experimental Setup

Figure 6.7 depicts the experimental setup used in this work as well as some examples of the transmitted and received signal spectra (insets a-c). The OFDM signal of each user has 64 subcarriers and 8 samples per symbol are used as cyclic prefix. Acquisitions are composed of 300 OFDM symbols. Mapping and power per subcarrier are chosen according to its SNR through the Levin-Campello rate adaptive algorithm. Before numerical upconversion, the complex baseband OFDM signals are first oversampled to $12GS/s$, which is the maximum sampling rate per output of the Arbitrary Waveform Generator. Users 1 and 2 are centered at $1.2GHz$ and $3.4GHz$ respectively and both have a $2GHz$ bandwidth. The same approach could have been realized with lower sampling rate DAC and electronic up-conversion with local oscillators and IQ mixers, as we saw in section 5.4. Digital-to-analog conversion is performed by the AWG with 10-bits resolution. The signal RF powers, which correspond to $-6.9dBm$ at the outputs of the AWG, are increased by means of electrical amplifiers and an electrical attenuator helps optimizing the powers of the signals that modulate each laser from 18 to $5.4dBm$ according to the fiber span length. The same RF powers are used for both users.

The $16GHz$ DFB lasers are directly modulated after proper biasing at $135mA$ with corresponding mean output optical power of $12.3dBm$. A 2×1 coupler is used to combine both signals. After the coupler, a variable optical attenuator fixes the input power of the $8GHz$ APD in order to avoid saturation. The optical power budgets per user are fixed at $29dB$. Different SSMF spans from 20 to $100km$ are used in the measurements. After photo-detection, the signal is captured and digitized by an oscilloscope at $20GS/s$ with an 8-bits resolution. Downconversion to baseband is performed digitally and the OFDM signal of each user is off-line demodulated. In order to study the degradations due to the wavelength separation, user 1 (reference laser) is fixed at $\lambda_1 = 1551.42nm$ ($193.2379THz$) while user 2 has its wavelengths shifted from $\lambda_2 = \lambda_1 - 0.06nm$ to $\lambda_2 = \lambda_1 - 0.8nm$ through temperature variations from 30 to 22^oC respectively. For such temperature shift, the laser's frequency response change is negligible, as we can see from the measurements of Figure 6.8.

Figures 6.9(a) and (b) show respectively the mean optical power and wavelength variation of the DFB lasers with the polarization current and operation temperature. Runs 1 and 2 correspond respectively to the DFB models EM4 E0037751 and EM4 E0037752.

From Figure 6.9(a), it is possible to see that the lasers do not present many differences regarding their linear operation region and threshold currents. The lasers' threshold is approximately $23mA$ and linear operation can be obtained from 25 to $175mA$. The main difference between both Runs is in the electro-optical efficiency, which can be characterized by the slope of the $P \times i$ curve. Run 2 is slightly less efficient than Run 1. Also, the increase of the operation temperature decreases the electro-optical conversion efficiency of both lasers. From Figure 6.9(b), we can see that the lasers can be tuned up to $2.5nm$ by changing the operation temperature in the range from 15 to 40^oC.

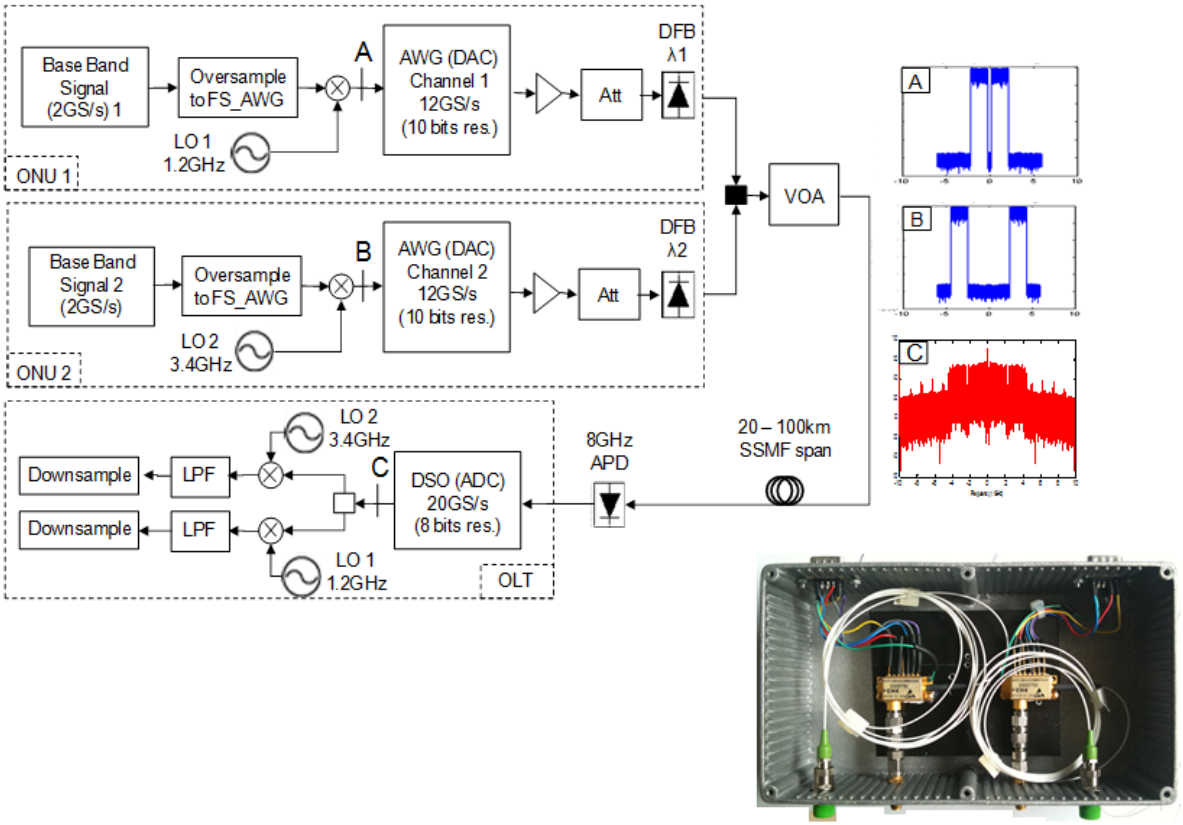

Figure 6.7: Experimental setup.

6.3.2 Results and Discussions

Figure 6.10 shows the global bit-rate (user 1 + user 2) evolution of the system with the optical carrier separation for several fiber spans and a target $2.2 \cdot 10^{-3}$ mean BER. The inset depicts an example of bit, power and SNR distribution per subcarrier for both users. We have found that the minimum separation for the back-to-back scenario corresponds to $0.2nm$ ($25GHz$).

A very interesting point is that the minimum separation decreases with increasing the span lengths. This can be explained by the fact that the signal RF power has been optimized for each fiber length. Indeed, the optimized RF power in back-to-back was $18dBm$ while for $100km$ it was decreased to $5.4dBm$. At this point the reader should remember that the spectral broadening in single-longitudinal-mode lasers occurs primarily due to direct intensity modulation and the resulting frequency chirp (and secondarily to phase noise). A smaller RF power would account then for less spectral broadening.

The variation of the laser spectrum width with the modulation power at $0.005nm$ resolution shown in Figure 6.11(a) confirms the phenomenon and may explain why the minimum separation between wavelengths found by us is greater than the one found in [9]. The linewidth enhancement factor of the laser, which was measured according to the procedure shown in chapter 4, is 3.8. The laser chirp will also change the frequency response of a dispersive channel and we have seen in section 2.5 that some frequency spans of the channel could actually benefit from the use of chirped lasers. The results of the bit rate variation of user 1 and 2 for different fiber lengths shown in Figure 6.11(c) and the channel measurements shown in Figure 6.11(b) corroborate this idea. This explains the bit rate increase of user 2 (whose signal is in the $2.4 - 4.4GHz$ window) from 20 to $60km$. The improvement of SNR of user 2 can also be evidenced on the insets of Figure 6.11(c).

We have shown in this section that the laser chirp of an intensity modulated laser will not only

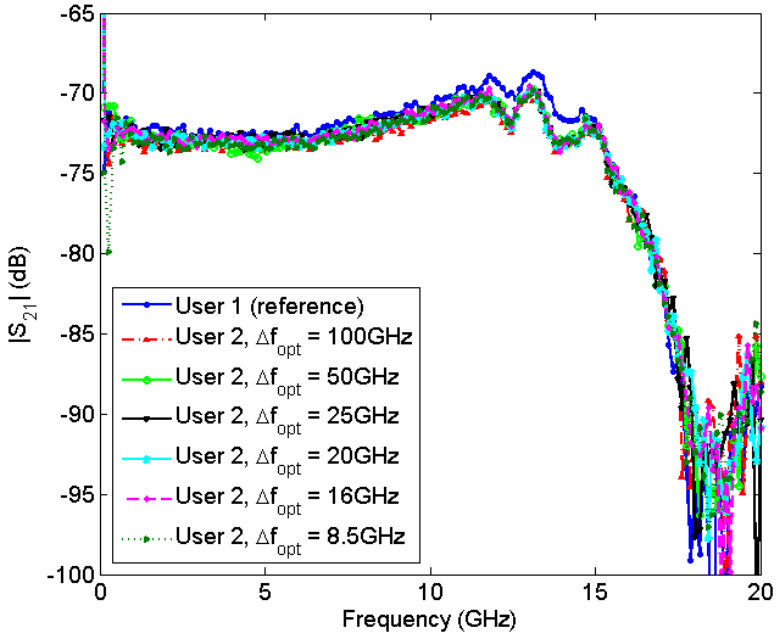

Figure 6.8: Lasers frequency response variation. Reference laser is fixed and laser 2 operation temperature is varied to provide different separations from reference laser.

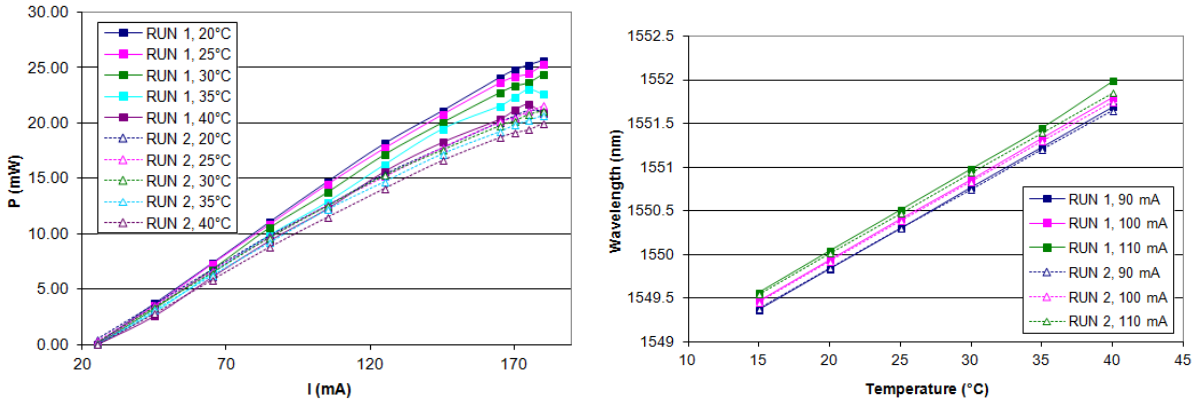

(a) (b)

Figure 6.9: Lasers power and wavelength variation for different polarization currents and operation temperatures.

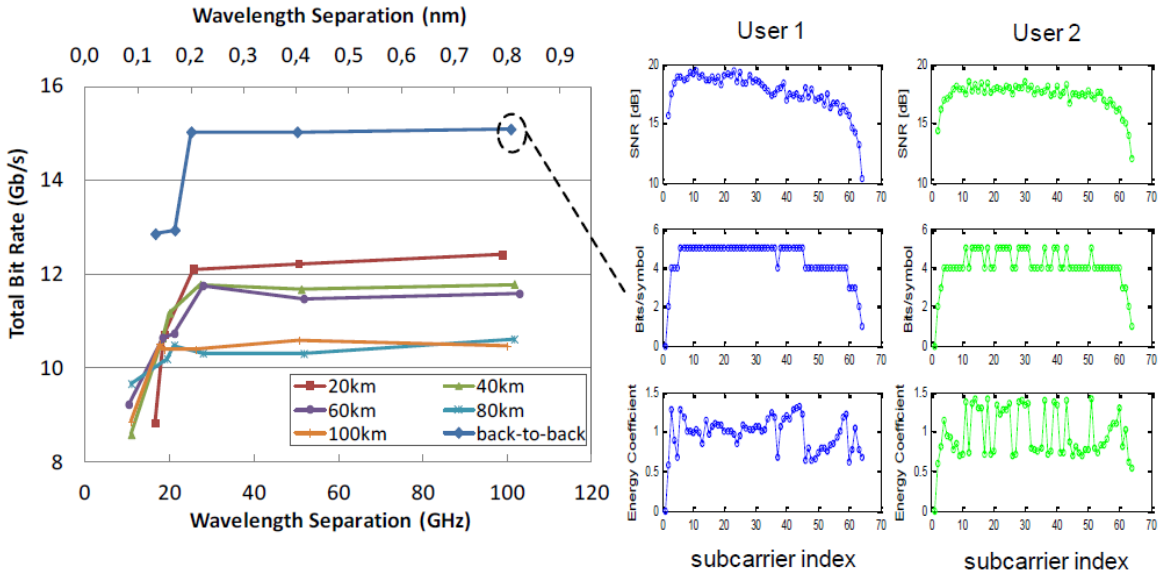

Figure 6.10: Global bit-rate variation with wavelength separation and fiber length.

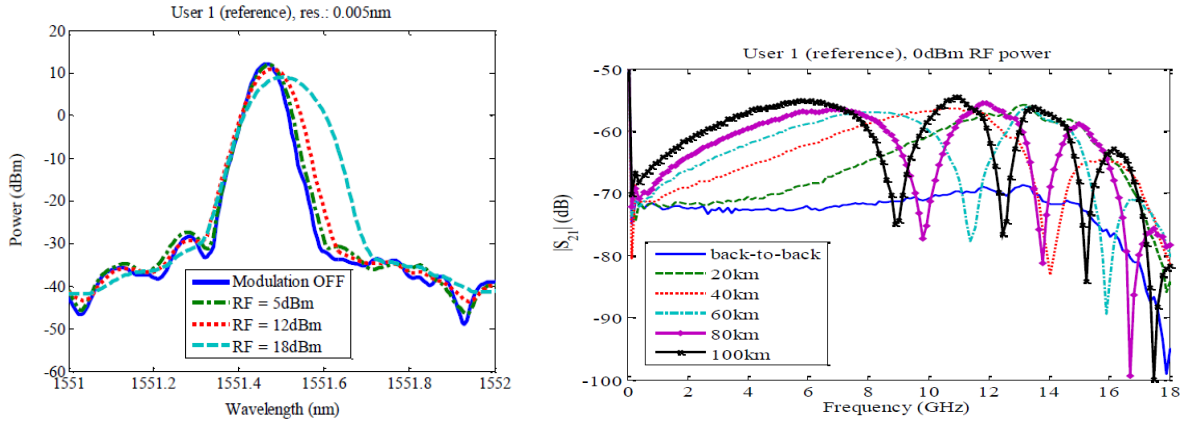

(a) (b)

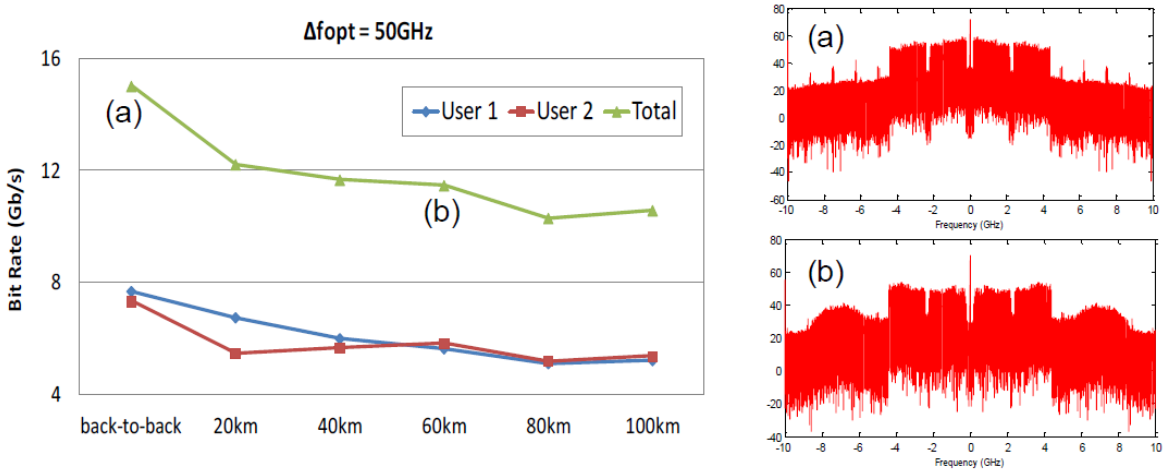

(c)

Figure 6.11: (a) Spectrum variation with RF power. (b) Frequency responses for different spans. (c) Bit-rate variation with fiber span.

influence the channel frequency response thus characterizing the performances on each FDMA sub-band but will also play an important role on defining the minimum wavelength separation between adjacent wavelengths.

Despite the fact that adaptively modulated optical OFDM can be used to optimize the throughput according to the SNR of each user, further investigations on IMDD WDM-FDMA-OFDM architecture are still necessary since the scheme manages to offer cost-effectiveness and simplicity by means of a dynamic bandwidth allocation[1]. Indeed, it would be extremely important to extrapolate this scenario to as many users/wavelengths/sub-bands as possible by means of simulations so that the limitations due to optical beat interference between the signals could be well established. Such extrapolation would also allow the investigation of other potential sources of degradation such as the accumulated RIN and the increase of the photodiode's shot noise with increasing numbers of subscribers in the network. However, if those degradations can be circumvented by means of bit/power loading schemes and RF power optimization, then we would need a tunability of $\sim 13nm$ to accommodate 64 users. Also, if we recall the wavelength plan shown in chapter 1 and imagine that the upstream channels could be located at the highest available spectrum (from $1360nm$ to $1480nm$), then this approach would be limited to about 590 users per PON tree.

References

[1] P. Chanclou et al. "Technical options for NGPON2 beyond 10G PON". In: *Optical Communication (ECOC), 2011 37th European Conference and Exhibition on*. Sept. 2011, pp. 1 –3 (cit. on p. 144).

[2] P. Chanclou et al. "Network operator requirements for the next generation of optical access networks". In: *Network, IEEE* 26.2 (Mar. 2012), pp. 8 –14. ISSN: 0890-8044. DOI: 10.1109/MNET.2012.6172269 (cit. on pp. 144, 145).

[3] Qian Déniel et al. "Transmission Jusqu'à 10Gbit/s basée sur un Laser à Cavité Externe Utilisant un RSOA et un Réseau de Bragg Photo-inscrit sur Fibre pour WDM PON". In: *Journées Nationales d'Optique Guidée (JNOG)*. 2012 (cit. on p. 145).

[4] T. Duong et al. "Experimental demonstration of 10 Gbit/s upstream transmission by remote modulation of 1 GHz RSOA using Adaptively Modulated Optical OFDM for WDM-PON single fiber architecture". In: *Optical Communication, 2008. ECOC 2008. 34th European Conference on*. Sept. 2008, pp. 1 –2. DOI: 10.1109/ECOC.2008.4729576 (cit. on p. 145).

[5] C. Desem. "Optical interference in subcarrier multiplexed systems with multiple optical carriers". In: *Selected Areas in Communications, IEEE Journal on* 8.7 (Sept. 1990), pp. 1290 –1295. ISSN: 0733-8716. DOI: 10.1109/49.59129 (cit. on p. 149).

[6] T.H. Wood and N.K. Shankaranarayanan. "Operation of a passive optical network with subcarrier multiplexing in the presence of optical beat interference". In: *Lightwave Technology, Journal of* 11.10 (Oct. 1993), pp. 1632 –1640. ISSN: 0733-8724. DOI: 10.1109/50.249905 (cit. on p. 149).

[7] Xiaoting Xie, Yaojun Qiao, and Yuefeng Ji. "The study of wavelength interval between adjacent ONUs in OFDMA-PON". In: *Communications and Photonics Conference and Exhibition (ACP), 2010 Asia*. Dec. 2010, pp. 621 –622. DOI: 10.1109/ACP.2010.5682657 (cit. on p. 151).

[1] The notion of dynamic bandwidth allocation also exists in TDMA-PON, in which case, it actually consists of a queue management and not a dynamic allocation of the physical resources of the link.

[8] N.K. Shankaranarayanan, S.D. Elby, and K.Y. Lau. "WDMA/subcarrier-FDMA lightwave networks: limitations due to optical beat interference". In: *Lightwave Technology, Journal of* 9.7 (July 1991), pp. 931 –943. ISSN: 0733-8724. DOI: 10.1109/50.85796 (cit. on p. 151).

[9] I. Cano et al. "Dimensioning of OFDMA PON with non-preselected-independent ONUs sources and wavelength-control". In: *Optical Communication (ECOC), 2011 37th European Conference and Exhibition on*. Sept. 2011, pp. 1 –3 (cit. on pp. 152, 153).

Chapter 7

Prospective Studies on Metropolitan Networks and Energy-efficient Approaches

7.1 Introduction

In this last chapter, we shall present firstly an interesting comparison between IMDD OFDM and other direct-detection approaches in terms of bit-rates and transmission distances. Indeed, we push OFDM's robustness to chromatic dispersion to a limit by evaluating, for the first time, the performances of an IMDD transmission over more than $500km$ SSMF in a point-to-point architecture with in-line amplification but without any kind of electronic or optical dispersion compensation. The study-case of an IMDD OFDM transmission over a typical Dispersion Managed Fiber submarine network is also provided as well as an investigation of the degradation of the transmission's bit-rate with the amount of accumulated dispersion in the link.

In the second experiment, we introduce a bit and power loading algorithm developed to address the reduction of the electrical consumption of high-speed converters in passive optical networks. We propose the solution of a twofold optimization problem that allows adapting the OFDM signal's bandwidth to a power constraint and a specific demand in terms of bit-rate. Basically, it comes to a mix of both rate and margin adaptive solutions which allows to create a new degree of freedom on the OFDM signal parameters, namely the converter's sampling ratio.

7.2 10Gb/s IMDD over 513km Uncompensated SSMF Link

To satisfy the growing needs of higher bit rates and extended reach in optical networks, it is essential to privilege technologies capable of providing cost-effective solutions beyond $10Gb/s$ while maintaining compatibility with small-sized packages and reduced power consumption. Directly modulated lasers are well established in access networks because of their high output power and low threshold current. However, their use in long reach transmissions over SSMF with naive NRZ is limited due to dispersive frequency response of the optical channel arriving from the interaction between laser chirp and fiber chromatic dispersion. In [1], $10Gb/s$ over $100km$ SSMF has been demonstrated with a DML thanks to electronic dispersion compensation.

Externally modulated lasers (EML) hold the record bit-rate in directly detected systems but still at reduced distances. $100Gb/s$ EML transmission has been recently demonstrated over $10km$ SSMF and equivalent dispersion-compensation fiber (DCF) [2]. Furthermore, Chirp Managed Lasers (CML) appear as one alternative to extrapolating reach limitations. Transmissions over $1200km$ Nonzero Dispersion-Shifted Fiber (NZDSF) were demonstrated in [3] but for a accumulated dispersion of only $5300ps/nm$. In [4], $10Gb/s$ over $675km$ SSMF has been established

with a CML but at the cost of four cascaded tunable Optical Dispersion Compensators (ODC) and EDC whereas the uncompensated transmission itself was limited to $4000ps/nm$. Figures 7.1(a) and (b) show respectively these and other key reports on directly detected transmissions over the last years as a function of the accumulated dispersion on the link and length of fiber.

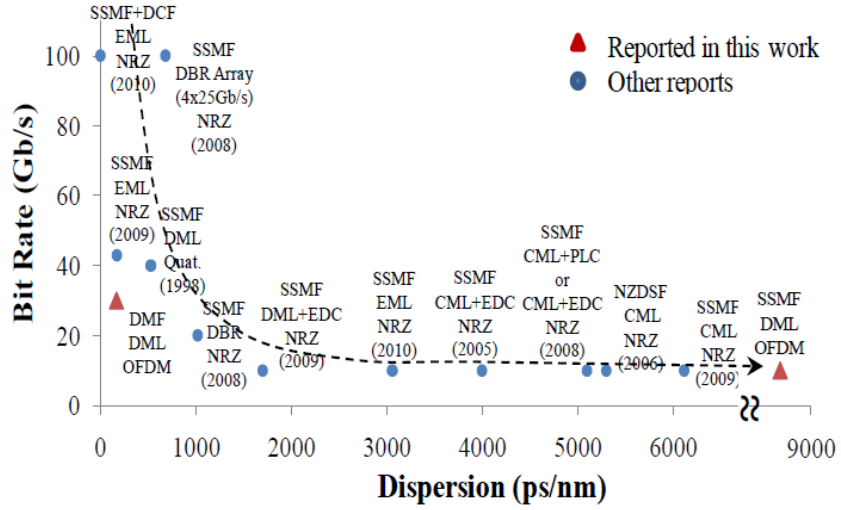

(a)

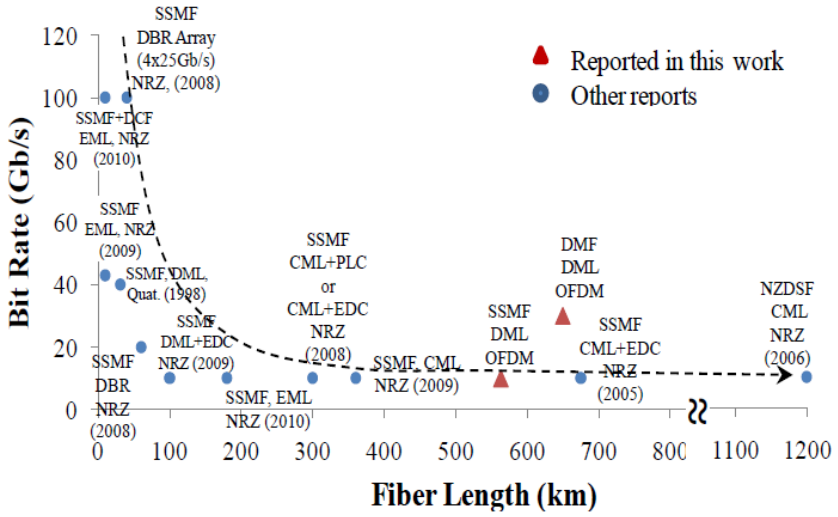

(b)

Figure 7.1: Recent reports on CML, DML and EML directly detected transmissions as a function of (a) the accumulated dispersion on the link and (b) fiber length.

In this section, we address a record of $11.5Gb/s$ over more than $500km$ SSMF ($8500ps/nm$) without any kind of optical or electronic dispersion compensation as well as $30Gb/s$ over $650km$ of Dispersion Managed Fiber with simple direct modulation and direct detection-based components thanks to AMOOFDM.

7.2.1 Experimental Setup

Figure 7.2 depicts the experimental setup used in this work. The AMOOFDM signals are composed of 512 sub-carriers, 255 of which carry real data. The analogue waveform generated by the Arbitrary Waveform Generator is a real-valued $12GHz$ baseband signal obtained by Hermitian Symmetry of the input symbols. Sixteen samples are used as cyclic prefix and each acquisition is composed of 300 OFDM frames. The Levin-Campello rate adaptive bit-loading

algorithm is implemented to optimize the transmission's throughput. The modulation levels of the subcarriers varied from BPSK to 64QAM. The signal's sampling ratios were $24GS/s$ at the transmitter side and $40GS/s$ at the receiver side.

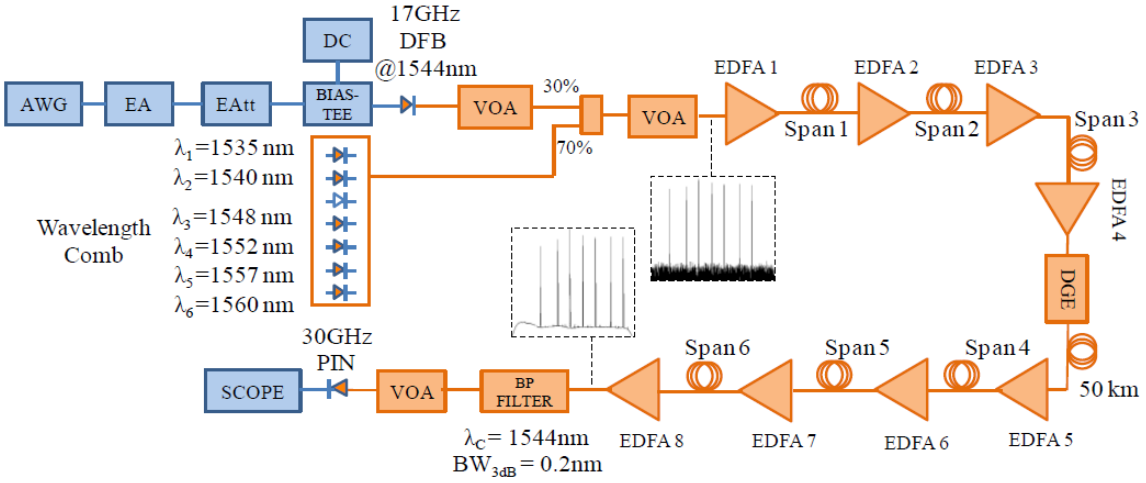

Figure 7.2: Experimental setup.

The modulation power is set by means of an electrical amplifier and a variable electrical attenuator. The OFDM signal is used to directly modulate the $17GHz$ Distributed Feedback (DFB) prototype laser from 3SP model 14B7M after biasing with an optimum current. The generated optical signal is then coupled with a comb of 6 DFB unmodulated lasers which are used only to flatten the Erbium Doped Fiber Amplifiers' gain curve. A first optical attenuator is used to change the ratio between the optical power of the signal and the optical power of the wavelengths of the comb. A second VOA sets the optimal input power of the first EDFA of the link. Next, the signal propagates through three $22dB$ fiber spans, each one followed by an in-line EDFA. It then reaches a Dynamic Gain Equalizer (DGE) which is used to reduce uneven wavelength gain ripple generated by the optical amplifiers (notably around $1530nm$). After the DGE, the signal propagates through three other $22dB$ spans. The last EDFA is used to preamplify the received signal and a $0.2nm$ band-pass filter centered at $1544nm$ is used to separate the desired wavelength from the comb. The insets on Figure 7.2 show the signal's optical spectrum after and before propagation through the optical link. The Noise Figure of the EDFAs is in average $4.7dB$ and they are all set to Automatic Gain Control mode, i.e. fixed output powers. A third VOA is used to adjust the input power of a $30GHz$ PIN photodiode which directly detects the AMOOFDM signals. Finally, a DSO performs analogue to digital conversion for subsequent offline processing.

As far as the fiber spans are concerned, two options have been analyzed in the experiments: either a standard single mode fiber span or a dispersion managed fiber span composed of a combination of 2/3 of $+20ps/km \cdot nm$ fiber ($A_{eff} = 105\mu m^2$) and 1/3 of $-40ps/km \cdot nm$ fiber ($A_{eff} = 30\mu m^2$), as depicted in Figure 7.3(a). The $22dB$ optical budgets per span corresponded to $100km$ DMF and $76 - 100km$ SSMF according to each fiber spool loss level. A total length between $563km$ (all-SSMF configuration) and $650km$ (all-DMF configuration) is assured for all scenarios. It should be noticed that the DGE is followed by another fixed $50km$ DMF to equal the span losses.

Figure 7.3(b) shows the dispersion map of the link in the all-DMF configuration.

7.2.2 Results and Discussions

The first measurements consisted of evaluating the bit error rate and bit rate variation with the signal power for the all-DMF configuration (6 DMF spans) in order to assess the degradations

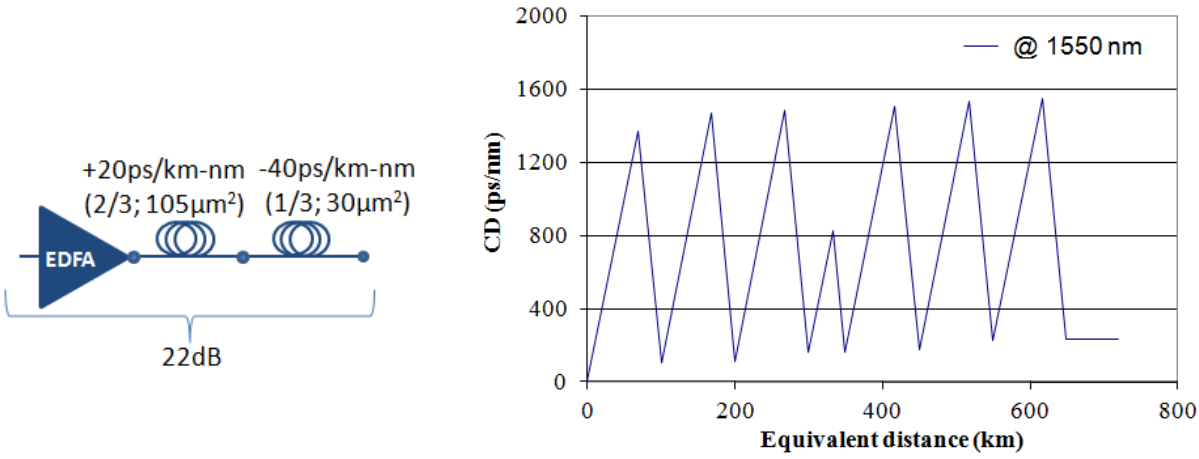

(a) (b)

Figure 7.3: (a) DMF fiber configuration per spool. (b) Dispersion map in all DMF configuration.

due to fiber non-linear effects. Figure 7.4(a) shows the bit rate evolution with the power ratio ΔP between the signal power and the lowest power of the wavelength comb for a fixed BER of 10^{-3}. Different output powers at the Line Amplifiers (LA) are evaluated and EDFA 8's output power is fixed at $17.3dBm$. The RF power of the modulating AMOOFDM signal at the transmitter is set to $8.7dBm$. The laser bias is $71mA$ and the input optical power on the PIN photodiode is $-2dBm$. Figure 7.4(b) shows an analogue analysis, this time fixing the bit rate at $20Gb/s$ and verifying the BER evolution with ΔP. It can be seen that the transmission is very sensitive to increases of the optical amplifiers' output power which highlights the expected degradation due to nonlinear effects in directly modulated and directly detected OFDM transmissions. However, by finding the appropriate compromise between the noise levels and nonlinear effects on the fiber, a bit rate of up to $29.5Gb/s$ could be demonstrated in the all-DMF configuration after $650km$.

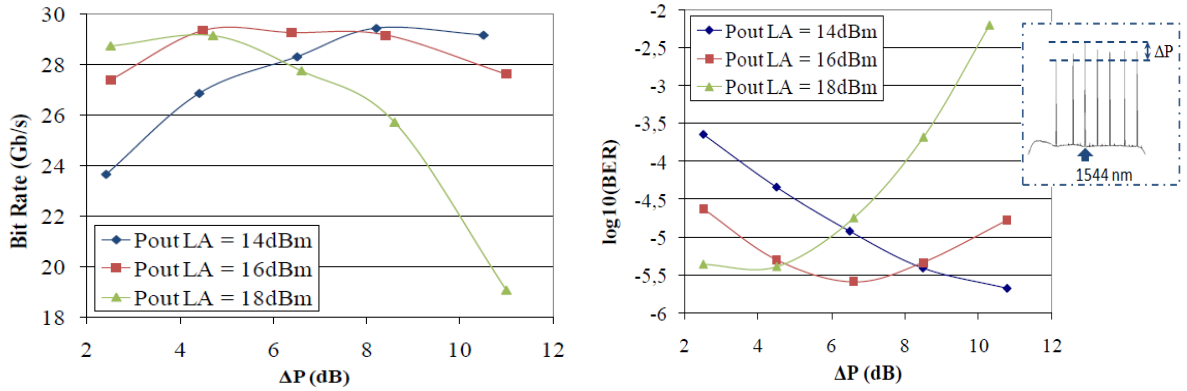

(a) (b)

Figure 7.4: 6 DMF spans configuration. (a) Bit rate evolution with ΔP for fixed 10^{-3} BER (b) BER evolution with ΔP for fixed $20Gb/s$.

The second analysis consisted of evaluating a mixed scenario, in which we have varied the number of DMF and SSMF spans in order to investigate the bit rate evolution with the amount of accumulated dispersion in the link.

Figure 7.5 illustrates the system's bit rate evolution with the number of SSMF spans for a

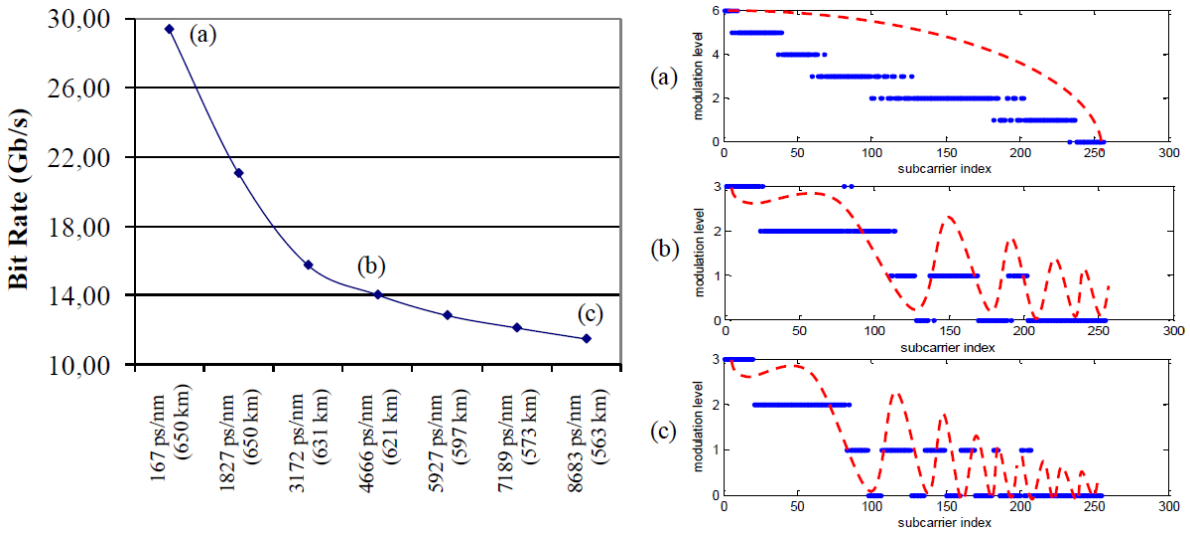

Figure 7.5: Bit Rate evolution with the amount of dispersion in the line. (a) 6 DMF spans (b) 3 DMF + 3 SSMF spans (c) 6 SSMF spans.

fixed BER of 10^{-3}. The x-axis shows the amount of dispersion and total transmission lengths for each combination. The modulation level per subcarrier for the 6 DMF, 3 DMF + 3 SSMF and 6 SSMF span configurations (insets (a), (b) and (c) respectively) is also shown in the figure. The expected increase of the number of transmission lobes with the dispersion in the estimated frequency response of the link (red dotted lines) can be evidenced by the modulation level distribution per subcarrier in each case. It should be noticed that a signal distortion proportional to the number of SSMF spans was observed and compelled the authors to optimize the signal's RF power and bias current (from $8.7dBm$ to $0dBm$ and from $71mA$ to $75mA$ respectively). Nevertheless, a bit rate of up to $11.5Gb/s$ is still feasible after $8683ps/nm$ without any kind of optical or electrical dispersion compensation.

7.3 Bandwidth-Adaptive OFDM

Since the very beginning of this work, we have been trying to highlight the advantages of transferring the complexity of future passive optical network from the optical plane to the digital signal processing domain. Indeed, we have been able to demonstrate that superior performances in terms of spectral efficiency and robustness to fiber impairments could be obtained with unsophisticated optical devices and simple architectures by means of reliable and well known digital techniques.

However, as far as a cost-effective bit-rate increase is concerned, we can evidence one crucial limitation of the OFDM approach: the need of using converters at high sampling rates that allow dealing with higher bandwidth signals. Indeed, a high bit-rate optical OFDM system would certainly require DSP-based components much more evolved than the ones that are currently mass-commercialized in other OFDM applications [5]. Even though Moore's conjecture [1] on DSP advancements had been quite precise for the past decades, at the present time high-performance converters are still very expensive and economically unfeasible for practical implementation, notably at the ONU side.

In this section, we address a solution in which lower sampling-rate converters work in parallel to provide a higher overall sampling rate. As far as the cost-effectiveness of a high-performance

[1]Moore's Law is based on observations made by Intel co-founder Gordon Moore and states that the number of transistors on a chip doubles every 2 years. It has been quite representative of the advancements of semiconductor's performances for the past 40 years.

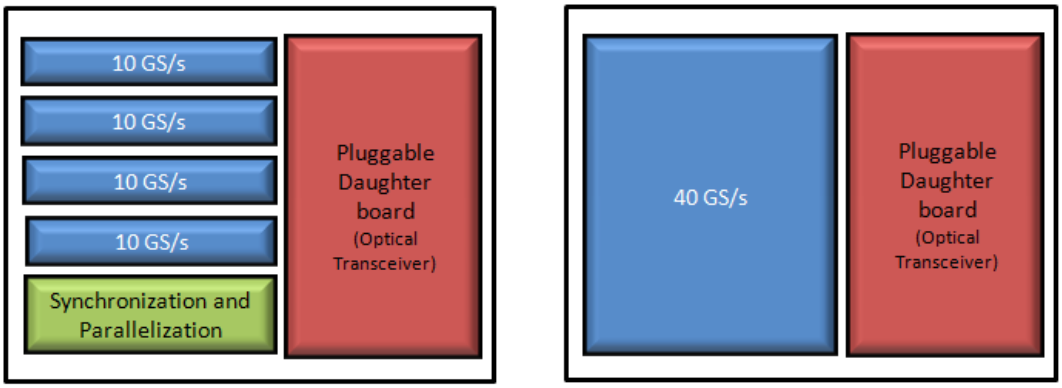

Figure 7.6: Two possible solutions to offer 40GS/s: one single 40GS/s module or four parallel 10GS/s modules.

ADC/DAC is concerned, such evolution in terms of architecture seems more immediate and cost-effective than increasing the sampling rate of one module individually. By means of advanced synchronization techniques, it would then be possible to consider a group of off-the-shelf converters that could work in parallel to achieve a higher overall sampling rate rather than conceiving one single ground-breaking high-sampling rate converter with an advanced technology. Figure 7.6 shows an example of both approaches, one with $4 \times 10GS/s$ converters working in parallel to enable $40GS/s$ operation and other with one single converter at $40GS/s$.

Based on the assumption of the parallel operation of lower-sampling-rate converters, we propose an algorithm whose principle is to adjust the bandwidth of the OFDM signal, i.e. the sampling rate of the converters, according to different objectives:

- Power-saving: an OFDM signal whose bandwidth can be adapted to the traffic variations would allow optimizing the number of sub-DAC/ADC and all the circuitry in each of the converters [6] according to the bit-rate demands of the users. Figure 7.7(a) (from [7]) shows an example of the daily variation of the traffic on France-IX Internet Exchange. For instance, we could envisage the use of a lower bandwidth and consequently lower bit-rate OFDM signal from 2 to 4 AM thus allowing some sub-converters at the OLT/ONU to be turned off. The user is referred to [8, 9] for an interesting evaluation of the design parameters for real-time high-speed OFDM transceivers, including the analysis of power consumption and footprint of Application Specific Integrated Circuit (ASIC) of different configurations.

- Technological survivability: the solution would also allow a gradual evolution of the network according to the increase on the user demands over the years. We could think namely of a single upgradeable motherboard with its pluggable converters, as shown in Figure 7.7(b).

- Versatility: the approach is also suitable for alowing the coexistence of services at different bit-rates in the same network. In addition, since the sub-converters setup is completely reconfigurable, the technique would be suitable for different kinds of optical components with their specific bandwidth characteristics. This would increase the niches of the market that are spotted by the solution, thus increasing the possibility of cost reduction.

- Personalized service per user: the flexible arrangement of parallel converters could be used to improve the quality of the signal provided to each user, thus allowing different levels in terms of Quality of Service (QoS).

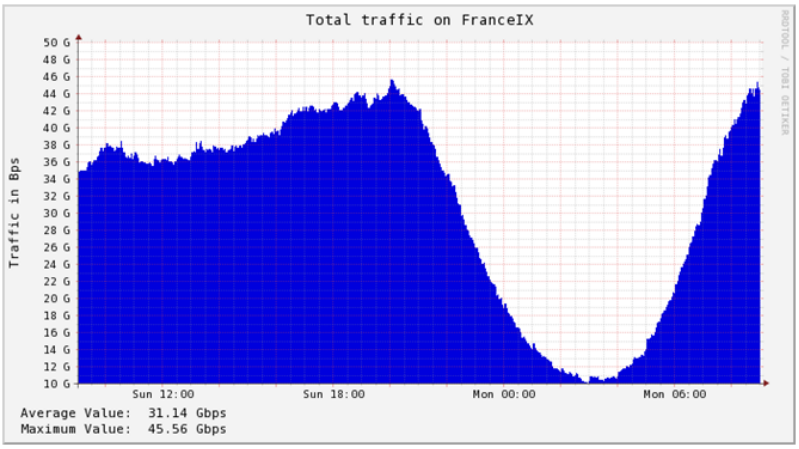

(a)

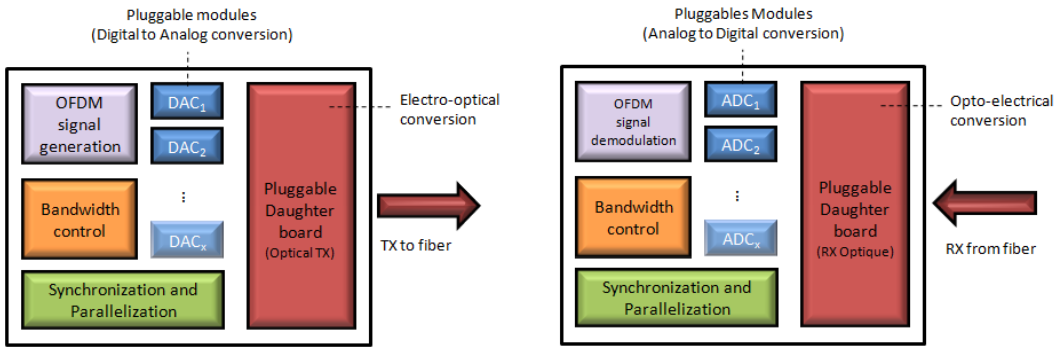

(b)

Figure 7.7: (a) Daily traffic variation on Internet Exchange France-IX. (b) Transmitter and Receiver generic motherboards with their pluggable converters.

- Liability: the proposed solution would also allow some degree of robustness to malfunctioning of one of the sub-converters, in which case, it could be easily excluded from the system by simple reconfiguration of the circuitry and without the need of human intervention [10–12].

The algorithm proposed in this section resembles very much the ones described in section 3.7. Actually, it consists of merging both rate-adaptive and margin-adaptive solutions and adapting them to a bandwidth minimization problem. In other words, by using both energy and bit-rate constraints at the same time, it is possible to identify the minimum signal bandwidth as well as the mappings and powers per subcarrier that would respect such constraints. Indeed, the solution allows an analogy between an accordion and the OFDM signal, whose bandwidth is expanded and contracted to provide the necessary bit-rates on the network.

7.3.1 Mathematical Description of the Problem

Let $\mathcal{W}$ be the OFDM signal bandwidth, T_s the OFDM symbol duration, R the target bit rate, E the target signal energy, N_D the number of subcarriers and N_{CYP} the number of samples of the cyclic prefix. The bandwidth minimization problem and its constraints can be described by:

$$\begin{gathered} min(\mathcal{W}^2), \quad s.t.: \\ \frac{1}{T_S}\sum_{k=1}^{N_D} b_k = R \\ \sum_{k=1}^{N_D} \varepsilon_k = E \end{gathered} \tag{7.1}$$

with

$$T_S = \frac{2\left(N_D+1\right)+N_{CYP}}{2\mathcal{W}} \tag{7.2}$$

Note that we have chosen to minimize $\mathcal{W}^2$ instead of $\mathcal{W}$ to exclude the possibility of generating a mathematically possible but unfeasible solution with a negative bandwidth. The double-constrained minimization problem can be described through the Lagrangian:

$$\mathfrak{L}\left(\varepsilon_k, \lambda_1, \lambda_2, \mathcal{W}\right) = \mathcal{W}^2 - \lambda_1\left(\sum_{k=1}^{N_D}\log_2\left(1+\frac{g_k\varepsilon_k}{\Gamma}\right) - \frac{P}{\mathcal{W}}\right) - \lambda_2\left(\sum_{k=1}^{N_D}\varepsilon_k - E\right) \tag{7.3}$$

with

$$P = R\left(\frac{2\left(N_D+1\right)+N_{CYP}}{2}\right) \tag{7.4}$$

The solution is found when $\nabla\mathfrak{L}\left(\varepsilon_k, \lambda_1, \lambda_2, \mathcal{W}\right) = 0$. The partial derivatives $\frac{\partial\mathfrak{L}}{\partial\lambda_{1,2}}$ give the bit rate and energy constraints whereas $\frac{\partial\mathfrak{L}}{\partial\mathcal{W}}$ and $\frac{\partial\mathfrak{L}}{\partial\varepsilon_k}$ will state that the solution is stationary (maximum or minimum):

$$\frac{\partial\mathfrak{L}}{\partial\mathcal{W}} = 0 \therefore \mathcal{W} = \left(\frac{\lambda_1 P}{2}\right)^{\frac{1}{3}} \tag{7.5}$$

$$\frac{\partial\mathfrak{L}}{\partial\varepsilon_k} = 0 \therefore \frac{\Gamma}{g_k} + \varepsilon_k = \frac{-\lambda_1}{\lambda_2\ln(2)} = constant \tag{7.6}$$

Equation 7.6 shows that the the bandwidth adaptive (BA) problem also obeys the water-filling-like solution (see section 3.7) where $\frac{-\lambda_1}{\lambda_2 \ln(2)}$ represents the level of water of the system. We find ourselves with a group γ of $N_D + 3$ variables $(\varepsilon_1, \varepsilon_2, \ldots, \varepsilon_{N_D}, \lambda_1, \lambda_2, \mathcal{W})$ and $N_D + 3$ equations:

$$\begin{aligned} f_k(\gamma) &= \tfrac{\Gamma}{g_k} + \varepsilon_k + \tfrac{\lambda_1}{\lambda_2 \ln(2)}, \quad k = 1, 2, \ldots, N_D \\ f_{N_D+1}(\gamma) &= \sum_{k=1}^{N_D} \log_2\left(1 + \tfrac{g_k \varepsilon_k}{\Gamma}\right) - \tfrac{P}{\mathcal{W}} \\ f_{N_D+2}(\gamma) &= \sum_{k=1}^{N_D} \varepsilon_k - E \\ f_{N_D+3}(\gamma) &= \mathcal{W} - \left(\tfrac{\lambda_1 P}{2}\right)^{\frac{1}{3}} \end{aligned} \tag{7.7}$$

Note that in order to assure the physical coherence of the solutions, λ_1 must be positive and λ_2 must be negative. The solution of this system can be numerically found by the Newton-Rhapson method. Given a function $f(x)$ and its first derivative $f'(x)$, the method states that the roots of $f(x)$ can be found from an initial guess x_0 after several iterations. Indeed:

$$x_1 = x_0 - \frac{f(x_0)}{f'(x_0)} \tag{7.8}$$

will be a better approximation to the root of $f(x)$ than x_0. Geometrically, x_1 is the intersection of a tangent to $f(x)$ at $f(x_0)$ with the x-axis. The procedure can be repeated until a sufficiently exact value for the root is found. The same principle can be used for a group of $N_D + 3$ variables through:

$$\gamma_1 = \gamma_0 - [\mathsf{J}]^{-1} \begin{bmatrix} f_1(\gamma_0) \\ f_2(\gamma_0) \\ \vdots \\ f_{N_D+3}(\gamma_0) \end{bmatrix} \tag{7.9}$$

where [J] represents the Jacobian matrix given by:

$$\begin{aligned} [\mathsf{J}] &= \begin{bmatrix} \frac{\partial f_1}{\partial \varepsilon_1} & \frac{\partial f_1}{\partial \varepsilon_2} & \cdots & \frac{\partial f_1}{\partial \varepsilon_{N_D}} & \frac{\partial f_1}{\partial \lambda_1} & \frac{\partial f_1}{\partial \lambda_2} & \frac{\partial f_1}{\partial \mathcal{W}} \\ \frac{\partial f_2}{\partial \varepsilon_1} & \frac{\partial f_2}{\partial \varepsilon_2} & \cdots & \frac{\partial f_2}{\partial \varepsilon_{N_D}} & \frac{\partial f_2}{\partial \lambda_1} & \frac{\partial f_2}{\partial \lambda_2} & \frac{\partial f_2}{\partial \mathcal{W}} \\ \vdots & \vdots & & \vdots & \vdots & \vdots & \vdots \\ \frac{\partial f_{N_D+1}}{\partial \varepsilon_1} & \frac{\partial f_{N_D+1}}{\partial \varepsilon_2} & \cdots & \frac{\partial f_{N_D+1}}{\partial \varepsilon_{N_D}} & \frac{\partial f_{N_D+1}}{\partial \lambda_1} & \frac{\partial f_{N_D+1}}{\partial \lambda_2} & \frac{\partial f_{N_D+1}}{\partial \mathcal{W}} \\ \frac{\partial f_{N_D+2}}{\partial \varepsilon_1} & \frac{\partial f_{N_D+2}}{\partial \varepsilon_2} & \cdots & \frac{\partial f_{N_D+2}}{\partial \varepsilon_{N_D}} & \frac{\partial f_{N_D+2}}{\partial \lambda_1} & \frac{\partial f_{N_D+2}}{\partial \lambda_2} & \frac{\partial f_{N_D+2}}{\partial \mathcal{W}} \\ \frac{\partial f_{N_D+3}}{\partial \varepsilon_1} & \frac{\partial f_{N_D+3}}{\partial \varepsilon_2} & \cdots & \frac{\partial f_{N_D+3}}{\partial \varepsilon_{N_D}} & \frac{\partial f_{N_D+3}}{\partial \lambda_1} & \frac{\partial f_{N_D+3}}{\partial \lambda_2} & \frac{\partial f_{N_D+3}}{\partial \mathcal{W}} \end{bmatrix} \\ &= \begin{bmatrix} 1 & 0 & \cdots & 0 & B & G & 0 \\ 0 & 1 & \cdots & 0 & B & G & 0 \\ \vdots & \vdots & & \vdots & \vdots & \vdots & \vdots \\ 0 & 0 & \cdots & 1 & B & G & 0 \\ A_1 & A_2 & \cdots & A_{N_D} & 0 & 0 & H \\ 1 & 1 & \cdots & 1 & 0 & 0 & 0 \\ 0 & 0 & \cdots & 0 & F & 0 & 1 \end{bmatrix} \end{aligned} \tag{7.10}$$

with:

$$A_k = \frac{1}{\ln(2)\left(\frac{\Gamma}{g_k}+\varepsilon_k\right)},\ k = 1, 2, ..., N_D$$

$$B = \frac{1}{\lambda_2 \ln(2)}$$

$$F = -\frac{1}{3}\left(\frac{P}{2\lambda_1^2}\right)^{\frac{1}{3}} \tag{7.11}$$

$$G = \frac{-\lambda_1}{\lambda_2^2 \ln(2)}$$

$$H = \frac{P}{W^2}$$

After some iterations, the roots of the equations will be found according to the error margin defined by the user. Since the determinant of $[\mathtt{J}]$ is not null, $[\mathtt{J}]$ is invertible and the bandwidth of the OFDM signal as well as the mappings and powers per subcarrier that correspond to the energy and bit-rate constraints of the problem can be found from an initial guess γ_0. It is also desirable to consider the granularity of the sub-converters on the system. For example, if the bandwidth found by the algorithm for a specific power and bit-rate constraints is 2.3GHz for a transmitter that has 10 sub-converters at $1GS/s$ each, then it is possible to use only 5 of these converters to reach $5GS/s$. The exceeding bit-rate may be used, for instance, for the transmission of additional overhead information or may be simply discarded.

It is important to highlight, however, that the algorithm will find non-integer values for b_k, likewise the water-filling solution seen in section 3.7. That's the reason why two complementary steps in the algorithm must follow. Firstly, b_k is rounded to its closest integer value. This procedure will cause $\sum_{k=1}^{N_D} \varepsilon_k$ to diverge from the initial energy constraint but this problem can be solved by proceeding to Campello's E-tightening which will add or remove bits in the appropriate subcarriers until the energy constraint is satisfied. The following procedures summarize the algorithm implementation:

1. Numerically solve the group of $N_D + 3$ equations to find the signal bandwidth as well as the subcarriers' ε_k and b_k (non-integer) distributions that satisfy both energy and bit-rate constraints.

2. Round b_k and find the corresponding ε_k.

3. E-tight ε_k.

The main limitation of the Newton-Rhapson approach is that it is not necessarily globally convergent, meaning that it may not converge for any starting guess for the parameters. To circumvent this problem, we add an adjustable step size μ_{NR} to 7.9 after trying $\mu_{NR} = 1$ if ever the solution diverges [13]:

$$\gamma_1 = \gamma_0 - \mu_{\mathrm{NR}} \left[\mathtt{J}\right]^{-1} \begin{bmatrix} f_1(\gamma_0) \\ f_2(\gamma_0) \\ \vdots \\ f_{N_D+3}(\gamma_0) \end{bmatrix} \tag{7.12}$$

Currently, we are still investigating on how to automatically choose an optimum step size that will always assure the convergence of the algorithm. We must recall, however, that other optimization approaches exist such as the Steepest Descent and the Secant method.

Also, we must disconsider the solutions that are mathematically possible but which are unfeasible in a real-life system such as, for instance, those culminating on a negative or complex-valued bandwidth. Our algorithm is programmed to start the Newton-Rhapson method again using a different starting guess each time these situations happen. For instance, if ever the optimization using the full $12GHz$ frequency response converges to a negative bandwidth, the code is set to retry to find a physically feasible solution using, let's say $10GHz$ bandwidth as the starting guess.

Figures 7.8 to 7.11 show four examples of the implementation of the algorithm over the $40km$ IMDD channel that has been adopted as reference example in section 3.7. The target BER is 10^{-3} and the target bit-rate has been set to $15Gb/s$, $10Gb/s$, $5Gb/s$ and $2.5Gb/s$ respectively. The subconverter's granularity is $500MS/s$. The number of data subcarriers is 255 (512 inputs at the (I)FFT with Hermitian symmetry) and the number of cyclic prefix samples is 8. The algorithm starts from a reference $12GHz$ probing measurement of the channel gain coefficients g_k and interpolates it at each iteration to find the corresponding g_k related to a specific signal bandwidth.

Figure 7.12 shows the occupation matrix of the $24GS/s$ ($48\times500MS/s$) capable DACs/ADCs of each example. For instance, for $2.5Gb/s$ operation, only 1/8 of the total of sub-converters is needed.

The reader should notice that since the resulting OFDM signals occupy narrower bandwidths and N_D is the same as the original probing signal, the BA algorithm will culminate on a smaller separation between adjacent subcarriers. This may aggravate the degradations imposed by sampling frequency offset (refer to subsection 3.5.3). The problem, however, can be solved very simply by fixing the spacing Δf between the subcarriers and letting N_D vary in the algorithm. In this case, instead of generating a "stretchable" OFDM signal, the BA algorithm would instead find the appropriate "cropped" version of the original signal allowing both bit-rate and energy constraints to be obeyed.

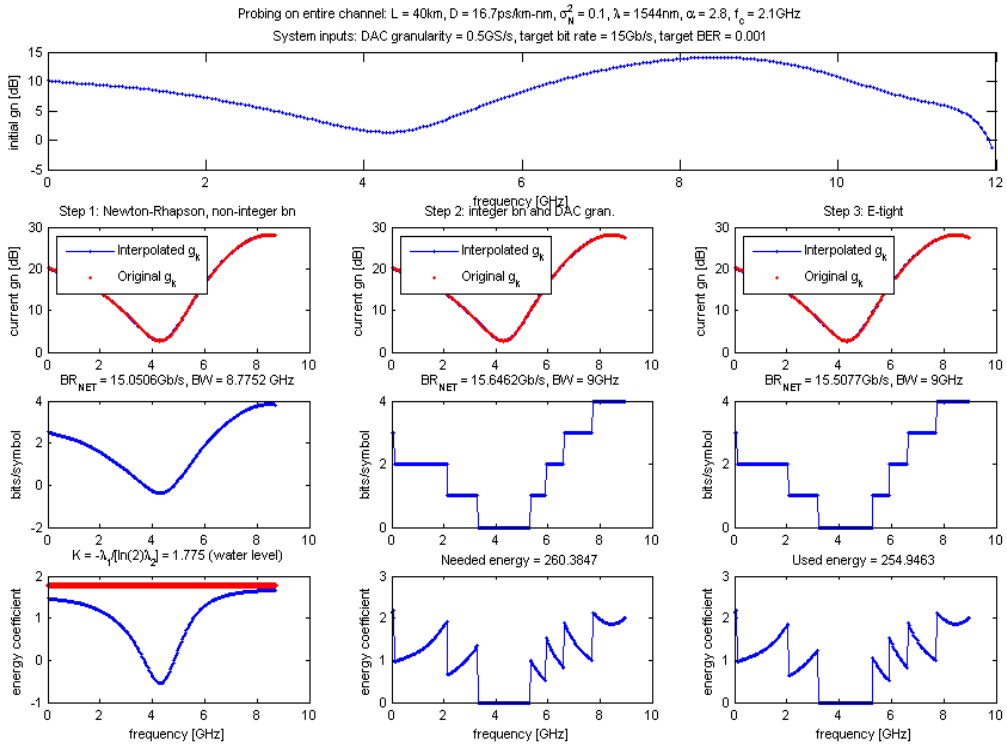

Figure 7.8: BA-OFDM example on 40km SSMF IMDD channel and $15Gb/s$ target bit rate.

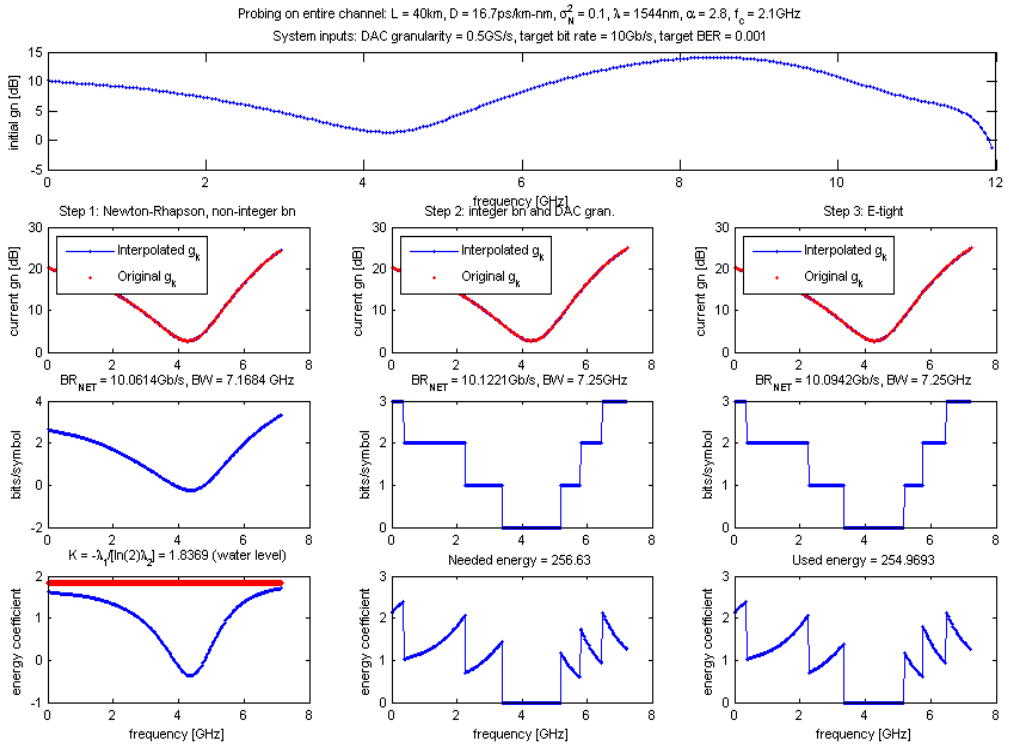

Figure 7.9: BA-OFDM examples on 40km SSMF IMDD channel and $10Gb/s$ target bit rate.

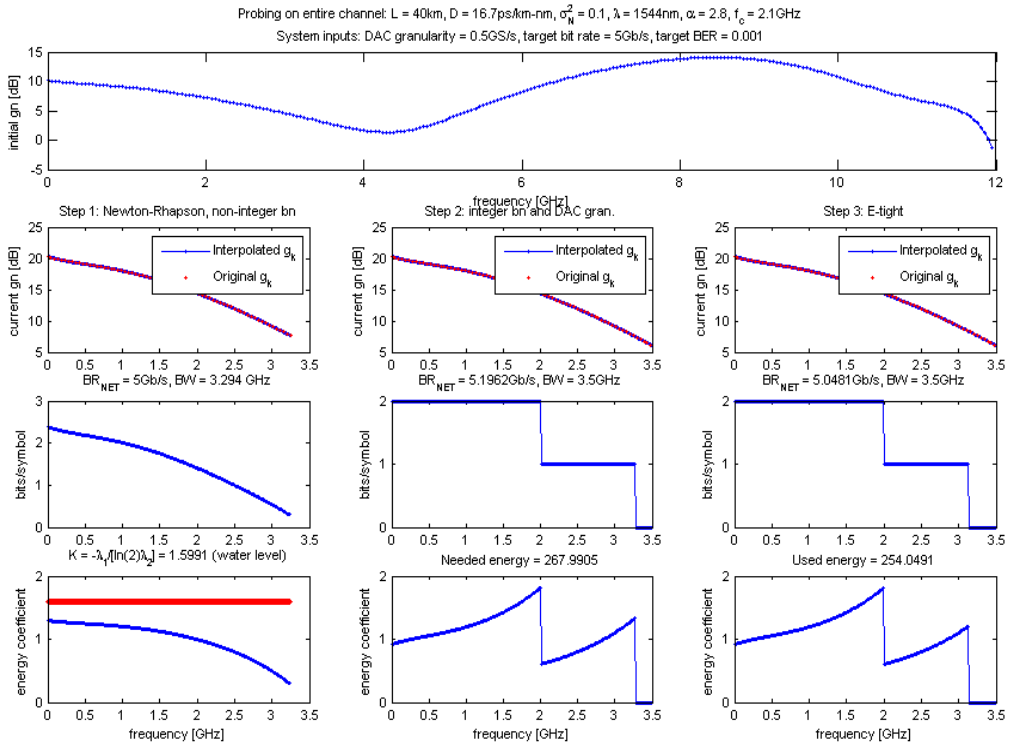

Figure 7.10: BA-OFDM examples on 40km SSMF IMDD channel and $5Gb/s$ target bit rate.

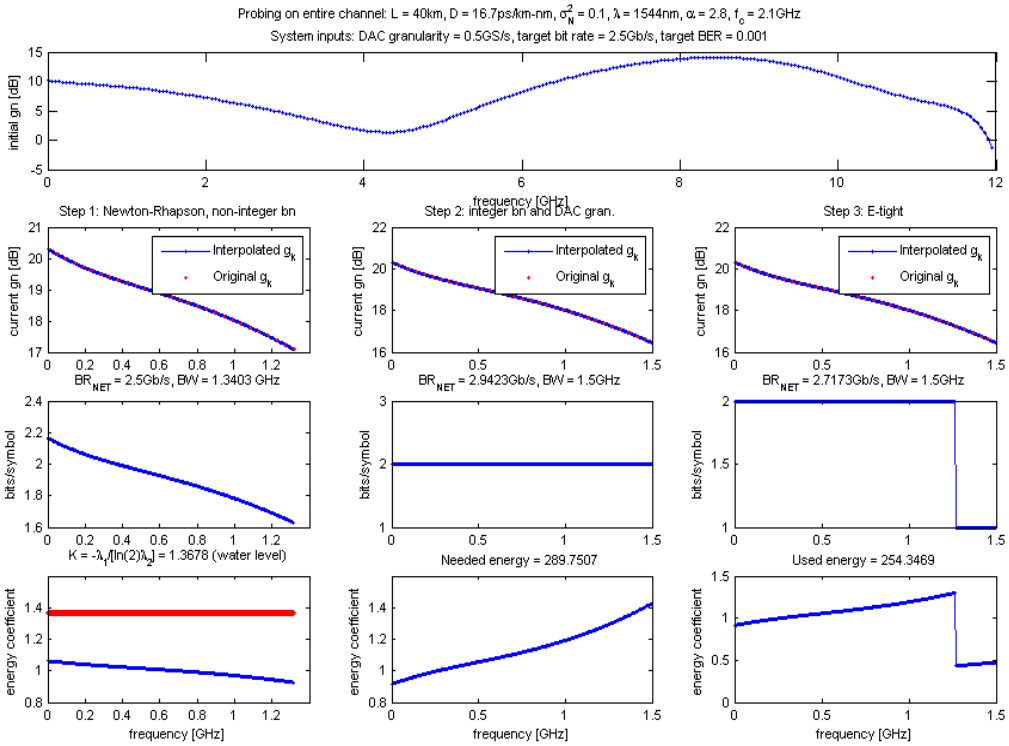

Figure 7.11: BA-OFDM examples on 40km SSMF IMDD channel and $2.5Gb/s$ target bit rate.

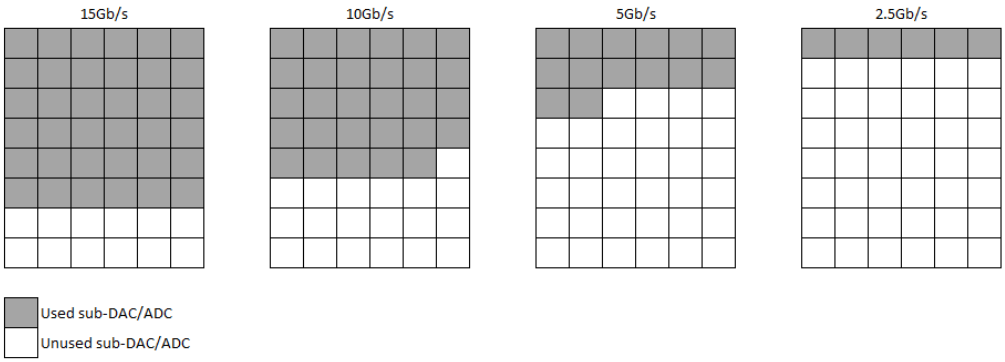

Figure 7.12: Matrices showing the necessary numbers of sub-converters to attain each of the targeted bit-rates.

7.4 Conclusions

If the long reach transmissions shown in section 7.2 demonstrated the potential of OFDM in view of the metro-access network integration, further studies still have to be conducted regarding the bandwidth adaptive OFDM algorithm presented in section 7.3. Notably, the numerical resolution of the proposed equations has to be ameliorated to avoid or at least perfectly circumvent the solutions that are mathematically possible but not physically feasible. Other methods beyond the Newton-Rhapson approach should be tested for this matter.

The structuring and resolution of a more complex strand of the algorithm in which the bandwidth span can be chosen no matter where in the frequency span should also be considered to allow the implementation of the algorithm under the MB-OFDM approach.

References

[1] D. Torrientes et al. "10Gbit/s for next generation PON with electronic equalization using un-cooled 1.55um directly modulated laser". In: *Optical Communication, 2009. ECOC '09. 35th European Conference on*. Vol. 2009-Supplement. Sept. 2009, pp. 1 –2. URL: http://ieeexplore.ieee.org/search/srchabstract.jsp?tp=&arnumber=5395701&openedRefinements%3D*%26filter%3DAND%28NOT%284283010803%29%29%26searchField%3DSearch+All%26queryText%3Dtorrientes (cit. on p. 158).

[2] M. Chacinski et al. "ETDM Transmitter Module for 100-Gb/s Ethernet". In: *Photonics Technology Letters, IEEE* 22.2 (Jan. 2010), pp. 70 –72. ISSN: 1041-1135. DOI: 10.1109/LPT.2009.2036146 (cit. on p. 158).

[3] S. Chandrasekhar et al. "Chirp-managed laser and MLSE-RX enables transmission over 1200 km at 1550 nm in a DWDM environment in NZDSF at 10 gb/s without any optical dispersion compensation". In: *Photonics Technology Letters, IEEE* 18.14 (July 2006), pp. 1560 –1562. ISSN: 1041-1135. DOI: 10.1109/LPT.2006.879810 (cit. on p. 158).

[4] S. Chandrasekhar et al. "Flexible transport at 10-Gb/s from 0 to 675 km (11,500 ps/nm) using a chirp-managed laser, no DCF, and a dynamically adjustable dispersion-compensating receiver". In: *Optical Fiber Communication Conference, 2005. Technical Digest. OFC/NFOEC.* Vol. 6. Mar. 2005, 3 pp. Vol. 5. DOI: 10.1109/OFC.2005.193208 (cit. on p. 158).

[5] N. Cvijetic. "OFDM for Next Generation Optical Access Networks". In: *Lightwave Technology, Journal of* PP.99 (2011), p. 1. ISSN: 0733-8724. DOI: 10.1109/JLT.2011.2166375. URL: http://ieeexplore.ieee.org/stamp/stamp.jsp?tp=&arnumber=6004799 (cit. on p. 162).

[6] Junqiang Hu, Dayou Qian, and Ting Wang. "Energy efficient OFDM transceiver based on traffic tracking and adaptive bandwidth adjustment". In: *Optical Communication (ECOC), 2011 37th European Conference and Exhibition on*. Sept. 2011, pp. 1 –3 (cit. on p. 163).

[7] FranceIX. *Statistiques de trafic*. URL: https://www.franceix.net/page.php?MP=editorial&ST=section&op=page&artid=48 (cit. on p. 163).

[8] Rachid Bouziane et al. "Design Studies for ASIC Implementations of 28 GS/s Optical QPSK- and 16-QAM-OFDM Transceivers". In: *Optics Express* 19 (2011), pp. 20857–20864. URL: http://users.ece.cmu.edu/~pam/publications.html (cit. on p. 163).

[9] Peter A. Milder et al. "Design and simulation of 25 Gb/s optical OFDM transceiver ASICs". In: *Opt. Express* 19.26 (Dec. 2011), B337–B342. DOI: 10.1364/OE.19.00B337. URL: http://www.opticsexpress.org/abstract.cfm?URI=oe-19-26-B337 (cit. on p. 163).

[10] R.A.T. van den Hoven et al. *A parallel current-steering DAC architecture for flexible and improved performance*. URL: http://www.google.fr/url?sa=t&rct=j&q=a+parallel+current-steering+dac+architecture+for+flexible+and+improved&source=web&cd=2&ved=0CCwQFjAB&url=http%3A%2F%2Fciteseerx.ist.psu.edu%2Fviewdoc%2Fdownload%3Fdoi%3D10.1.1.96.9438%26rep%3Drep1%26type%3Dpdf&ei=g-hAUMHlGY-WhQfz14DoDw&usg=AFQjCNHyHP_x0zB_xBbeRckXmqzrconCyw (cit. on p. 165).

[11] G.L. Radulov et al. "Parallel current-steering D/A Converters for Flexibility and Smartness". In: *Circuits and Systems, 2007. ISCAS 2007. IEEE International Symposium on.* May 2007, pp. 1465 –1468. DOI: 10.1109/ISCAS.2007.378579 (cit. on p. 165).

[12] A. Zanikopoulos et al. "A flexible ADC approach for mixed-signal SoC platforms". In: *Circuits and Systems, 2005. ISCAS 2005. IEEE International Symposium on.* May 2005, 4839 –4842 Vol. 5. DOI: 10.1109/ISCAS.2005.1465716 (cit. on p. 165).

[13] Trond Hjorteland. *The Newton-Rhapson Method*. July 1999. URL: `trond.hjorteland.com/thesis/node28.html` (cit. on p. 167).

Part III

General Conclusions

Highlights of this Work

In this work, we have studied the potentialities of IMDD OFDM to address the needs of future optical access networks. The context and motivations of this thesis have been presented in chapter 1, where the importance of next-generation optical networks for circumventing the access bottleneck has been highlighted with a view to increase demands for higher bit-rates. In this context, we have focused our study on passive point-to-multipoint architectures, which offer the advantage of allowing the mutualization of the infrastructure of the network among different users.

In the same chapter, we recall the main characteristics of the different existing PON standards under IEEE and ITU specifications and we present several approaches used by different telecommunications operators for deploying the optical fiber to the subscribers. We show then the main drivers and requirements for the evolution towards NG-PON2 namely:

- the capacity of offering sustainable $1Gb/s$ per user,
- allowing network consolidation through a reduction in the number of central offices and an increase in the number of subscribers in the network,
- preserving interoperability with formerly deployed generations and services while maintaining cost-effective solutions at the user side and
- providing long-term flexibility for current and future applications.

We finish the chapter with some advantages and drawbacks of the main technological candidates for NG-PON2: pure WDM, UDWDM, TWDM and naturally OFDM.

Part I is dedicated to a theoretical overview of the subjects presented in this thesis. We also provide valuable inputs for practical work and some interesting simulations to help understanding different concepts. It begins with chapter 2, where we present some methods to characterize the optical components of the transmission chain and we investigate how they will influence the performances of the system. Still on the same chapter, we show the classical approach on the study of the propagation in optical fibers using the Non-linear Shrödinger Equation. The fundamentals of fiber attenuation, chromatic dispersion and non-linear effects are then presented. One of the most important subjects is left, however, for the end of the chapter: we present a complete investigation on the effects of fiber's dispersion and laser's adiabatic and transient chirp on the frequency response of an IMDD channel. Such analysis is extremely interesting when we need to evaluate the impacts of the channel on signals that do not have a time-domain representation as simple as that of a NRZ signal. It provided thus a substantial help for understanding the impacts of the frequency-selective channel on each subcarrier of the OFDM signal.

While in chapter 2 we focus on the optical components and the physical phenomena related to the propagation through an optical fiber, in chapter 3 we unravel the principles of OFDM modulation, a widely adopted technique that has been used in different standards, including wireline ADSL and VDSL and wireless WLAN, WiMAX and LTE. A thorough step-by-step analysis of the modulation and demodulation block diagrams is presented based on our own "home-made" program and a special attention is given to the important mechanisms of time and frequency synchronization. We also present the different OFDM modulation approaches in the optical domain and a very detailed analysis of the principles of bit and power loading optimization is given. From the familiar water-filling principle, we recall Campello's and Chow's approaches and we later present our own versions of the rate and margin adaptive algorithms with integer number of bits per symbol per subcarrier. Finally, two multiuser versions of Campello's algorithm are presented in which several subscribers of a PON with their specific frequency responses share the subcarriers of an OFDM signal. The sub-wavelength granularity allowed by

the Multiband and Sparsely-Distributed Subcarriers approaches constitute one interesting asset for future point-to-multipoint optical networks.

We have also seen that if the sparse distribution of subcarriers allowed the maximization of the throughput per wavelength, it certainly imposed serious economical limitations on the user-side equipment due to the need of high-sampling ratio converters capable of dealing with subcarriers that could be potentially located anywhere in the received signal spectrum. On the other hand, the simpler but less efficient multi-band approach could allow the use of lower-sampling ratio ADC at the ONU through electrical downconversion of the frequency spans associated to each user. The cost-effectiveness of this approach would, however, be limited to the desired level of tunability of the LO.

Chapter 3 was certainly the most dense chapter of this thesis. Indeed, the construction of a reliable modulator and demodulator was a sine qua non of the optical transmissions shown in part II and much effort has been devoted for giving practical leads on the implementation of an offline OFDM experiment.

In part II, we focus on the experimental results of this thesis. In chapter 4, we propose a fitting procedure based on the Nelder-Mead Simplex Downhill algorithm which allowed measuring the fiber's dispersion parameter and the laser's chirp components. From simple measurements of the frequency response of an IMDD channel, we were able to estimate the adiabatic and transient chirp parameters of different light sources, including several DFBs, an EML and even a RSOA+FBG. However, we have also determined that even if the IMDD channel models allowed a fast and efficient characterization of the chirp parameters of different light sources, the propagation of an OFDM signal was subjected to more complex phenomena. We have verified that the optimum modulation index of a multicarrier signal will be subjected to an intricate dispersion and chirp-dependent interference pattern and has thus to be carefully chosen to avoid SNR degradation and pronounced levels of out-of-band noise in the transmission.

In chapter 5, we have seen that the downstream transmissions of an OFDM signal were not problematic and we have managed to obtain some very interesting results using conventional photodiodes and different emitters, including a miniaturized DML TOSA. We have seen that the performance of the OFDM transmissions in terms of optical budgets could be considerably improved by means of optical amplification but preserving a passive outside plant. The use of EDFA's in either the OLT or ONU sides allowed $20Gb/s/\lambda$ operation compatible with classes B+ and C+ optical budgets respectively and transmission through up to $100km$ SSMF. Remarkably, we have managed to obtain $40Gb/s$ on a single wavelength using a $12GHz$ bandwidth, which corresponds to a spectral efficiency of more than $3bits/s/Hz$. Later, we have recapped the effects of the laser chirp on the channel frequency response and extended the study on the context of the bit and power allocation of the OFDM subcarriers.

Also, we have seen that OFDM allows creating a whole new dimension for sharing the network resources amongst the subscribers thus providing a degree of flexibility that can be transparently used with other multiplexing strategies in a PON. Indeed, since it enables higher spectral efficiencies when compared to conventional NRZ, the "life expectation" of TDM-OFDM as far as the CDR problematic is concerned could be soared to allow higher bit-rates in burst mode operation without demanding complex synchronization solutions at the ONU receiver. The adoption of subcarrier allocation in a time-multiplexed solution would also solve a fundamental limitation of TDM: the fact the all users have to work at the line-rate even though they might require only a small percentage of that speed. The data rate of each user could be defined by the number of subcarriers allocated to him on a burst. In addition, this approach would allow transmissions of two or more users in the same burst, which is not possible in conventional NRZ-TDM systems.

Furthermore, WDM could be easily implemented with OFDM if in a static or quasi-static configuration by stacking of fixed optical channels. Indeed, OFDM can be used to allow dynamic resource allocation through subcarrier multiplexing without the need for costly wavelength-agile

structures and devices. Some extra care might have to be taken, however, in dense WDM-OFDM approaches due to the out-of-band noise arriving from the dispersion and chirp induced distortions on the OFDM signal.

In chapter 6, we have seen that the upstream transmission remained the major challenge of future NG-PON2. Indeed, current NRZ TDMA will not be capable of providing alone the needed performances in terms of aggregate bit-rate, distance and number of users per PON tree. We have demonstrated, however, promising results using TDMA-OFDM and cost-effective VCSELs without temperature control.

We have also investigated Frequency Division Multiple Access (FDMA) as an option for the upstream in which the signals of all ONU can be detected by a single photodiode at the OLT and the legacy infrastructure of the network can remain unchanged. We have seen that an upstream IMDD FDMA scheme required a complementary time or wavelength multiplexing dimension due to optical beat interference arriving from the direct detection at the receiver side. Despite the fact that adaptively modulated optical OFDM could be used to optimize the throughput according to the SNR of each user, further investigations on the WDM-FDMA architecture are still necessary to extrapolate this scenario to as many users/wavelengths/sub-bands as possible so that the limitations due to optical beat interference can be well established. Such extrapolation would also allow determining the impact of other potential sources of degradation such as the accumulated RIN of the emitters and the addition of the photodiode's shot noise with increasing numbers of subscribers in the network.

Even if we managed to demonstrate interesting performance on TDMA-OFDM and WDMA-FDMA-OFDM, it is highly probable that a new technological brick will have to be developed to allow unconstrained performances for the upstream transmission in NG-PON2.

Finally, in chapter 7, we have exceeded our expectations concerning OFDM's robustness to chromatic dispersion. Indeed, we have even demonstrated $> 10Gb/s$ transmissions over more than $500km$ SSMF without any kind of electronic or optical dispersion compensation mechanism, which constituted an interesting experiment from the point of view of a possible metro-access network integration. In the same chapter, we have also proposed a Bandwidth-Adaptive OFDM algorithm to address the limitations imposed by the converters at the customers' premises. The algorithm consisted of a solution to adaptively choose the bandwidth of the signal and mapping and power of the subcarriers according to a specific need in terms of bit-rate.

The FSAN Comes to a Decision

On July 16th 2012, three months before the end of this thesis, the FSAN officially announced TWDM with optional WDM overlay extensions as the technological choice for NG-PON2. NG-PON2 standardization works will now follow through contributions to ITU-T Study Group 15 - Question 2 Access Working Group (Q2/SG15) to complete ITU-T's G989.1. Standards can be ratified as early as 2013, giving the industry a clear path to evolve. The first platforms may be deployed in 2015.

FSAN's decision was clearly taken by considering principally the availability time-frame of the different candidates. Indeed, $40Gb/s$ can be implemented through a relatively simple stacking of 4 XG-PON1 optical channels using transceivers that have already achieved their time to market and without the need of conceiving a whole new set of communication protocols. Also, it is probably the less disruptive approach regarding currently deployed systems.

Unfortunately and despite its success in countless other standards, optical OFDM is not yet enough mature to be considered to the next PON generation, even though some more disruptive candidates have been seriously considered by the FSAN. Indeed, we are giving up all the advantages of OFDM which allow loosening the requirements on the optical plan through simple digital signal processing. Ultimately, OFDM could have been used in a TWDM approach to give some time to wavelength-agile systems to become economically interesting and sufficiently

efficient for future generations.

Such hurry on defining NG-PON2 rules even though XGPON1 has not even been deployed yet is also part of a strong pressure exerted by some operators. For instance, those who have great part of their technological park based on BPON, which is not compatible with GPON, will be more interested in migrating directly to NG-PON2 so that the risks in terms of components and architectures can be reduced and more business cases can be addressed such as the mobile backhauling. On the other hand, the operators who have already decided to migrate to XGPON1 due to an urgency in addressing their customers' needs will prefer to wait until the expenses on the new generation systems can be recovered from the profits of the provided services.

TWDM will face several challenges. For instance, one major difficulty appears when we think of implementing flexible resource allocation in the network using the wavelength dimension. Indeed, wavelength agility in a network with potentially hundreds of subscribers has never been seen before in the optical domain. It will not only impose a great challenge in terms of operation and control but will also depend on the time it takes to wavelength agnostic components to mature and provide performing and economically viable options for agile and unconstrained allocation per subscriber.

Another point concerns the wavelengths drifting of the emitters, specially at the ONU side. Indeed, lower-cost transceivers have less performing characteristics in terms of wavelength control and it results in a potential problem when we remember the limited wavelength span in which NG-PON2 should operate. In addition, in order to reduce the electrical consumption of these devices, they should ideally not possess any temperature control mechanism. In other words, colorless operation should be guaranteed on a extremely limited wavelength range, under rather variable temperature conditions and without exploding the electrical consumption of the equipments.

From our analysis in this work, this decision does not change the fact that OFDM is a very interesting and strong technological alternative on the evolution of passive optical networks. Indeed, one first important advantage of OFDM is its capacity to transfer the system's complexity from the optical plan to the electronic domain. It allows keeping the simple and cost-effective IMDD solution and still guarantees increased spectral efficiencies and improved robustness to chromatic dispersion if compared to naive NRZ. In addition, thanks to well-known bit and power loading algorithms, OFDM is capable of circumventing the frequency selective channel response characterized by the interplay between fiber chromatic dispersion and the laser transient and adiabatic chirp components to optimize the transmission throughput without any kind of optical or electronic dispersion compensation module. Furthermore, it allows creating a whole new dimension when sharing the resources of the network between different users through subcarrier multiplexing.

For now, however, let's just live on the hope that this announcement forestalls a new working group, this time for the NG-PON3 where OFDM will certainly be able to fight again for some space. Let's also hope that it will not discourage the researches from maintaining their interest on the subject so that OFDM can finally achieve a higher degree of maturity in the optical domain and that electronics can continue to evolve to allow cost-efficient converters at higher sampling rates.

Part IV

Appendix

Appendix A

Estimation of the Nonlinearities of the IM3 Characterization Chain

In this section we provide the estimation of the nonlinearities of the ESA and the power coupler used in the measurement of the IM3 of the transmission chain. Actually, the linear operation of the local oscillators must also be verified but we will consider that these are working in their linear region. Indeed, the local oscillators are equipped with a "leveled/unleved" indicator, a feature which helps assuring that the outputted powers of the signals are in accordance with the desired levels. Once the nonlinear characteristics of the equipments are found, we will be able to find an operation region in which they will not affect the characterization of the transmission chain.

The ESA used in the IP3 measurements is an Anritsu MS2719B. Its internal attenuator is set to zero at this stage. We perform the IM3 characterization from 2 to $19GHz$ and in each measurement the fundamental tones generated by two Anritsu MG3692B signal generators are separated by $10MHz$. The lower and higher limitations on the frequency span are respectively due to a frequency limitation and power leveling issues on the local oscillators. Ideally, an isolator or circulator is inserted after each LO to avoid the reflections of the signals, which may disturb the measurement. However, since we vary our frequency span considerably, we could not use any kind of isolator after the signal generators. We consider that the coupler, a PULSAR PS2-18-450/9S, provides for the needed isolation.

To improve the signal-to-noise ratio of the ESA measurement and reduce the variance of the measured distortion products that appear close to the noise floor, we set the ESA's resolution bandwidth (RBW) and video bandwidth (VBW) to very low values: 3 and $1Hz$ respectively. In order to reduce the measurement time caused by such small values of RBW and VBW, we place the ESA in very narrow spans ($500Hz$) where only one of the fundamental tones or distortion products is displayed at a time. We perform then 4 measurements: one for each fundamental tone f_1 and f_2, one for the left-side IM3 $2f_1 - f_2$ and the other for the right-side IM3 $2f_2 - f_1$. The clock references of the signal generators and the ESA are all locked to one same reference to provide better results.

Figure A.1 shows the measurement of the ESA and power coupler nonlinear characteristics. Right-hand side insets shows the measurement at $18.805GHz$ central frequency and $-4dBm$ input power. The reader should notice that the signals' levels may be slightly different one for the other and the same may happen with the IM3 products. We chose a conservative approach by taking the worst-case IM3. The ratio between the angular coefficients a_2/a_1, which is ideally 3, is used to provide an estimation of the quality of the linear fittings that are necessary to find the intersection of the curves. From it, we deduce a maximum fitting error of $\pm 6\%$.

From Figure A.1, we can consider a worst-case IIP3 (OIP3) of 22.8dBm (16.16dBm). In order to avoid the influence of the ESA and coupler on the nonlinearities estimation of the optical components, we can take, for instance, a $20dB$ back-off. In such case, the input power

at the ESA should not exceed $2.8dBm + 3dB = 5.8dBm$. Here, we have already added up the powers of both local oscillators.

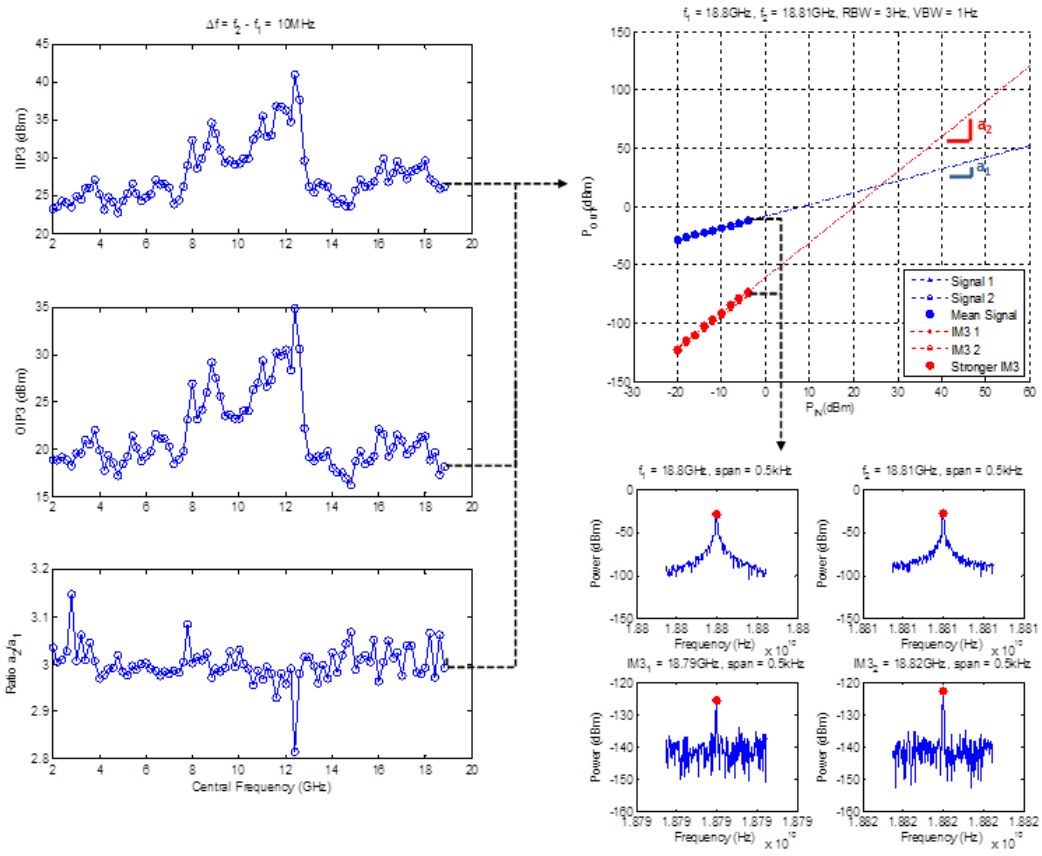

Figure A.1: Nonlinear characterization of ESA and power coupler.

Appendix B

Generation of Squared and Rectangular Gray-mapped Constellations

Figure B.1 shows the procedure allowing to create a gray-mapped constellation from a binary sequence. The same procedure can be adopted when b is an odd number by separating it into $\frac{b+1}{2}$ bits for the I component and $\frac{b-1}{2}$ for the Q component (or vice versa) and changing the summing factor from $\left[-\left(2^{\frac{b}{2}}-1\right)\right]$ to $\left[-\left(2^{\frac{b+1}{2}}-1\right)\right]$ and $\left[-\left(2^{\frac{b-1}{2}}-1\right)\right]$ for the I and Q bits respectively. This results in a Gray-mapped rectangular constellation.

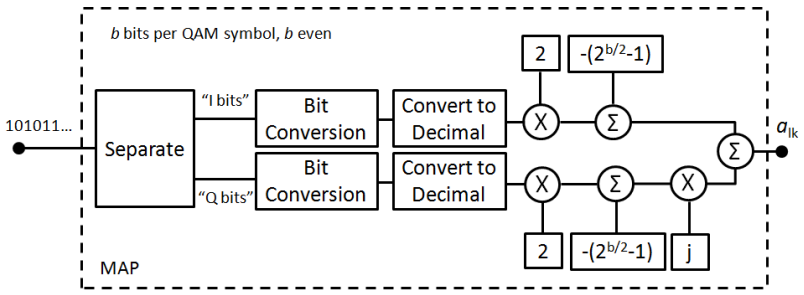

(a)

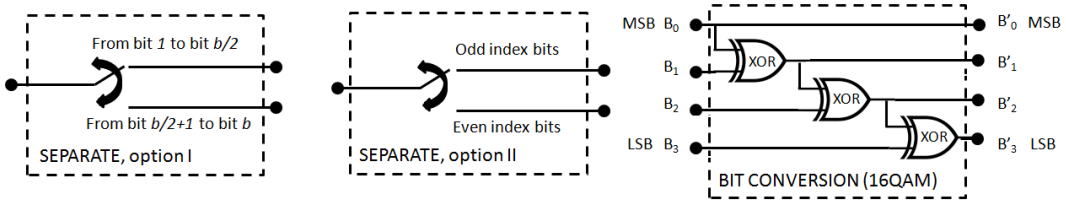

(b)

Figure B.1: (a) Block diagram for squared QAM constellation generation. (b) Detail on the sub-blocks "Separate" and "Bit-conversion" (16QAM example).

Appendix C

TOSA-DFB Chirp Measurements

Figures C.1 to C.5 shows the $|S_{21}|$ measurements for different bias currents and the corresponding values of α, f_c and D found after fitting using the Nelder-Mead algorithm.

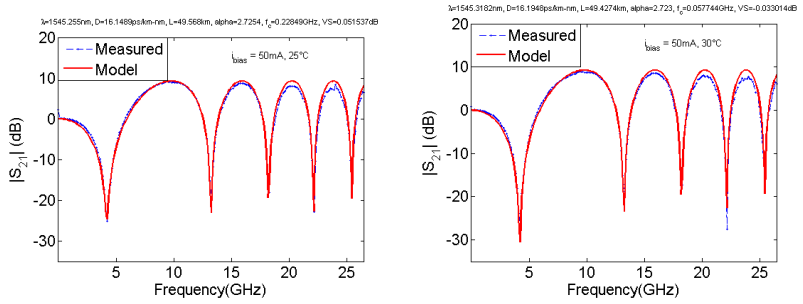

(a) (b)

Figure C.1: Chirp measurements based on IMDD IM+PM+FM model for 50mA at (a) 25°C and (b) 30°C.

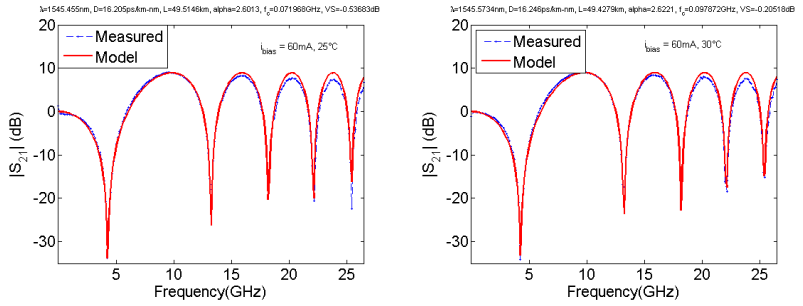

(a) (b)

Figure C.2: Chirp measurements based on IMDD IM+PM+FM model for 60mA at (a) 25°C and (b) 30°C.

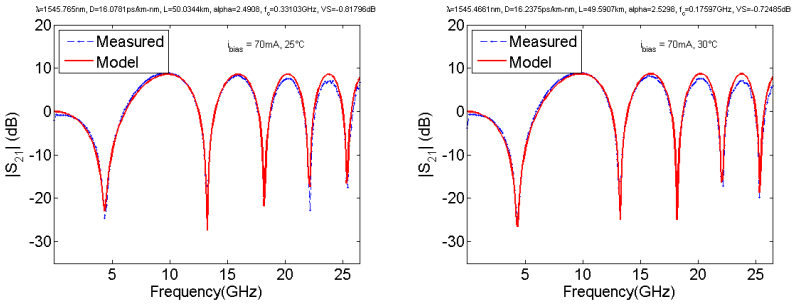

(a) (b)

Figure C.3: Chirp measurements based on IMDD IM+PM+FM model for 70mA at (a) 25°C and (b) 30°C.

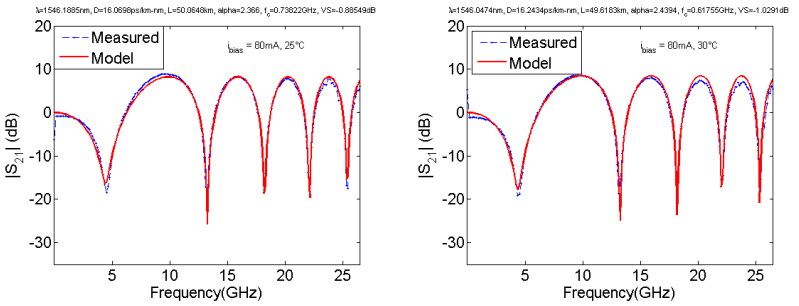

(a) (b)

Figure C.4: Chirp measurements based on IMDD IM+PM+FM model for 80mA at (a) 25°C and (b) 30°C.

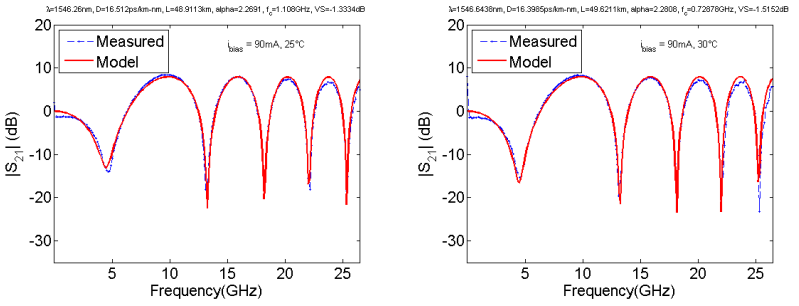

(a) (b)

Figure C.5: Chirp measurements based on IMDD IM+PM+FM model for 90mA at (a) 25°C and (b) 30°C.

Appendix D

Publications as First Author

- High Bit Rate Burst Mode Optical OFDM for Next Generation Passive Optical Networks, *ECOC 2010*
- Transmissions OFDM en Mode Rafale avec des Composants à Faible Bande Passante pour les Réseaux d'Accès, *JNOG 2010*
- 10Gb/s continuous Clock and Data Recovery for Burst Mode Transmissions with Externally Modulated Laser, *ANIC 2010*
- Up to 40Gb/s Optically Amplified AMOOFDM for Next Generation PON Networks, *OFC/NFOEC 2011*
- On the Interest of Chirped Lasers for AMOOFDM Transmissions through Long Distance PON Networks, *OFC/NFOEC 2011*
- 10Gb/s over 513km Uncompensated SSMF Link Using Direct Modulation and Direct Detection, *ECOC 2011*
- On the Limitations of IM/DD WDM FDMA-OFDM PON with Single Photodiode for Upstream Transmission, *OFC/NFOEC 2012*
- Experimental Investigation of Dispersion-induced Distortions in IMDD OFDM PON Transmissions, *ECOC 2012*
- Simple Estimation of Fiber Dispersion and Laser Chirp Parameters Using the Downhill Simplex Fitting Algorithm, *Journal of Lightwave Technology 2012*

Appendix E

Co-authored Publications

- Optical Transmission Performance for DML Considering Laser Chirp and Fiber Dispersion using AMOOFDM, *FOAN 2010*
- Technical Options for NGPON2 Beyond 10G PON, *ECOC 2011*
- Optical Transmission Performance for Directly Modulated Laser Considering Laser Chirp and fiber Dispersion Using Adaptively Modulated Optical Orthogonal Frequency Division Multiplexing, *FIO 2011*
- Up to 10Gbit/s Transmission in WDM-PON Architecture using External Cavity Laser based on Self-tuning ONU, *OFC/NFOEC 2012*
- Transmission jusqu'à 10Gbit/s Basée sur un Laser 'Cavité Externe Utilisant un RSOA et un Réseau de Bragg Photo-inscrit sur Fibre pour WDM-PON, *JNOG2012*
- On the Performance of Timing Synchronization Techniques for Optical OFDM IMDD Transmission, *IEEE Photonics conference 2012*

Contents

Acronyms

10G-EPON 10 Gigabit Ethernet PON

ADC Analog-to-Digital Converter

ADSL Asymmetric Digital Subscriber Line

AGC Automatic Gain Control

ALPHA Architectures for Flexible Photonic Home and Access Networks

AMOOFDM Adaptively Modulated Optical OFDM

APD Avalanche Photodiode

APON ATM-based PON

ARCEP Autorité de Régulation des Communications Électroniques et des Postes

ASHA Advanced Studies on Home and Access networks

ASIC Application Specific Integrated Circuit

ATM Asynchronous Transfer Mode

AWG Arbitrary Waveform Generator

AWGg Arrayed Waveguide Grating

AWGN Additive White Gaussian Noise

BA Bandwidth Adaptive

BER Bit Error Rate

BL Bit rate-distance Product

BONE Building the Future Optical Network in Europe

BPON Broadband PON

C2S2 Composants, Circuits, Signaux et Systèmes Haute Fréquence

CAPEX Capital Expenditure

CBU Cell-site Backhaul

CCDF Complementary Cumulative Distribution Function

CDR Clock and Data Recovery

CFO Carrier Frequency Offset

CIR Channel's Impulse Response

CML Chirp Managed Lasers

CO-OFDM Coherent OFDM

CP Cyclic Prefix

CW Continuous-wave

CWDM Coarse WDM

DAB Digital Audio Broadcasting

DAC Digital-to-Analog Converter

DC Direct Current

DCF Dispersion-compensating Fibers

DD-OFDM Directly-Detected OFDM

DFB Distributed Fedback Laser

DFE Decision Feedback Equalizer

DGD Differential Group Delay

DGE Dynamic Gain Equalizer

DMF Dispersion Managed Fibers

DML Directly Modulated Laser

DSF Dispersion-shifted Fiber

DSL Digital Subscriber Line

DSO Digital Sampling Oscilloscope

DSW Double-sliding-window

DWDM Dense WDM

EA Electrical Amplifier

EDC Electronic Dispersion Compensation

EDFA Erbium Doped Fiber Amplifiers

EM External Modulator

EML Externally Modulated Lasers

EPOD Enhanced PON using OFDM Modulation Format

ESA Electrical Spectrum Analyzer

EVM Error Vector Magnitude

FAON Frequency Based Access Optical Network

FBG Fiber Bragg Grating

FDE Frequency Domain Equalization

FDM Frequency Division Multiplexing

FDMA Frequency Division Multiple Access

FEC Forward Error Correcting

FFT Fast-Fourier-Transform

FM Frequency Modulation

FSAN Full Service Access Network

FTTB Fiber-To-The-Building

FTTbs Fiber-To-The-base-station

FTTC Fiber-To-The-Curb

FTTdp Fiber-To-The-distribution-point

FTTH Fiber-To-The-Home

FTTLA Fiber-To-The-Last-Amplifier

FTTP Fiber-To-The-Premises

FWM Four-Wave Mixing

GDSH Gated-delayed Self-homodyne

GEPON Gigabit Ethernet PON

GPON Gigabit PON

GVD Group-Velocity Dispersion

HD High Definition (Video)

ICI Inter-carrier Interference

IDFT Inverse Discrete Fourier Transform

IEEE Institute of Electrical and Electronics Engineers

IFFT Inverse Fast Fourier Transform

IM Intensity Modulation

IM3 Third-order Intermodulation Distortion

IMDD Intensity modulation and direct detection

IP Internet Protocol

ISI Inter-symbol Interference

ITU International Telecommunication Unions

LA Line Amplifiers

LCA Levin-Campello Algorithm

LE Linear Equalization

LMS Least Mean Square

LS Least Square

LSB Left-side Band

LSR Large-Signal Regime

LTE Long Term Evolution

MA Margin Adaptive

MB-OFDM Multiband OFDM

MCM Multi-carrier Modulation

MDU Multi-dwelling Unit

ML Maximum Likelihood Criteria

MMSE Minimum Mean-Square Error estimator

MODULE Modulation Duale d'un Composant Intégré

MZM Mach-Zehnder Modulator

NF Noise Figure

NG-PON Next-Generation Passive Optical Network

NG-PON1 Next Generation PON 1

NG-PON2 Next Generation PON 2

NGOA Next Generation Optical Access

NLSE Non-linear Shrödinger Equation

NRZ Non-Return-to-Zero

NZDSF Nonzero Dispersion-Shifted Fiber

OBI Optical Beat Interference

OBPF Optical Band-Pass Filter

ODC Optical Dispersion Compensator

ODN Optical Distribution Network

ODSB Optical Double-Side-Band

OEO Optical-electrical-optical Conversion

OFDM Orthogonal Frequency Division Multiplexing

OLT Optical Line Termination

ONT Optical Network Termination

ONU Optical Network Unit

OOK On-off Keying

OSA Optical Spectrum Analyzer

OSNR Optical Signal-to-noise Ratio

OSSB Optical Single-Side Band

OTDR Optical Time Domain Reflectometer

P2MP Point-to-multipoint

P2P Point-to-point

PAM Pulse Amplitude Modulation

PAPR Peak-to-Average Ratio

PIN P-type, Intrinsic, N-type Photodetector

PLC Power Line Communications

PM Phase Modulation

PMD Polarization Mode Dispersion

PON Passive Optical Network

PRBS Pseudorandom Binary Sequence

PSK Phase-Shift Keying

QAM Quadrature-Amplitude Modulation

QoS Quality of Service

R-EAM-SOA Reflective Electroabsorption Modulators with Semiconductor Optical Amplifiers

RA Rate Adaptive

RIN Relative Intensity Noise

RLS Recursive Least Squares

RSB Right-side Band

RSOA Reflective Semiconductor Optical Amplifier

SBS Stimuated Brillouin Scattering

SBU Single-business Unit

SC Single Carrier

SCM Subcarrier Multiplexed

SD-OFDM Sparsely-Distributed OFDM

SER Symbol Error Rate

SFDR Spurious-free Dynamic Range

SFO Sampling Frequency Offset

SFU Single-family Unit

SI-POF Step-index Plastic Optical Fibers

SMS Short-Message Service

SNR Signal-to-noise Ratio

SPM Self-phase Modulation

SRS Stimuated Raman Scattering

SSMF Standard Single-Mode Fiber

SSR Small-Signal Regime

STO Sample Timing Offset

SVEA Slowly Varying Envelope Approximation

SW Sliding-window

TDE Time Domain Equalization

TDM Time Division Multiplexing

TDMA Time Division Multiple Access

TIA Transimpedance Amplifier

TOD Third-Order Dispersion

TOSA Transmission Optical Sub-assembly

TRILOB Modules de Transmission et Réception pour Liaison Optique à fort Budget

TWDM Time and Wavelength Division Multiplexin

UDWDM Ultra-dense WDM

VCSEL Vertical Cavity Surface Emitting Laser

VDSL2 Very-High-Bit-Rate Subscriber Line 2

VOA Variable Optical Attenuator

VOD Video on Demand

VSSB Virtual Single Sideband

WDM Wavelength Division Multiplexing

WDMA Wavelength Division Multiple Access

WF Water-filling

WiMAX Worldwide Interoperability for Microwave Access

WLAN Wireless Local Area Network

XG-PON1 10 Gigabit PON

XPM Cross-phase Modulation

ZF Zero-forcing

List of Figures

List of Tables

Doctorat de l´Université de Limoges, spécialité: Électronique des Hautes Fréquences et Optoélectronique.
Soutenu le 14/12/2012 par Luiz Anet Neto

STUDY OF THE POTENTIALITIES OF MULTICARRIER MODULATION TECHNIQUES FOR FUTURE WDM AND TDM PASSIVE OPTICAL ACCESS NETWORKS

Abstract: Despite its success in radio-frequency applications, OFDM has only recently started to draw the attention of the optical community owing principally to the outstanding advancements in electronics and the increasing demands in terms of bit-rates in the last miles of the network. OFDM appears as one possible solution to cost-effectively provide the long-awaited flexibility that lacks on today's somewhat "rigid" passive optical networks (PON). It may also allow their evolution towards higher bit-rates, longer transmission distances and increased number of subscribers per PON tree. Here, we focus on the IMDD approach, which can manage to keep the simplicity and cost-effectiveness at the optical plane by transferring the "hard work" to the digital signal processing domain.

We focus this work on two main axes. In the first one, we study the influence of the dispersive IMDD channel frequency response characterized by the interplay between fiber chromatic dispersion and the parasite phase modulation of the light source (chirp) and the ways of optimizing the system's throughput by means of bit and power loading algorithms. Secondly, we evaluate the IMDD OFDM approach under different architectures. Those architectures characterize distinct solutions to share the network resources between the subscribers, namely time, wavelength and frequency multiplexing.

Key-words: Passive Optical Networks, Orthogonal Frequency Division Multiplexing, Intensity Modulation and Direct Detection, Time Division Multiplexing, Time Division Multiple Access, Frequency Division Multiplexing, Frequency Division Multiple Access, Wavelength Division Multiplexing, Wavelength Division Multiple Access, Transient Chirp, Adiabatic Chirp, Chromatic Dispersion, Next Generation Passive Optical Networks

ÉTUDE DES POTENTIALITÉS DES TECHNIQUES DE MODULATION MULTIPORTEUSE POUR LES FUTURS RÉSEAUX D'ACCÈS OPTIQUE WDM ET TDM PON

Résumé: Malgré son succès dans le domaine des radio-fréquences, l'OFDM n'a que récemment commencé à attirer l'attention de la communauté optique grâce à une remarquable évolution de l'électronique et aux demandes de débit de plus en plus élévées dans les réseaux d'accès. OFDM apparaît comme un très fort candidat pour fournir la flexibilité tant attendue dans les réseaux d'accès optiques "rigides" d'aujourd'hui ayant aussi le potentiel de permettre une évolution vers des débits, portées et nombre d'abonnés plus élévés. Dans cette thèse, nous nous concentrons sur une approche de modulation en intensité et détection directe (IMDD) qui permet de conserver la simplicité sur le plan optique en transférant la complexité de la transmission au domaine du traitement numérique du signal.

Ce travail se base sur deux axes principaux. Dans le premier, nous étudions l'influence de la réponse fréquentielle du canal, caracterisée par l'interaction entre la dispersion chromatique de la fibre optique et la modulation parasite en phase provenant de la source optique et les moyens d'optimiser le débit du système avec des algorithmes d'allocation de puissance et modulation. Deuxièmement, nous évaluons l'approche IMDD OFDM sous différentes architectures et techniques de partage des ressources du réseau entre les abonnées, à savoir les multiplexages en temps, longueur d'onde et fréquence.

Mots-clés: Réseaux Optiques Passifs, Multiplexage par Division en Fréquences Orthogonales, Modulation en Intensité et Détection Directe, Multiplexage par Division Temporelle, Accès Multiple par Division Temporelle, Multiplexage par Division en Fréquences, Accès Multiple par Division en Fréquences, Multiplexage par Division en Longueur d´Onde, Accès Multiple par Division en Longueur d´Onde, Chirp Transitoire, Chirp Adiabatique, Dispersion Chromatique, Réseaux Optiques Passifs de Nouvelle Génération.

Institut XLIM, Département C2S2 - 123 Avenue Albert Thomas, 87060 Limoges Cedex, France.
Tél.: 33 (0)5 55 45 72 50, Fax: 33 (0)5 55 45 76 97 - http://www.xlim.fr